

Ruhr-Universität Bochum
Institut für Geologie, Mineralogie und Geophysik



Experimental Deformation of Jadeite

Dissertation von

Jens Orzol

Vorgelegt zur Erlangung des Grades eines Doktors der Naturwissenschaften.

Juni 2002

Contents

1	Introduction and scope	1
1.1	Introduction	1
1.2	Scope of the study	2
2	Background	4
2.1	Phase transformation and crystallization	4
2.2	Defects, deformation mechanisms and flow laws	5
2.2.1	Point defects and diffusion creep	6
2.2.2	Dislocations and dislocation creep	7
2.2.3	Mechanical twinning	10
2.2.4	Method for the determination of flow law parameters	10
3	Stability field and physical properties of jadeite	13
4	Sample material	16
4.1	Synthesis of jadeitite aggregates	16
4.1.1	Introduction	16
4.1.2	Method	17
4.1.2.0.1	Preparation of the glass	17
4.1.2.0.2	Sample preparation, apparatus and experimental procedure	18
4.1.3	Overview of synthesis experiments	19
4.1.4	Sample analysis	22
4.1.5	Results and discussion of the synthesis experiments	24
4.1.6	Description of standard samples for deformation experiments	31
4.1.7	Fourier-transform infrared measurements	33
4.2	Description of natural jadeitite samples	36
5	Deformation experiments	39
5.1	Method	39
5.1.1	The solid-medium apparatus	39
5.1.2	Confining medium and sample preparation	39

5.1.3	The pressure cell	41
5.1.4	Assemblage of the pressure cell	43
5.1.5	Experimental procedure	43
5.2	The force versus displacement curve	44
5.3	Derivation of stress versus strain curves from force versus displacement curves	48
6	Results of the deformation experiments	51
6.1	Mechanical data	51
6.1.1	Mechanical data for synthetic jadeitite samples	51
6.1.2	Mechanical data for natural jadeitite samples	56
6.2	Microstructural observations on deformed jadeitite samples	59
6.2.1	Microstructural observations on deformed synthetic jadeitite samples	59
6.2.2	Microstructural observations on deformed natural jadeitite samples	65
6.3	Critical resolved shear stress for twinning	68
6.3.1	Method	68
6.3.2	Results	69
7	Discussion	71
7.1	Uncertainties in differential stress, temperature, confining pressure and strain rate	71
7.1.1	Uncertainty in differential stress	71
7.1.2	Uncertainties in strain rate, temperature and confining pressure . .	75
7.2	Derivation of flow law parameters	78
7.2.1	Derivation of the flow law parameters for synthetic jadeitite samples	78
7.2.2	Derivation of the flow law parameters for natural jadeitite samples .	81
7.2.3	Discussion of the activation energy for dislocation creep of jadeite .	84
7.3	Interpretation of microstructures of deformed samples	85
7.3.1	Interpretation of microstructures of deformed synthetic samples . .	86
7.3.2	Interpretation of microstructures of deformed natural samples . . .	89
7.4	Errors inherent in the extrapolation to natural strain rates	90
7.5	Normalized representation of flow laws	93
7.6	Comparison of natural and synthetic samples	95

<i>CONTENTS</i>	iii
7.7 Application of results to geological processes	98
8 Summary	102
References	105
A Overview of deformation experiments	116
B Force versus displacement curves	119
C Stress versus strain curves	137

List of Figures

1	Phase equilibria	14
2	Paths of synthesis experiments 1	20
3	Paths of synthesis experiments 2	21
4	Grain size distributions	25
5	Micrographs of synthetic jadeitite samples	29
6	Undeformed reference sample	32
7	Two infrared spectra of synthetic jadeitite samples	34
8	X-ray diffraction patterns	38
9	Sketch of the sample assembly	42
10	A typical force vs. displacement curve	45
11	Slopes prior to the hit-point	50
12	Results of deformation experiments on synthetic samples	55
13	Results of deformation experiments on natural samples	58
14	Micrographs of deformed synthetic samples	61
15	Pole figures showing crystallographic orientation in synthetic samples	65
16	Micrographs of deformed natural samples	67
17	Estimate of uncertainty in stress	74
18	Relative oven power as a function of temperature	76
19	Estimate of confining pressure from force vs. displacement curves	77
20	Fit of the experimental data by the power law flow law for synthetic samples	80
21	Fit of the experimental data by the power law flow law for natural samples	83
22	Uncertainty of the extrapolation of the flow law	92
23	Normalized flow laws	94
24	Comparison of stress vs. strain curves for synthetic and natural jadeitite samples	97
25	Extrapolation of relevant flow laws	100

List of Tables

1	Physical properties of jadeite	15
2	X-ray fluorescence analysis of glasses	18
3	Overview of synthesis experiments	22
4	Grain size of synthesized samples	26
5	Water content of deformed and undeformed synthetic jadeitite samples	36
6	Microprobe analyses of natural jadeitite	37
7	Sample dimensions	49
8	Mechanical data of synthetic samples	53
9	Mechanical data of natural samples	57
10	Resolved shear stresses related to mechanical twinning	69
11	Effect of temperature gradients on differential stresses	72
12	Data of synthetic jadeitite used for derivation of flow law parameters	78
13	Data of natural jadeitite used for derivation of flow law parameters	81
14	Comparison of flow law parameters for natural and synthetic jadeitite	95
15	Flow law parameters for diopside and jadeitite	99

List of symbols and abbreviations

symbol	explanation	unit
l_0	initial length of sample	<i>mm</i>
d_0	initial diameter of sample	<i>mm</i>
V_0	initial volume of sample	<i>mm</i> ³
l_f	final length of sample	<i>mm</i>
d_f	final diameter of sample	<i>mm</i>
V_f	final volume of sample	<i>mm</i> ³
Δl	sample shortening	<i>mm</i>
ε	true strain	
$\dot{\varepsilon}$	strain rate	<i>s</i> ⁻¹
$\Delta\sigma$	differential stress	<i>MPa</i>
T	temperature	$^{\circ}\text{C}$
T_{Melt}	melting temperature	$^{\circ}\text{C}$
n	stress exponent	
Q	activation energy	<i>kJ/mol</i>
A	preexponential factor in power law	<i>MPa</i> ^{-n} <i>s</i> ⁻¹
G, μ	shear modulus	<i>GPa</i>
v_p	velocity of axial piston	<i>mm/s</i>
\vec{m}	model vector	
\vec{d}	data vector	
$\vec{\varepsilon}$	error vector	
k	Boltzmann constant	<i>JK</i> ⁻¹
R	gas constant	<i>Jmol</i> ⁻¹ <i>K</i> ⁻¹
m_{pre}	slope of force vs. displacement curve prior to hit point	<i>kN/mm</i>
m_{post}	slope of force vs. displacement curve at nominal elastic loading	<i>kN/mm</i>
$\delta\sigma$	change in dynamic friction	<i>MPa</i>
OP	relative oven power	%
EBSD	electron backscatter diffraction	
CPO	crystallographic preferred orientation	
SPO	shape preferred orientation	
TEM	transmission electron microscopy	

1 Introduction and scope

1.1 Introduction

Oceanic lithosphere is continuously formed at mid-ocean ridges. It typically shows a layered structure with a 6-7 km thick basaltic crust as the upper layer that is underlain by a 16-20 km thick harzburgite layer and a 50-60 km thick lower layer of lherzolite (Nicolas, 1989). When oceanic lithosphere is subducted, the basaltic upper layer adapts to the change in pressure and temperature conditions by transforming to eclogite. To reach eclogite facies conditions, temperatures in excess of approximately 380°C and pressures above 1.2 GPa are necessary (Bucher and Frey, 1994). When kinetics is sluggish, however, transformation might require considerable overstepping of these conditions. Reactions may be accelerated by the presence of an aqueous fluid. Although poorly constrained by experimental work (Peacock, 1996), complete transformation in subduction zones is expected at depths ranging between 40 km and 80 km. In contrast to the basalt, the eclogite layer has a higher density relative to the adjacent mantle which contributes to slab-pull forces. This eclogitisation is assumed to be a key factor in plate tectonics, as it influences a variety of aspects related to subduction, as for the instance the rheology, seismicity, buoyancy or water content of the subducting oceanic crust (e. g. Hacker, 1996).

The prominent position of the eclogite layer as the upper part of the subducted lithosphere explains the importance of its rheological properties, as it is in direct contact with the base of the overriding lithospheric plate. The knowledge of the state of stresses within the eclogite layer is poor, however. Estimates of the stresses vary between a few MPa to about 100 MPa (Scholz, 1980; Molnar and England, 1990; Hyndman and Wang, 1993; Ruff and Tichelaar, 1996; Peacock, 1996; Stöckhert *et al.*, 1997; Wang and He, 1999; Piepenbreier and Stöckhert, 2001).

Peacock (1996) found by numerical modelling that the rate of shear heating largely controls the thermal structure of subduction zones and thus the petrological structure. The amount of thermal energy is linearly related to the rate of convergence and the shear stress (Turcotte and Schubert, 2002). Scholz (1980) showed that for ductile flow to be an effective mechanism of heat generation, stresses of approximately 130 MPa are required, provided that a convergence rate of 3 cm/y is maintained over 10^7 years. Intensive heating

of the core of such shear zones may promote concentration of deformation and thermal softening. Molnar and England (1990) proposed using heat flow measurements to constrain the magnitude of shear stresses. They concluded that stresses of 100 MPa may be exceeded.

Philippot and van Roermond (1992) presented evidence for the delamination of the oceanic crust at a depth of 40-50 km from the microstructures of exhumed rocks. Delamination is promoted by the occurrence of relatively weak zones within the crust due to major changes in rheology (Kearey, 1993). It may be that the deformation becomes localized within the eclogite layer.

Stöckhert *et al.* (1997) pointed out the potential for constraining the state of stress along plate boundaries by analysing naturally-deformed rocks. In their analysis of naturally-deformed rocks, Philippot and van Roermond (1992) found that omphacites constitute interconnected weak layers. This is confirmed by van der Klauw *et al.* (1997) and Lorimer (1976), who showed that garnets are contained as rigid inclusions within a highly strained omphacite matrix, indicating contrasting strengths of the two main constituents of eclogite (Hacker, 1996). Buatier *et al.* (1991) determined that dislocation creep was the dominant deformation mechanism in deformed omphacites by examining the microstructure and dislocation substructure. Piepenbreier and Stöckhert (2001) made similar observations and constrained the temperatures for deformation in the dislocation creep regime by thermobarometry and microstructural analysis to below 500°C. In contrast, existing experimentally-calibrated flow laws for the pyroxene solid-solution end-member diopside (e.g. Boland and Tullis, 1986; Bystricky and Mackwell, 2001) predict unrealistically high strength for temperatures lower than 700°C. Higher homologous temperatures (T_{Melt}/T) for the sodic end-member jadeite and for omphacite suggest lower stresses, being consistent with the findings for naturally-deformed rocks (Stöckhert and Renner, 1998).

1.2 Scope of the study

The introduction elucidated the importance of eclogite rheology for interplate coupling, shear heating and the necessity of providing better input parameters for the modelling of subduction processes (Gerya *et al.*, 2002). Jadeite and omphacite are better indicators for the prediction of the bulk strength of the eclogite layer than diopside. This was suggested

by e.g. Piepenbreier and Stöckhert (2001) on the basis of microstructural analysis of naturally-deformed rocks together with considerations on presently available flow laws for diopside. Although it has been observed that natural omphacites deform by dislocation creep, Stöckhert and Renner (1998) assumed that dissolution precipitation creep may be the dominant deformation mechanism in subduction zones at much lower stresses. Nevertheless, the knowledge of dislocation creep rheology of jadeite will be useful for constraining the upper limits of shear stresses in the eclogite layer.

It is not expected though, that the mechanical behaviour of omphacite, which is of primary interest as it is dominant in eclogites, equals the mechanical behaviour of jadeite. Jadeite is the end-member of the solid-solution series jadeite-diopside, whereas omphacite is of the intermediate composition. The dependence of mechanical properties on the composition in solid solution is not known at present and needs to be explored. The rheology of diopside is already constrained by several experimental studies and, as a systematic approach the rheology of jadeite is investigated here. Investigation of the rheology of the intermediate omphacite composition will be the subject of future studies.

Objective of this study is the experimental calibration of a mechanical equation of state that describes the rheology of jadeite in the dislocation creep regime at conditions prevailing in subduction zones. Compression tests on polycrystalline samples under high confining pressure were used to constrain the rheological properties. First, the mode of performing the deformation experiments had to be adjusted with respect to those employed previously (Konrad, 1997; Rybacki *et al.*, 1998; Renner *et al.*, 2001). The adjustments involved changes in the test assembly as well as the experimental procedure. Experiments were carried out on synthetic jadeite samples and on natural jadeite samples. The results for the synthetic and natural samples are compared and the relative merits of the different kinds of samples are shown. Analysis of the deformed natural samples allows the determination of the critical resolved shear stress for twinning in jadeite. From the results conclusions are drawn for the rheology of eclogite.

2 Background

2.1 Phase transformation and crystallization

Overviews of the theories for phase transformations and related aspects are given in the literature of material sciences (Pelton, 1991; Jena and Chaturvedi, 1992; Porter and East-erling, 1997). Application to geological materials is emphasized by Putnis and McConnel (1980). Cited works in that section may only serve as examples.

Commonly, theories consider the transition from one crystalline phase to another. However, the general principles apply also to the transition from a glass to a crystalline phase. A glass may be defined as 'an amorphous solid usually formed by the solidification of a melt without crystallisation' (Hlaváč, 1983). Crystallisation from a glass is controlled by its melting temperature, the nucleation rate and the crystal growth rate. Here, some basic principles will be summarized.

Systems aim to minimize their Gibbs free energy $G=H-TS$, given in terms of enthalpy H , entropy S and temperature T , to yield an equilibrium state. The basic condition for a phase transformation to occur is the departure from an equilibrium state (Jena and Chaturvedi, 1992). Adjustment of the system to the new conditions allows further minimisation of its energy. Transformations may be classified into first and second order transformations by characteristics of the first derivative of the Gibbs free energy or by the structural differences of the phases involved (Putnis and McConnel, 1980). With the enthalpy $H = U + pV$ (U : internal energy of the system, p : pressure, V : volume of the system) the Gibbs free energy is a function of pressure and temperature. Phase diagrams may then be derived to display the equilibrium conditions of the phases as a function of pressure and temperature. Provided temperature is high enough to allow for reasonable fast kinetics, a glass crystallizes when subject to pressure and temperature conditions below the liquidus, as the crystalline phase exhibits a lower Gibbs free energy. Thermal fluctuations may randomly generate nuclei of the stable phase (homogeneous nucleation) or nucleation may occur at interfaces to foreign particles, pores or the walls of the container (heterogeneous nucleation). The bulk free energy decrease is opposed by the increase of surface and elastic strain energy with increasing size of the nuclei (Rao and Rao, 1978). An energy balance shows that a critical radius r_c is required for the nuclei to grow further. For

$r \leq r_c$ the so-called embryo are unstable and disappear. The size of the critical radius is a function of undercooling, which represents the deviation from equilibrium (Fine, 1965). A similar argument applies to the nucleation rate, which is the number of nuclei appearing per unit volume of the parental phase per unit of time. With deviation from equilibrium, a small interval ΔT is observed first, for which the nucleation rate is small or negligible. This is followed by a rapid increase in nucleation rate with increasing undercooling, until a critical undercooling is reached. Further undercooling leads to a decrease in nucleation rate (Hlaváč, 1983). Introduction of crystalline nucleation agents drastically lowers the required degree of undercooling for crystallisation. The strain energy introduced by the different specific volumes of the relevant phases also affects nucleation rate.

Once the radius of a newly formed nucleus exceeds a critical radius it is continuously growing. The growth rate of the nuclei, i.e. the velocity of the migrating boundaries obeys the same qualitative dependence on undercooling as the nucleation rate (Hlaváč, 1983). Besides, it is strongly affected by the temperature-dependent viscosity of the melt or glass. A low viscosity provides a poor mobility of the structural units. Surfaces with high energies exhibit continuous growth, whereas layer growth occurs on smooth, planar surfaces (Putnis and McConnell, 1980). When atoms attach to edges of layers or steps, the rate of their lateral spreading is a function of the rate of arriving atoms, their motion on the surface, or on the interfacial reactions. All of these processes are thermally activated.

2.2 Defects, deformation mechanisms and flow laws

Estimation of shear strength as the theoretical elastic limit of an ideal crystal structure predicts stresses on the order of a tenth of the shear modulus (Frenkel, 1926). In contrast, it is observed that the actual elastic limit is several orders of magnitude lower. This contradiction requires the introduction of defects within the lattice of the crystal to account for intracrystalline plasticity (e.g. Nicolas and Poirier, 1976). Movement of these defects causes irreversible deformation. Microphysical models aim to predict the macroscopic behaviour of crystalline solids on the basis of the defect mobility as a function of external variables, in particular differential stress and temperature. From these models, mechanical equations of state, commonly called flow laws, can be derived. A general mechanical equation of state relates the strain rate to the applied differential stress, temperature,

grain size, composition, strain and microstructure of the material (Poirier, 1985).

Some of the basic principles will be outlined below. For a detailed description, the reader is referred to the rockphysics literature (Nicolas and Poirier, 1976; Rummel, 1982; Poirier, 1985; Evans and Kohlstedt, 1995; Poirier, 1995; Ranalli, 1995). Most of the basic concepts have been developed in the field of physical metallurgy for simple metallic structures. With some limitations, principles are similar for the silicates in geological materials which, however, are more complex in terms of lattice symmetry and bonding.

2.2.1 Point defects and diffusion creep

Defects break the periodicity of the crystal structure and can be classified according to their dimension. Point defects are zero-dimensional defects. One example is a vacancy, which is an empty lattice site. An atom that does not occupy a regular lattice site represents an interstitial point defect. On the other hand, a regular lattice site may be occupied with a foreign atom, an 'impurity'. For a given temperature, an equilibrium number of vacancies exists at the state of minimum free enthalpy of the crystal in the intrinsic regime. In the extrinsic regime, the concentration of vacancies is determined by the concentration of impurities. Point defects are charged in ionic crystals and occur in oppositely charged groups to ensure charge neutrality (Schottky pairs). For the same reason, aliovalent impurities require formation of additional point defects. Solid-state diffusion is the result of migration of point defects. Most deformation processes involving diffusion rely on the migration of vacancies. Vacancies move to level out gradients in point defect concentrations that are caused by differential stresses (Turcotte and Schubert, 2002). Vacancy mobility is given in terms of a diffusion coefficient and a concentration. The most prominent deformation mechanisms that rely solely on diffusion are Coble creep and Nabarro-Herring creep. Coble creep requires the existence of grain boundaries that serve as pathways for diffusion. For Nabarro-Herring creep vacancies move through the bulk volume. Nabarro-Herring creep is effective at higher temperature than Coble creep as the activation energy for lattice diffusion is higher than that for grain boundary diffusion (Poirier, 1985).

For both mechanisms, the strain rate is a linear function of the applied differential stress. The activation energy for diffusion creep equals the activation energy for self

diffusion of the slowest moving species in the crystal (Poirier, 1985). For the case of Nabarro-Herring creep, the strain rate is proportional to the inverse of the square of the grain size (d). For Coble creep, the strain rate is proportional to $1/d^3$. Both mechanisms may occur simultaneously with different contributions to the overall strain rate. Diffusion creep is effective at high temperature and a differential stress that is low enough to prevent activation of other deformation mechanisms like dislocation creep (Schmid, 1982). Lower grain size favours diffusion creep.

2.2.2 Dislocations and dislocation creep

Dislocations are one-dimensional defects in crystals. A dislocation is described by its Burgers vector \vec{b} and the direction of the dislocation line. The Burgers vector closes a circuit around the dislocation in a section normal to the dislocation line. For an edge dislocation the dislocation line and Burgers vector are perpendicular, whereas for a screw dislocation they are parallel. Mixed dislocations of these end-members do naturally occur (Hull, 1979). Dislocation lines do not end within a crystal; they either form closed loops that separate slipped parts of the crystal from unslipped parts, or they end at a surface or at a dislocation junction. Dislocation loops expand outwards under differential stress until they leave the crystal or encounter obstacles. Due to an elastic distortion of the crystal lattice in the vicinity of the dislocation line, elastic strain energy is introduced in the crystal. The energy of a single dislocation is a function of the square of the Burgers vector magnitude and of the dislocation density, which is the length of dislocation lines per unit volume. Dislocations interact through their stress fields, which may impede their relative motion. As dislocations progressively leave the crystal there is a need for their multiplication to produce high strain. A commonly quoted mechanism is the Frank-Read source (Read, 1953). Dislocation loops are emitted from a segment of a dislocation line which is pinned at two points and subject to stresses in excess of a critical stress.

Glide of dislocations within the glide plane is impeded by other defects and by the Peierls force, which results from the periodic potential energy associated with the lattice. It is caused by the need to break bonds for further migration of the dislocation line. Migration can be facilitated by formation of double kinks, which is thermally activated. These are bends in the dislocation line, whose lateral spreading is energetically more

favourable than overcoming the periodic potential energy barrier simultaneously for the whole dislocation. Dislocation glide is conservative by which no transport of matter is required. Dislocation glide leads to a hardening of the material with increasing strain, as the increasing number of dislocations impede each others motion.

At higher temperature the dislocation line acts as a source or sink of vacancies, allowing the dislocation to move out of its original glide plane. This process is called climb. It is a non-conservative process, as it requires mass transfer. To avoid the need for simultaneous removal or addition of whole rows of atoms, jogs are formed, which are analogous to kinks. They introduce a step in the dislocation line which spreads laterally. The climb velocity is controlled by thermally activated diffusion of vacancies to or from the dislocation (Poirier, 1995). Dislocation climb allows activation of softening mechanisms that lower the dislocation density and therefore counteract the hardening effect of dislocation glide.

The most common deformation mechanism at elevated temperatures and medium stresses involves dislocation glide and climb. At such conditions, strain is mainly produced by the glide of dislocations and the rate controlling process is dislocation climb. When the contributions of hardening and softening mechanisms are balanced, steady-state creep that can produce unlimited strain occurs at a constant stress.

A description of the bulk rheology is derived from Orowan's equation. It is a general mechanical equation of state which is based on microphysical properties:

$$\dot{\epsilon} = \rho \cdot b \cdot v. \quad (1)$$

It relates the strain rate $\dot{\epsilon}$ to the density of mobile defects ρ , their velocity v and a characteristic length b . In the case of dislocation creep, corresponding quantities are the density of mobile dislocations, the magnitude of their Burgers vector and their climb velocity. Numerous models have been developed that give these quantities as a function of stress, temperature, coefficient of self-diffusion and density of defect sources (Poirier, 1985). The most general is one first derived by Weertman (1968). For the case of dislocation creep, the Weertman equation gives the strain-rate as:

$$\dot{\epsilon} = \dot{\epsilon}_0 \left(\frac{\Delta\sigma}{\mu} \right)^n \exp \left(-\frac{\Delta H_{SD}}{kT} \right), \quad (2)$$

with $\dot{\epsilon}_0$ being a constant, μ the shear modulus, n the stress exponent, k the Boltzmann's

constant, T the absolute temperature, σ the differential stress and $\Delta H_{SD} = \Delta Q_{SD} + pV$ the activation enthalpy. Q_{SD} is the activation energy of self diffusion of the slowest moving species, p denotes pressure and V the volume of the system. The pressure dependence introduced by pV is usually neglected. The stress exponent is predicted to be in the range 3 to 5. Due to the dependence of $\dot{\epsilon}$ and $\Delta\sigma$, equation 2 is commonly referred to as power law. It is found empirically that a relation of the following form can be fit to the creep data. This relation is a special case of equation (2) (Ranalli, 1995):

$$\dot{\epsilon} = A \cdot \Delta\sigma^n \cdot \exp\left(-\frac{Q}{RT}\right), \quad (3)$$

with Q being the molar activation energy of the rate controlling mechanism, A a constant and R the gas constant. Besides the fit of the data to such a relation, identification of the mechanism of creep by climb-controlled glide requires the simultaneous appearance of the following features (Nicolas and Poirier, 1976):

- activation energy for creep corresponds to the activation energy for self-diffusion of slowest species,
- stress exponent in the range from 3 to 5,
- characteristic steady-state microstructure,
- little or no influence of the grain size.

The correspondance of activation energies for creep and diffusion is well established for metals (Ashby and Verral, 1977), but is not experimentally proven for geological materials. One problem is the fact that conditions of diffusion experiments deviate from conditions under which deformation experiments were carried out. This makes a comparison of the data difficult. Recently Chakraborty and Becker (2002) have overcome experimental difficulties and measured an activation energy for Si-diffusion in olivine similar to that found for climb-controlled dislocation creep (Ricoult and Kohlstedt, 1985).

For stresses exceeding one thousandth of the shear modulus, strain rates are higher than that predicted by the power-law (Frost and Ashby, 1982). The power law is replaced by an exponential dependence, leading to:

$$\dot{\epsilon} = A \cdot \exp(b\Delta\sigma) \cdot \exp\left(-\frac{Q}{RT}\right). \quad (4)$$

This power-law breakdown (Frost and Ashby, 1982) is explained by an increasing contribution of dislocation glide to the strain rate. Tsenn and Carter (1987) proposed different possibilities to estimate the upper limit of applicability of the power law and concluded that for silicates it holds for stresses up to $\sigma_b = 10^{-2}\mu$. Evans and Kohlstedt (1995) pointed out that only limited data are available to constrain that limit. They gave stresses ranging from about 100 MPa for calcite rocks up to more than 10 GPa for quartz rocks.

2.2.3 Mechanical twinning

Mechanical twinning is a deformation mechanism of crystal plasticity which has been observed for several minerals including plagioclase, calcite and clinopyroxenes. Twinning occurs when the critical shear stress on a twin plane in the appropriate direction is exceeded. The critical stress does not exhibit a strong dependence on temperature or strain rate. Mechanical twins occur in naturally and experimentally-deformed rocks. Raleigh and Talbot (1967) proposed to determine the orientation of the principle stresses of naturally-deformed rocks from the occurrence of twinning. Tullis (1980) pointed out the merits of using twins as an indicator of stress magnitude, provided critical stresses for twinning are experimentally calibrated.

2.2.4 Method for the determination of flow law parameters

Mechanical data from deformation experiments may be fitted to a power law equation as introduced above. The relation (3) was derived from a model and relates the measured data, which are triplets of differential stress $\Delta\sigma$, temperature T and strain rate $\dot{\epsilon}$ to the parameters of the model. In this case the model parameters are the activation energy for creep Q , the stress exponent n and a preexponential factor A .

Model parameters may be obtained using traditional methods. The parameters are found by representing the data in plots of $\ln \Delta\sigma$ versus $\ln \dot{\epsilon}$ and $\ln \Delta\sigma$ versus the inverse absolute temperature. By fitting lines to the data points, the stress exponent and the activation energy are obtained. The method offers the possibility to identify single data points that do not fit a general trend. Though widely used, many inadequacies are inherent to this procedure. The model parameters are found independently by fitting the data at a constant temperature or strain rate. Only part of the data set is used for the determination

of one parameter. This is a particular problem when only few data points are available. Poirier *et al.* (1990) proposed a method which overcomes such drawbacks. The global inversion method uses all data simultaneously and generally yields more reliable results. It can account for experimental uncertainties and provides estimates for the uncertainty of the parameters.

For the inversion of the data, the mechanical constitutive equation is simplified to a linear inversion problem by taking the natural logarithm of the flow law (equation 3). For $i = 1 \dots N$, a set of linear equations is obtained with N denoting the number of data triplets. For each data set from a single experiment the following equation holds:

$$\ln \dot{\varepsilon}_i = \ln A + n \ln \sigma_i + \frac{-Q}{R} \frac{1}{T_i}. \quad (5)$$

In matrix notation one obtains:

$$\begin{pmatrix} \ln \dot{\varepsilon}_1 \\ \vdots \\ \ln \dot{\varepsilon}_N \end{pmatrix} = \begin{pmatrix} 1 & \ln \sigma_1 & 1/T_1 \\ \vdots & \vdots & \vdots \\ 1 & \ln \sigma_N & 1/T_N \end{pmatrix} \cdot \begin{pmatrix} \ln A \\ n \\ -Q/R \end{pmatrix} \quad (6)$$

which is equivalent to the short form:

$$\vec{d} = G \vec{m}. \quad (7)$$

Herein the model vector \vec{m} is traditionally named the set of unknowns and \vec{d} is the set of data (Tarantola and Valette, 1982). If no strict inverse of G^{-1} which satisfies

$$\vec{m} = G^{-1} \vec{d} \quad (8)$$

can be given, a generalized inverse $H = G^{-1}$ is found by inverting G after decomposition in its singular values. A numerical approximative procedure is used here to invert the matrix G . The errors of the components of the model vector \vec{m} can be estimated by a standard Gaussian error analysis. A vector containing the errors of \vec{m} can be given using H (Müller, 1991):

$$\Delta m_j^2 = \sum_{k=1}^N \left(\frac{\partial m_j}{\partial d_k} \Delta d_k \right)^2 = \sum_{k=1}^N H_{jk}^2 \Delta d_k^2, \quad (9)$$

Herein j denotes the components of the model vector and $k = 1 \dots N$ denotes the components of the vector Δd that contains the errors of the components of the data vector.

Assuming all components of \vec{d} have the same error, Δd_k^2 is estimated to be:

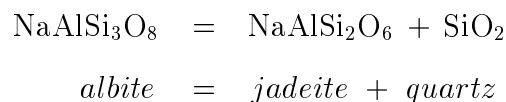
$$\Delta d_k^2 = \Delta d^2 = \frac{1}{N} |\vec{\varepsilon}|^2 \quad (10)$$

with $\vec{\varepsilon} = \vec{d} - G \vec{m}$. The magnitude of this vector quantifies the deviation of measured data and the data predicted by the model. It can be used to assess the quality of the data fit.

3 Stability field and physical properties of jadeite

The single chain silicate jadeite is a clinopyroxene with the general structural formula $M1M2Si_2O_6$. The M1 sites are occupied by Na atoms and the M2 sites are occupied by Al atoms. Jadeite is of monoclinic symmetry and belongs to the space group C2/c. SiO_4 tetrahedra are arranged in such a way, that two out of four corners connect to neighbouring tetrahedra. Within the resulting structure of SiO_4 chains, the M1 atoms are generally located between the apices of the tetrahedra and the M2 atoms are found between the bases of the tetrahedra (Putnis and McConnell, 1980). Diopside ($CaMgSi_2O_6$) has the same structure. For the intermediate composition of omphacite ordering and disordering of the atoms on the M1 and M2 sites may occur (Holland, 1983; Brenker *et al.*, 2002).

Jadeite is of major importance for a variety of petrological and geophysical aspects such as the seismic velocities of eclogitic assemblages or the development of mineralogic models (Deer, 1962; Holland, 1980; Kandelin and Weidner, 1988). This explains the early efforts of Eskola to synthesize jadeite in the 1920s (Adams, 1953), followed by many other experimentalists (e.g. Yoder, 1950). They were not successful, however, mainly due to the extreme sluggishness of the involved reactions (Boettcher and Wyllie, 1968). This motivated attempts to constrain the stability field from calculations based on thermodynamic data (Adams, 1953). Two reactions are commonly explored:



Robertson *et al.* (1957) investigated the first reaction at temperatures between 600°C and 1200°C and for pressures ranging from 1 GPa to 2.5 GPa using a Bridgeman's double press. The authors used a synthetic glass of jadeite composition as a starting material because crystallisation was more rapid than it was with natural mineral precursors. The derived equilibrium curve is shown in Figure 1. Newton and Kennedy (1968) used a piston-cylinder apparatus and natural minerals to investigate the transition at temperatures below 800°C and pressures below 1.7 GPa. They also investigated the reaction albite = jadeite + quartz

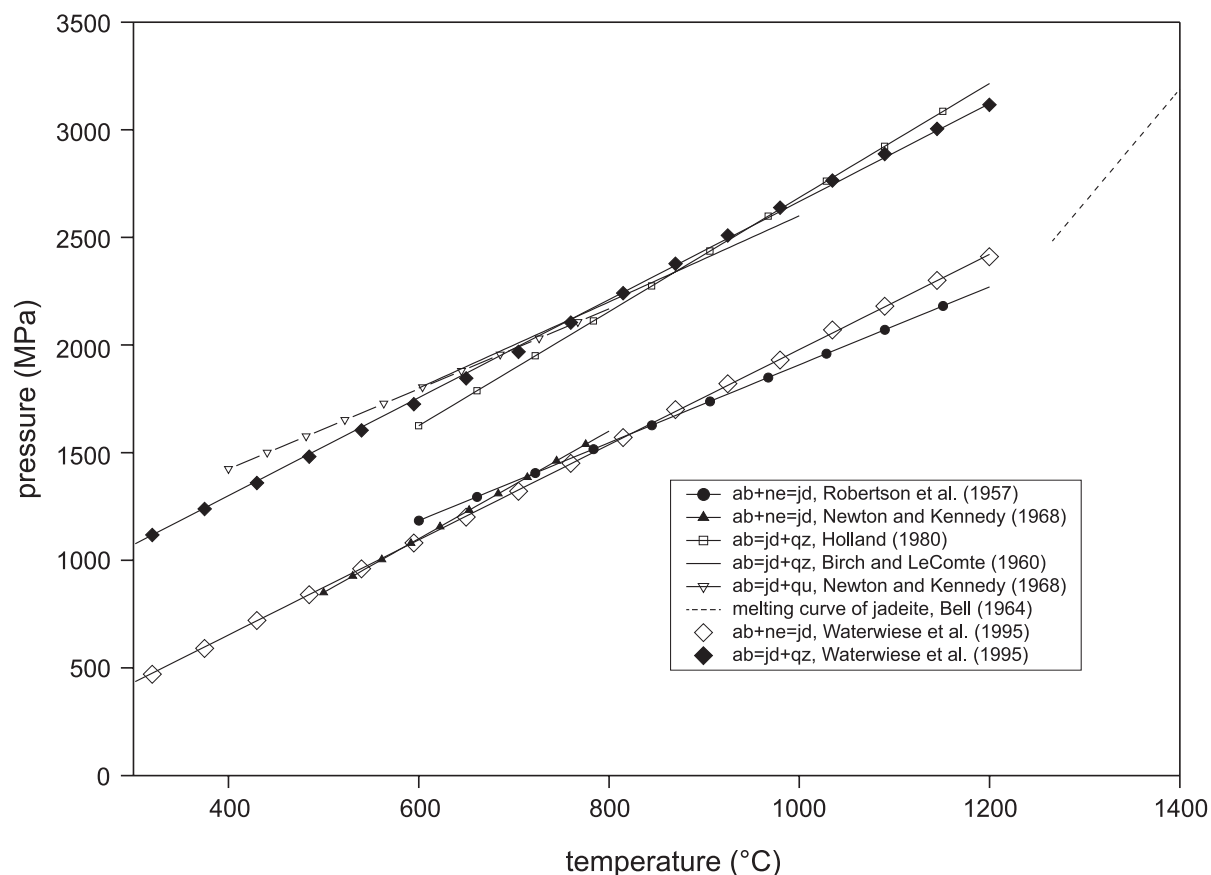


Figure 1: Phase equilibria of the relevant reactions $ne+ab=qz$ and $ab=jd+qz$. The following abbreviations for the phases are used: ne: nepheline, ab: albite, qz: quartz, jd: jadeite. Open and closed diamonds indicate data points calculated by Waterwiese *et al.* (1995). Here, they were fit by a linear regression.

for the same temperature range at pressures up to 2.4 GPa. Their results are close to those obtained by Birch and LeComte (1960). These authors investigated in the temperature range from 600°C to 1000°C and the pressure range from 1.5 GPa to 2.5 GPa. Natural quartz, albite and jadeite were used as starting materials. Holland (1980) used a piston-cylinder apparatus with NaCl as confining medium and prepared his samples from natural quartz and jadeite as well as from a synthetic jadeite glass. Maximum pressure was 3.3 GPa and temperature ranged from 600°C to 1200°C. Waterwiese *et al.* (1995) presented a combined experimental and thermodynamic study of both reactions. From experimentally derived thermodynamic properties they computed a phase diagram. Zhao *et al.* (1995)

reported on the synthesis of jadeite and diopside in gemstone quality from synthetic glasses. They investigated a temperature range of 800°C to 1900°C and pressures from 1 GPa to 5.5 GPa. The melting temperature of jadeite as a function of pressure has been determined by Bell (1964).

Table 1 compiles physical properties of jadeite aggregates. The full tensor of elastic properties of jadeite is given by Kandelin and Weidner (1988). From these measurements, upper and lower bounds for an isotropic aggregate can be constrained by Voigt- and Reuss moduli (Gebrande and Kern, 1982). Kumazawa (1969) showed that the Reuss' average is the one to be expected as representative under high pressure.

density ρ [g/cm^3]	3.18 ¹ - 3.44 ⁷
adiabatic bulk modulus K [GPa]	92 ² - 143 ⁴
$\partial K/\partial p$	4.5 ⁹
$\partial K/\partial T$ [GPa/K]	1.7 ⁹
shear modulus G [GPa]	69 ³ - 85 ⁴
$\partial G/\partial p$	0.016 ⁹
$\partial G/\partial T$ [GPa/K]	0.013 ⁹
seismic velocity v_p [km/s]	7.60 ³ - 8.78 ^{5,4}
seismic velocity v_s [km/s]	4.65 ³ - 5.05 ^{6,4}
Youngs modulus E_{Voigt} [GPa]	218 ⁴
Youngs modulus E_{Reuss} [GPa]	160 ⁴
Youngs modulus E [GPa]	200 ⁸

Table 1: Physical properties of jadeite. Aggregate elastic properties derived from single crystal measurements are based on Kandelin and Weidner (1988). (1: Christensen und Salisburg (1972); 2: Deer (1962); 3: Birch (1960); 4: Kandelin und Weidner (1988); 5: Simmons und Brace (1965); 6: Hughes und Nishitake (1963) ; 7: Dorner (1999); 8: Bradt *et al.* (1973) ; 9: Duffy and Anderson (1989)).

4 Sample material

4.1 Synthesis of jadeitite aggregates

The necessity for the use of synthetic samples in the deformation experiments is shown as well as the applied methodology. An overview of the experiments is given and after introducing the applied methods for the analysis of the samples the results are presented and discussed. For that purpose, the applied P-T-t paths will be divided into groups and qualitative descriptions of the microstructures will be given. The effect of doping will be shown. Special attention is attributed to the standard procedure for the synthesis of appropriate samples for later deformation experiments.

4.1.1 Introduction

To contribute to the reliability and reproducibility of the results of the deformation experiments, the samples should meet definite requirements. The starting microstructure and physical properties of the specimens should be similar for each run. The microstructure should not display any features of deformation such as lattice- or shape-preferred orientation (Paterson, 1987; Rybacki *et al.*, 1995). Dislocation density should be low. Dislocation creep is best studied using large grains, where diffusion creep processes are not favoured. In contrast, grain size should not be larger than 10 % of the sample diameter to enable homogeneous deformation. Larger grain size also facilitates optical microscopy. The grain size distribution may also have an impact on the rheological behaviour of polycrystalline material (de Bresser *et al.*, 2001). In order to reduce the number of parameters that impact the deformation behaviour, it is often desired to work with samples of high purity.

Often synthetic aggregates are chosen for deformation studies as natural material is not readily available (e. g. synthetic coesite used by Renner *et al.*, 2001) or natural material is of insufficient quality (Rybacki *et al.*, 1995). Luan and Paterson (1992) demonstrated that by using a synthetic starting material, good control of the starting grain size is possible. More generally, Rutter (1993) stressed that there is increasing use of synthetic samples due to the inherent possibility of controlling chemistry and starting microstructure of the material. Stöckhert and Renner (1998) stated that natural ultra-high pressure rocks are generally not appropriate as they have been subject to retrogression and deformation

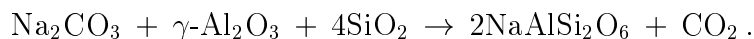
during exhumation.

To synthesize a material with an appropriate microstructure the nucleation and growth of the crystals need to be controlled. Influential parameters are the choice of the starting material (glass, gel, mixture of oxides), the pressure-temperature-time path, the final pressure and temperature conditions of the synthesis experiment and the properties of the starting material. Constraints for the pressure-temperature paths are given by the relevant phase equilibria.

All synthesis experiments using glass as a starting material begin at conditions that are far from equilibrium; hence the driving force for crystallization is very high. At present it is not possible to crystallize jadeite aggregates from a melt with our apparatus due to temperature limitations. This technique has been used by Zhao *et al.* (1995) and is reported as a common method by Lofgren (1974). With this method, crystals can grow to large sizes because few nuclei are formed.

4.1.2 Method

4.1.2.0.1 Preparation of the glass Synthetic samples may be crystallized from a gel, a glass or a dry mixture of oxides. Edgar (1973) gives an overview about the relative merits of the different starting materials. Due to the results of experiments described by Dorner (1999) glass was chosen as a starting material. A detailed description of the preparation of glasses is given by Schairer (1973). For the preparation of the glass the relevant amounts of the oxides are mixed to allow for the reaction:



The water content of $\gamma\text{-Al}_2\text{O}_3$ is determined by heating the material to 1150°C. The calculated amount of $\gamma\text{-Al}_2\text{O}_3$ is corrected for the weight loss. Generally, batches of approximately 10 g are prepared to minimize weighing errors on the one hand and to ensure homogeneity on the other hand. Heating of the oxide mixture is done slowly to prevent sodium from escaping along with the degassing CO_2 (Seifert and Langer, 1971). The mixture is held 24h at 700°C, 800°C, 900°C and 1000°C prior to fusing at 1350°C for several hours. The viscous melt is then quenched in water and milled to a grain size below 100 μm using an agate mortar and pestle. Homogeneity is increased by repeated melting,

quenching and milling. This is especially needed in the case of jadeite, as the viscosity of the melt is high even at a high temperature of 1350°C (Kushiro, 1976). The glass powder is stored in a drying oven at 150°C. X-ray fluorescence measurements using a Philips PW 2404 X-ray spectrometer confirm that the composition of the glass is stoichiometric. Table 2 shows results for two batches of glass. Deviation from the theoretical composition is within the limit of error of the measurement.

In some runs, the glass was doped with crystalline material; first crystalline jadeite was ground to a grain size below 50 μm . Twenty wt-% of the crystalline powder was then added to the jadeite glass precursor. Although it is common to use a much smaller wt-% of doping material, such a high percentage was necessary due to the sluggish nucleation kinetics. Experiments by Dorner (1999) revealed that addition of 5 wt-% crystalline jadeite had no significant effect on the resulting microstructure.

glass	SiO_2	Al_2O_3	Na_2O
DEZ00	59.2	25.2	14.7
JUL01	59.8	25.6	15.1
theoretical	59.5	25.2	15.3

Table 2: Results of X-ray fluorescence analysis of two batches of jadeite glass, given in wt-%

4.1.2.0.2 Sample preparation, apparatus and experimental procedure For the preparation of the samples, gold capsules with a length of 12 mm and an outer diameter of 4 mm are fit into a vacuum die. They are then filled with the glass powder in two or three steps, each followed by uniaxial pressing for one minute at a pressure of approximately 200 MPa and subsequently for 3 minutes at about 1400 MPa. After drying the samples at 150°C for at least 12 hours, the capsules are mechanically sealed and stored in the oven.

A piston cylinder apparatus is used for the synthesis experiments. It is equipped with a servohydraulic-control unit for the confining pressure and a programmable controller for the temperature control. Two or three samples can be synthesized in one run. Dry

NaCl is used as confining medium. Heating is provided by a straight graphite resistance furnace. A NiCr-Ni thermocouple is positioned so that the temperature is measured at a level that corresponds to half of the sample height. Referring to the results of Getting and Kennedy (1970), Renner *et al.* (1997) assumed that the temperature difference between the sample ends does not exceed 30°C at 1170°C. As most experiments of the present study were carried out at 1000°C, temperature differences are lower as they correlate with the maximum temperature. The nominal confining pressure is calculated from the readings of an oil pressure gauge. Mirwald *et al.* (1975) showed that pressure corrections with these cells are negligible provided that lubrication of the cell and the piston is sufficient and that the pressure is changed slowly.

Following the assemblage of the pressure cell and its insertion into the apparatus, pressure and temperature conditions are built up simultaneously. After a fixed hold at the final run conditions, pressure and temperature are reduced following the same path but using higher rates.

4.1.3 Overview of synthesis experiments

Fifty synthesis experiments were carried out to optimize the starting microstructure and to produce samples for deformation tests. The experiments are described according to the P-T-t path leading to final conditions, the run time at final conditions and to the starting material. Table 3 gives an overview over the experiments. A set of 13 exploratory experiments (JD1 to JD13) is described by Dorner (1999). The paths used are also listed in Table 3. Confining pressures in the present study ranged from 1800 MPa to 3400 MPa, while temperature varied from 900°C to 1200°C. Different paths were tested (Figures 2 and 3). Run time was generally 24 hours. Only for path Ib it was 6 hours and for Ie less than 1 minute. Using path Ia and Ic, a pressure of 1800 MPa and a temperature of 1000°C was maintained for 6 hours prior to reaching final conditions. Pure glass as well as doped samples were used.

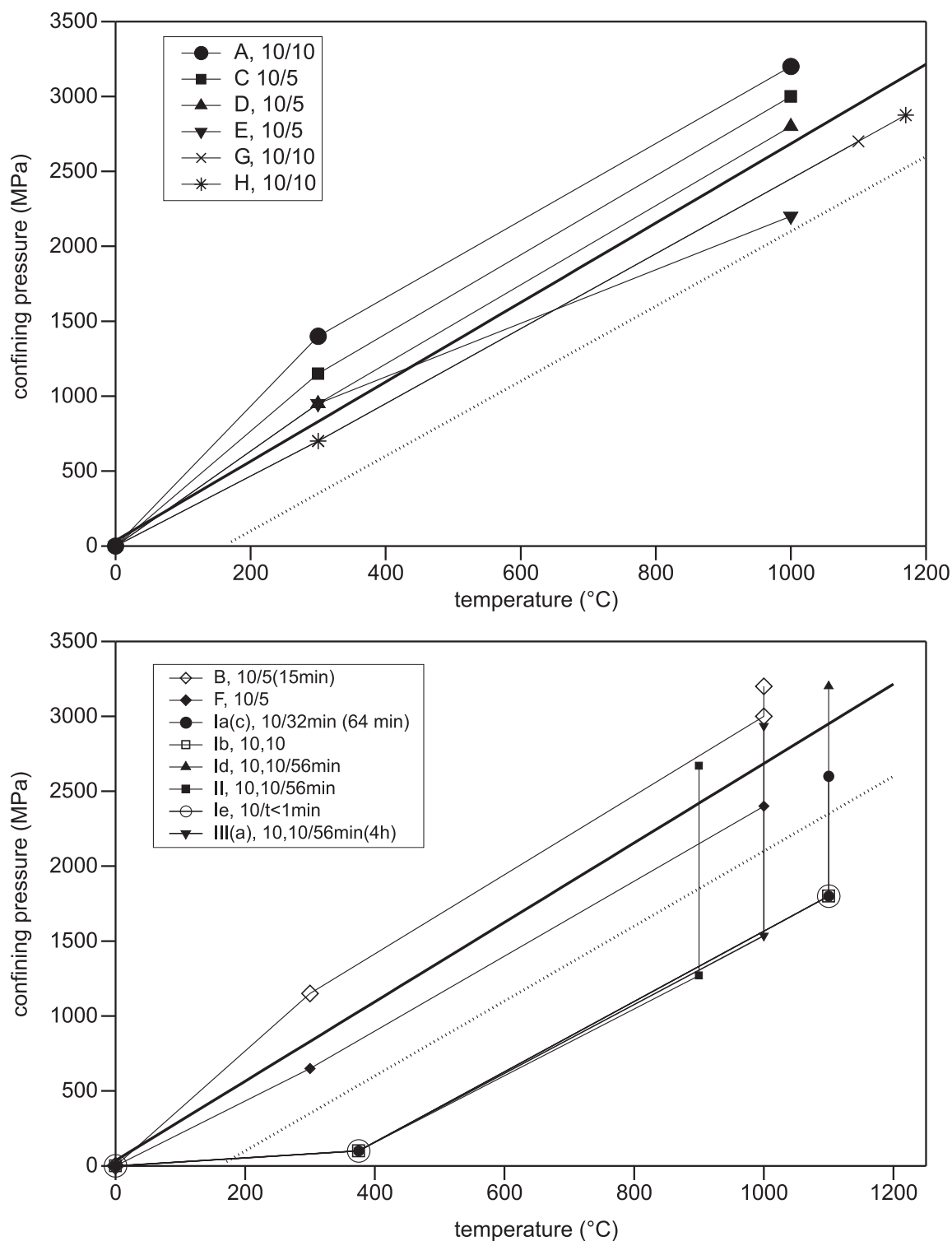


Figure 2: The different P-T-t paths of the synthesis experiments are denoted by letters or numbers. Numbers in the legend give heating rates for the segments in °C/min, numbers stated in minutes give times for isothermal ramp up of pressure. In addition, extrapolations of two phase equilibria are displayed: the thick solid line shows the equilibrium $alb=jd+qu$ from Holland (1980), the dotted line represents the $alb+ne=jd$ equilibrium (Newton and Kennedy, 1968).

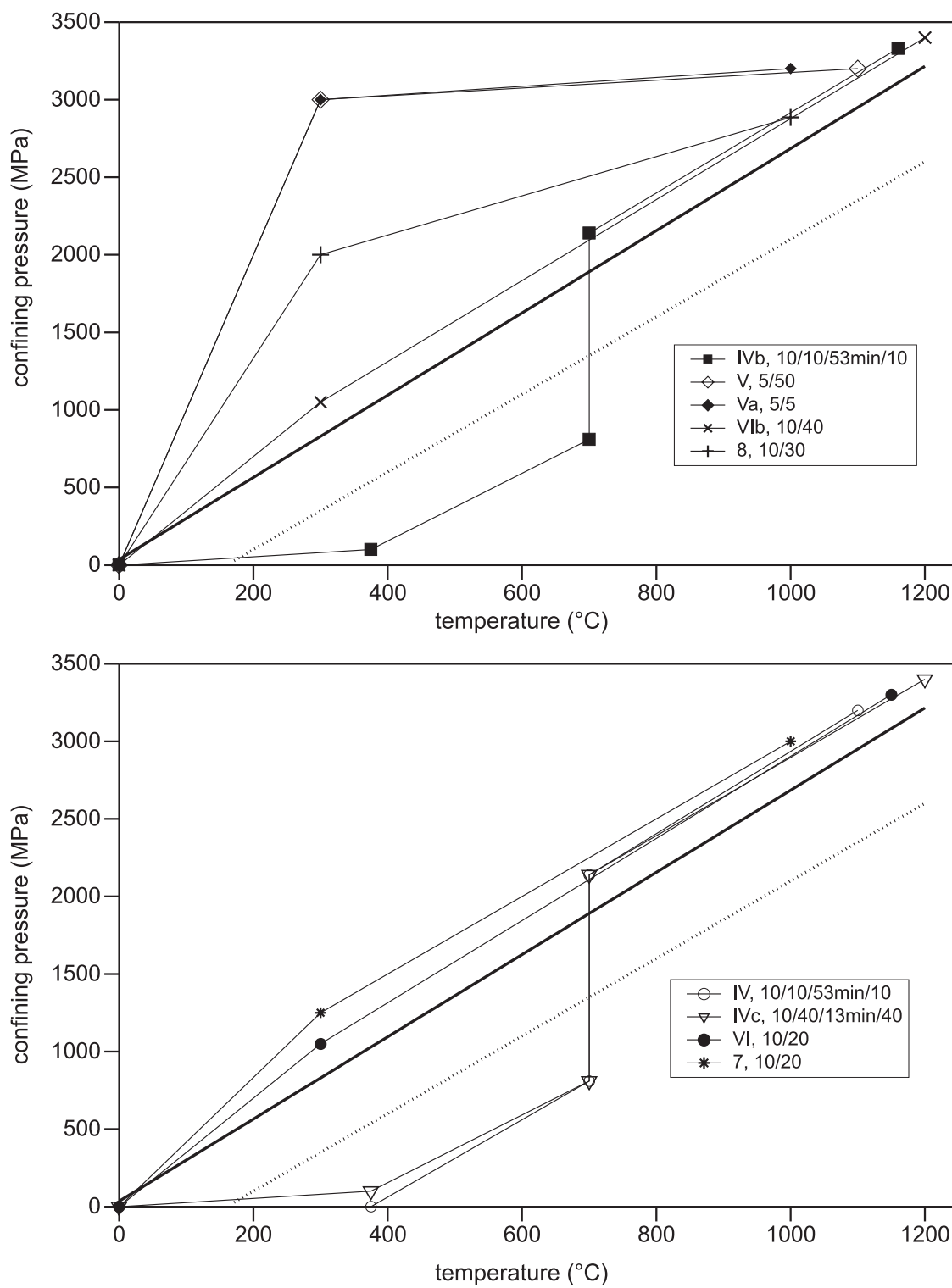


Figure 3: Paths of synthesis experiments. For explanations see figure 2.

experiment	path	doping
JD1	A	
JD2	B	
JD3	B	
JD4	B	
JD5	B	
JD6	C-5	
JD7	B	
JD8	D	
JD9	B	
JD10	C	
JD11	C	
JD12	E	
JD13	F	
JD14	G	
JD15	G	
JD16	H	
JD17	I	
JD18	Ib	
JD19	Ia	
JD20	Ia	
JD21	Ia	
JD22	Ic	
JD23	Id	
JD24	Id	
JD25	Id	
JD26	Id	
JD27	II	
JD28	III	
JD29	Id	
JD30	Ie	
JD31	IV	
JD32	V	

experiment	path	doping
JD33	VI	
JD34	VI	
JD35	IVb	
JD36	VIb	
JD37	IVc	
JD38	7	
JD39	8	
JD40	IIIa	• Id
JD41	C-5	• Id
JD42	Va	
JD43	IIIb	• Va
JD44	IVb	• Va
JD45	C-5	(•) C-5
JD46	IIIa	• C-5
JD47	C-10	
JD48	IIIa	• C-10
JD49	IIIa	(•) C-10
JD50	7	
JD51	7b	
JD52	Va	
JD53	IIIa	• Va
JD54	IIIa	• Va
JD55	C-10	
JD56	IIIa	• C-10
JD57	IIIa	• C-10
JD58	IIIa	• C-10
JD59	C-10	
JD60	IIIa	• C-10
JD61	IIIa	• C-10
JD62	C-10	
JD63	C-5	• C-10

Table 3: Overview of synthesis experiments. The dot indicates that the glass is doped with 20 weight-percent of crystallized jadeitite from earlier experiments. Brackets indicate that not all samples within a run were doped. The path along which the doping material has been crystallized is also given. The number after the hyphen denotes the heating rate in °C/min (e. g. Path C-10 corresponds to 10°C/min).

4.1.4 Sample analysis

The procedure and analysis described here applies to deformed samples as well as to undeformed reference samples. The length and diameter of the capsules were determined

using digital calipers. Capsules were weighed and photos were taken for documentation. One sample of each synthesis run was selected as a reference sample and was divided into halves along the sample axis. A polished thin section was prepared from one half for optical microscopy. The grain size could not be determined easily using an optical microscope. Images of the samples were taken from the thin sections using a scanning electron microscope (SEM, LEO 1530). Grain boundaries were traced on transparencies, which were then scanned. Further processing was done using the image analysis software ScionImage (NIH). This approach analyses two-dimensional sections of a complex three-dimensional structure. It is the scope of stereology to draw conclusions concerning the properties of a structure in space from the analysis of two-dimensional images (Weibel, 1967). Apparent small grains in two-dimensional sections may be an effect of sectioning. No conclusions concerning the shape of the grains may directly be drawn. For complex and irregular shaped objects, stereology offers methods for an approximate description of the shape and, average size parameters are given. For most regular objects, however, quantitative expressions for the shape and particle size are developed in stereology (Underwood, 1969).

The diameter of an equal area circle was calculated for each grain and an average value for all traced grains was reported as a two-dimensional grain size. In addition, the data were fit to a log-normal distribution and the average logarithmic diameters are given. Ranalli (1984) pointed out that grain sizes are typically distributed log-normal. An average of more than 600 grains per sample was used for grain size determination. Heilbronner and Bruhn (1998) showed that a two-dimensional grain size distribution may not be appropriate when grain size and grain size distribution affect the rheology. For this study determination of a two-dimensional grain size was sufficient as it allowed to detect whether changed conditions in the synthesis procedure led to a different grain size.

Preparation of samples for electron-backscatter diffraction measurements (EBSD) involved mechanical and chemical polishing of the thin sections with a colloidal silica (SYTON) and subsequent coating with a thin carbon layer (Prior *et al.*, 1999). Pole figures were generated from automated EBSD measurements, which are described in Chapter 6.2.1. Manual EBSD measurements were also performed to investigate mechanical twinning (Chapter 6.3.1). The accelerating voltage was 25 kV, sample tilt was 70° and the distance between the sample and the gun was 25 mm. Indexing of the EBSD patterns

was done automatically by the HKL software CHANNEL 4 (Schmidt and Olesen, 1989).

The remaining half of the reference sample was split into two pieces. One was ground to a fine powder for structural analysis using X-ray diffraction measurements. A Siemens APD D500 was used. The remaining piece was used for Fourier Transform Infrared-spectroscopy (FTIR) to determine the water content, or, otherwise for transmission electron microscopy analysis (TEM). FTIR-measurements were done on polished slabs with a thickness of approximately 210 μm using an IFS-48 Bruker Fourier transform infrared spectrometer (den Brok *et al.*, 1994).

4.1.5 Results and discussion of the synthesis experiments

The synthesis experiments of the present study yield two distinct types of microstructures: one type is characterized by a fine grain size and the other type is characterized by spherulites. The small grains are difficult to analyse by optical microscopy and minor changes that may result from the influence of a different P-T-t path are difficult to detect.

Except for the spherulitic aggregates no crystallographically preferred orientations are observed. Microstructures are reproducible from run to run and identical in different samples from the same run. The overall appearance of the microstructures is generally homogeneous throughout the whole sample.

For some paths the average grain size and aspect ratio were determined. They are compiled in Table 4. The grain size distributions do not always obey a log-normal relation (Figure 4). Therefore, standard two-dimensional grain sizes were given in addition to the log-normal average and standard deviation. The fit of the data was obtained by plugging the average logarithmic grain size \bar{x} and standard deviation σ into an equation of the form:

$$w(x) = \frac{1}{\sqrt{2\pi}\sigma} \cdot \exp\left(-\frac{(x - \bar{x})^2}{2\sigma^2}\right). \quad (11)$$

The microstructures obtained along paths A, B, C, D, E and F are very similar, though the final pressures ranged from 2.2 GPa to 3.2 GPa. The average grain size varies between 4 μm and 6 μm . A precise description of the shape of the grain boundaries is not possible by optical microscopy, as several layers of grains lay on top of each other within the 30 μm thick thin section. Images taken with the SEM reveal straight grain boundaries (Figure 5a).

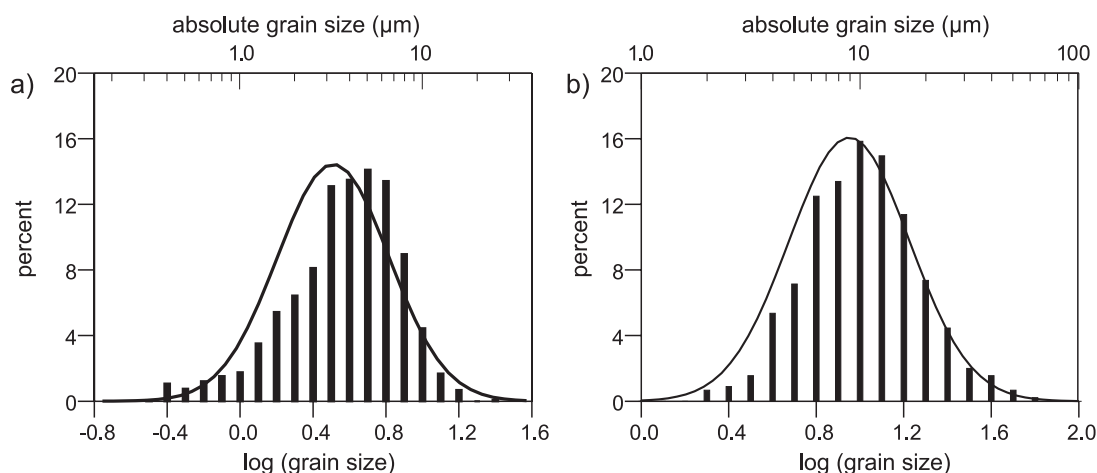


Figure 4: Grain size distribution for two samples. a) The grain size distribution for sample JD6.A is not symmetric and does not obey a log-normal distribution. b) The fit for sample JD34.B is better.

Microstructures from paths G and H are similar to those from paths A - F, even though temperatures were higher (up to 1170 °C), indicating that crystallization may already be completed at temperatures below 1000 °C. Nucleation in a highly reactive glass will start as soon as the temperature is high enough to allow for diffusion. This is consistent with the observations from Lüttge *et al.* (1998), who reported that the initial heating stage is instrumental in determining the crystallization characteristics. Higher heating rates as employed in path VIb and VI do not lead to substantial differences in microstructures. Experiment JD33 following path VI, was terminated at a temperature of approximately 800°C. Optical inspection of the thin section showed that more than 95% of the glass had already crystallized. Paths IV and IVc also lead to a fine-grained microstructure. The isothermal pressure increase of 1.3 GPa at 700°C does not seem to have any influence on the resulting microstructure, which is similar to the ones described above. In combination with observations from experiment JD33, the predominant nucleation period may be constrained to temperatures between 700°C and 850°C.

Though similar to Path C, Path 7a also leads to a fine-grained microstructure. However, it is observed that in some regions single grains are arranged into radial structures. This effect is more pronounced for Path 7b and 8 (Figure 5b). Images taken with the SEM show straight high-angle grain boundaries and abundant rational grain boundaries

sample	path	doping	grain size			aspect-ratio
			logarithmic	inv.log.av. (μm)	standard (μm)	
JD5.B	B		0.45±0.34	2.8	4.0±2.9	1.75
JD6.A	C-5		0.51±0.31	3.2	4.0±2.5	1.70
JD12.C	E		0.61±0.39	4.1	5.8±5.2	1.81
JD13.C	F		0.65±0.37	4.5	6.0±4.2	1.76
JD34.B	VI	•	0.95±0.26	8.9	10.8±7.2	
JD37.A	IVc		0.55±0.37	3.5	4.8±3.6	1.80
JD37.B	IVc		0.55±0.36	3.5	4.7±3.5	1.73
JD39.2	8		0.39±0.33	2.5	3.2±2.7	1.74
JD40.A	IIIa		0.85±0.52	7.1	11.9±10.9	1.84
JD40.C	IIIa	•	1.20±0.42	15.8	24.7±25.0	2.05
JD41.A	C-5	•	0.48±0.35	3.0	4.2±4.1	1.79
JD41.B	C-5		0.55±0.27	3.5	4.3±3.3	1.69
JD42.B	Va		0.54±0.36	3.5	4.7±3.9	1.86
JD48.B	IIIa	•	1.14±0.39	13.8	18.6±13.0	
JD49.A	IIIa	•	1.16±0.26	14.5	21.4±12.0	
JD51	7b		0.39±0.31	2.5	3.2±2.6	1.90
JD53.C	IIIa	•	1.00±0.38	10.0	13.5±11.3	1.86
JD55	C-10		0.47±0.35	3.0	4.2±5.0	1.74
JD56.A	IIIa	•	1.01±0.33	10.2	13.1±9.2	1.85
JD57.C	IIIa	•	0.93±0.35	8.5	11.2±8.4	1.82
JD59	C-10		0.42±0.32	2.6	3.2±2.9	1.89

Table 4: Grain size of synthesized samples; • denotes that glass was doped with 20 wt-% of crystallized jadeite. The inverse of the logarithmic average is given also.

from idiomorphic crystals. A similar microstructure is obtained using Path Va. Increasing the heating rate of Path Va by a factor of 10 to 50°C/min (Path V) leads to an entirely spherulitic microstructure (Figure 5c).

Experiments where the stability field of jadeite is entered by an isothermal increase of pressure at the final run temperature lead to microstructures which are characterized by spherulitic growth of crystals. One spherulite is considered as one grain that grows from a single nucleus. From that, a low nucleation rate can be inferred from the occurrence of large spherulites. In general, the single blades or fibres of the spherulites differ slightly in orientation from each other (Lofgren, 1971). A spherulite growth theory was developed by Keith and Padden (1964) for organic polymers. They pointed out, however, that it cannot easily be applied to silicate systems. They also studied silicate melts and observed that the different forms of spherulites are dependent on a particular set of growth conditions. They correlated spherulites with rapid quenching of melts and established relationships between the degree of undercooling and the shape of the spherulites.

Paths I, Ia, Ib, Id, II, III lead to different forms of spherulites with varying blade widths. The diameter of spherulites varies from 20 μm to a maximum of 700 μm (Figure 5d). Experiment JD30 (Path Ie) was terminated shortly after reaching the final temperature, but before the pressure was raised to a value within the jadeite stability field. In this manner, the microstructure from which spherulites are derived can be investigated. Many grains are extremely fine with an average grain size well below 2 μm . X-ray diffraction analysis reveals albite and nepheline besides jadeite. In contrast X-ray analysis of spherulitic samples only reveals jadeite. That means that the jadeite spherulites grow from a mixture of crystalline jadeite, albite and nepheline. For the paths mentioned above it takes approximately one hour to ramp up to the final pressure conditions once the final run temperature is achieved. However, if pressure is ramped up slowly over four hours (path IIIa) no spherulites develop and a fine-grained microstructure is obtained (Figure 5e). With the slower ramp up of pressure, the glass is longer exposed to the conditions, where nucleation rates are high and likewise more nuclei emerge (Chapter 2.1).

Another approach to influence the microstructure is doping or seeding, which involves adding crystalline jadeite to the glass to overcome barriers to nucleation. Doping and following path C does not yield a distinctly higher average grain size, although an effect is observed in the logarithmic representation (Table 4). The overall appearance is determined by the larger grains (Figure 5f,g). Presumably, they represent the original grains and

correlate with a local maximum in the grain size distribution at approximately $20 \mu\text{m}$. From optical inspection the doped sample crystallized along Path IIIb seems to display a higher average grain size than that obtained for the undoped case (Figure 5h). A similar result is obtained when comparing seeded and unseeded samples using Path IVb. For Path IIIa a marked increase in the average grain size is observed.

In addition, the material used for doping also influences the resulting microstructure: using material ground from an originally spherulitic microstructure leads to coarse grains with an average grain size of $25 \mu\text{m}$ with a tendency of formation of spherulites (JD40.C). Use of fine-grained jadeitite as seeds yields lower grain sizes varying from $8 \mu\text{m}$ (JD57.C) to $14 \mu\text{m}$ (JD48.B). With a grain size of $50 \mu\text{m}$ for the seeds, the fine-grained jadeitite provides polycrystalline seeds, whereas parts of single crystals are used as seeds when the spherulites with a large grain size serve as seeds.

Figure 5: For further explanations, refer to the text.

- a) SEM image of Sample JD6.A
- b) Optical micrograph of Sample JD39.2 (crossed polarizers)
- c) Optical micrograph of Sample JD32.C (crossed polarizers)
- d) Optical micrograph of Sample JD29.B (crossed polarizers, RED I compensator)
- e) Optical micrograph of Sample JD40.A (crossed polarizers)
- f) Optical micrograph of Sample JD41.A (crossed polarizers)
- g) Optical micrograph of Sample JD41.B (crossed polarizers)
- h) Optical micrograph of Sample JD43.2 (crossed polarizers)

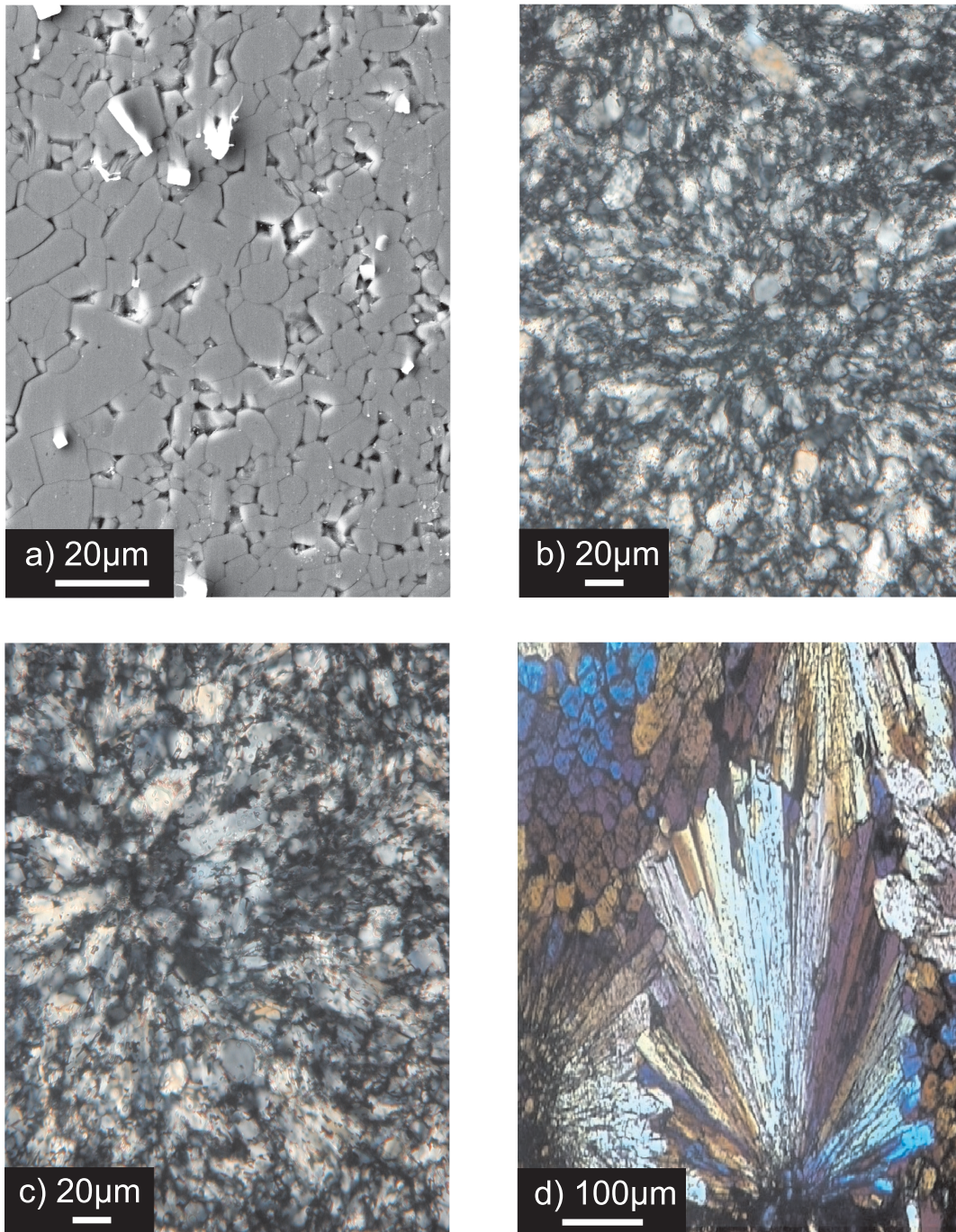


Figure 5: Micrographs of synthetic jadeitite samples. For explanation refer to the caption on the previous page and the text.

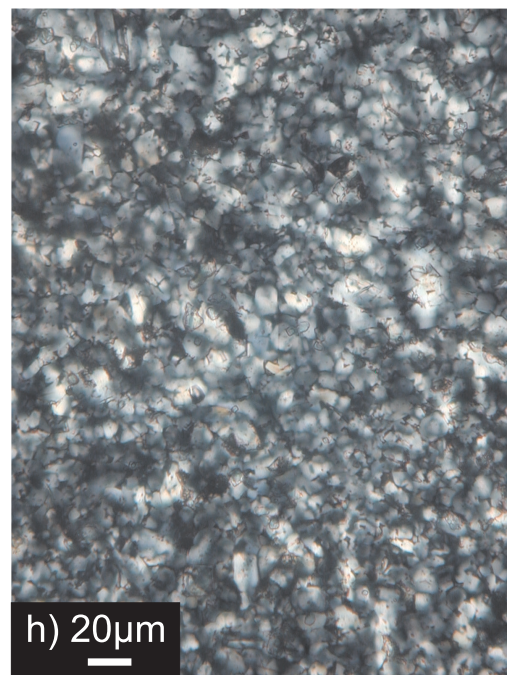
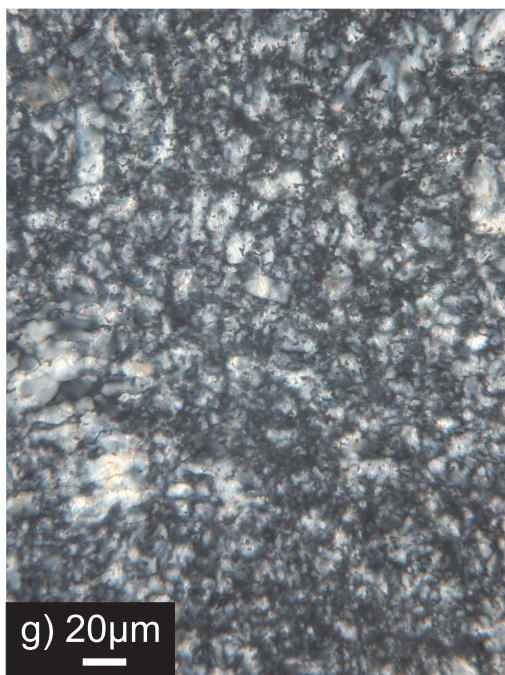
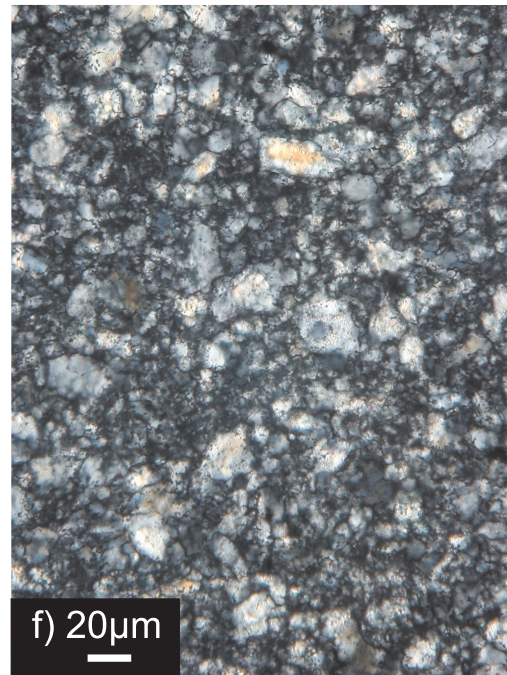
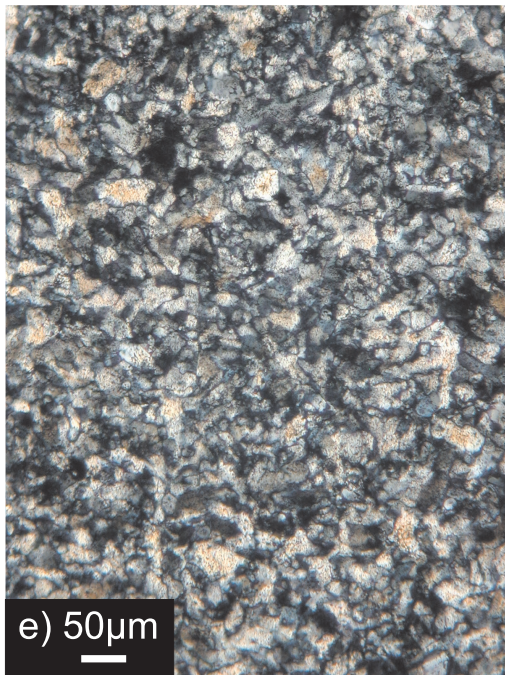


Figure 5 continued.

4.1.6 Description of standard samples for deformation experiments

An appropriate microstructure of samples for deformation experiments is obtained using Path IIIa and seeding the glass with 20 wt-% crystalline jadeitite that was crystallized along Path C-10. X-ray diffraction confirms that no other phase than jadeite is present within the detection limit of the method (Figure 8, Chapter 4.2).

An optical micrograph shows the resulting microstructure (Figure 6b). SEM pictures were taken from polished thin sections (Figure 6a) and from broken sample surfaces. The average grain size is 16 μm . Smaller grains are isometric and occur in clusters, while larger grains are elongated with an aspect ratio of approximately 1.8. High-angle grain boundaries are predominantly smoothly curved (label '1' in Figure 6). Few rational grain boundaries occur. A tendency to form a foam structure, including some unilaterally rational high-angle grain boundaries is observed (label '2' in Figure 6). In some areas, wavy high-angle grain boundaries can be found (label '3' in Figure 6). They show a wavelength of approximately 10 μm . This characteristic shape is indicative of strain-induced grain boundary migration caused by heterogeneous deformation. Deformation is presumably driven by internal stresses caused by the volume change and subsequent compaction when the glass is transformed to a crystalline aggregate. Microstructural observations of polished surfaces are consistent with SEM inspection of broken surfaces.

Thin sections were analysed using a polarizing microscope with a 552 nm red I compensator inserted. This analysis, along with EBSD measurements (Figure 15, Chapter 6.2.1), clearly shows that no crystallographic preferred orientation has developed in the synthesized material. Crystallization from a glass may therefore be advantageous in comparison to hot-pressing of ground natural materials. For instance, Mauler *et al.* (2000) observed a significant crystallographic preferred orientation (CPO) in undeformed samples which were hot-pressed from clinopyroxenite powders.

Samples of the present study exhibit intergranular and intragranular porosity that is estimated to be below 2 %. Intergranular porosity is low, with only few pores located along grain boundaries. In some places, pores appear as triangular sections of tubes along grain edges, with a diameter of up to approximately 5 μm . Larger pores with a diameter of up to 20 μm occur at places where high-angle boundaries meet. They are mostly irregular in shape, yet sometimes partly bound by rational faces. Also, part of the

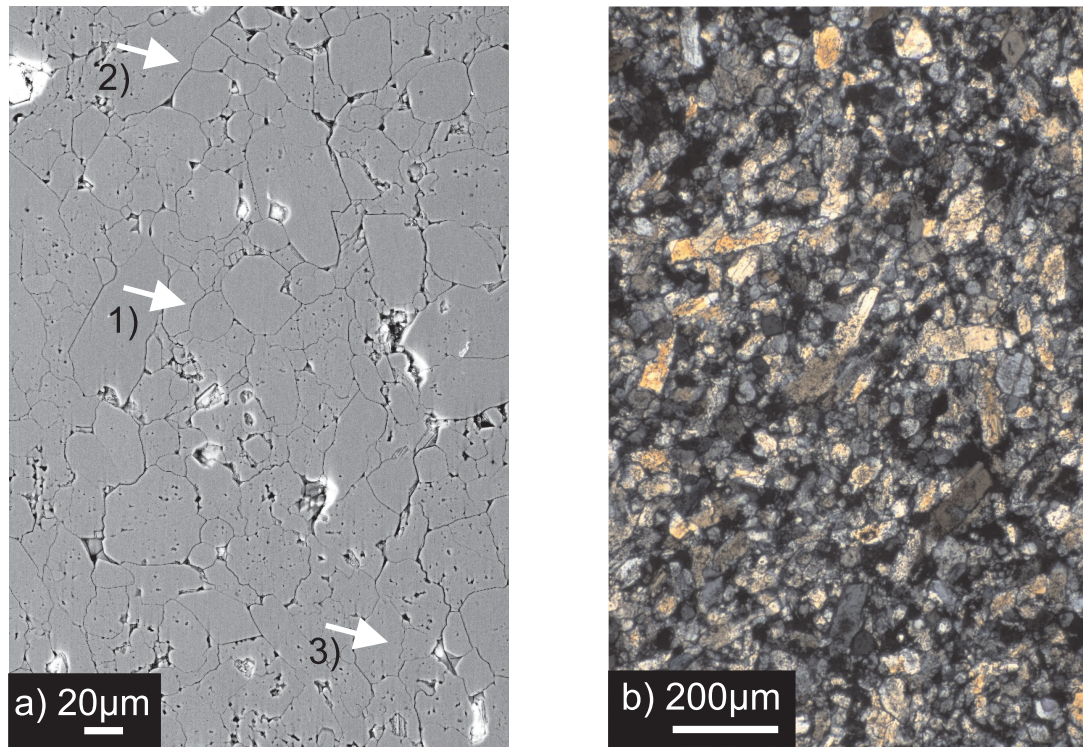


Figure 6: Standard synthesis sample JD53.C. a) SEM image showing 1) smoothly curved high-angle boundaries, 2) indications for a foam structure and 3) locally indications for strain-induced grain boundary migration. b) optical micrograph taken with crossed polarizers showing elongated grains within a matrix of smaller, isometric grains.

intergranular porosity will certainly be due to plugging out of grains during preparation of the thin sections.

For approximately half of the grains, an intragranular porosity is discernible. Pores with a size of less than $2 \mu m$ are homogeneously distributed within the grains with a typical spacing larger than $5 \mu m$.

It will be shown later (Chapter 6.1.1), that the main problem in the evaluation of the mechanical data derived for the synthetic samples is inhomogeneous deformation. This often leads to a considerable underestimation of the sample strength. It is assumed that the inhomogeneous deformation is caused by the geometry of the synthesized samples. Using path IIIa it is observed that samples generally have a smaller diameter in the

upper half than in the lower half. This applies to the outer gold jacket as well as to the sample material: diameters of upper and lower faces differ by $0.06 \text{ mm} \pm 0.04 \text{ mm}$. Although the gold capsule is ground down to a cylinder after the synthesis experiment, a non-cylindrical shape of the jadeitite sample remains, which is assumed to promote inhomogeneous deformation. About 20% of the samples which were synthesized along a path different to IIIa show that problem, whereas it occurs for more than two third of the samples crystallized along Path IIIa. In contrast to other paths leading to similar pressure and temperature conditions, this path involves an isothermal pressure increase of approximately 1.5 GPa at a temperature of 1000°C. It is therefore assumed that this isothermal pressure increase gives rise to the development of a non-cylindrical shape of the samples. An inhomogeneous pressure distribution may occur during that stage and may cause non-uniform crystallization of the jadeite glass or non-uniform compaction. On the other hand temperature is high and pressure is raised slowly over four hours. As such major inhomogeneities of pressure within the cell should be excluded. Inhomogeneous compaction of the graphite furnace leading to changes in its wall thickness, and, changes in its resistance may create an non-uniform temperature distribution. This could also cause non-uniform transformation behaviour within the sample. This can not be examined, however, as only one thermocouple is used.

4.1.7 Fourier-transform infrared measurements

Jadeite is a nominal anhydrous mineral, in that no hydrogen is essentially built into the crystal structure. Even in nominal anhydrous minerals, however, trace amounts of water may be present as inclusions of free water, defect clusters, or, hydrogen may be incorporated into some preferential lattice sites (point defects), dislocation cores or planar defects (Ingrin *et al.*, 1989). The detection of water with infrared spectroscopy and its quantitative determination relies on the fact that the OH-groups efficiently absorb electromagnetic radiation in the $3 \mu\text{m}$ region (Aines and Rossman, 1984). Structurally bound water is discernible by the occurrence of sharp absorption bands. In contrast, inclusions of free water cause a broad absorption band with a maximum close to 3400 cm^{-1} . The sharp bands are caused by stretching absorption of the OH-dipoles. It has been shown for quartz that specific types of point defects lead to peaks at specific wavenumbers

in the absorption spectra (Aines and Rossman, 1984). Characteristic absorption bands are also obtained for the different modes of vibration of the H_2O molecules in free water and ice inclusions. Paterson (1982) suggested a method to infer the water content of minerals from infrared absorption spectra. This method is commonly used and will be used here also.

The measurements were done at room temperature on polished slabs with a thickness of approximately $210 \mu\text{m}$. Spectra were acquired at low temperatures also, by cooling the stage with liquid nitrogen. In this manner, structurally bond water could be distinguished from free water. All samples that were used for the measurements were synthesized according to the standard procedure presented in Chapter 4.1.6.

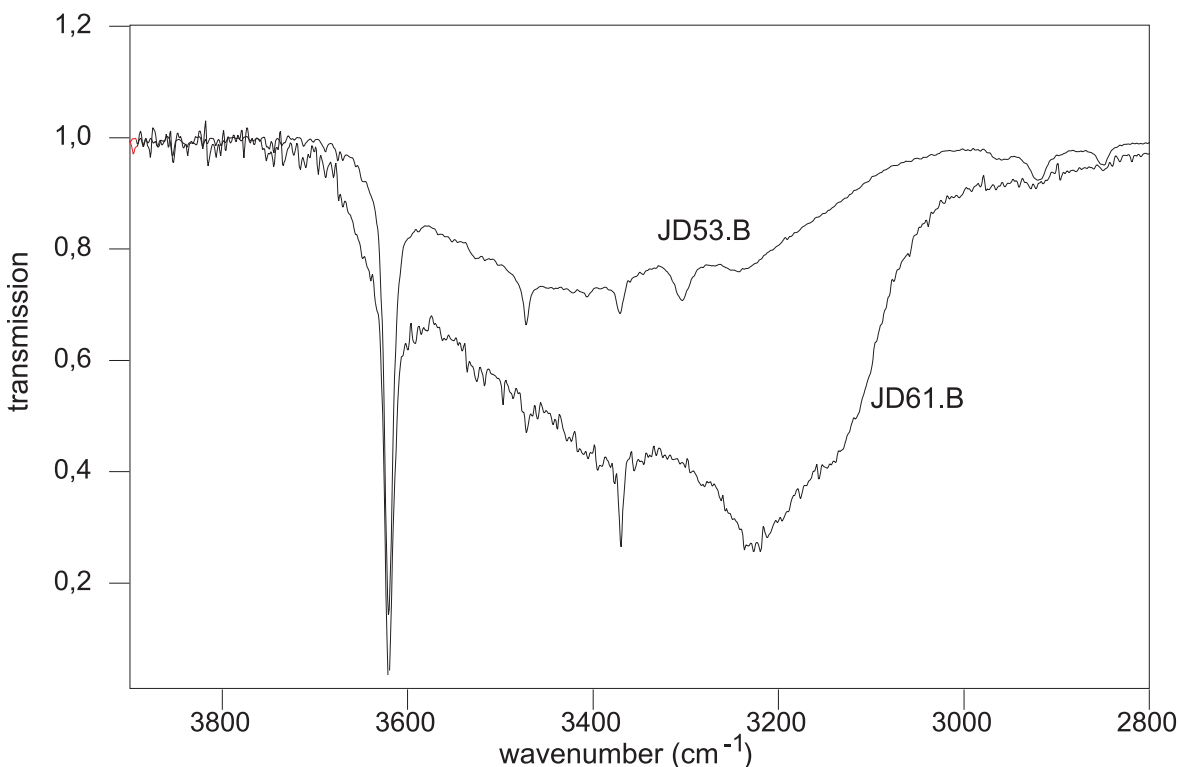


Figure 7: Low temperature infrared transmission spectra of an undeformed reference sample of synthetic jadeitite (JD61.B) and a deformed sample (JD53.B). The wave-number of the sharp peaks did not change. In contrast, the change in the shape and level of the broad absorption band reveals, that the lower water content of the deformed sample is due mainly to fewer freezable inclusions.

For some measurements, a considerable decrease of intensity due to scatter within the

sample was encountered, leading to noisy spectra (e.g. JD61.B in Figure 7). Peaks at approximately 2920 cm^{-1} and 2850 cm^{-1} observed for sample JD53.B are caused by the glue that was used to fix the sample onto the sample stage. Room temperature and low temperature spectra reveal sharp peaks (Figure 7). The most pronounced peak occurs at a wavelength of approximately 3620 cm^{-1} for the deep temperature spectra and 3612 cm^{-1} for the room temperature spectra. Peaks at wavelength of approximately 3471 cm^{-1} and 3371 cm^{-1} do not shift position. In addition to these peaks, broader absorption bands indicate the presence of free water inclusions for all samples. The occurrence of steep flanks on the edges of broad absorption bands in the low temperature spectra reveal that for the undeformed samples and the deformed samples JD56.B and -C at least half of the water is present as freezable inclusions. The lower water content in samples JD53.B and JD61.C seems to correlate with fewer inclusions of freezable water, as the indications for free water inclusions in the spectra for those samples are less pronounced (Figure 7).

Table 5 summarizes the results of the quantitative evaluation of the spectra. No simple correlation of the water content of the deformed samples with either the duration of the deformation experiment or with the temperature at which the sample was deformed is discernible. Instead the measurements can be divided in three groups; the undeformed reference samples show both a similar water content and a similar type of defect. Deformed samples JD53.B and JD61.C have water contents that are distinctly lower, whereas for the deformed samples JD56.B and JD56.C, a water content was revealed close to the water content of the undeformed reference samples. This indicates a water loss for the samples JD53.B and JD61.C during the deformation experiment. These samples were surrounded by a thin-walled platinum capsule, while samples JD53.B and JD61.C were surrounded by a thick-walled gold capsule. It appears that water loss was enhanced through the platinum jacket. This reasoning is supported by Popp and Frantz (1977), who stated that platinum capsules serve as semi-permeable membranes for hydrogen, whereas gold jackets limit the flux of hydrogen.

No study of infrared absorption of jadeite is reported in the literature, although studies have been performed on other clinopyroxenes. Ingrin *et al.* (1989) determined the water content of wet diopside crystals and found absorption bands at a wavelength of 3640 cm^{-1} , 3535 cm^{-1} , 3460 cm^{-1} and 3355 cm^{-1} . Skogy *et al.* (1990) reported the occurrence

Sample	ref/def	water content		t	T
		mol H ₂ O/l	wt-%	[min]	[°C]
JD53.C	reference	0.20	0.11		
JD61.B	reference	0.21	0.11		
JD53.B	deformed	0.12	0.07	1390	1000
JD61.C	deformed	0.12	0.07	3100	900
JD56.B	deformed	0.18	0.10	150	800
JD56.C	deformed	0.21	0.11	2500	1000

Table 5: Water content given in units of mol H₂O/l of the deformed and undeformed synthetic jadeitite samples inferred from infrared absorption spectra following the calibration of Paterson (1982). The water content in wt-% is calculated using the molar mass of water and an average density of jadeite of 3.3 g/cm³. 't' denotes the duration of the actual deformation experiments, which corresponds to the duration at final pressure and temperature conditions. 'T' gives the temperature at which the sample was deformed.

of a prominent absorption band at a wavelength of 3470 cm⁻¹ for one omphacite sample. Smyth *et al.* (1991) acquired room temperature infrared absorption spectra for different omphacites. For jadeite-rich compositions they found a strong γ -polarized absorption band at a wavelength of 3620 cm⁻¹ and a strong α -polarized absorption band at a wavelength of 3470 cm⁻¹ for a diopside-rich composition. This is in good agreement with two of the prominent absorption peaks observed for the synthetic jadeitite of this study.

4.2 Description of natural jadeitite samples

Two pieces of natural jadeitite (JC and FC3) from Burma (Harlow and Sorensen, 2001) were kindly provided by Guanghai Shi. Optical microscopy of these samples reveals a heterogeneous microstructure (Figure 16a in Chapter 6.2.2). Elongated, lath shaped grains with an aspect ratio of 3 to 5 are conspicuous. The maximum grain diameter is about 2.5 mm. The grain shape and the large aspect ratio preclude the quotation of a physically meaningful average grain size. For most grains, the long dimension ranges from 0.8 mm to 2 mm. Some smaller grains with an apparent size of about 150 μ m are

distributed throughout the sample. Locally, clusters of grains with a diameter below 50 μm occur between larger grains with rational boundaries.

When examined with the polarizing microscope, most grains show a uniform extinction and only few grains show a weak undulose extinction. Grain boundaries tend to be unilaterally rational. Otherwise, they are irregular; a foam microstructure is not developed. Favourably-oriented grains exhibit distinct microcracks along crystallographic directions (cleavage planes $\{110\}$). No shape- or crystallographic-preferred orientation is detected. No twinning is observed. The material is free of porosity.

oxide component	wt-%
SiO ₂	59.43±0.37
Al ₂ O ₃	24.53±0.86
Na ₂ O	14.68±0.45
CaO	0.75±0.67
MgO	0.56±0.48
total	99.96

Table 6: Average of 59 microprobe analyses on samples of natural jadeitite.

Microprobe analysis was carried out on three undeformed samples. Fifty-nine measurements were performed on profiles parallel and perpendicular to the sample axis. As the results along the profiles for the different samples are nearly identical, only the average values are reported in Table 6. No other chemical components were detected. An average composition of Jd₉₇Di₃ was determined. (Di is the abbreviation for diopside.) X-ray diffraction patterns fit the reference pattern for jadeite well (ASTM data set No. 22-1338). The diffraction patterns for synthetic and natural samples are very similar (Figure 8).

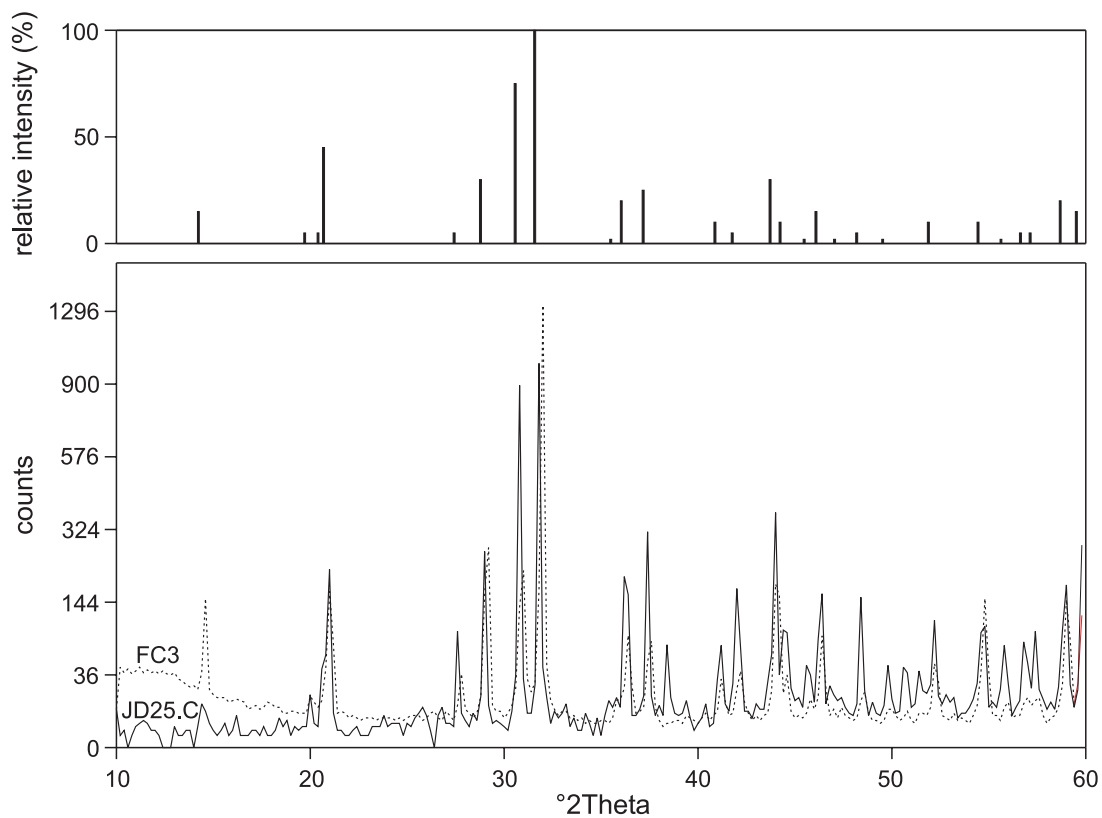


Figure 8: ASTM reference pattern for jadeite (top) and X-ray diffraction patterns of natural jadeite FC3 (broken line) and of a synthetic sample (JD25.C) (bottom). Additional peaks in the diffraction pattern for the synthetic sample are due to the gold of the capsule used for synthesis.

5 Deformation experiments

5.1 Method

Rheological properties of rocks and minerals are derived from deformation experiments that are usually carried out on cylindrical samples. The samples are subject to a confining pressure and shortened in the axial direction. For the case of jadeite, a minimum pressure of 2.4 GPa is necessary to prevent the breakdown of jadeite to nephelin and albite at higher temperatures. Such high confining pressures cannot be reached in a conventional gas-medium apparatus with the present pressure limitation distinctly below 1 GPa, but require the use of a solid-medium apparatus (Rybacki, 1991). The classical solid-medium apparatus (Griggs, 1967) was improved by Green and Borch by using a pressure-transmitting salt that is molten at experimental conditions. The apparatus used here has undergone additional modifications (Rybacki *et al.*, 1998).

5.1.1 The solid-medium apparatus

The apparatus consists of three systems that control the confining pressure, the axial load on the sample and the temperature. Confining pressure and axial load are controlled by fast-reacting servo hydraulic systems (Rummel and Fairhurst, 1970; Scholz and Koczyński, 1979). A feedback signal for the control of the axial load is given by a load cell (Schenk PMK 160kN) or one of two displacement transducers (HBM-W, ranges of $\pm 5\text{mm}$ and $\pm 50\text{mm}$). Control signals are generated by an internal function generator. The output-signal of a pressure gauge (HBM P3MB) provides the feedback signal for the control of the confining pressure. Heating is provided by a graphite resistance furnace. Electrical current is regulated by a thyristor and a programmable controller using NiCr-Ni-thermocouples for automatic temperature control.

5.1.2 Confining medium and sample preparation

Salts that are molten under experimental conditions are used as pressure media for the deformation experiments. They improve the stress resolution substantially by reducing friction (Gleason and Tullis, 1995). In the apparatus used in the present study, Rybacki *et al.* (1998) successfully used a LiCl-KCl eutectic for experiments on aragonite. In con-

trast, experiments on jadeitite samples coated by either gold, platinum or nickel were not successfully when using this mixture. Samples exhibited axial fractures and green discoloration. A sudden stress drop was observed in many cases. These effects may be attributed to a contamination of the sample by penetration of salt following a corrosion of the capsule material. Bloom (1967) reported corrosion of platinum by a water-bearing LiCl-KCl eutectic. Tingle *et al.* (1993) and Gleason and Tullis (1995) pointed out similar problems when using molten salts and discussed probable causes. They suggested that the permeability of the platinum increases due to grain growth enabling subsequent intrusion of salt.

While experiments on samples of natural eclogites and novaculites were subject to similar problems, inconel and nickel samples were unaffected by the molten salt. This confirms that interaction between capsule material, pressure medium and sample caused the brittle deformation of the samples. As all efforts to completely dry out the strongly hygroscopic LiCl/KCl mixture failed, other salt mixtures were tested. The mixture of KCl and MgCl₂ is also hygroscopic and therefore was rejected. The AgCl-KCl mixture has good mechanical properties, but reacted with the gold sample jacket. The eutectic mixture of CsCl and NaCl (34.5 mol % NaCl and 65.5 mol % CsCl) is appropriate: it is only moderately hygroscopic and is molten at pressures of 2.5 GPa and temperatures of approximately 990°C (Kim *et al.*, 1972). Brittle failure was not observed after the introduction of the CsCl-NaCl salt eutectic.

Synthesized samples were prepared for deformation experiments by grinding the gold jacket to an outer diameter of 3.4 mm and 3.8 mm respectively. The diameter of the jadeitite cylinders is about 3.0 mm. Natural samples were drilled from a piece of rock using a diamond drill bit with an inner diameter of 3.8 mm. The samples were ground plan-parallel to a length of 6.7 mm using silicon carbide abrasive papers with 600 and 1200 grade. Numerous measurements of the sample dimensions were done with a binocular microscope to determine an average and standard deviation of the sample length and diameter. Afterwards, samples were oven-dried at 250°C for a duration of at least 12h. Either gold capsules (outer diameter = 4,0 mm, inner diameter = 3,4 mm) or platinum capsules (outer diameter = 4,0 mm, inner diameter = 3,8 mm) were used. If gold was used as a capsule material, the sample was pushed tightly into the capsule and its top was

covered with a gold lid. The upper end of the sample jacket is folded to the middle to mechanically seal the capsule. When platinum was used, an open-ended capsule was made by folding one end of a thin-walled tube (0.1 mm) and pressing it flat in a die. This technique has the advantage of providing a good seal on the bottom and a good cylindrical form. A flat capsule bottom similar to that of the gold capsule is obtained.

5.1.3 The pressure cell

The assembly used for the present experiments is similar to the 3 GPa sample assembly described by Rybacki *et al.* (1998). The dimensions of some parts were adjusted (e. g. outer salt ring, graphite furnace) and an additional aluminum ring was introduced around the tin plug (Figure 9) to prevent hydraulic fracturing of the core by the molten tin.

An iron disc separates the tin from the lower part of the assembly. At the top, sealing is provided by an aluminum disc and two delta rings (Figure 9). Two drillholes in the inner pyrophyllite tube are provided for the thermocouples. Together with the outer pyrophyllite sleeve it stabilizes the graphite furnace. The pyrophyllite electrically isolates the graphite furnace from the molten salt. Special attention was given to the firing procedure, as it determines the strength and water content of the pyrophyllite. Firing at 950 °C/min for one hour yielded the best results. This procedure is commonly referred to as soft-firing (Tingle *et al.*, 1993). Before filling the inner pyrophyllite tube with the salt, an inconel tube is inserted. It serves to minimize temperature gradients in the vicinity of the sample. The pyrophyllite tube is then heated using a gas torch. Solid pieces of the salt mixture are held above the tube and melted, such that the inner hole is filled with molten salt. A 1-2 mm salt cap is provided by overfilling the inner hole. Slow cooling of the melt avoids formation of cavities. Afterwards a 4 mm central hole for the sample and piston was drilled. Attempts to replace the inconel ($\lambda = 28 \text{ W/mK}$ at 800 °C) by graphite, which has a much higher thermal conductivity ($\lambda = 168 \text{ W/mK}$) failed as the graphite did not stay in position during drilling of the central borehole. The salt on top is machined such that 0.7 mm high cap with an outer diameter of 0.9 mm remains above the pyrophyllite.

The graphite furnace rests on a steel plug to close the electrical circuit. The steel plug is isolated from the walls of the pressure chamber by a pyrophyllite ring. On top, a

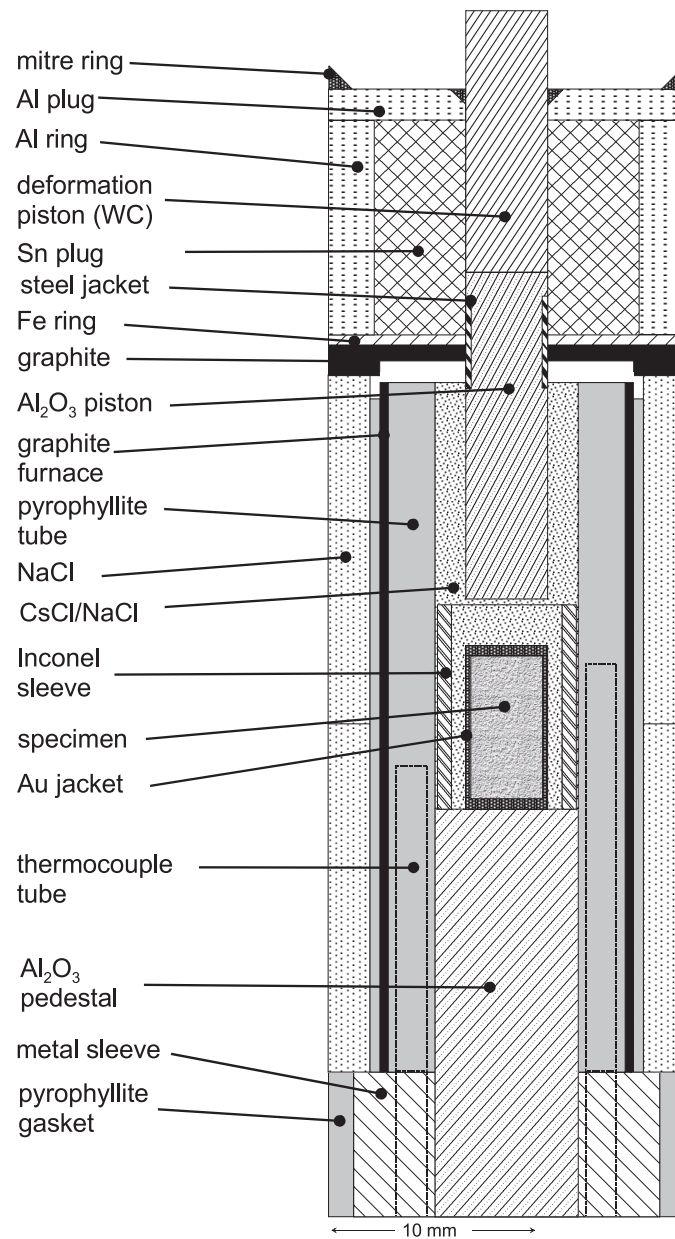


Figure 9: Sketch of the sample assembly, modified in comparison to Rybacki *et al.* (1998).

graphite disc provides electrical contact to the furnace. An Al₂O₃ piston is permanently attached to the axial tungsten-carbide piston by a metal sleeve, which is welded in place. The encapsulated sample rests on an Al₂O₃ piston.

5.1.4 Assemblage of the pressure cell

To assemble the pressure cell, the two thermocouples are led first through the base plate of the pressure chamber. The position of the thermocouples is chosen so that it corresponds to the upper and lower end of the sample. The thermocouple bead is covered with aluminum oxide paste for protection. Inspection of assemblies after the experiments revealed that in some cases the position is lower than it was at the start of the run. This might affect the temperature measurements. The lower steel plug and pyrophyllite ring is put over the thermocouples. A mica plate with a central hole is used on the bottom for electrical insulation. The sample is pressed into the prepared pyrophyllite tube and is covered with a 3 mm layer of compacted CsCl-NaCl powder. The lower ceramic piston is inserted into the central hole of the steel plug, followed by the inner pyrophyllite tube, the graphite furnace, the outer pyrophyllite tube and the outer NaCl ring. Parts which might take up water are stored in an oven at 150°C prior to assemblage. The pressure chamber is then placed over the sample assembly. Its walls are covered with a solid film lubricant (Molykote G-n) to reduce friction. The graphite disc, the iron disc, the aluminum-tin plug, the aluminum disc and the outer delta ring are then put into position. A tight fit for these parts is a vital prerequisite for the sealing of the high pressure region. The axial piston is then fed through the upper confining pressure piston and the inner hole of the sample assembly until it comes to rest on the salt reservoir above the sample.

The pressure chamber and supporting plate are positioned on the lower base plate of the apparatus. The outer ram that axially prestresses the tungsten carbide core, and the inner ram that advances the confining pressure piston are lowered, using a manually controlled pump driven by compressed air. Connections for the thermocouples, for the cooling circuit, and for electrical power are established.

5.1.5 Experimental procedure

At low pressures and temperatures considerable deviation of actual and nominal confining pressure may occur in Griggs-type apparatus due to limited deformability of the pressure transmitting parts. It is probable, that at an early stage a major fraction of the load exerted by the confining pressure piston may be taken up by the inner pyrophyllite tube. Yet, as no direct internal measurement is feasible, confining pressure is determined converting

the measurements of oil pressure according to the area ratios of the rams and pistons. The obtained pressures were calibrated against known phase transitions. To avoid breakdown of jadeite to nepheline and albite, the P-T-t path should enter the stability field of jadeite at sufficiently low temperatures. Damage of the graphite furnace introduced in early stages generally leads to high temperature gradients within the cell. To account for these problems, different paths for the build-up of pressure and temperature conditions were tested. Best results were obtained by applying the following procedure:

The pressure is increased to a nominal confining pressure of 150 MPa within approximately 20 minutes. During this stage the gap that initially exists between the graphite furnace and the graphite disc is closed. Heating rates of $5^{\circ}\text{C}/\text{min}$ are used to heat the assembly to 100°C . This stage is followed by a 30 minutes hold to allow seating of the parts. Temperature is then increased to 250°C , upon which it is held for another 30 minutes. Then the pressure is increased isothermally with a rate of approximately 6 MPa/min to 500 MPa. From thereon pressure and temperature are simultaneously ramped up to final conditions of 2.5 GPa and 800°C , 900°C , 1000°C or 1100°C . With heating rates of $4^{\circ}\text{C}/\text{min}$ or $5^{\circ}\text{C}/\text{min}$ this takes approximately 2.5 hours. The axial piston is periodically advanced into the assembly manually, using displacement increments of about $30\ \mu\text{m}$.

In the case of low strain-rate experiments a hit-point search is performed to locate the sample. To do so, the piston is moved into the assembly at a velocity of $3 \cdot 10^{-3}\ \text{mm}/\text{s}$ until a distinct increase of the force with increasing displacement is observed. The piston is then withdrawn approximately 1 mm at the same velocity. If no hit-point search is done, the piston is advanced with the appropriate velocity until the desired strain is obtained. If step tests are performed, the piston is withdrawn approximately 1 mm after a deformation step and is readvanced afterwards with a different velocity or at a different temperature. Prior to ramping down temperature and pressure, the piston is retracted at least 1 mm from the sample. Temperatures are lowered with rates of $30^{\circ}\text{C}/\text{min}$ to $50^{\circ}\text{C}/\text{min}$, using the same path as for pressurization.

5.2 The force versus displacement curve

As explained previously, the axial piston is advanced at a constant velocity to shorten the sample axially at a constant strain rate that is determined based on the sample length.

A typical record of the resulting force vs. displacement curve is shown in Figure 10. Its shape is determined by frictional forces exerted on the piston and by the strength of the sample. This chapter summarizes some ideas for the interpretation of these curves. The force vs. displacement curve can be divided into several characteristic stages as shown in Figure 10.

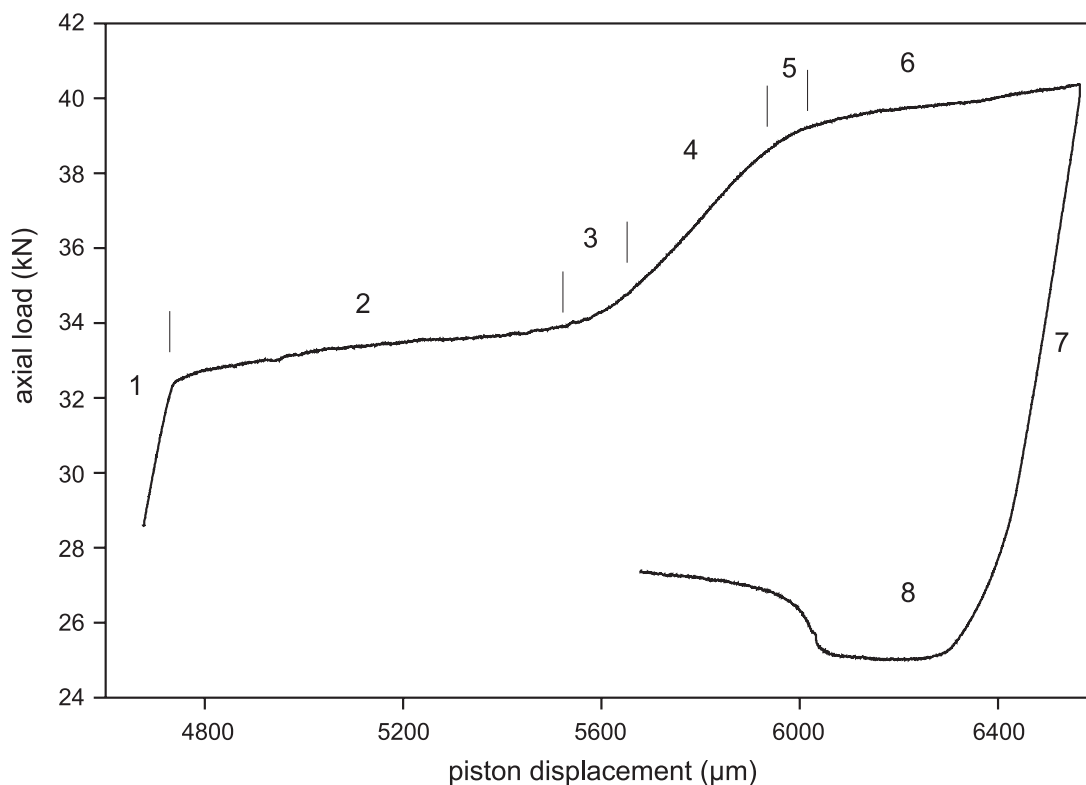


Figure 10: Record of a typical force vs. displacement curve (Sample JD48.A) and its subdivision into characteristic stages.

Initially, the force increases very steeply (stage 1). The width of this region varies between $30\mu\text{m}$ and $150\mu\text{m}$ and slopes range from 30 kN/mm to 80 kN/mm . The average slope of 58 kN/mm is similar to the stiffness of the axial column of 55 kN/mm . This indicates that the loading column takes up the deformation first, as a high static friction hinders the axial piston from moving into the assembly. When the static friction is overcome, the deformation piston actually starts to intrude into the assembly with a constant velocity. This reasoning is confirmed by the observation that the slopes are not

affected by either the velocity of the piston or the temperature.

After a short transition a stage follows, where the force increases linearly with a much lower slope (stage 2). As the piston advances through the molten salt, frictional forces need to be overcome. Figure 11 gives an overview of the measured slopes. At 1000°C no dependence seems to exist on the velocity, whereas at lower temperatures, slopes are higher with increasing velocity (Figure 11). It is striking that for the cycles aimed to locate the sample, average slopes of only approximately 1 kN/mm are observed although the piston is moved with a much faster velocity of $3 \cdot 10^{-3} \text{ mm/s}$. This observation was made at all temperatures.

Several reasons for the linear increase of the force in stage 2 are discussed. One possibility is that the confining pressure increases due to the insertion of the axial piston into a fixed volume. As the ceramic piston is incompressible, the confining pressure piston should compensate this by a backward movement. Although it could be argued that the nominal confining pressure is kept constant servohydraulically, it cannot be excluded that high seal friction prevents a backward movement of the confining pressure piston for compensation. It is not possible, however, to monitor the movement of the confining pressure piston. Thus, this possibility can neither be confirmed nor rejected. Second, the viscous drag of the molten salt may increase due to a greater contact area as the piston is advanced. This would be referred to as an increase in dynamic friction forces. Third, forces required to displace the salt between sample and piston might increase when gradually higher flow rates are needed in the salt. It has been assumed that for molten pressure media the dynamic friction forces are much greater than the forces needed to displace the salt (Rybacki *et al.*, 1998; Green and Borch, 1990; Tingle *et al.*, 1993). This is presupposed also in the present study.

Prior to loading the sample a transition region is found, where slopes gradually increase. It has a typical width of $300 \mu\text{m} \pm 200 \mu\text{m}$. In this region the capsule material between piston and sample is flattened. In one experiment, where an Al_2O_3 sample was deformed elastically without a jacket, the width of the transition region was approximately $10 \mu\text{m}$. This test provides direct evidence that the presence of capsule material affects the shape of the hitpoint. Rybacki *et al.* (1998) interpreted the transition as an indication for incomplete melting of the confining medium.

The next stage represents nominal elastic loading of the sample. The slope of the force vs. displacement curve should reflect the Young's modulus of the sample after correcting for machine stiffness. An average Young's modulus of $24 \text{ GPa} \pm 8 \text{ GPa}$ and $34 \text{ GPa} \pm 20 \text{ GPa}$ was found for the synthetic and natural jadeitite, respectively. It is observed that the modulus obtained in successive deformation cycles increases with increasing maximum force of the single cycles. For a maximum axial load of 55 kN a maximum modulus of 80 GPa is obtained. However, this value is far from the estimate of approximately 250 GPa as calculated for a pressure of 2.5 GPa and a temperature of 1000°C using the pressure and temperature derivatives for the shear and bulk-modulus from Duffy and Anderson (1989). Other studies on the deformation of polycrystalline aggregates often find similar low moduli (e.g. Kronenberg and Tullis (1984) or Jin *et al.* (2001)). In the present study, however, it was possible to determine the Young's modulus of an Al_2O_3 sample. From that it is concluded, that the measurement of the Young's modulus is affected by either the sample itself or the capsule material of the sample. The bottom of the platinum capsules has a thickness of up to 0.5 mm, which still might not be squeezed out completely at this stage. After the experiments it is observed that only a very thin layer with a thickness below 0.1 mm of capsule material is left at the faces of the samples. The width of the stage of nominal elastic loading varies between 200 μm and 800 μm . This is much wider than expected from the high elastic moduli of silicate rocks (Kirby, 1980) and thus gives further indication that the capsule material is still squeezed out at that stage. SEM pictures of undeformed reference samples reveal intragranular pores (Chapter 4.1.6). Although the pores are small and represent a small fraction (below 1%), they potentially contribute to a lower Young's modulus. It will be shown later that intracrystalline porosity has vanished in the deformed samples.

After yielding (stage 5) the sample is deformed inelastically (stage 6). The advance of the piston is stopped, when the desired strain is accumulated. As the piston inside the pressure chamber is held by static friction, retraction of the outer axial load piston causes a rapid decay in the measured load (stage 7). This is confirmed by the similarity of the slopes recorded for stages 1 and 7. When static friction is overcome, the axial piston retracts from the sample chamber. This requires intrusion of molten salt between the piston and the sample, which is commonly associated with a distinct flattening of the

slope. During stage 8, the behaviour is non-uniform. The force either stays constant or increases with displacement.

5.3 Derivation of stress versus strain curves from force versus displacement curves

The recordings of axial load and piston displacement need to be corrected to derive stress vs. strain curves. A friction correction and a correction for the elastic distortion of the axial load column is applied. Stresses are calculated assuming deformation at constant volume. An average strain rate is determined.

Experiments were performed using a salt mixture in the interior of the assembly which is molten at experimental conditions. A clear hit-point was detected in each experiment indicating that the strength of the confining pressure medium is much lower than the sample strength. A displacement dependent dynamic friction correction was applied. It assumes that frictional forces mainly act parallel to the sample and are caused by frictional drag of all components of the assembly being in contact with the moving piston. Stage 2 of the force vs. displacement curve (Figure 10) is linearly extrapolated and serves as a baseline. The hit-point is defined by the intersection of that dynamic friction baseline with a line fit through stage 4 of the force vs. displacement curve. The displacement is corrected for the elastic distortion of the axial column, with the stiffness being $S_C = 54.7kN/mm$. The stiffness was derived from experiments on an Al_2O_3 sample (Lawlis and Orzol, 2000). Calculation of the strain is based on the initial length of the sample at room conditions.

The macroscopic axial shortening of the samples is determined by measuring its lengths before and after the experiment. The displacement from the end of stage 4 to the intersection of stage 7 with the dynamic friction baseline may be also an estimate of sample shortening. For most experiments a close correspondance between both measurements is observed. An increase of diameter during ongoing deformation is taken into account, assuming deformation at constant volume (Poirier, 1985). The assumption of constant volume holds for more than 80 % of the samples if an average error of $2 mm^3$ is allowed for the volume (Table 7). This has been verified for additional 20 samples that are not listed here. Also the final diameter calculated from the measured length and the initial diameter is in good agreement with the measured final diameter. An average strain rate

is determined from the shortening of the sample and the velocity of the axial piston.

Sample No.	l_o [mm]	d_o [mm]	V_o [mm ³]	l_f [mm]	d_f [mm]	V_f [mm ³]	Δl [mm]
JD49.B	6.60	3.06	48.8	5.19	3.28	43.9	1.41
JD45.B	6.71	2.95	45.3	5.36	3.21	43.4	1.35
JD57.A	6.60	3.01	47.0	4.72	3.53	46.2	1.88
JD53.B	6.71	3.08	49.0	5.12	3.38	45.9	1.41
JD53.A	6.58	3.04	46.8	-	-	-	-
JD48.A	6.58	3.12	50.3	5.36	3.21	43.4	1.22
JC2	6.73	3.72	73.1	5.71	4.00	71.8	1.02
FC3-1	6.54	3.75	72.2	5.89*	3.95	72.2	0.65
FC3-2	6.54	3.78	73.4	5.96	3.81	67.9	0.58
FC3-5	6.57	3.78	73.7	6.11	4.01	77.1	0.46
FC3-7	6.59	3.77	73.6	6.03	3.95	73.9	0.56
FC3-8	6.57	3.77	73.1	6.13	3.93	74.4	0.44

Table 7: Sample length and diameter measured before (l_o and d_o) and after deformation (l_f and d_f) for experiments that are used for the evaluation of flow law parameters. The sample volumes V_o and V_f are calculated from the measured dimensions (*calculated from the force vs. displacement curve).

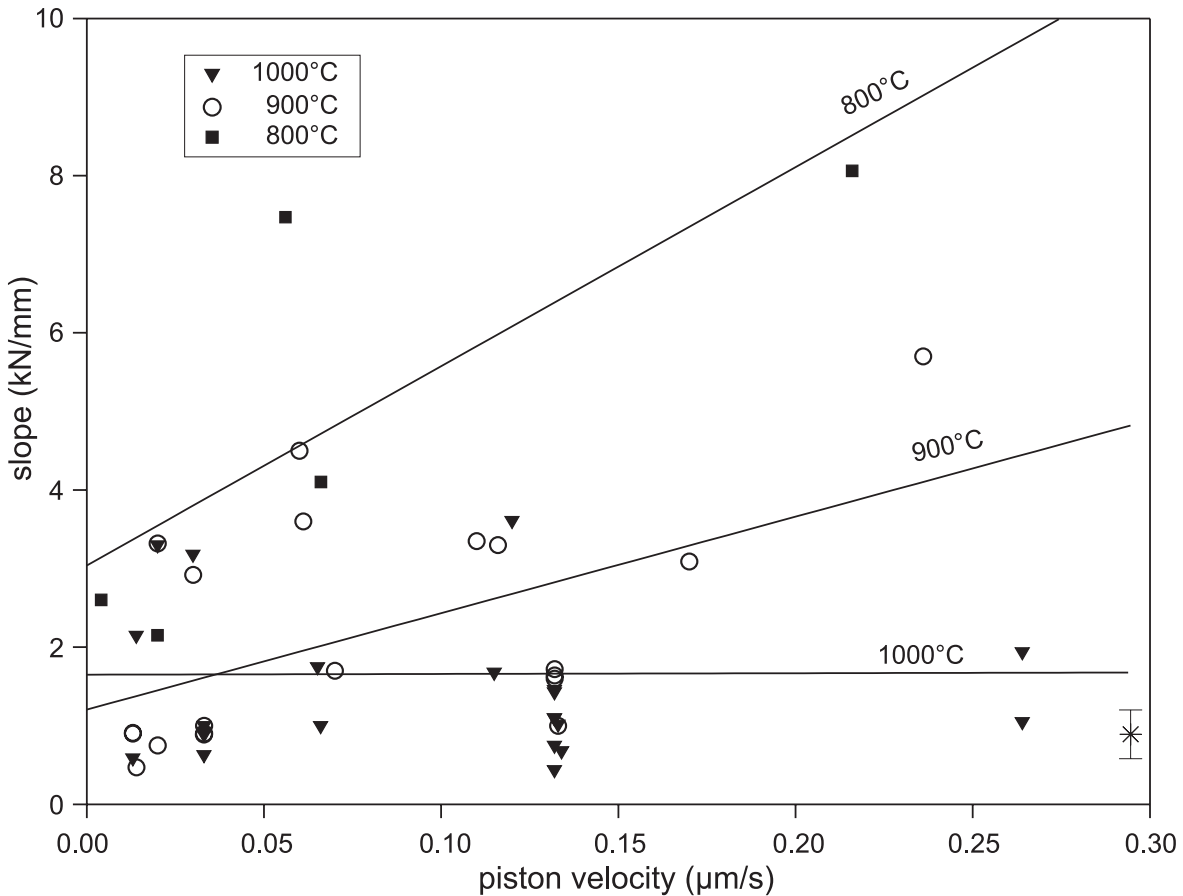


Figure 11: Slopes of stage 2 of the force vs. displacement curve (Figure 10) as a function of piston velocity and temperature. Straight lines represent linear regression fits of the data for the different temperatures. The error bars at the star that is displayed at a velocity of approximately 0.29 mm/s indicate the range of slopes obtained from cycles that aimed to locate the hitpoint. These were performed at a higher velocity of $3\mu\text{m/s}$.

6 Results of the deformation experiments

The following chapters summarize the results of the deformation experiments on both the synthetic and natural samples. It is subdivided into three sections, of which the first presents the mechanical data of the experiments on the synthetic and the natural samples. The second section describes the microstructural features that were observed in the deformed synthetic and natural samples. The critical resolved shear stress for twinning is derived by microstructural analysis of deformed natural samples together with the mechanical data, and is presented in the third section.

6.1 Mechanical data

About 20 experiments were performed to explore the optimum experimental conditions. Following this exploratory phase, 38 experiments were carried out on synthetic samples and natural samples. These experiments are listed in Appendix A and the force vs. displacement curves are given in Appendix B. All runs were performed at a nominal confining pressure of 2500 MPa. Within one experiment, the sample was loaded up to three times at different temperatures or strain rates. Stress vs. strain curves were derived wherever possible. These are displayed in Appendix C.

6.1.1 Mechanical data for synthetic jadeitite samples

Twenty-eight experiments were carried out on synthetic samples. Table 8 summarizes the mechanical data. Reported stresses are maximum or steady-state stresses. Temperature varied from 800°C to 1100°C and the strain rate covered a range from $4 \cdot 10^{-4} \text{ s}^{-1}$ to $2 \cdot 10^{-6} \text{ s}^{-1}$, corresponding to a stress between 150 MPa and 1370 MPa. In some of the experiments (JD43.1, JD44.C, JD44.B, JD43.2, JD38.A, JD45.B, JD63), other than the standard starting material (Chapter 4.1.6) were used.

Inhomogeneous deformation of samples is often observed in the case of the synthetic samples. This becomes discernible by a tilting of the samples, so that the sample axis is not aligned with the loading axis. In the case of pronounced sample tilting, the recorded stresses underestimate the real sample strength, as inferred from comparing tilted and untilted samples. Nevertheless, samples with moderate inhomogeneous deformation may

still yield useful information. For some experiments a sudden drop in axial load occurred during deformation. Most likely, failure of the jacket enabled penetration of the molten salt into the sample. This caused brittle failure due to reduced effective pressure.

Evolution of stress with increasing strain is often described as steady-state creep, strain softening, or strain hardening. These different cases are denoted in Table 8. It should be clear (Chapter 7.1), however, that this classification may not be significant due to the uncertainty inherent in the evaluation procedure, which relies on a steady increase of background friction with ongoing piston displacement. For instance, it is observed that tilting of samples always correlates with apparent strain softening.

Figure 12 presents the mechanical data in a log-log plot of stress versus strain rate and a semilog plot of stress versus inverse temperature. To maintain clarity only experiments with strain rates of $2 \cdot 10^{-5} s^{-1}$ and $5 \cdot 10^{-6} s^{-1}$ are shown in the upper part of the plot. The large scatter in the data indicates that many of the derived differential stresses do not reflect the real sample strength. For the same experimental conditions, stresses eventually vary by a factor greater than two. Data points that do not fit the general trend, however, can be identified and discarded, still leaving a big enough data base for the determination of flow law parameters (Chapter 7.2).

Sample No.	T [°C]	$\Delta\sigma$ [MPa]	$\dot{\varepsilon}$ [s ⁻¹]	ε [%]	stress evolution
JD43.1	891 ± 37	850	2.1 · 10 ⁻⁵	20	softening
JD44.C	973 ± 37	460	2.2 · 10 ⁻⁵	26	steady-state
JD44.B	998 ± 2	510	2.1 · 10 ⁻⁵	17	softening
JD43.2	921 ± 79	150	2.0 · 10 ⁻⁵	14	softening
JD38.A	992 ± 9	350	2.0 · 10 ⁻⁵	23	steady-state
JD45.B-1	882 ± 18	1370	2.0 · 10 ⁻⁵	11	steady-state
JD45.B-2	880 ± 20	870	5.0 · 10 ⁻⁶	9	steady-state

Table 8: Mechanical data for deformation experiments on synthetic samples. $\Delta\sigma$ denotes the differential stress, $\dot{\varepsilon}$ the strain rate and ε the strain. Temperature T is an average of the readings of two thermocouples. Thermocouple readings are not corrected for pressure. For JD57.A, the second thermocouple failed; it is assumed that the average deviation of 20°C is not exceeded. A '+' denotes that a sudden drop in load occurred. The stress vs. strain curves are shown in Appendix C.

Sample No.	T [°C]	$\Delta\sigma$ [MPa]	$\dot{\epsilon}$ [s ⁻¹]	ϵ [%]	stress evolution
JD46.C-1	973 ± 27	500	2.0 · 10 ⁻⁵	13	steady-state
JD46.C-2	973 ± 27	240	5.0 · 10 ⁻⁶	8	softening
JD46.C-3	973 ± 27	650	8.0 · 10 ⁻⁵	8	softening
JD46.B-1	991 ± 9	470	1.0 · 10 ⁻⁵	7	softening
JD46.B-2	891 ± 9	780	1.0 · 10 ⁻⁵	8	steady state
JD46.B-3	794 ± 6	1060	1.0 · 10 ⁻⁵	7	hardening
JD49.B	897 ± 3	700	4.5 · 10 ⁻⁶	20	hardening
JD48.A-1	985 ± 15	670	1.9 · 10 ⁻⁵	10	steady-state
JD48.A-2	885 ± 15	1290	1.7 · 10 ⁻⁵	9	softening
JD53.B-1	992 ± 8	915	1.8 · 10 ⁻⁴	12	softening
JD53.B-2	992 ± 8	390	5.0 · 10 ⁻⁶	11	steady-state
JD53.A	1096 ± 4	520	9.0 · 10 ⁻⁵	7	+
JD56.B	1024 ± 24	365	3.8 · 10 ⁻⁴	10	softening
JD57.B-1	990 ± 10	590	3.7 · 10 ⁻⁵	11	steady-state
JD57.B-2	893 ± 7	690	3.8 · 10 ⁻⁵	8	softening
JD57.B-3	794 ± 6	750	4.0 · 10 ⁻⁵	9	+
JD57.A-1	900	770	2.8 · 10 ⁻⁶	13	softening
JD57.A-2	900	1190	2.8 · 10 ⁻⁵	16	softening
JD56.C	808 ± 8	940	3.0 · 10 ⁻⁶	25	softening
JD58.B	997 ± 3	650	3.0 · 10 ⁻⁶	11	softening
JD61.A	990 ± 10	410	2.0 · 10 ⁻⁶	14	steady-state
JD63.1-1	995 ± 5	850	5.0 · 10 ⁻⁶	6	hardening
JD63.1-2	993 ± 7	990	2.0 · 10 ⁻⁵	4	steady-state
JD63.1-3	993 ± 7	1075	8.0 · 10 ⁻⁵	5	steady-state
JD63.2	975 ± 25	1340	4.0 · 10 ⁻⁴	5	hardening
JD61.C	883 ± 17	930	2.0 · 10 ⁻⁶	8	steady-state

Table 8 continued.

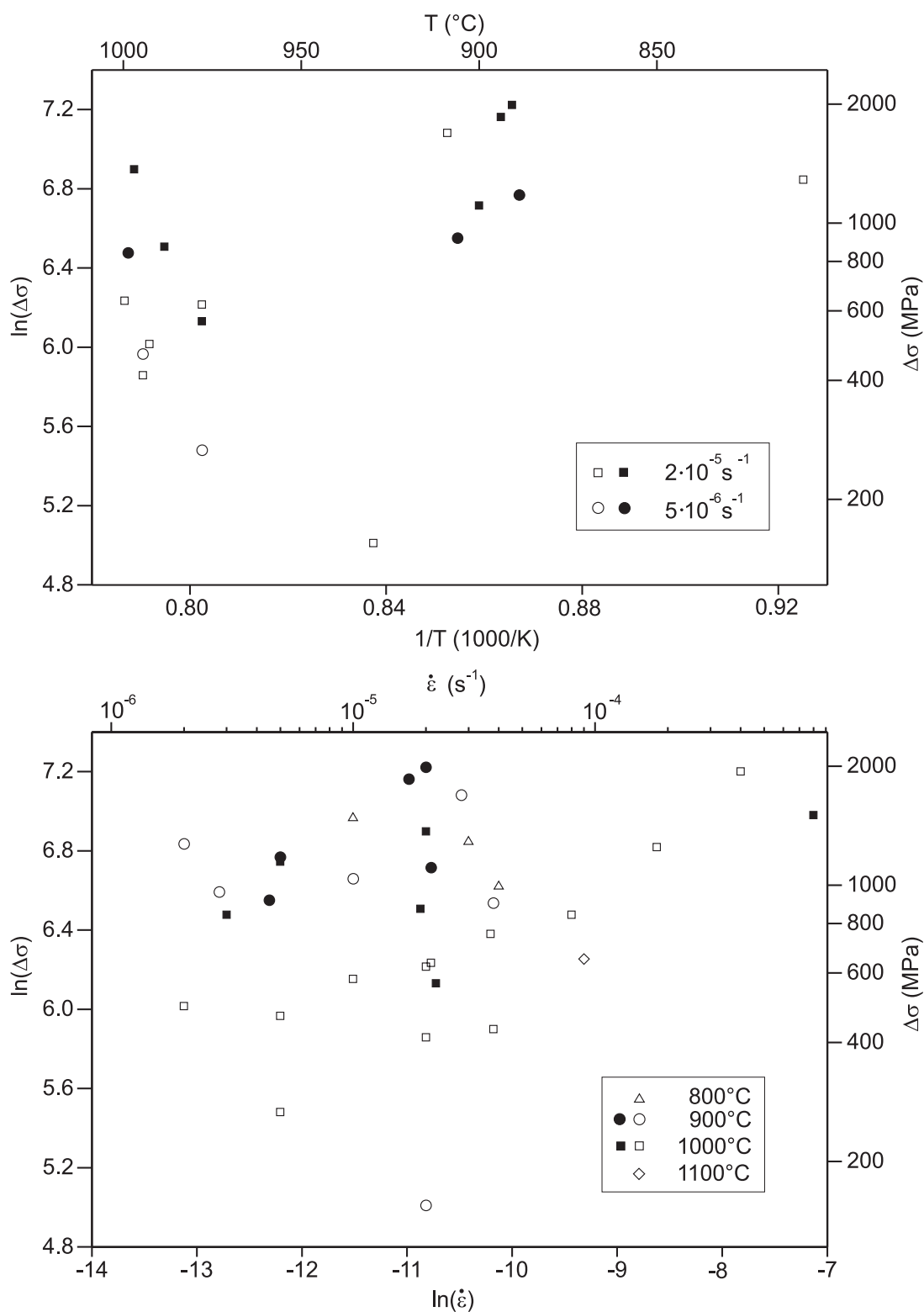


Figure 12: Graphical representation of the results of the deformation experiments on synthetic jadeitite in a semilog plot of differential stress $\Delta\sigma$ versus inverse temperature $1/T$ (top) and log-log plot of differential stress $\Delta\sigma$ versus strain rate $\dot{\epsilon}$ (bottom). Empty symbols indicate that the samples were tilted. Full symbols denote samples that remained cylindrical during deformation.

6.1.2 Mechanical data for natural jadeitite samples

Ten experiments were carried out using natural samples. Temperature covered a range from 850°C to 1100°C and the strain rate varied from $9 \cdot 10^{-5} \text{ s}^{-1}$ to $2 \cdot 10^{-6} \text{ s}^{-1}$. Sudden load drops were observed also. In the case of the natural samples, however, they were caused by a failure of the axial load piston. As the natural samples exhibit a higher strength than the synthetic samples, the piston's maximum compressive strength was exceeded at a load of approximately 55 kN. For other experiments (JC.2-2 and FC3-8-2) piston advance was stopped to prevent a catastrophic failure. Consequently, these experiments yield lower limits of the sample strength.

Tilting of natural samples did not occur. This may be due to the perfect cylindrical shape of the cored samples and their larger diameter of 3.8 mm. Table 9 summarizes the mechanical data, which are represented graphically in Figure 13. Although only few experiments were performed on natural samples, one can clearly identify a decrease in sample strength with higher temperature or lower strain rate. The scatter in the data is significantly lower than that for the synthetic samples.

Sample	T [°C]	$\Delta\sigma$ [MPa]	$\dot{\epsilon}$ [s ⁻¹]	ϵ	stress evolution
JC.2-1	996 ± 4	1030	1.9 · 10 ⁻⁵	0.08	hardening
JC.2-2	899 ± 1	1430	1.8 · 10 ⁻⁵	0.06	hardening
JC.3	1000	480	1.9 · 10 ⁻⁵	0.10	+
FC3-1	1000	835	5.0 · 10 ⁻⁶	0.10	softening
FC3-2	898 ± 2	1260	5.0 · 10 ⁻⁶	0.09	hardening
FC3-4	1111 ± 11	360	5.0 · 10 ⁻⁶	-	+
FC3-5	1000 ± 0	805	5.0 · 10 ⁻⁶	0.07	steady-state
FC3-6-1	988 ± 12	760	9.0 · 10 ⁻⁵	0.13	steady-state
FC3-6-2	986 ± 14	870	5.0 · 10 ⁻⁵	0.04	hardening
FC3-7	990 ± 10	630	1.9 · 10 ⁻⁶	0.08	steady-state
FC3-8-1	895 ± 5	1055	5.0 · 10 ⁻⁶	0.07	steady-state
FC3-8-2	845 ± 5	1380	1.9 · 10 ⁻⁶	-	hardening

Table 9: Mechanical data obtained in deformation experiments on natural samples. $\Delta\sigma$ denotes the differential stress, $\dot{\epsilon}$ the strain rate, ϵ the strain and T the temperature. '+' denotes that a sudden drop in axial load occurred. For sample FC3-4 final strain was not determined due to extensive fracturing of the sample. Inelastic loading in the second cycle of experiment FC3-8 was not sufficient to determine a strain. The stress vs. strain curves are shown in Appendix C.

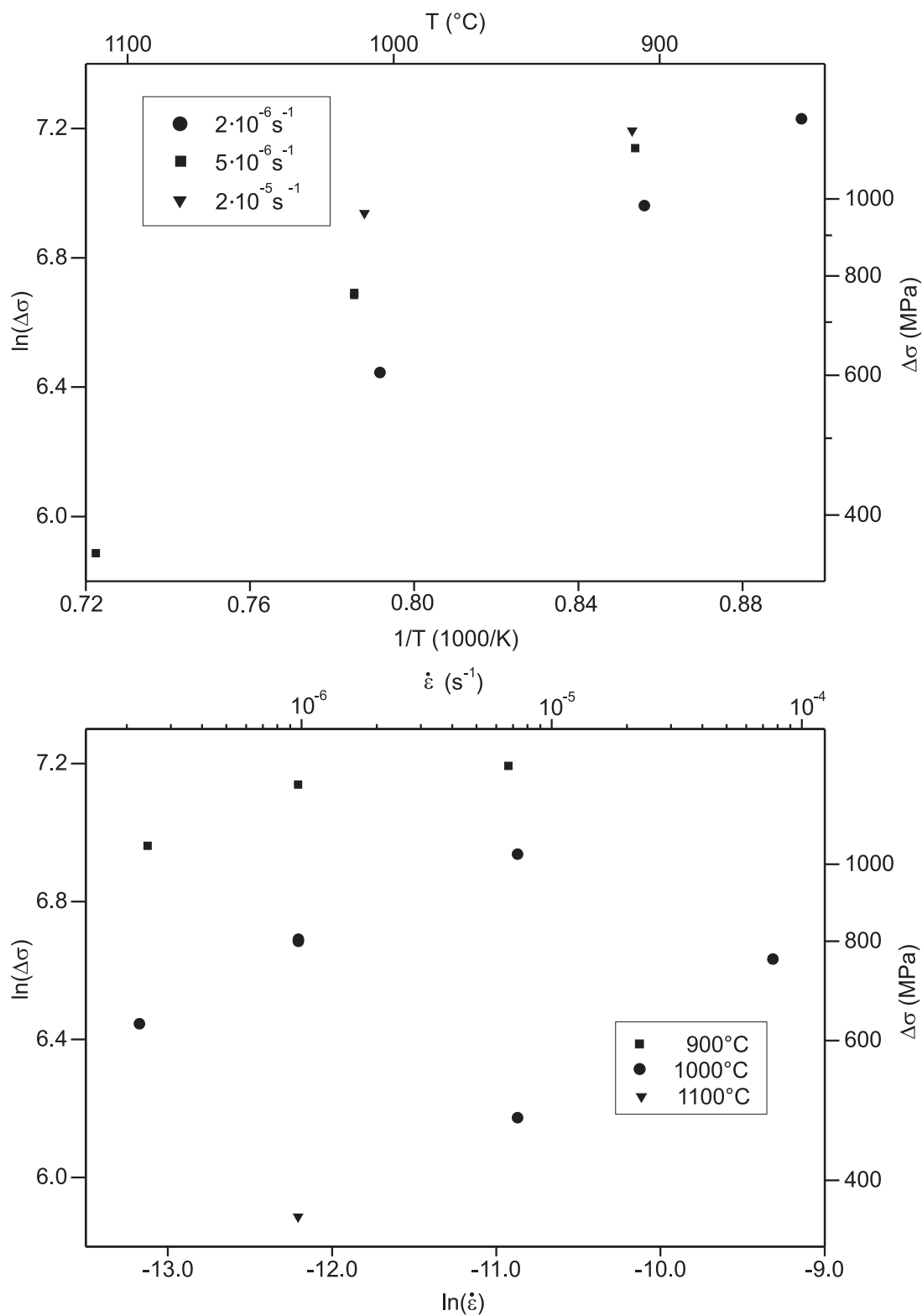


Figure 13: Graphical representation of the result of deformation experiments on natural jadeitite samples in a semilog plot of differential stress $\Delta\sigma$ versus inverse temperature $1/T$ (top) and log-log plot of differential stress $\Delta\sigma$ versus strain rate $\dot{\epsilon}$ (bottom).

6.2 Microstructural observations on deformed jadeitite samples

6.2.1 Microstructural observations on deformed synthetic jadeitite samples

The microstructure of deformed specimens differ markedly from that of undeformed reference samples. Generally, the microstructures are similar from sample to sample (Figures 14a-h). Characteristic deformation features are more pronounced with increasing strain. Microstructures are homogeneous across the whole sample, indicating that major temperature gradients within the sample do not occur (Figures 14e,f).

The deformed specimens show a marked shape-preferred orientation (SPO) with a typical aspect ratio of 2. The long axis is oriented perpendicular to the direction of shortening. Grains have a maximum diameter of approximately $100 \mu m$ (Figures 14a-d). A few blasts with tabular shape occur in both deformed and undeformed specimens. Anisotropic grain growth probably contributed to the SPO, as the aspect ratios are higher than expected for the given strain.

A crystallographic preferred orientation (CPO) is evident from optical microscopy (Figures 14a-h). Comparison of EBSD measurements on an undeformed reference sample and on three deformed samples confirm that a CPO was developed perpendicular to the shortening direction during deformation (Figure 15). The strongest CPO is found in the sample with the highest strain (JD57.A). In contrast, CPO is not pronounced for sample JD53.B, though that sample experienced a higher strain than samples JD45.B, where a CPO is discernible. For the $\langle 001 \rangle$ direction a wide point maximum is observed perpendicular to the shortening direction. A girdle maximum, however, was expected due to the rotational symmetry of the deformation of the sample.

The smoothly curved high-angle grain boundaries which were common in the synthetic samples are missing. No tendency towards a foam structure remains. Instead, sutured high-angle grain boundaries with a wavelength of approximately $2 \mu m$ are commonly observed. Also unilaterally rational high-angle grain boundaries appear to be more common compared to undeformed samples (Figures 14i,j).

The porosity of the deformed samples is reduced relative to the undeformed samples. The remaining pores are mainly found on grain boundaries. Intragranular porosity has nearly disappeared (Figures 14i,j). Grains show more or less pronounced undulose ex-

tion. Twinning is observed and becomes more widespread with increasing maximum stress. The critical stress for twinning will be discussed in Chapter 6.3.

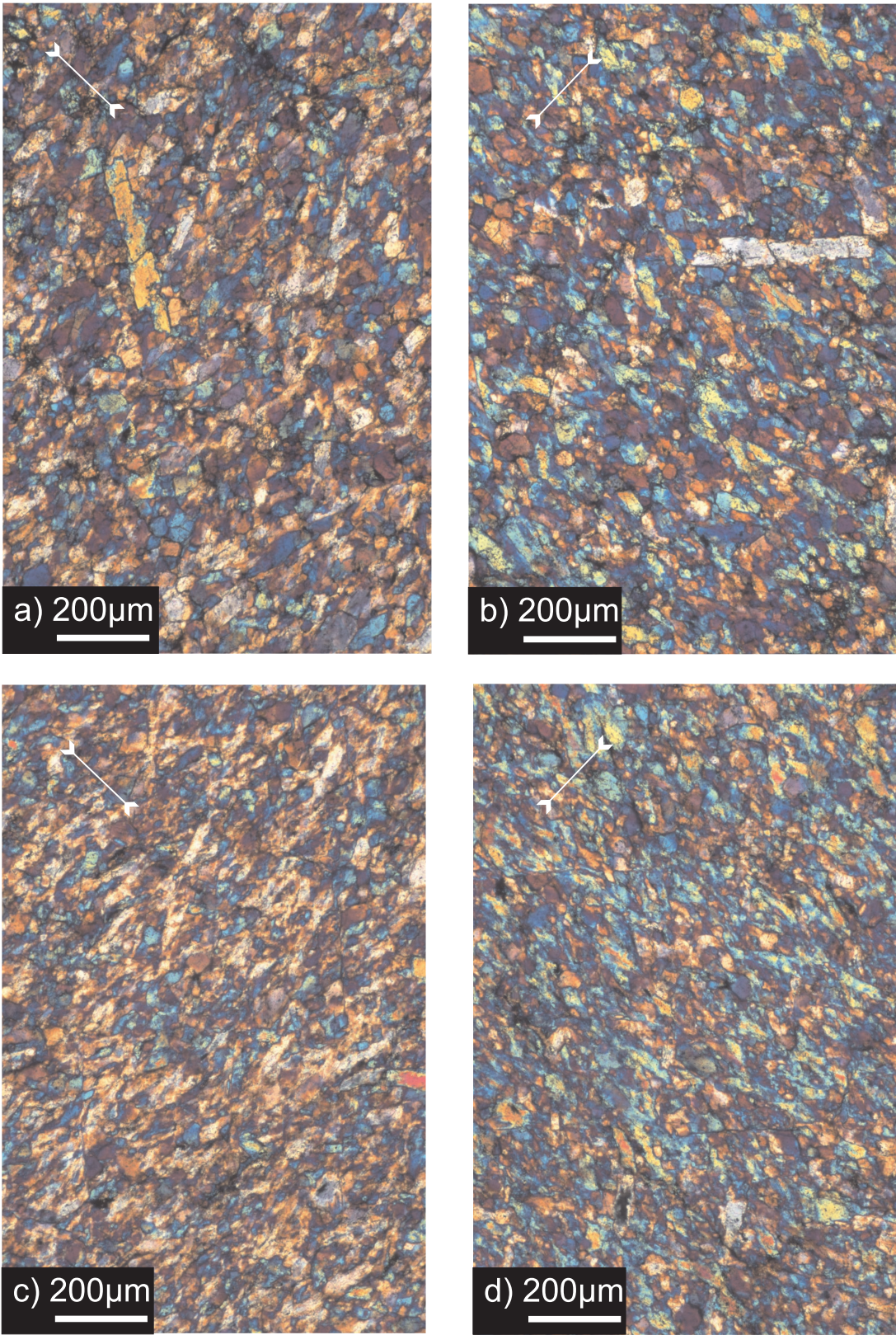


Figure 14: Micrographs of deformed samples. Explanations follow the figures.

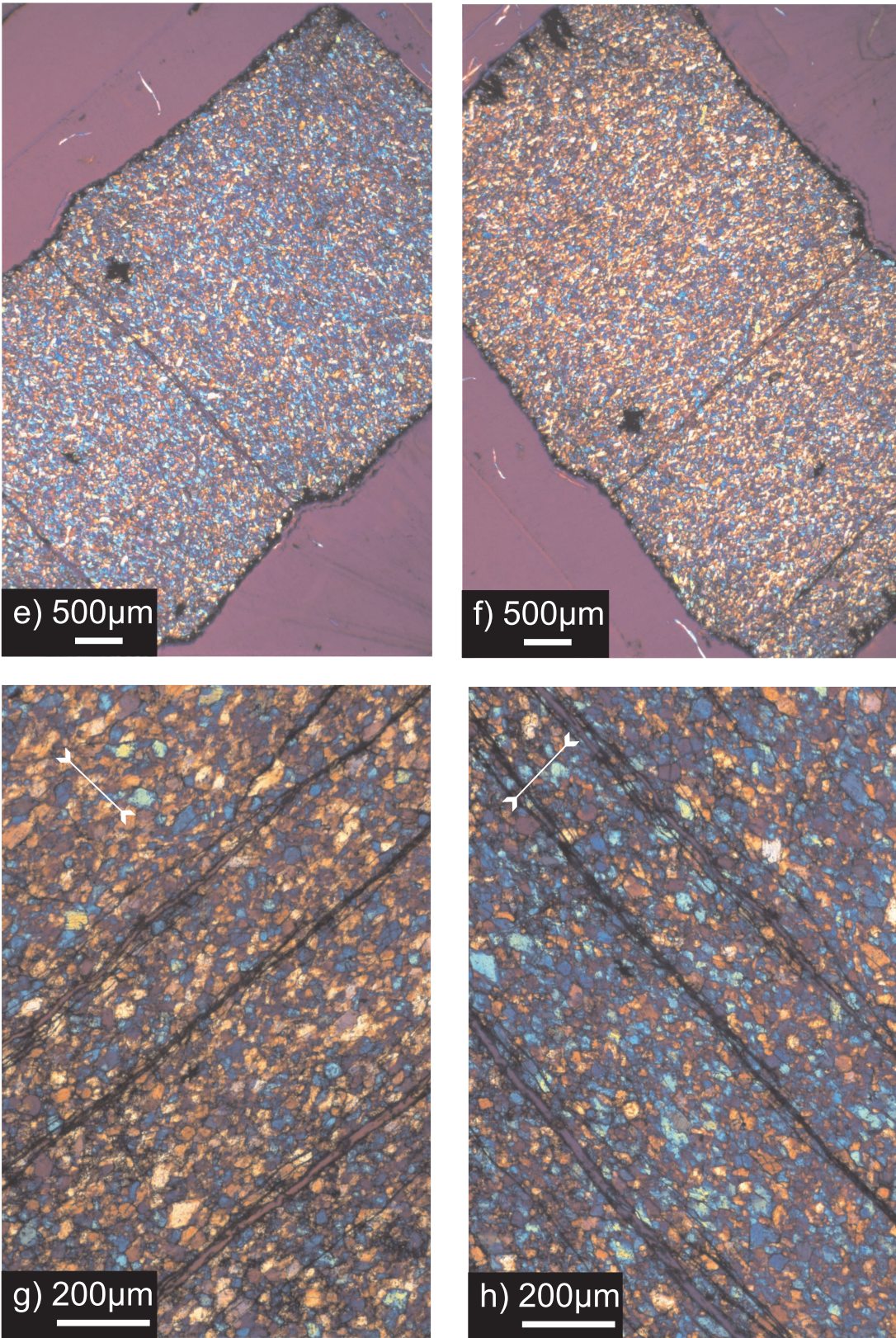


Figure 14 continued.

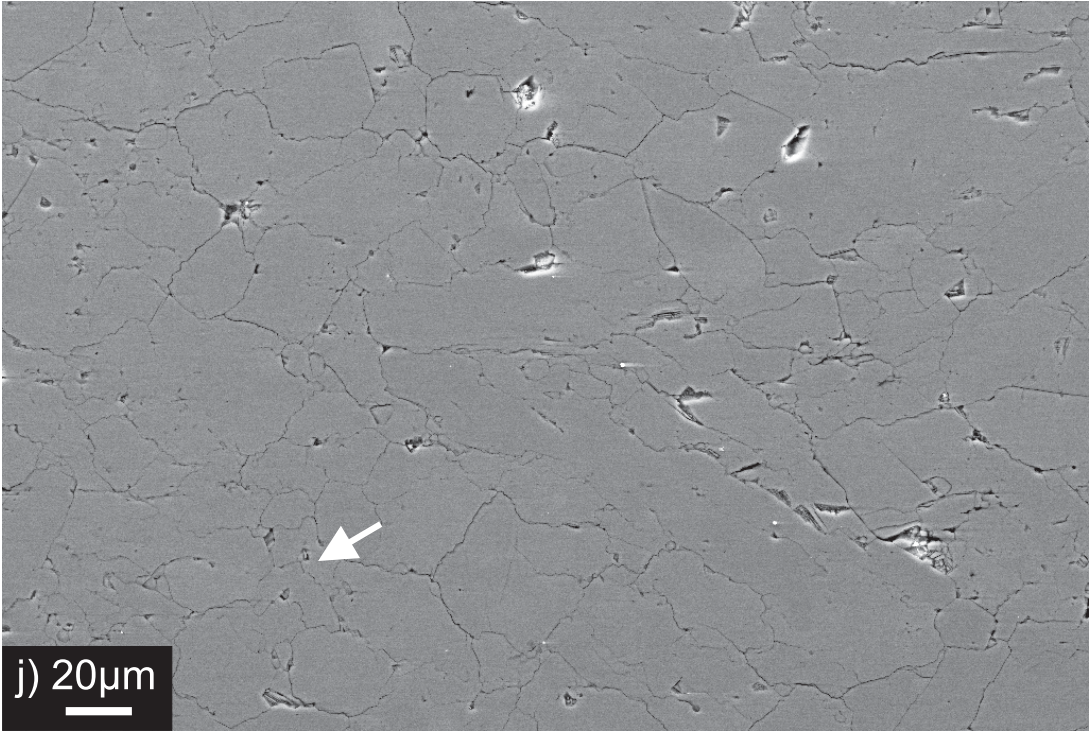
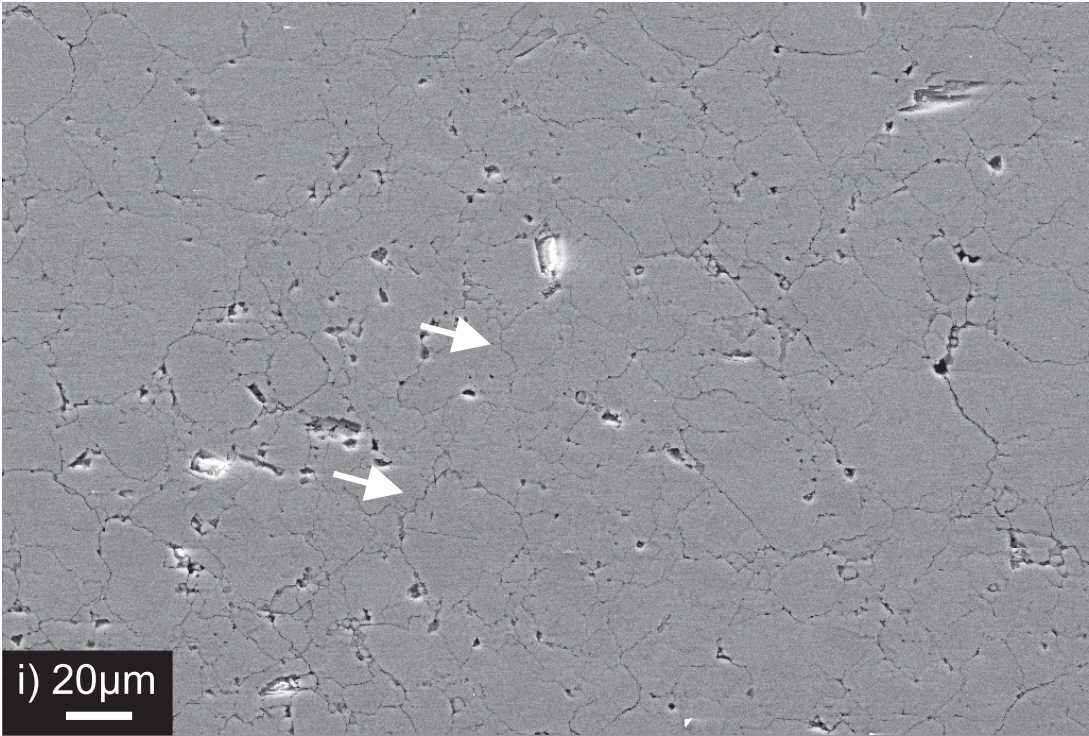


Figure 14 continued.

Figure 14: Microstructures of deformed synthetic jadeitite samples.

Optical micrographs were taken with crossed polarizers and compensator RED I; the direction of the axial shortening is indicated by white arrows.

a, b) Optical micrographs of Sample JD53.B deformed at 1000°C, $2 \cdot 10^{-4} s^{-1}$ and $5 \cdot 10^{-6} s^{-1}$ at a stress of 915 MPa and 390 MPa to a strain of 23%. A shape preferred orientation with the long axis of the grains perpendicular to the shortening direction is observed. A CPO is evident by the widespread blue or yellow colors that are observed when the microscope stage is turned by 90°.

c, d) Optical micrographs of Sample JD57.A deformed at 900°C, $3 \cdot 10^{-6} s^{-1}$ and $3 \cdot 10^{-5} s^{-1}$ at a stress of 770 MPa and 1190 MPa to a strain of 29%. Observations are similar to a) and b), but grains are more elongated and the foliation is more pronounced.

e, f) Optical micrographs of Sample JD48.A deformed at 1000°C and 900°C, $2 \cdot 10^{-5} s^{-1}$ at a stress of 670 MPa and 1290 MPa to a strain of 19%. A homogeneous microstructure and a CPO are discernible. Major temperature gradients can be excluded in agreement with the record of the thermocouples (see Chapter 7.1).

g, h) Optical micrographs of Sample JD45.B deformed at 900°C, $2 \cdot 10^{-5} s^{-1}$ and $5 \cdot 10^{-6} s^{-1}$ at a stress of 1370 MPa and 870 MPa to a strain of 20%. Despite the different conditions of deformation, the microstructural features are similar to those shown in the previous figures.

i) SEM image of Sample JD45.B, deformed at 900°C, $2 \cdot 10^{-5} s^{-1}$ and $5 \cdot 10^{-6} s^{-1}$ at a stress of 1370 MPa and 870 MPa to a strain of 20%. Compared to undeformed samples (Figure 5 a), porosity is reduced. Intragranular porosity is negligible. Sutured grain boundaries with a short wavelength of approximately $2 \mu m$ are common.

j) SEM image of Sample JD53.B, for deformation conditions see a) and b). A SPO is discernible. Hardly any intragranular porosity is observed.

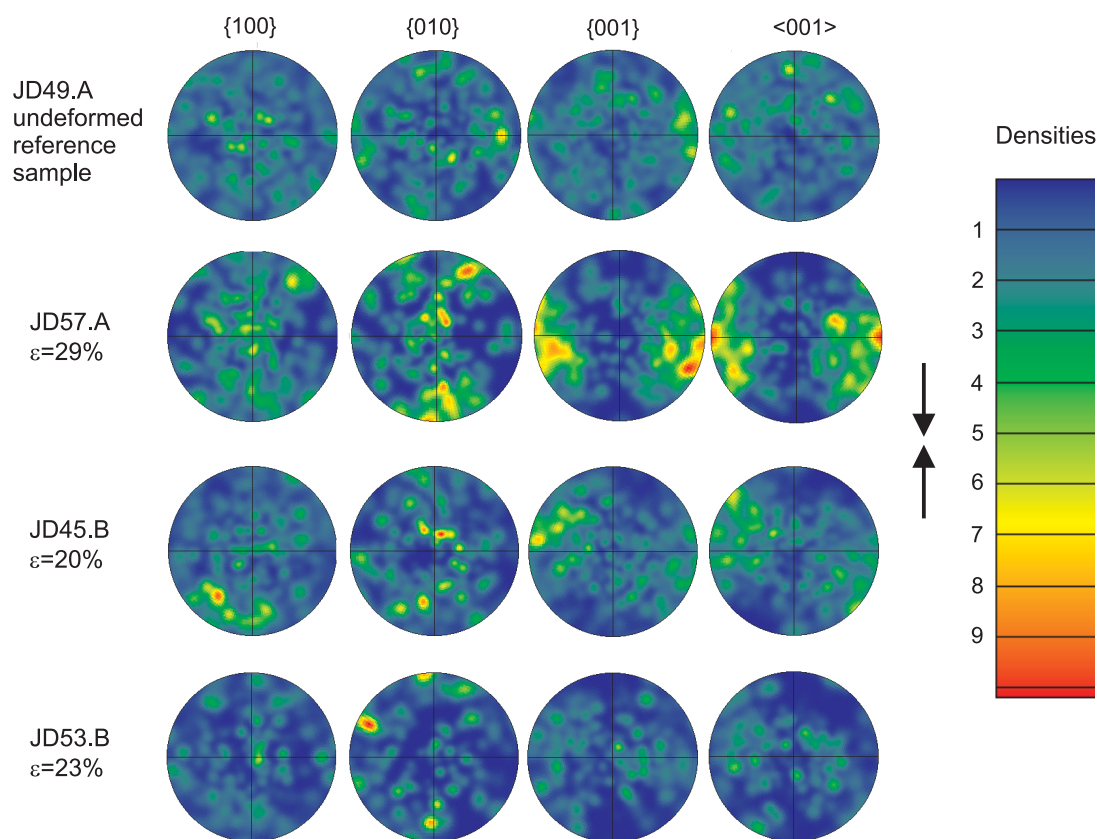


Figure 15: Pole figures showing crystallographic orientation in synthetic samples for a undeformed reference sample and three deformed samples. Different colors correspond to different densities of poles per area. Pole figures are oriented with the cylinder axis vertical. CPO is not equally pronounced for each deformed samples. The strongest CPO is found in the sample with the highest strain.

6.2.2 Microstructural observations on deformed natural jadeitite samples

The microstructures of the deformed natural and synthetic samples differ markedly, as do those of the starting material. In contrast to the synthetic starting material, the undeformed natural material reveals a complex microstructure with a coarse grain size (Figure 16a). Such microstructure favours inhomogeneous deformation and precludes formation of a homogeneous microstructure.

Undulose extinction is observed in most grains (Figures 16b,c). Twinning occurs in suitably oriented grains, with a width of lamellae below $1 \mu m$. No shape or crystallographic preferred orientation can be detected (Figures 16b,c,d). In few cases, small domains, bound by rational high-angle boundaries of larger grains, contain smaller highly-strained grains. Within these regions, the grains developed a CPO.

High-angle grain boundaries of deformed samples appear to be more irregular than those of the undeformed samples (Figure 16). Very few locations are found where grain boundaries form bulges. A major difference compared to the undeformed microstructure is the extensive microcracking (Figure 16c). All samples exhibit microcracks oriented perpendicular to the direction of shortening. These cracks are transgranular and their spacing is on the order of $100 \mu m$ to $150 \mu m$. These cracks are attributed to unloading following the deformation stage.

In addition, suitably oriented grains contain networks of nearly perpendicular microcracks. Their orientation is not correlated to the direction of compression, but is controlled by the $\{110\}$ cleavage of jadeite. The (110) and $(1\bar{1}0)$ planes enclose an angle of 87° (Deer, 1962). Spacing of cracks is approximately $10 \mu m$. The microcracking is more pronounced at higher strains. These cracks are induced by deformation rather than by the preparation of the thin section, as they do not occur in undeformed samples. High stresses within the grains may also have contributed to the generation of microcracks. For the sample with the highest strain (FC3-6), a dense pattern of microcracks is observed throughout the whole sample.

Due to the starting microstructure, the deformed samples exhibit inhomogeneous deformation. No steady-state microstructure is developed with the limited introduced strain.

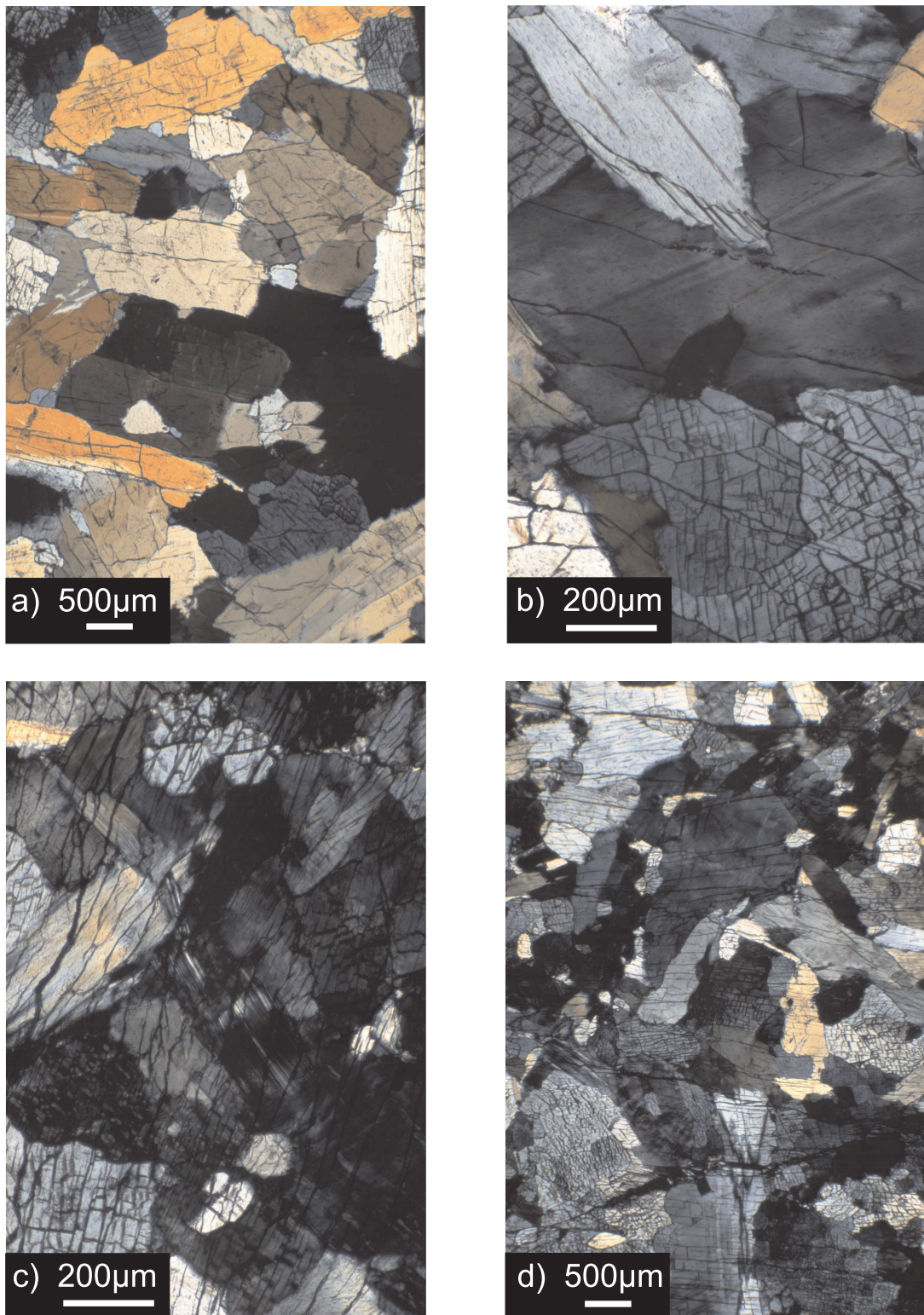


Figure 16: Optical micrographs of deformed natural jadeitite samples taken with crossed polarizers. For a description see next page.

Figure 14: Microstructures of deformed natural jadeitite samples.

a) The undeformed reference sample (FC3) has a coarse grain size and a complex, heterogeneous microstructure.

b) FC3-7, deformed at 1000°C, $2 \cdot 10^{-6} s^{-1}$ at a stress of 630 MPa to a strain of 8%.

c, d) FC3-8 deformed at 900°C and 850°C, $2 \cdot 10^{-6} s^{-1}$ at a stress of 1055 MPa and a minimum of 1380 MPa to a strain of 7%.

Deformed grains exhibit undulose extinction. Evidence of recovery is not detectable by optical microscopy. Mechanical twinning occurs in favourably oriented grains, e. g. in the center of c).

6.3 Critical resolved shear stress for twinning

Recently Trepmann and Stöckhert (2001) analysed mechanical twins in a metagranite from the Sesia Zone, Western Alps, to estimate stresses that occurred during synseismic loading and postseismic creep. However, they had to assume that the critical resolved shear stress for twinning of jadeite corresponds to that of diopside, as no experimental data were available for jadeite. Kollé and Blacic (1982) determined a critical stress of 140 ± 10 MPa for hedenbergite and 100 ± 10 MPa for chrome diopside.

The deformed jadeitite samples from this study exhibit mechanical twinning. Jadeite forms lamellar twins parallel to the (100) plane by shear in the [100] direction. No twinning occurs when the sense of shear related to twinning is in the opposite direction even if the critical stress is exceeded (Kirby and Kronenberg, 1984).

6.3.1 Method

The critical shear stress for twinning can be calculated by knowing the maximum axial stress applied during deformation. In addition, the orientation of the twinned crystals needs to be determined. This is done using EBSD measurements. Schmid's formula gives the resolved shear stress on the relevant plane using the angle between the load axis and twin plane as well as the angle between the load axis and slip direction (Poirier, 1985).

The angles can be derived from the measured orientation data. This procedure is applied for a sufficient number of twinned and un-twinned grains. In the ideal case, untwinned grains correspond to low resolved shear stress and twinned grains correspond to higher resolved shear stress. The critical resolved shear stress defines the boundary between these regions. For more details the reader is referred to Trepmann and Stöckhert (2001).

6.3.2 Results

Two deformed samples of natural jadeitite were analysed. 65 crystal orientations were acquired for sample JC2 and 52 for sample FC3-2. Measurements where stresses on the glide plane were not favourably oriented were neglected. Table 10 gives the resolved stress on the (100) plane in units of MPa; the horizontal line separates twinned grains from untwinned. Only measurements where stresses are in the vicinity of 150 MPa are reported here. Suitably oriented grains with a resolved shear stress in excess of 155 MPa all exhibit twinning. No twinning was observed for stresses lower than 150 MPa.

sample	shear stress [MPa]	
	JC2	FC3-2
untwinned	26	
	35	
	64	
	132	
	143	51
	150	116
twinned	155	165
	175	166
	182	175
	210	203

Table 10: Resolved shear stresses on the (100) plane in [001] direction, with sense appropriate for twinning, determined from samples JC2 and FC3-2.

In none of the samples twinning was observed for resolved stresses lower than 155 MPa.

When stresses exceeded 155 MPa in sample JC2 or 165 MPa in sample FC3-2, however, all grains were twinned. From sample JC2 the critical stress is confined to stresses between 150 MPa and 155 MPa, from sample FC3-2 stresses are poorly constrained between 116 MPa and 165 MPa. From these results a critical stress of 155 MPa is proposed, as the transition is well defined for sample JC2. From a Gaussian error estimate, an uncertainty of 20 MPa is derived for the resolved shear stress.

7 Discussion

In this chapter, the errors of the stress measurements are discussed first. Afterwards, flow law parameters for a power law equation are derived for synthetic and natural jadeitite. Interpretation of the microstructure of the deformed samples reveals the dominant deformation mechanisms. An error for the extrapolation of the flow law for synthetic jadeitite to low natural strain rates will be constrained and the magnitude of stress in eclogites will be estimated. Normalised representation of flow laws might reveal a similarity in the rheological behaviour of the solid-solution end members jadeite and diopside. Synthetic and natural samples are compared.

7.1 Uncertainties in differential stress, temperature, confining pressure and strain rate

A discussion of the errors is of particular importance when using a solid medium apparatus. Besides errors due to the accuracy of the employed gauges, one has to consider uncertainties inherent in the method. The main emphasize of this chapter will be on the uncertainties in the derived stresses.

7.1.1 Uncertainty in differential stress

Calculation of differential stress is based on sample dimensions measured at room conditions and the assumption of constant volume. Comparison of initial and final sample dimensions (Table 7) justifies this assumption. A load cell with an accuracy of 0.02% over the range of 160 kN and an estimated uncertainty in sample diameter of 0.1 mm lead to a stress uncertainty on the order of 20 MPa.

Another approach to determine stress uncertainty is to check the reproducibility of differential stress measurements. For instance, experiments FC3-1 and FC3-5 on natural samples yielded stresses which nominally deviate by just 5 MPa. From experiments on synthetic samples, differential stresses of 460 MPa, 510 MPa, 350 MPa, 670 MPa and 500 MPa are obtained for the same temperature and strain rate. The standard deviation of approximately 110 MPa is not a suitable measure of the error of stress determination, however, as samples with different starting microstructures as well as experiments with

tilted samples were taken into account.

When stress vs. strain curves are given for a common average temperature, additional errors are incurred in the stress. These errors correlate with temperature uncertainty during the experiment. The error $\delta\sigma$ is calculated using the following equation:

$$\ln\left(1 + \frac{\delta\sigma}{\Delta\sigma}\right) = \frac{Q}{nR}\left(\frac{1}{T} - \frac{1}{T_{ave}}\right), \quad (12)$$

where $\Delta\sigma$ is the differential stress, T_{ave} is the average temperature of the two thermocouples, T is the temperature of each individual thermocouple and R is the gas constant. The creep parameters Q and n are calculated in Chapter 7.2.1. The results are listed in Table 11. For the experiments on natural jadeitite samples, calculated deviations from the reported differential stresses are below 30 MPa due to a more homogeneous temperature distribution. Rybacki *et al.* (1998) have shown for a similar sample assembly that temperature gradients in the vicinity of the sample are considerably lower than those measured by the thermocouples. Consequently estimated deviations only yield upper limits for the uncertainty of stresses.

Sample No.	T (°C)	$\Delta\sigma$ (MPa)
JD49.B	897 ± 3	700 ± 17
JD45.B-1	882 ± 18	1370 ± 210
JD45.B-2	880 ± 20	870 ± 150
JD57.A-1	900 ± 15	770 ± 100
JD57.A-2	900 ± 15	1190 ± 150
JD53.B-1	992 ± 8	915 ± 50
JD53.B-2	992 ± 8	390 ± 20
JD53.A	1096 ± 4	520 ± 10
JD48.A-1	985 ± 15	670 ± 70
JD48.A-2	985 ± 15	1290 ± 140

Table 11: Uncertainty in differential stress $\Delta\sigma$ calculated from the temperature measurements of the thermocouples.

The force vs. displacement data are corrected for dynamic friction as described in Chapter 5.3. This requires an extrapolation of the background friction curve over the entire piston displacement during deformation. It might occur, however, that friction changes with ongoing piston displacement after hitting the sample. This results in an over- or underestimation of the sample strength. To evaluate the change of friction with ongoing piston displacement, experiments were performed where the deformation piston was backed off after deformation and advanced into the assembly again (Figure 17).

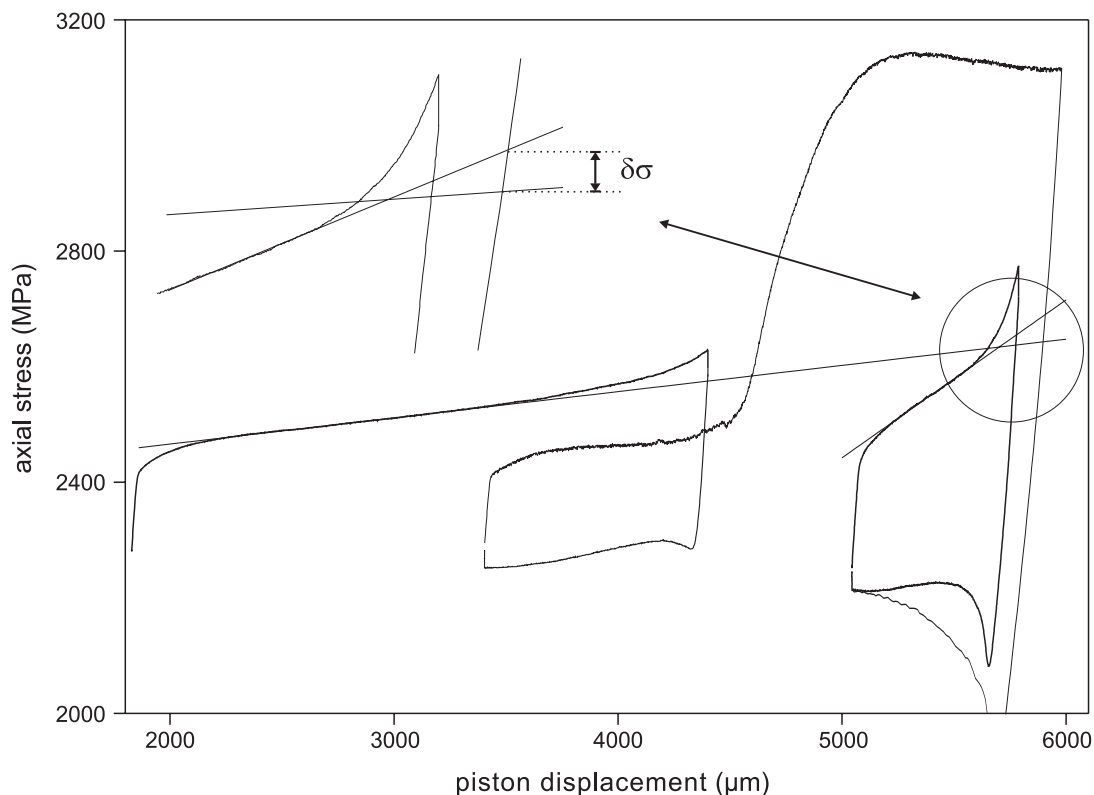


Figure 17: This figure suggests a way to obtain a measure of the error in the determination of axial stress. Records of three force vs. displacement curves with forces converted to stresses are presented. Besides the deformation cycle (thin line) one cycle was performed prior to deformation and one after deformation, both at the same velocity (thick lines). The linear portions of these latter cycles were linearly extrapolated to larger displacement as indicated by the corresponding straight lines. At a displacement that corresponds to the end of the deformation cycle a difference of the extrapolations is obtained. This difference may be considered as the uncertainty of differential stress determination. For a better illustration, the marked part of the graph is displayed enlarged.

These later cycles and the cycles prior to the deformation cycle were done at the same piston velocity. The linear portions of both of these cycles were then linearly extrapolated to larger displacement. At the position of the final piston displacement of the deformation cycle, an offset between these two extrapolations is observed. Its occurrence indicates a change in friction and its magnitude may be given as an estimate of uncertainty in differential stress. Step tests that were performed at a temperature of 1000°C can be evaluated in a similar way, as for 1000°C no dependence of the slope (stage 2 in Figure 10) on the piston velocity is observed (Figure 11). Altogether 11 cycles were analysed and on average, a change in friction corresponding to a stress uncertainty of 80 MPa is obtained.

The magnitude of all errors discussed above is either smaller than that estimate or they yielded an upper bound. Therefore, as a conservative estimate, an error of 80 MPa in differential stress is taken to be realistic.

7.1.2 Uncertainties in strain rate, temperature and confining pressure

The error in the determination of the strain rate is mainly given by the uncertainty in determining the amount of axial shortening. The uncertainty is calculated using a standard Gaussian error analysis. Assuming an error of 0.3 mm in determining the sample shortening, a typical error of 7% is introduced to the strain rate.

The uncertainty of the sample temperature is given by the uncertainty of the temperature measurements and by the arrangement of the thermocouples relative to the sample. The tolerance of the employed NiCr-Ni thermocouples is $\pm 1.5^\circ\text{C}$ at room pressure. Getting and Kennedy (1970) showed that pressure affects the temperature readings of Chromel-Alumel thermocouples considerably. No such correction was applied here, however, due to uncertainty in the seal temperature. Radial temperature gradients within the assembly are generally low and negligible (Leistner, 1979; Rybacki *et al.*, 1998). Recorded axial temperature gradients in this study are given in Table 11. The deviation from the average temperature is $19^\circ\text{C} \pm 19^\circ\text{C}$ for a 0.4 mm graphite wall thickness and $10^\circ\text{C} \pm 7^\circ\text{C}$ for a 0.5 mm graphite wall thickness. This higher reliability and reproducibility is reflected by the low scatter in relative oven power (Figure 18). The temperature gradients within the sample are expected to be considerably lower than those deduced from the

readings of the thermocouples (Rybacki *et al.*, 1998).

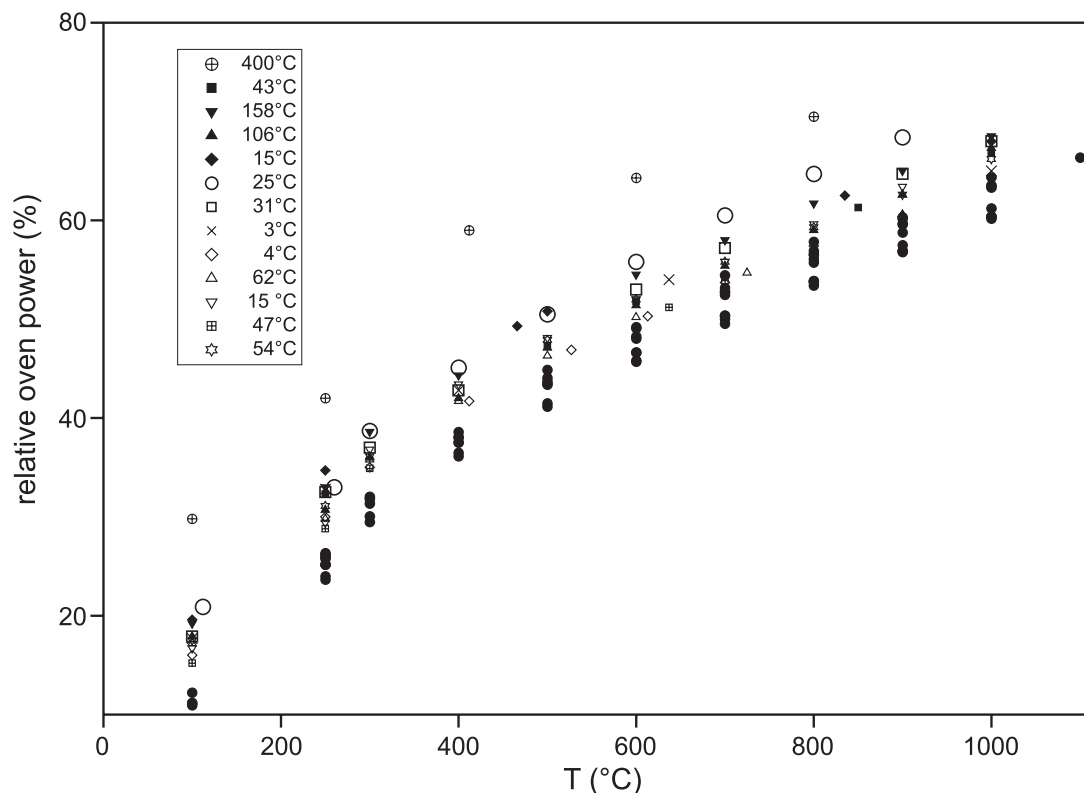


Figure 18: Relative oven power as a function of the temperature read by the controlling thermocouple. The legend gives the maximum recorded temperature difference for the different experiments that are indicated by different symbols. Solid dots correspond to runs using a graphite furnace with a wall thickness of 0.5 mm instead of 0.4 mm. Lower temperature differences and higher reliability and reproducibility is obtained if a graphite furnace with a larger wall thickness is used.

Nominal confining pressure is calculated from the oil pressure acting on the confining pressure piston and the ratio of the different piston areas. Accuracy is not limited by the accuracy of the gauges, but by friction losses within the assembly. All experiments were carried out at a nominal confining pressure of 2500 MPa, which at 1000°C is 400 MPa over the equilibrium pressure of the reaction albite+nepheline=jadeite (Figure 1). Consequently, no albite or nepheline was detected by X-ray diffraction upon termination of the experiment (Chapter 4.1.5). Yet, the reaction yielding albite and nepheline may be sluggish, such that no detectable amounts are generated. Various authors have discussed

the complex dependency of the deviation of 'sample pressure' from 'nominal pressure' (Kim, 1974; Johannes, 1978; Mirwald *et al.*, 1975). Their results, however, are not easily transferable, as they are specific to the individual set-ups.

Figure 19 shows force vs. displacement curves for cycles designed to locate the sample hitpoint. Stress was determined from the average force for the forward and backward movement of the piston. Assuming that friction is equal and opposite for advancing and retreating, this provides a measure of the confining pressure. Only two cycles yield calculated confining pressures close to the nominal confining pressure of 2500 MPa. The calculated confining pressure is usually 100 MPa below the calibration. The calculation provides only a rough guide to confining pressure, however, as the confining pressure piston is coupled to the axial piston by a dynamic seal.

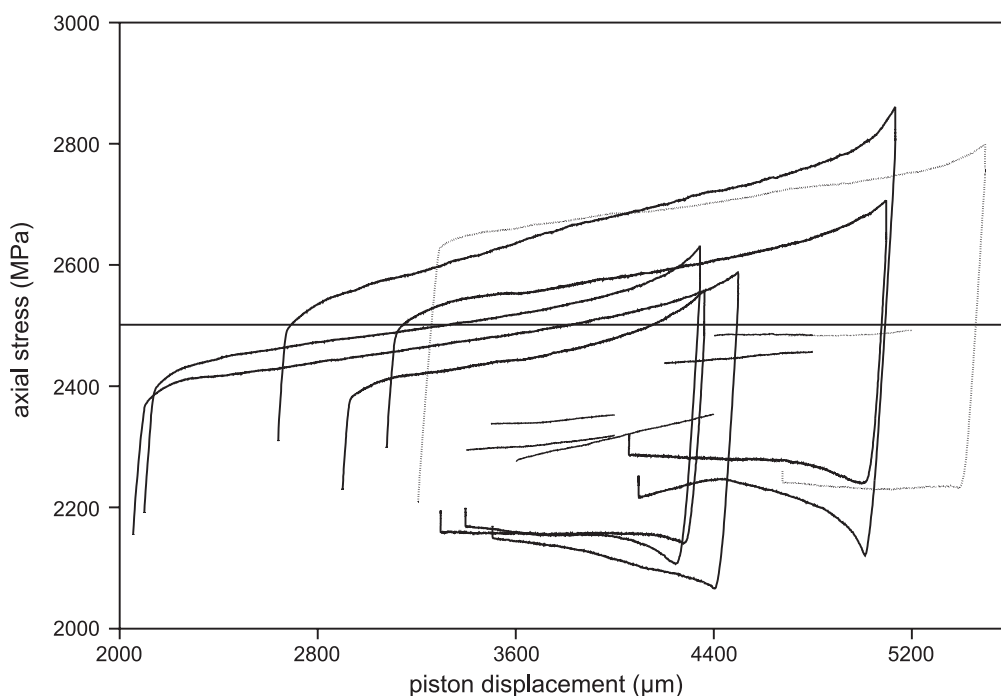


Figure 19: This figure presents an estimate of confining pressure from the recorded force vs. displacement curves. Force is converted to stress using the diameter of the piston. Average stresses were calculated from corresponding portions of the force vs. displacement curves obtained for advance and retraction of the piston. These are indicated by the near horizontal lines. Under the assumption of symmetric friction the average stress during advance and retreat may serve as a measure of the confining pressure. The nominal confining pressure of 2500 MPa is indicated by a horizontal line.

7.2 Derivation of flow law parameters

7.2.1 Derivation of the flow law parameters for synthetic jadeitite samples

Creep data were selected or rejected based on predefined criteria. Data from all runs where the samples were clearly tilted were discarded. When evaluation of the step tests yielded unrealistic values for the stress exponent and the activation energy respectively, these data were neglected. Results from step tests that were not self-consistent (JD48.C, Figure 11 in Appendix C), were not considered also. As an example, the stress derived from a temperature-stepping test on sample JD48.C did not decrease with increasing temperature at a similar strain rate. The set of data which is finally used to derive flow law parameters for the synthetic jadeitite samples is given in Table 12. Results from step tests as well as from single cycle deformation experiments are included. The advantage of using step tests is that effects due to sample-to-sample variation are minimized (Kronenberg and Tullis, 1984).

Sample	T [°C]	$\Delta\sigma$ [MPa]	$\dot{\epsilon}$ [s ⁻¹]	ϵ [%]	stress evolution
JD45.B-1	882 ± 18	1370	2.0 · 10 ⁻⁵	11	steady-state
JD45.B-2	880 ± 20	870	5.0 · 10 ⁻⁶	9	steady-state
JD49.B	897 ± 3	700	4.5 · 10 ⁻⁶	20	hardening
JD48.A-1	985 ± 15	670	1.9 · 10 ⁻⁵	10	steady-state
JD48.A-2	885 ± 15	1290	1.7 · 10 ⁻⁵	9	softening
JD53.B-1	992 ± 8	915	1.8 · 10 ⁻⁴	12	softening
JD53.B-2	992 ± 8	390	5.0 · 10 ⁻⁶	11	steady-state
JD53.A-1	1096 ± 4	520	9.0 · 10 ⁻⁵	7	steady-state,+
JD57.A-1	900	770	2.8 · 10 ⁻⁶	13	softening
JD57.A-2	900	1190	2.8 · 10 ⁻⁵	16	softening

Table 12: Selected mechanical data of synthetic jadeitite for derivation of flow law parameters. T , $\Delta\sigma$, $\dot{\epsilon}$ and ϵ denote temperature, differential stress, strain rate and strain. '+' denotes that a sudden drop of load occurred, after steady-state was achieved.

Creep data were fit by a power law equation (equation 3), using the method that was described in Chapter 2.2.4. Inversion yields the following parameters:

$$n = 3.7 \pm 0.4$$

$$Q = 326 \pm 27 \text{ kJ/mol}$$

$$\ln A = -3.3 \pm 2.0 .$$

For comparison a flow law with an exponential form (equation 4) was fitted as well. In this case, the following parameters were obtained:

$$b = 42 \cdot 10^{-4} \pm 6 \cdot 10^{-4}$$

$$Q = 310 \pm 35 \text{ kJ/mol}$$

$$\ln A = 16.0 \pm 3.1$$

Figure 20 shows the data for synthetic jadeitite fit by the power law equation. For clarity, the exponential law is not included in the plot. To quantify the quality of the fits of both flow laws, the norm of the error vector $\vec{\varepsilon}$ was determined (Chapter 2.2.4). For the power law $|\vec{\varepsilon}| = 1.0$ is obtained and for the exponential form $|\vec{\varepsilon}| = 1.4$ is obtained, indicating that the power law fit is more appropriate. Using the measured temperatures and differential stresses, the power law predicts strain rates which differ from the experimentally determined strain rates by 60% to 180%, i. e. they deviate by less than a factor of two. These deviations are substantially larger when the exponential law is applied.

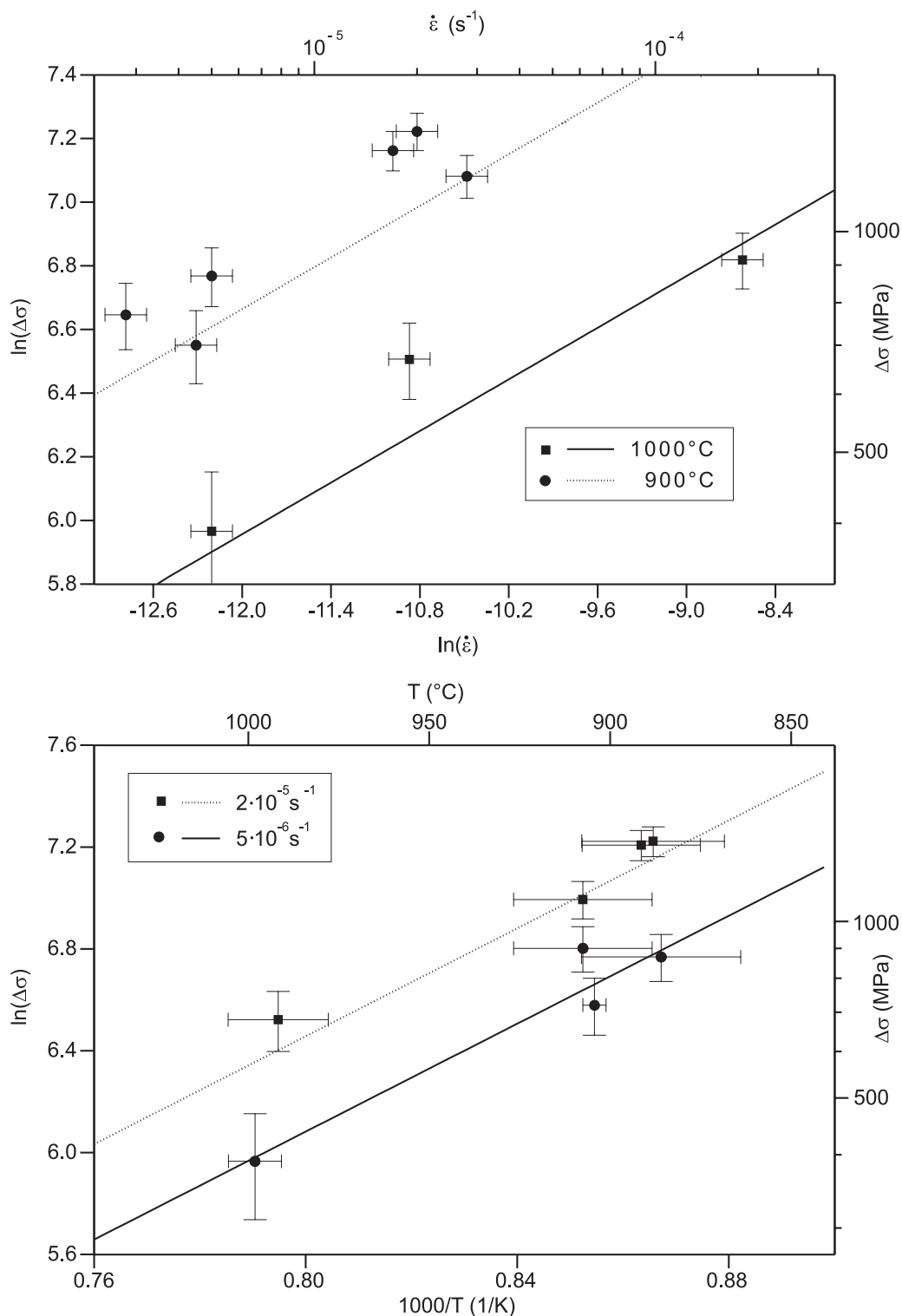


Figure 20: Plots show the fit of the experimental data of synthetic jadeitite (indicated by symbols) by the power law (solid and dotted line). Error bars according to chapter 7.1. Top: log-log plot of stress versus strain rate shows the fit of the data by the flow law evaluated for temperatures of 900°C and 1000°C, bottom: semilog plot of stress versus inverse temperature shows how the flow law fits the data for strain rates of $2 \cdot 10^{-5} \text{ s}^{-1}$ and $5 \cdot 10^{-6} \text{ s}^{-1}$.

7.2.2 Derivation of the flow law parameters for natural jadeitite samples

For the natural jadeitite, no data had to be excluded from the inversion due to inhomogeneous deformation of the samples. However, brittle failure during runs FC3-4 and JC.3 (Figures 10 and 15 in Appendix C) preclude their use for deriving flow stresses. Due to the high strength of natural jadeitite, for some experiments no mechanical steady-state level could be obtained as maximum axial forces are constrained to approximately 55 kN by the strength of the WC-pistons. Catastrophic failure of the axial piston was encountered at a force of 54 kN during the run FC3-6 (Figure 16 in Appendix C). Table 13 summarizes the data to be used for the determination of flow law parameters.

Sample	T [$^{\circ}C$]	$\Delta\sigma$ [MPa]	$\dot{\epsilon}$ [s^{-1}]	ϵ [%]	stress evolution
JC.2-1	996 ± 4	1030	$1.9 \cdot 10^{-5}$	8	hardening
FC3-1	1000 ± 10	800	$5.0 \cdot 10^{-6}$	10	softening
FC3-5	1000 ± 0	805	$5.0 \cdot 10^{-6}$	7	softening
FC3-7	990 ± 10	630	$1.9 \cdot 10^{-6}$	8	steady-state
FC3-2	898 ± 2	1260	$5.0 \cdot 10^{-6}$	9	hardening
JD3-8-1	895 ± 5	1055	$2.0 \cdot 10^{-6}$	10	steady-state

Table 13: Mechanical data from experiments on natural samples that are used for derivation of flow law parameters. T , $\Delta\sigma$, $\dot{\epsilon}$ and ϵ denote temperature, differential stress, strain rate and strain.

A power law equation was used to fit the data. Inversion of the data yields:

$$n = 4.4 \pm 0.3$$

$$Q = 263 \pm 19 \text{ kJ/mol}$$

$$\ln A = -16.8 \pm 1.6.$$

An error vector of 0.3 is calculated, which is considerably lower than that for the synthetic jadeitite samples. This is surprising, as large sample-to-sample variations were expected due to the inhomogeneity of the undeformed microstructure. The data set is smaller and

a more narrow range of temperature und strain-rate was covered in comparison to the data of the synthetic jadeitite. However, Figure 21 confirms the good fit to the power law equation. The magnitude of the stress exponent and the good correspondance to a power law equation are indicative of deformation in the dislocation creep regime. As indicated in Chapter 2.2, accompanying occurrence of microstructural features is required to confirm that samples were deformed in the regime of dislocation creep (compare Chapter 7.3).

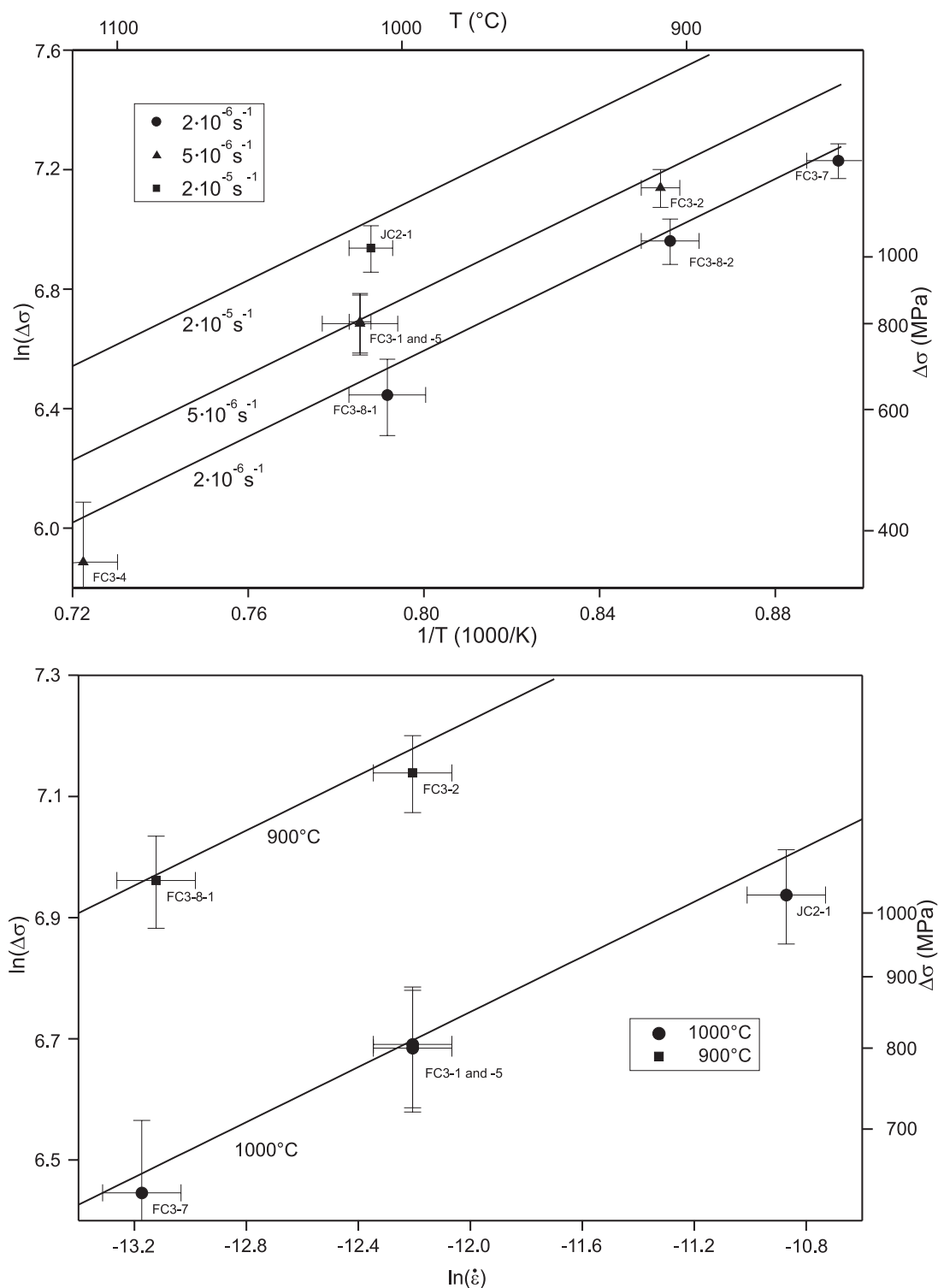


Figure 21: Plots show the fit of the experimental data of natural jadeitite (indicated by symbols) by a power law equation. Top: semilog plot of differential stress $\Delta\sigma$ versus inverse temperature $1/T$ is presented at strain rates of $2 \cdot 10^{-6} \text{ s}^{-1}$, $5 \cdot 10^{-6} \text{ s}^{-1}$ and $2 \cdot 10^{-5} \text{ s}^{-1}$. Bottom: log-log plot of differential stress $\Delta\sigma$ versus strain rate $\dot{\epsilon}$ is shown at temperatures of 900°C and 1000°C.

7.2.3 Discussion of the activation energy for dislocation creep of jadeite

The micromechanical model underlying the power law developed by Weertman (1968) demands that the activation energy for creep corresponds to the activation energy for diffusion of the slowest moving species. For metals, an extensive set of data confirms this assumption (Weertman, 1968). For the present study, the activation energy for the diffusion of the slowest moving species of jadeite would need to be compared to the activation energy for dislocation creep of jadeite. Microstructural evidence for dislocation creep in natural jadeite is not present, however (Chapter 7.3). Consequently, the following considerations will be restricted to the results obtained for the synthetic samples. A discussion of the activation energy for dislocation creep of jadeite would be difficult, as no diffusion data are presently available for jadeite.

In contrast, diffusion experiments were carried out for all atomic species of diopside and their corresponding activation energies were derived (Farver, 1989; Ryerson and McKeegan, 1994; Dimanov and Ingrin, 1995; Bějina and Jaoul, 1997; Azough *et al.*, 1998; Pacaud *et al.*, 1999). Activation energies for dislocation creep of diopside range from 380 kJ/mol to 760 kJ/mol (Table 15). Simple averaging yields an activation energy for dislocation creep of diopside of approximately 540 kJ/mol. This is distinctly higher than the activation energy determined for the dislocation creep of jadeite. Consequently, it is expected that the activation energies for diffusion in jadeite and diopside should differ also. From this reasoning, the diffusion data for diopside are not directly applicable to the case of jadeite. From an overview of the diffusion data for diopside, it is notable that no simple and clear correlation between the diffusion data and the activation energies for creep of diopside is evident.

It could be argued, however, that the diffusion data derived for diopside should be applicable to the creep of jadeite for the following reasons: Both minerals have the same crystal structure and, as will be shown in Chapter 7.5, their rheological behaviour is similar to some extent at laboratory conditions. In addition, for both minerals, the corresponding ionic radii are comparable. Beiser (1982) gave ionic radii of 0.095 nm for Na^+ , 0.050 nm for Al^{3+} , 0.099 nm for Ca^{2+} and 0.065 nm for Mg^{2+} .

In general, it might be too naive an approach for complex crystal structures like silicates to simply equate the activation energies for creep and self-diffusion of the slowest

moving species. Diffusion in clinopyroxene, involves the motion of charged defects. As such, the kinetics of diffusion are governed by a coupled diffusion process that is determined by the coefficients of self-diffusion of every involved atomic species (Pacaud *et al.*, 1999). More elaborate models might be needed for a better understanding of the quantitative dependence of creep on diffusion.

In summary, it is concluded that a discussion of the activation energy obtained for the creep of synthetic jadeitite on the basis of diffusion data derived for the atomic species of diopside is not straightforward. Diffusion experiments on jadeitite, however, have recently been proposed by Chakraborty and Dohmen (personal communication). These data will provide a better basis for discussion.

7.3 Interpretation of microstructures of deformed samples

Several mechanisms are active in the dislocation creep regime. The strain producing mechanism is mainly dislocation glide. Dislocation climb can occur at higher temperature, which allows line defects to recover in lower energy configurations. Recovery includes the annihilation of dislocations and the formation of low-angle grain boundaries by the arrangement of geometrically necessary dislocations in arrays (e.g. Barber, 1990). In addition, the dislocation density is lowered locally by dynamic recrystallization. Grain boundary migration recrystallization involves growth of grains with a low dislocation density at the expense of grains with a high dislocation density, eventually leading to bulges in the grain boundaries. Formation of new grains by ongoing migration of geometrically necessary dislocations into low-angle boundaries is termed subgrain rotation recrystallization. Operation of these mechanisms give rise to the development of microstructural features that are indicative for dislocation creep.

Experimental rock deformation studies in the dislocation creep regime reveal that microstructures adjust to the differential stress with increasing strain (Nicolas and Poirier, 1976; Tullis, 1990). Steady-state flow causes the development of a steady-state microstructure (Etheridge and Wilkie, 1981). For metals, a strain of 10% is sufficient to obtain such a microstructure (Twiss, 1977). For rocks, the appearance of a steady-state microstructure is critically dependent on the starting grain size. Mercier *et al.* (1977) generally assumed a rapid achievement of a steady-state microstructure within a few hours at laboratory condi-

tions. Dell'Angelo and Tullis (1996) expected that complete recrystallization has to occur before a steady-state microstructure is obtained. From their experiments they concluded that steady-state will never be achieved under laboratory conditions when starting from a coarse grain size. Once a steady-state microstructure is developed, microstructural features such as dislocation density, subgrain size and dynamically recrystallized grain size are independent of strain and temperature, yet dependent on differential stress. This means that for a given differential stress during progressive deformation, a characteristic mean size of recrystallized grains will evolve (Twiss, 1977). Coarse grain size does not correspond to the range of stress that is commonly attained in experimental rock deformation. Therefore a substantial decrease in grain size is observed when coarse grains are used and strain is sufficiently high for recrystallization. This has recently been confirmed by experiments done on coarse-grained rock samples in torsion (Pieri *et al.*, 2001). These authors observed that a grain size reduction from 150 μm to a size of 10 μm was necessary to obtain steady-state microstructures.

Extrapolation of experimentally derived flow laws is only useful if flow laws are derived from steady-state data. This involves a mechanical steady-state as well as a steady-state microstructure.

7.3.1 Interpretation of microstructures of deformed synthetic samples

The active deformation mechanisms can be concluded from the microstructural observations. Microstructures of deformed synthetic samples clearly indicate deformation by dislocation creep.

It is inferred that two recovery mechanisms were active: highly sutured grain boundaries show that grain boundary migration recrystallisation was activated. The recrystallized volume is enhanced by the migration of high-angle boundaries in addition to bulging. The shape-preferred orientation is more pronounced than expected for the limited amount of strain introduced by the shortening of the samples. This is an indication that oriented growth of the grains along their c-axis occurred during deformation. Helmstedt *et al.* (1972) suggested previously that oriented growth of omphacite occurred during deformation. Growth mechanisms can be either grain boundary migration or diffusive mass transfer.

EBSD measurements (Figure 15) reveal a CPO within the deformed samples, which is caused by activation of the $[001](100)$ slip system. For samples JD57.A and JB45.B (Figure 15) a significant CPO is discernible, in contrast to the undeformed sample. No distinct CPO is discernible in sample JD53.B. Sample JD57.A has the most pronounced CPO. Automated EBSD measurements were performed over the entire sample using a grid mesh size of $25 \mu m$. For samples JD45.B and JD53.B, measurements were carried out on a narrow band (width: $100 \mu m$, length: $600 \mu m$) on the outer edge of the samples oriented parallel to the sample axis. A mesh size of $4 \mu m$ was used. As the strain is similar for all samples, it is suspected that the results of the EBSD measurements were affected by the choice of the analysed areas. It was expected, however, that the CPO is most pronounced at the edge of the sample.

An average grain size of $10 \mu m$ is observed for the deformed samples. Steady-state grain sizes from high strain experiments are on the same order of magnitude (Bystricky *et al.*, 2000; Pieri *et al.*, 2001). These studies needed very high strains to obtain a steady-state microstructure, as the starting material was coarse-grained. In the case of the present study, however, the grain size of the starting microstructure is already closer to the steady-state grain size. Steady state is achieved more quickly and little strain is required to obtain a steady-state microstructure.

When comparing experimentally-deformed rocks to naturally-deformed rocks, it is useful to identify the predominant deformation mechanisms. Mechanical data can only be reliably extrapolated when the deformation mechanisms are the same (Schmid, 1982; Buatier *et al.*, 1991; Dell'Angelo and Tullis, 1996; Handy *et al.*, 2001). As there is no description of naturally-deformed jadeitite, the microstructures of experimentally-deformed synthetic jadeitite will be compared to those of naturally-deformed omphacites in eclogites. Several studies attempt to constraint the rheology of eclogite from analysing the microstructural record (Philippot and van Roermond, 1992; Godard and von Roermond, 1995; van der Klauw *et al.*, 1997; Stöckhert *et al.*, 1997; Piepenbreier and Stöckhert, 2001). These studies aim to identify the operating deformation mechanisms, the temperature at which deformation took place and to relate the microfabrics to a flow stress or a strain rate. Piepenbreier and Stöckhert (2001) analysed microstructures of naturally-deformed eclogites from the Alps. They observed microstructural features in the omphacites from

high-strain regions similar to those in the experimentally deformed synthetic jadeitite samples. Irregular grain shapes and highly sutured high-angle boundaries were observed, in addition to low-angle boundaries. EBSD measurements reveal pronounced CPO for fine-grained aggregates (grain size 10 μm to 50 μm). Pole figures from EBSD measurements are similar to those from deformed synthetic jadeitite samples. A SPO was observed where strain was localized. From their observations, they concluded that dislocation creep was the dominant deformation mechanism.

Buatier *et al.* (1991) described similar microstructures for naturally-deformed eclogites, in which omphacite showed a high degree of ductility. A foliation was defined by a SPO of the omphacite grains and a CPO was observed within low and intermediate strain regions. With additional TEM investigations, they concluded that dislocation creep was the dominant deformation mechanism in the omphacite. They pointed out that for the assumed temperatures, flow laws for diopside predict a high creep strength, suggesting that omphacite should have low ductility. To explain this discrepancy, they suggested that hydrolytic weakening effects are operative.

Philippot and van Roermond (1992) observed a layering of moderately- and highly-strained mylonites. Omphacite grains in the latter have a recrystallized grain size of 5 μm . These grains are elongated with very high aspect ratios up to 20 and with irregular boundaries. They show undulose extinction and low-angle boundaries. The microstructures of these natural rocks reveal a qualitative similarity to the microstructures of the deformed synthetic jadeitite samples. They also infer that dislocation creep is the dominant deformation mechanism of omphacites in their studied samples.

The relatively low strength of omphacite in contrast to garnet has been confirmed with microstructural analysis of Alpine eclogites by Godard and van Roermond (1995). They identified dislocation creep mechanisms by TEM analysis. Deformed omphacite grains were more elongated than undeformed grains, suggesting that oriented growth occurred during recrystallization. A CPO evolved from the growth of elongated crystals. The occurrence of sutured high-angle grain boundaries in the omphacites indicates that grain boundary migration was operative. Godard and van Roermond (1995) conjectured that application of diopside flow laws to omphacite may not be appropriate, as an unreasonable high strength would be predicted.

Most of the omphacite grains investigated by Mauler *et al.* (2001) showed straight grain boundaries that were optically strain free. Dislocation creep mechanisms were identified in some grains by TEM analysis. The omphacite grains define a foliation by a SPO. Different types of CPO were detected using EBSD techniques. In contrast to other studies that identified dislocation creep as the dominant deformation mechanism, these authors suggested oriented growth as the main deformation mechanism in omphacites. They proposed a diffusive mass transfer processes.

The (100)[001] slip system that is active in synthetic jadeitite has also been reported for experimental deformation of diopside by Avé Lallement (1978) and Kirby and Kronenberg (1984). The [001] slip direction corresponds to the shortest Burgers vector in diopside (Nicolas and Poirier, 1976). The studies on naturally deformed omphacite mentioned above have confirmed glide on that slip system and have identified additional active slip systems. For example, Godard *et al.* (1995) identified $\{110\}[001]$ and $1/2(\bar{1}10)\langle 110\rangle$ as slip systems. Philippot and van Roermond (1992) found $\{110\}[001]$, $1/2\{110\}\langle\bar{1}10\rangle$, (100)[001] and $1/2(010)[100]$ to be active slip systems. $1/2\{110\}\langle 110\rangle$, $\{110\}[001]$ and (100)[001] were inferred by Buatier *et al.* (1991).

Comparison of the microstructures of deformed synthetic jadeitite samples and naturally-deformed omphacites reveals many similarities. The same deformation mechanisms are inferred for both. In addition, the microstructures of deformed synthetic jadeitite samples appear to reflect a microstructural steady-state. One can conclude therefore, that extrapolation of the rheological data for synthetic jadeitite to natural conditions is possible.

7.3.2 Interpretation of microstructures of deformed natural samples

The occurrence of undulose extinction is commonly used to infer that dislocation glide was an active intracrystalline deformation mechanism. In contrast, Philippot and van Roermond (1992) determined from ultra-thin sections of naturally-deformed omphacites that undulatory extinction can be attributed to a subgrain microstructure. Such a microstructure is indicative for recovery-controlled dislocation creep (Barber, 1990; Nicolas and Poirier, 1976). In the experimentally-deformed samples, evidence of recovery by dislocation climb is not discernible by optical microscopy. Twinning occurs more frequently

with increasing stress. In accordance with the observed strain hardening, these observations indicate that deformation takes place in the regime of low-temperature plasticity. Contributions from dislocation creep, however, cannot be excluded.

Accumulated strain was mostly accommodated by inhomogenous deformation of the grains as revealed from the observation of undulose extinction. Recrystallisation was not effectively activated. A coarse-grained sample requires high strain at typical laboratory stresses to develop features characteristic of steady-state microstructure.

It is concluded that the microstructures of the deformed natural samples do not represent a steady-state microstructure. Thus, stresses derived from deformation experiments are presumably not steady-state. Therefore, it is of limited use to extrapolate the obtained flow law for natural jadeitite to natural conditions. Observations from deformed natural samples demonstrate the importance of reaching steady-state deformation, and suggest that synthetic samples, are a better choice for achieving steady-state quickly.

7.4 Errors inherent in the extrapolation to natural strain rates

Application of experimentally-derived flow laws to natural conditions requires extrapolation of applicability over several orders of magnitude in time and length scale (Paterson, 1987). Also, experimental studies generally use temperatures that are much higher than those existing in natural settings. It is often uncertain if the same processes and mechanisms are active in laboratory studies and under natural conditions (e.g. Stöckhert and Renner, 1998). Laboratory experiments often neglect factors such as the chemical environment, which may be of significance to the actual deformation processes (Paterson, 2001). Neglecting these general problems, it has to be considered that the stress exponent, the activation energy and the preexponential factor of the flow law are subject to errors, which will lead to respective uncertainties. The following considerations will focus on the mechanical data of synthetic jadeitite aggregates.

The flow law is applied using low natural strain rates on the order of 10^{-14} s^{-1} . A maximum uncertainty in temperature for a given stress is obtained by a combination of upper and lower bounds of the parameters of the flow law (Figure 22). In the present case a lower bound is obtained from the combination $n - \Delta n, Q - \Delta Q, \ln A + \Delta \ln A$. In contrast, the combination $n + \Delta n, Q + \Delta Q, \ln(A) - \Delta \ln A$ yields an upper bound for the

temperature at a given stress (Figure 22). This method results in a broad range of stress. However, it should be noted that the errors of the individual flow law parameters for synthetic jadeitite are well within the range of errors given for other published flow laws.

The applied procedure for an estimate of the errors of extrapolation is not satisfying, however, as the corresponding sets of flow law parameters do not provide a good fit to the creep data. This is confirmed by a high magnitude of the error vector $\vec{\varepsilon}$ (Chapter 2.2.4). For the given combinations of parameters, the error vector exceeds the error vector that is obtained using n , Q and $\ln A$ by a factor of twenty. From that, it is concluded that the flow law parameters cannot be varied independently within the ranges given by their errors.

To obtain a better constraint on the resulting uncertainty, a different approach is followed: one flow law parameter p is fixed to either $p + \Delta p$ or $p - \Delta p$, first. For each of these fixed upper and lower bounds, the other two parameters are redetermined by inversion of the creep data. The inversion method described in Chapter 2.2.4 is adopted accordingly, which in this case leads to:

$$\begin{pmatrix} \ln \dot{\varepsilon}_1 - \ln A_{min/max} \\ \vdots \\ \ln \dot{\varepsilon}_N - \ln A_{min/max} \end{pmatrix} = \begin{pmatrix} \ln \sigma_1 & 1/T_1 \\ \vdots & \vdots \\ \ln \sigma_N & 1/T_N \end{pmatrix} \cdot \begin{pmatrix} n \\ -Q/R \end{pmatrix}. \quad (13)$$

From this n and Q are determined for $\ln A_{min}$ and for $\ln A_{max}$, such that two new pairs of n_{min} , Q_{min} and n_{max} , Q_{max} are obtained. An appropriate combination of these parameters with the fixed $\ln A$ leads to upper and lower bounds in temperature in the extrapolation (Figure 22). An analogous procedure is repeated for the stress exponent and the activation energy. For a fixed Q_{min} and Q_{max} , $\ln A$ and n are obtained using:

$$\begin{pmatrix} \ln \dot{\varepsilon}_1 + (Q_{min/max}/R) \cdot 1/T_1 \\ \vdots \\ \ln \dot{\varepsilon}_N + (Q_{min/max}/R) \cdot 1/T_N \end{pmatrix} = \begin{pmatrix} 1 & \ln \sigma_1 \\ \vdots & \vdots \\ 1 & \ln \sigma_N \end{pmatrix} \cdot \begin{pmatrix} \ln A \\ n \end{pmatrix}, \quad (14)$$

and $\ln A$ and Q are determined for n_{min} and n_{max} by using:

$$\begin{pmatrix} \ln \dot{\varepsilon}_1 - n \cdot \ln \sigma_1 \\ \vdots \\ \ln \dot{\varepsilon}_N - n \cdot \ln \sigma_N \end{pmatrix} = \begin{pmatrix} 1 & 1/T_1 \\ \vdots & \vdots \\ 1 & 1/T_N \end{pmatrix} \cdot \begin{pmatrix} \ln A \\ -Q/R \end{pmatrix} \quad (15)$$

The low magnitude of the error vectors confirms the general applicability of that method. The outermost extrapolations from these three cases are regarded as realistic lower and upper bounds for the extrapolation of the flow law.

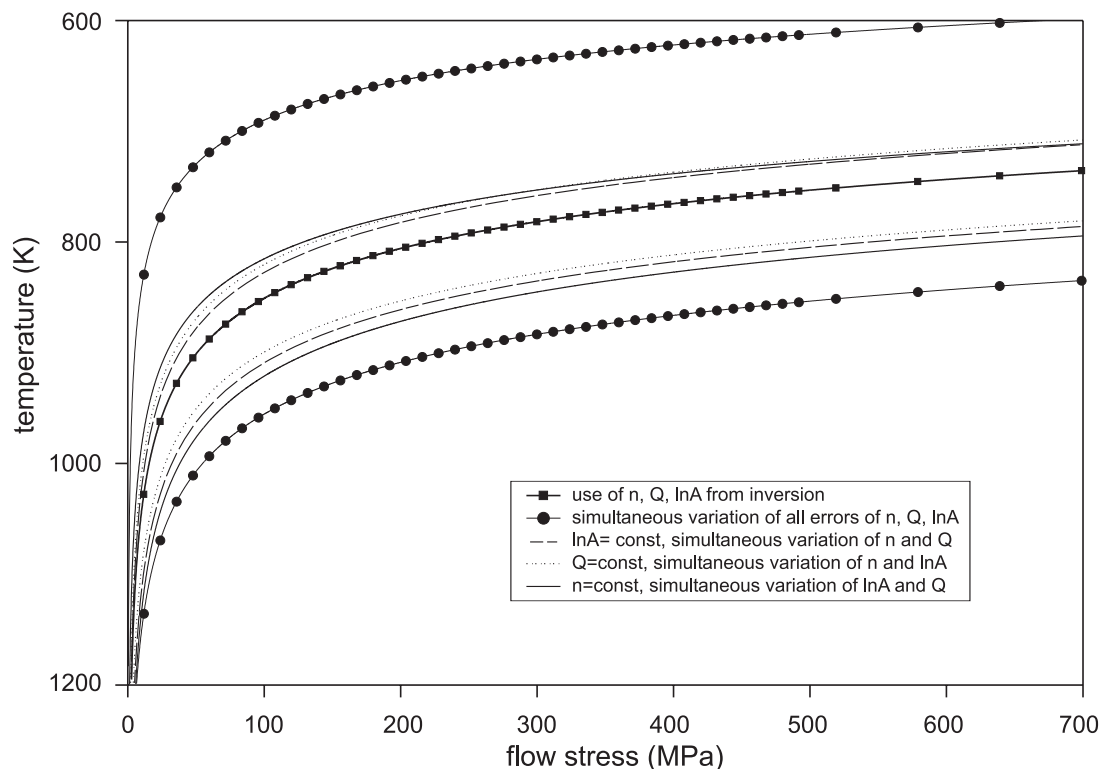


Figure 22: The flow law for synthetic jadeitite (Chapter 7.2.1) evaluated for a strain rate of $1 \cdot 10^{-14} \text{ s}^{-1}$ is indicated by the line with full squares. The curves labeled with dots show maximum uncertainty due to uncorrelated variation of all flow law parameters within the individual error bars. The bounds for correlated variations are indicated by different lines as explained in the legend. The solid line without symbols is a realistic estimate of the uncertainty in the extrapolation due to errors of the flow law parameters.

7.5 Normalized representation of flow laws

A comparison of the rheological behaviour of different minerals should be based on dimensionless variables to be of general value (Ranalli, 1995). Provided that properly scaled variables are chosen, polycrystalline aggregates with the same crystal structure and type of bonding should behave in a similar rheological manner. On this basis, Frost and Ashby (1982) defined isomechanical groups. Identification of isomechanical groups may allow the estimation of rheological properties for a material of interest, if the rheological properties of an analog material are known. This approach might be beneficial when experimental limitations prevent the characterisation of the rheology of the material of interest. This procedure entails the normalization of the temperature with respect to the melting temperature and the differential stress with respect to the shear modulus (Poirier, 1985).

Karato (1989) showed that for minerals with a rocksalt or an olivine structure, stress-temperature relationships for different compositions converge. The difference in strength of diopside, jadeite and omphacite may be caused by different melting temperatures. The concept of homologous temperature states that for a given temperature the mineral with the higher homologous temperature (T/T_{Melt}) is weaker (Poirier, 1985; Frost and Ashby, 1982). In a normalized representation this difference should vanish. The strength of diopside (Kirby and Kronenberg, 1984; Bystricky and Mackwell, 2001) and jadeite (this study) is compared using a normalized representation (Figure 23).

All flow laws concentrate in a band of normalized stresses having a width below one half of an order of magnitude for the investigated range. Extending the flow law for diopside from Kirby and Kronenberg (1984), the strength of synthetic jadeitite is bound by the data for diopside from Bystricky and Mackwell (2001) and Kirby and Kronenberg (1984). The natural jadeitite is stronger than the synthetic jadeitite and diopside (Kirby and Kronenberg, 1984). The slopes of the flow laws for natural jadeitite and diopside from Kirby and Kronenberg (1984), however, are similar. Comparison with the flow law for natural jadeitite is not ideal, however, as it does not present steady-state creep. The flow laws for diopside differ in strength and in their slopes. As both studies were performed on dry material from the same location, this indicates a possible range of experimental uncertainties. With such a width of uncertainty, it can be concluded that in a normalized representation, jadeitite shows the same mechanical behaviour as diopside.

These observations indicate that jadeitite and diopside belong to an isomechanical group. The rheological properties of omphacite for natural conditions may be obtained from a linear interpolation of relevant properties of jadeitite and diopside.

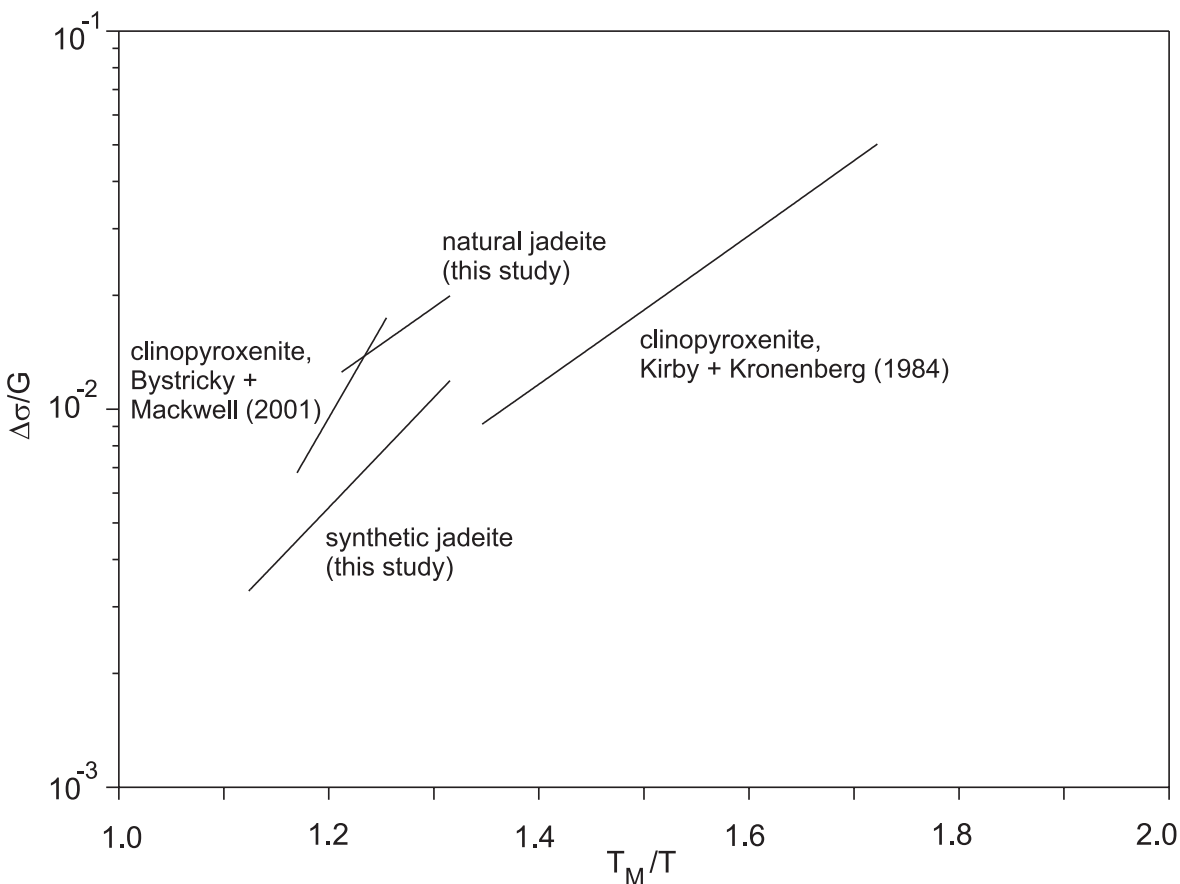


Figure 23: Normalized representation of flow laws for jadeitite and diopside. T/T_{Melt} is the homologous temperature, $\Delta\sigma$ is the differential stress and G is the shear modulus. Flow laws are evaluated for the temperature range of the corresponding studies and a strain rate of $1 \cdot 10^{-5} \text{ s}^{-1}$. The shear moduli and melting temperatures are determined separately for each study, based on the average temperature and pressure of the studies.

7.6 Comparison of natural and synthetic samples

It was pointed out in Chapter 7.3.2 that the differential stresses derived for natural jadeitite samples do not reflect mechanical steady-state behaviour. The microstructures also indicate that no microstructural steady-state was achieved. The flow law does not represent steady-state behaviour and consequently it is of limited use to compare it with other flow laws based on steady-state deformation.

It is noted, however, that the stress exponent and activation energy do not differ substantially from each other, considering the range of uncertainty (Table 14). The pre-exponential factor is higher for the natural samples, which translates to a greater strength (Figure 25 and Figure 23). At higher temperature the lower activation energy of the natural jadeitite determines its mechanical behaviour, and the relative strength of synthetic and natural jadeitite is reversed (Figure 25). It is noteworthy that extrapolation of the flow laws for natural and the synthetic jadeitite yields similar strengths.

parameter	natural	synthetic
n	4.4±0.3	3.7±0.4
Q	263±19 kJ/mol	326±27 kJ/mol
lnA	-16.8±1.6	-3.3±2.0

Table 14: Comparison of flow law parameters for natural and synthetic jadeitite. A is given in units of $\text{MPa}^{-n} \text{s}^{-1}$.

The strength of natural jadeitite is higher than that of synthetic jadeitite at similar deformation conditions (Figure 24). Similar observations were made in other studies that compared natural and synthetic rocks. Hacker and Christie (1990) encountered brittle behaviour for coarse-grained amphibolite, when a fine-grained synthetic amphibolite displayed ductile behaviour. They attributed the higher ductility of the synthetic samples to a greater concentration and variety of defects introduced during synthesis. Luan and Paterson (1992) compared natural and synthetic quartz with similar grain size and different water content. Natural quartz samples, having a lower water content were stronger than synthetic samples. For the case of diopside, the natural material was coarse-grained, whereas the hot-pressed samples were fine-grained (Bystricky and Mackwell, 2001). These

authors proposed that deformation of fine-grained samples is enhanced by an additional contribution of diffusion processes to dislocation creep. Tullis and Yund (1985) deformed fine-grained (2-10 μm) and coarse-grained (150-175 μm) feldspar aggregates and found a lower strength for the fine-grained material. They attributed the weakness of the fine-grained material to effective dynamic recrystallization.

The Hall-Petch relationship established in metallurgy, predicts an increasing flow stress with decreasing grain diameter, as grain boundaries act as obstacles to the glide of dislocations (e. g. Schmid, 1982). Such a relationship is not seen in the case of jadeite, for stresses increase with increasing grain size. The Hall-Petch relationship is not well documented for silicates as it is with metals.

In the present study, the apparent difference in strength is caused by the different microstructures of natural and synthetic samples (Chapter 7.3.1 and Chapter 7.3.2). Recrystallization mechanisms do not operate in the natural material at that low strains, and therefore, there is no reduction in flow stress. Despite the difficulties of inhomogeneous deformation in certain cases due to sample tilting, synthetic samples are advantageous, and should be used for future deformation studies.

It generally is a matter of debate whether a flow law derived from natural or synthetic samples is more applicable to natural conditions. For the reasons given in the previous chapters, here, more confidence is attributed to the flow law for the synthetic samples.

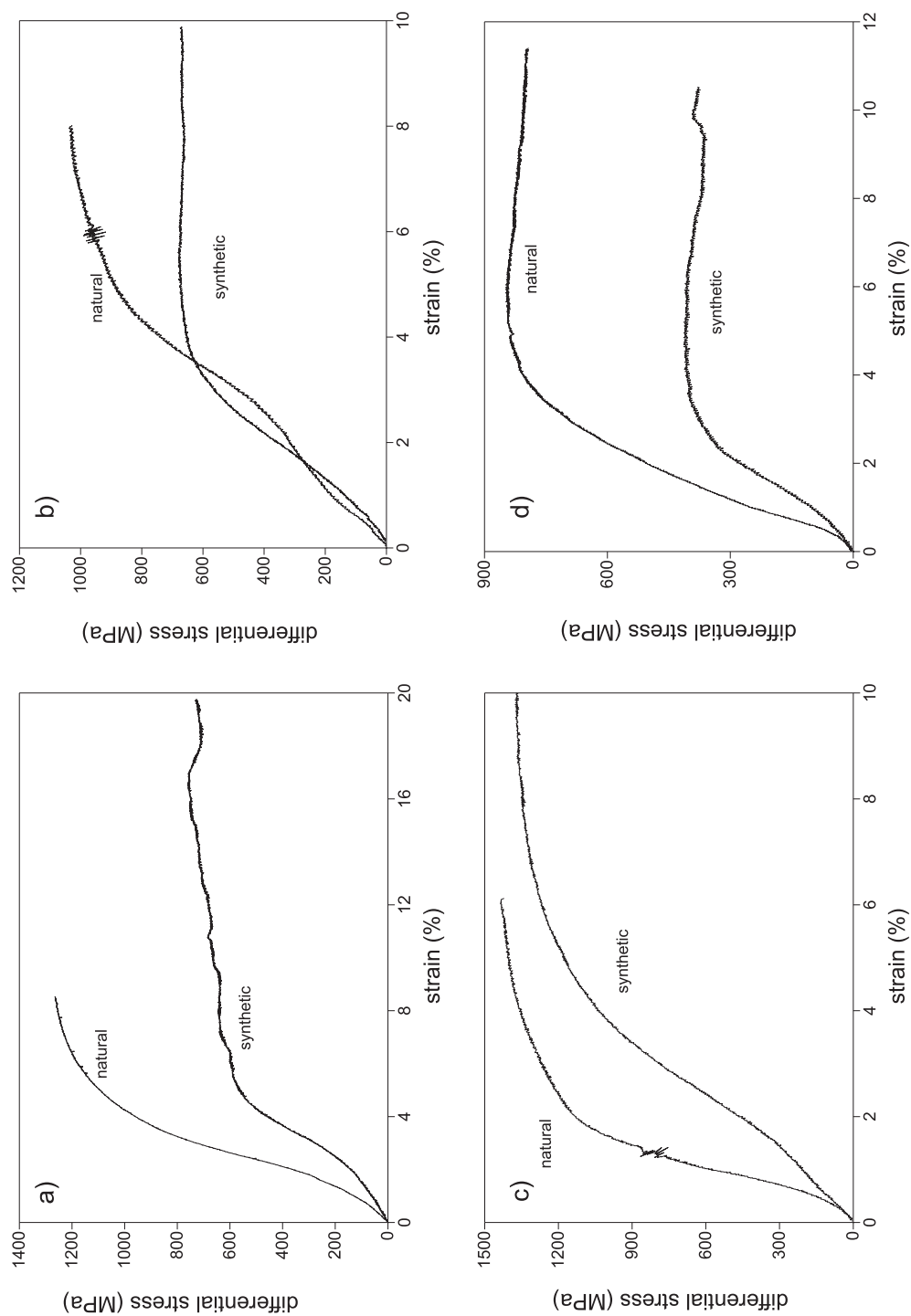


Figure 24: Comparison of stress vs. strain curves for synthetic and natural jadeitite samples. Natural samples generally yield higher stresses: a) FC3-2 and JD49.B at 900°C and $\dot{\epsilon} = 5 \cdot 10^{-6} s^{-1}$, b) JC2-1 and JD48.A-1 at 1000°C and $\dot{\epsilon} = 2 \cdot 10^{-5} s^{-1}$ c) JC2-2 and JD45.B-1 at 900°C and $\dot{\epsilon} = 2 \cdot 10^{-5} s^{-1}$, d) FC3-1 and JD53.B-2 at 1000°C and $\dot{\epsilon} = 5 \cdot 10^{-6} s^{-1}$.

7.7 Application of results to geological processes

The petrological structure of subducted lithosphere is composed of an oceanic mantle overlain by a basaltic crust, which transforms to eclogite during subduction. Numerical modelling of the thermal structure of subducted lithosphere shows that mantle isotherms get dragged downwards with the descending plate (Peacock, 1996; Turcotte and Schubert, 2002). The lithosphere is gradually heated up with increasing depth.

The top eclogite layer mainly consists of omphacite and garnet. The rheology of such a polyphase material can be approximated by the rheology of the weakest phase, if one mineral is sufficiently weak and makes up a sufficient large volume fraction (Handy, 1990). Such is the case for omphacite in eclogites as revealed from microstructural analysis of naturally-deformed rocks (Godard and von Roermond, 1995).

With an increase of temperature, the strength of the eclogite layer gradually decreases. It has been argued that deformation mechanisms other than dislocation creep are presumably dominant at conditions within a subduction zone. Stöckhert and Renner (1998) and Mauler *et al.* (2001) suggested that diffusion processes may prevail over dislocation creep processes in subduction zones. Stöckhert (2002) proposed dissolution precipitation creep as the dominant deformation mechanism. These mechanisms are operative at lower stresses than required for dislocation creep. Thus, a dislocation creep flow law would provide upper bounds for the differential stress.

Omphacite belongs to the solid-solution series jadeite-diopside, and has a composition that is intermediate between the end-members. Diopside flow laws have been used to approximate the rheology of omphacite. These flow laws predict unrealistically high stresses (Godard and von Roermond, 1995), indicating that diopside rheology may not be a good indicator for eclogite rheology (Piepenbreier and Stöckhert, 2001). The rheology of jadeite has been investigated in the present study. The rheology of diopside and jadeite should bracket the strength of omphacite. The mechanical behaviour of omphacite may be inferred based on its isomechanical group (Chapter 7.5). Deformation experiments are still needed, however, to constrain omphacite rheology. The mechanical behaviour of omphacite may change with ordering and disordering of cations, though (Brenker *et al.*, 2002).

Several flow laws for diopside are summarized below (Table 15). These studies used

natural diopside from the same locality (Sleaford Bay, South Australia). Boland and Tullis (1986) deformed natural diopside aggregates under 'wet' (1 wt% water added) and nominally 'dry' conditions in a gas-medium apparatus. They fit a power law to mechanical data from one experiment that involved several cycles. They observed that dislocation creep microstructures were accompanied by microcracking. Kirby and Kronenberg (1984) studied the mechanical behaviour at higher confining pressures (up to 2 GPa) and under dry conditions in a Griggs apparatus. They identified three different deformation regimes. At pressures above 1500 MPa and high temperature the microfabrics of deformed samples indicated recovery, multiple slip and recrystallization. Another study has recently been carried out by Bystricky and Mackwell (2001) using a gas-medium apparatus. They deformed natural dry diopside in the dislocation creep regime. In addition, they hot-pressed fine-grained samples from ground diopside and deformed them. They observed microstructural features showing that diffusion creep was active in addition to dislocation creep. Jin *et al.* (2001) deformed hot-pressed samples with an eclogitic composition at 3 GPa. Recently, Mei *et al.* (2001) and Zhang *et al.* (2001) reported preliminary results on the effect of water on the creep behaviour of diopside aggregates and eclogite. Parameters of flow laws quoted above are compiled in Table 15.

material	reference	n	Q [kJ/mol]	lnA [MPa ⁻ⁿ s ⁻¹]
synthetic jadeitite	this study	3.7±0.4	326±27	-3.3±2.0
natural jadeitite	this study	4.4±0.3	263±19	-16.8±1.6
'wet' diopside	Boland & Tullis (1986)	3.3±0.5	490±80	11.9
'dry' diopside	Kirby & Kronenberg (1984)	5.3±1.1	380±30	-11.5
'dry' diopside	Bystricky & Mackwell (2001)	4.7±0.2	760±40	22.6±1.2
'eclogite'	Jin <i>et al.</i> (2001)	3.4±0.2	480±30	7.6±2.1

Table 15: Experimentally determined power law parameters n, Q and lnA for diopside and jadeitite aggregates.

Extrapolation of the flow laws for synthetic jadeitite and diopside reveals a lower flow stress for jadeitite compared with diopside (Figure 25). This holds for all flow laws pre-

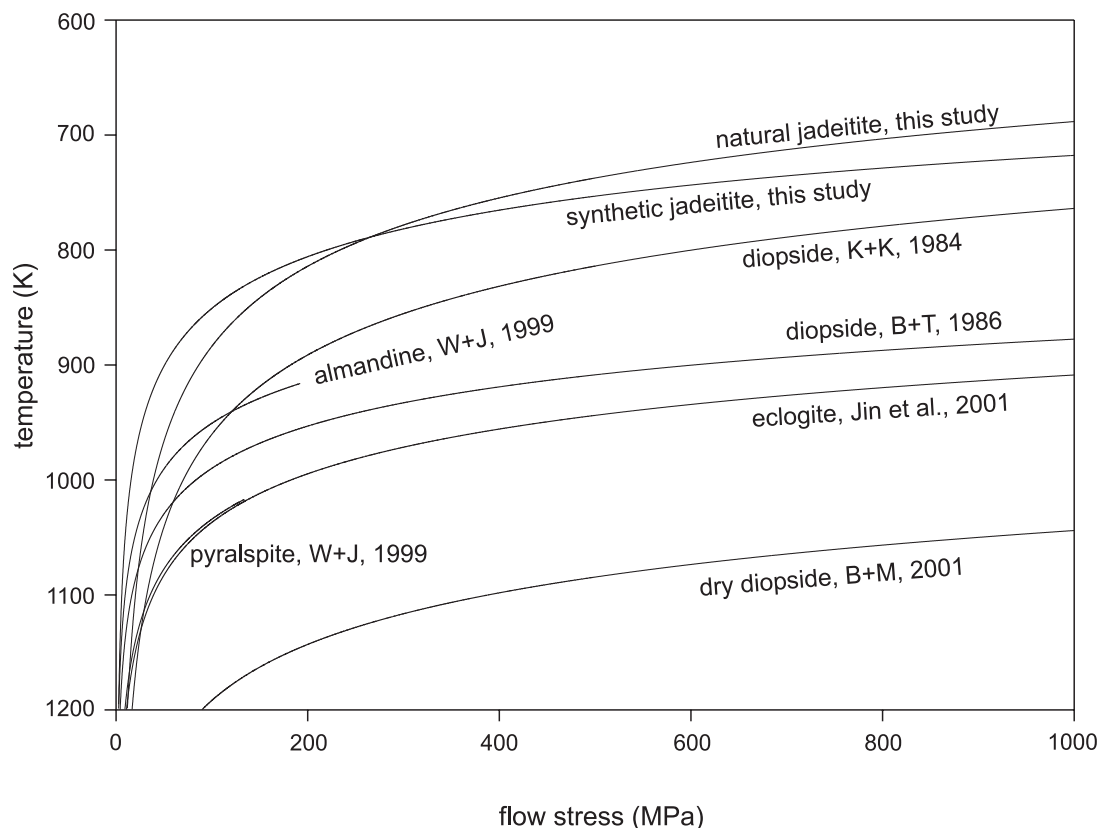


Figure 25: Extrapolation of flow laws for diopside, jadeitite and garnet to a low natural strain rate of 10^{-14}s^{-1} . Extrapolation of the flow law for natural jadeitite should be considered cautious, however. The flow laws for two representative types of garnet are shown for temperatures above the brittle-ductile transition. For references refer to Table 15 and the text.

sented in Table 15, although these cover a wide range of stresses for a given temperature. Extrapolation of relevant types of garnet (Nowlan *et al.*, 2000; Piepenbreier and Stöckhert, 2001) for temperatures above their brittle-ductile transition (Karato *et al.*, 1995; Wang and Ji, 2000) demonstrates that garnet is stronger than jadeite. These observations are in agreement with analysis of naturally-deformed rocks, that show that omphacite is weaker than diopside and garnet. The strength of omphacite must lie between that of jadeite and diopside. Stresses that were formerly derived for eclogite facies conditions using diopside data can now be constrained more realistically using the data for jadeite.

Recently, Jin *et al.* (2001) studied the rheology of hot-pressed eclogite samples. Extrapolation of their results (Figure 25) yields a strength of eclogite that lies between the

predictions for diopside from Boland and Tullis (1986) and that from Kirby and Kronenberg (1984), and predictions from Bystricky and Mackwell (2001). The strength of omphacite should be lower than that of diopside and of garnet. The data from Jin *et al.* (2001) do not support this supposition.

In summary, extrapolation of relevant flow laws to natural conditions shows that jadeite is distinctly weaker than diopside and garnet. This is in agreement with inferences made from studies on naturally-deformed rocks. A flow law for jadeite should provide a lower bound for the strength of omphacites in eclogites. Stresses in the eclogite layers in subduction zones must be considerably lower than those inferred from mechanical data on diopside, but are likely to be higher than stresses determined for jadeite.

8 Summary

At convergent plate boundaries oceanic crust is subducted. As the basaltic upper layer transforms to eclogite, the mineralogy becomes dominated by garnet and pyroxene (omphacite). Thus the rheology of eclogite has important implications for interplate coupling in subduction zones and its understanding is vital for the development of better models of convergent margins. Observations of naturally-deformed eclogites show rigid inclusions of garnet within a strongly deformed pyroxene matrix. Therefore it is assumed that the pyroxenes control the rheology of eclogites. At present, the rheology of the relevant diopside-jadeite solid solutions (termed omphacite) is unexplored. The microstructure of natural eclogites suggests that omphacite can be deformed by dislocation creep even at temperatures below 500°C (Piepenbreier and Stöckhert, 2001). In contrast, available experimental flow laws for the end-member diopside ($\text{CaMgSi}_2\text{O}_6$) predict an unrealistically high strength even for a temperature of 700°C. Thus, the data for diopside do not seem to be appropriate to describe the rheology of eclogite. As a systematic approach, the mechanical behaviour of the end member jadeite ($\text{NaAlSi}_2\text{O}_6$) was investigated.

To investigate the rheology of jadeite, deformation experiments were carried out on synthetic and natural jadeitite aggregates. Synthetic samples were crystallized in the stability field of jadeite from a synthetic glass precursor with a jadeite composition. The resulting microstructure correlates with the P-T-t path that is used to reach final pressure and temperature conditions. Doping of the glass with crystalline jadeite powder also has a marked effect on the resulting microstructure. A standard procedure was chosen to obtain reproducible starting microstructures for deformation experiments. This procedure yielded jadeitite aggregates with an average grain size of approximately 12 μm , which did not display deformation features or a crystallographic preferred orientation. Natural jadeitite samples from Burma, also used in deformation experiments, reveal a coarse grain size and a heterogeneous microstructure.

Deformation experiments were carried out at a confining pressure of 2.5 GPa in a modified Griggs apparatus. The confining medium was provided by a molten eutectic CsCl/NaCl mixture. Samples were shortened in the axial direction at a constant displacement rate and temperature between 800°C and 1100°C. Strain rate varied from $4 \cdot 10^{-4} \text{ s}^{-1}$ to $2 \cdot 10^{-6} \text{ s}^{-1}$. Stress vs. strain curves were derived from the force vs. displacement curves

to determine sample rheology. A typical uncertainty of 80 MPa was determined for the differential stress. A series of test that also involved step tests was performed on both natural and synthetic samples. A fraction of the mechanical data for the synthetic jadeitite was discarded, as inhomogenous deformation of samples led to a systematic underestimation of the sample strength. Natural samples yielded a higher strength than synthetic samples and strain hardening was frequently observed.

Optical microscopy of deformed synthetic samples reveal a pronounced shape preferred orientation and a crystallographic preferred orientation. Highly sutured grain boundaries indicate dynamic recrystallization by grain boundary migration. Development of a crystallographic preferred orientation was confirmed by automated electron backscatter diffraction measurements (EBSD) performed on undeformed and deformed synthetic samples. From these measurements, (100)[001] was identified as an active slip system. It was concluded from the microstructural observations that the synthetic samples were deformed in the dislocation creep regime and that a steady-state microstructure evolved during deformation. Grain boundary migration recrystallization and oriented growth of grains in the c-direction were identified. The mechanical data for synthetic jadeitite were fit by a power law. The flow law parameters were determined using a global inversion method. An activation energy for dislocation creep of $Q = 326 \pm 27 \text{ kJ/mol}$, a stress exponent of $n = 3.7 \pm 0.4$ and a preexponential factor of $\ln(A/(MPa^{-n} s^{-1})) = -3.3 \pm 2.0$ are found for synthetic jadeitite.

A power law equation was also used to fit the mechanical data for natural jadeitite. Clear evidence for dislocation creep was not discernible by optical microscopy. The occurrence of undulose extinction and twinning of grains are the dominant features associated with intracrystalline deformation. The coarse grain size of the natural samples yields a deformation microstructure that is far from steady-state. This implies that the flow law obtained for the natural material is not representative of a steady-state grain size, rendering the extrapolation to low natural strain rates uncertain. The critical resolved shear stress for the twinning of jadeite was determined from the orientation of twinned crystals and known stresses to be 155 ± 20 MPa.

Extrapolation of the flow law for synthetic jadeitite to low natural strain rates of 10^{-14} s^{-1} reveals that jadeite is significantly weaker than diopside. The extrapolation

yields a more realistic upper bound to the strength of the eclogite layer as a function of temperature, and correspondingly, a better estimate of the interplate shear stress in subduction zones. Stresses are considerably lower than those previously predicted using flow laws for diopside.

References

- Adams, L. H. 1953. A note on the stability of jadeite. *American Journal of Science*, **251**, 299–308.
- Aines, R. D. and Rossman, G. R. 1984. Water in minerals? A peak in the infrared. *Journal of Geophysical Research*, **89**(B4), 4059–4071.
- Ashby, M. F. and Verral, R. A. 1977. Micromechanisms of flow and fracture, and their relevance to the rheology of the upper mantle. *Philosophical Transactions of the Royal Society of London*, **A**(288), 59–95.
- Avé Lallement, H. G. 1978. Experimental deformation of diopside and debsterite. *Tectonophysics*, **48**, 1–27.
- Azough, F., Freer, R., Wright, K. and Jackson, R. 1998. A computer simulation study of point defects in diopside and the self-diffusion of Mg and Ca by a vacancy mechanism. *Mineralogical Magazine*, **62**(5), 599–606.
- Barber, D. J. 1990. Regimes of plastic deformation - processes and microstructures: an overview. *Pages 138–178 of: Barber, D. J. and Meredith, P. G. (eds), Deformation Processes in Minerals and Rocks*. Unwin Hyman Ltd.
- Beiser, A. 1982. *Atome, Moleküle, Festkörper*. Friedr. Vieweg und Sohn.
- Béjina, F. and Jaoul, O. 1997. Silicon diffusion in silicate minerals. *Earth Planetary Science Letters*, **153**, 229–238.
- Bell, P. M. 1964. High-pressure jadeite melting. *Carnegie Institute Washington Yearbook*, **63**, 171–174.
- Birch, F. 1960. The velocity of compressional waves in rocks to 10 kbars. *Journal of Geophysical Research*, **65**, 1083.
- Birch, F. and LeComte, P. 1960. Temperature-pressure plane for albite composition. *American Journal of Science*, **258**, 209–217.
- Bloom, H. 1967. *The Chemistry of Molten Salts*. W. A. Benjamin, Inc., New York.
- Boettcher, A. L. and Wyllie, P. J. 1968. Jadeite stability measured in the presence of silicate liquids in the system $\text{NaAlSi}_3\text{O}_8\text{-SiO}_2\text{-H}_2\text{O}$. *Geochimica et Cosmochimica Acta*, **32**, 999–1012.
- Boland, J. N. and Tullis, T. E. 1986. Deformation behaviour of wet and dry clinopyroxenite in the brittle to ductile transition region. *In: Hobbs, B. E. and Heard, H. C. (eds), Mineral and Rock Deformation: Laboratory Studies – The Paterson Volume*, vol. Geophysical Monograph 36. American Geophysical Union.
- Bradt, R. C., Newnham, R. E. and Biggers, J. V. 1973. The toughness of jadeite. *American Mineralogist*, **58**, 727–732.
- Brenker, F. E., Prior, D. J. and Müller, W. F. 2002. Cation ordering in omphacite and the effect on deformation mechanisms and lattice preferred orientation (LPO). *Journal of Structural Geology*. in press.

- Buatier, M., v. Roermond, H. L. M., Drury, M. R. and Lardeaux, J. M. 1991. Deformation and recrystallization mechanisms in naturally deformed omphacites from the Sesia-Lanzo zone; geophysical consequences. *Tectonophysics*, **195**, 11–27.
- Bucher, K. and Frey, M. 1994. *Petrogenesis of Metamorphic Rocks*. 6th edn. Springer Verlag.
- Bystricky, M. and Mackwell, S. 2001. Creep of dry clinopyroxene aggregates. *Journal of Geophysical Research*, **106**(B7), 13,443–13,454.
- Bystricky, M., Kunze, K., Burlini, L. and Burg, J.-P. 2000. High shear strain of olivine aggregates: rheological and seismic consequences. *Science*, **290**, 1564–1567.
- Chakraborty, S. and Becker, H. W. 2002. *Die Abhängigkeit des Versetzungskriechens von Umgebungsvariablen (P, T, Chemie): Die Kontrolle durch Punktdefekte in Mineralen*. Berichtsbereich Sonderforschungsbereich 526. Ruhr-Universität Bochum.
- Christensen, N. I. and Salisbury, M. H. 1972. Sea floor spreading, progressive alteration of layer two basalts, and associated changes in seismic velocities. *Earth Planetary Science Letters*, **15**, 251–260.
- de Bresser, J.H.P., ter Heege, J.H., and Spiers, C.J. 2001. Grain size reduction by dynamic recrystallisation: can it result in major rheological weakening? *International Journal of Earth Sciences*, **90**(1), 28–46.
- Deer, W. A. 1962. *Rock-Forming Minerals*. Longmans, Green and Co.
- Dell'Angelo, L. N. and Tullis, J. 1996. Textural and mechanical evolution with progressive strain in experimentally deformed aplite. *Tectonophysics*, **256**, 57–82.
- den Brok, B., Meinecke, J. and Röller, K. 1994. Fourier transform IR-determination of intergranular water content in quartzites experimentally deformed with and without added water in the ductile field. *Journal of Geophysical Research*, **99**(B10), 19,821–19,828.
- Derby, B. 1990. Dynamic recrystallization and grain size. In: Barber, D. J. and Meredith, P. G. (eds), *Deformation Processes in Minerals and Rocks*. Unwin Hyman Ltd.
- Dimanov, A. and Ingrin, J. 1995. Premelting and high-temperature diffusion of Ca in synthetic diopside: an increase of the cation mobility. *Physics and Chemistry of Minerals*, **22**, 437–442.
- Dorner, D. 1999. *Experimente zur Synthese von Jadeit*. Diploma thesis, Institut für Geophysik der Ruhr-Universität Bochum.
- Duffy, T. S. and Anderson, D. L. 1989. Seismic velocities in mantle minerals and the mineralogy of the upper mantle. *Journal of Geophysical Research*, **94**(B2), 1895–1912.
- Edgar, A. D. 1973. *Experimental Petrology, Basic Principles and Techniques*. Clarendon Press, Oxford.
- Etheridge, M. A. and Wilkie, J. C. 1981. An assessment of dynamically recrystallized grainsize as a paleopiezometer in quartz-bearing mylonite zones. *Tectonophysics*, **78**, 475–508.

- Evans, B. and Kohlstedt, D. L. 1995. Rheology of rocks. *In: Ahrens, T. J. (ed), Rock Physics and Phase Relations. A Handbook of Physical Constants, Vol. AGU Reference Shelf 3.* American Geophysical Union, Washington, D. C.
- Farver, J. R. 1989. Oxygen self-diffusion in diopside with application to cooling rate determinations. *Earth Planetary Science Letters*, **92**, 386–396.
- Fine, M. E. 1965. *Introduction to Phase Transformations in Condensed Systems.* Macmillan Series in Materials Science. The Macmillan Company, New York.
- Frenkel, J. 1926. Zur Theorie der Elastizitätsgrenze und der Festigkeit kristalliner Körper. *Zeitschrift für Physik*, **37**, 572–609.
- Frost, H. J. and Ashby, M. F. 1982. *Deformation-Mechanism Maps.* Pergamon Press.
- Gebrande, H. and Kern, H. 1982. Elastizität und Inelastizität. *In: Angenheister, G. (ed), Landolt-Börnstein: Zahlenwerte und Funktionen aus Naturwissenschaft und Technik, Neue Serie, Gruppe 5, Bd. 1b.* Springer-Verlag. 1-233.
- Gerya, T. A., Stöckhert, B. and Perchuk, A. L. 2002. Exhumation of high-pressure metamorphic rocks in a subduction channel - a numerical simulation. *Tectonics.* in review.
- Getting, I. C. and Kennedy, G. C. 1970. Effects of pressure on the emf of chromel-alumel and platinum-platinum 10% rhodium thermocouples. *Journal of Applied Physics*, **41**, 4552–4562.
- Gleason, G. C. and Tullis, J. 1995. A flow law for dislocation creep of quartz aggregates determined with the molten salt cell. *Tectonophysics*, **247**, 1–23.
- Godard, G. and von Roermond, H. L. M. 1995. Deformation-induced clinopyroxene fabrics from eclogites. *Journal of Structural Geology*, **17**(10), 1425–1443.
- Green, H. W. and Borch, R. S. 1990. High pressure and temperature deformation experiments in a liquid confining medium. *In: Duba, A. G., Durham, W. B., Handin, J. W. and Wang, H. F. (eds), The brittle-ductile transition in rocks.* American Geophysical Union : Washington, DC, United States. 195-200.
- Griggs, D. T. 1967. Hydrolytic weakening of quartz and other silicates. *Geophys. J. R. Astr. Soc.*, **14**, 19–31.
- Hacker, B. R. 1996. Eclogite formation and the rheology, buoyancy, seismicity and H₂O content of Oceanic Crust. *In: Bebout, G. E., Scholl, D. W., Kirby, S. H. and Platt, J. P. (eds), Subduction: Top to Bottom*, vol. Geophysical Monograph 96. American Geophysical Union.
- Hacker, B. R. and Christie, J. M. 1990. Brittle/ductile and plastic/cataclastic transitions in experimentally deformed and metamorphosed amphibolite. *Pages 127–148 of: Duba, A. G., Durham, W. B., Handin, J. W. and Wang, H. F. (eds), The Brittle-Ductile Transition in Rocks.* Geophysical Monograph, Vol. 56. American Geophysical Union, Washington, D.C.
- Handy, M. 1990. The solid-state flow of polymineralic rocks. *Journal of Geophysical Research*, **95**(B5), 8647–8661.

- Handy, M., Braun, J., Brown, M., Kukowski, N., Pareson, M. S., Schmid, S. M., Stöckhert, B., Stüwe, K., Thompson, A. B. and Wosnitza, E. 2001. Rheology and geodynamic modelling: the next step forward. *International Journal of Earth Sciences*, **90**, 149–156.
- Harlow, G. E. and Sorensen, S. S. 2001. Jade: occurrence and metasomatic origin. *Australian Gemmologist*, **21**, 7–10.
- Heilbronner, R. and Bruhn, D. 1998. The influence of three-dimensional grain size distribution on the rheology of polyphase rocks. *Journal of Structural Geology*, **20**(6), 695–705.
- Helmstedt, H., Anderson, O. L. and Gavasci, A. T. 1972. Petrographic studies of eclogite, spinel-websterite and spinel-lherzolite xenoliths from kimberlite-bearing breccia pipes in southeastern Utah and northeastern Arizona. *Journal of Geophysical Research*, **77**, 4350–4365.
- Hlaváč, J. 1983. *The Technology of Glass and Ceramics*. Glass Science and Technology, vol. 4. Elsevier Scientific Publishing Company.
- Holland, T. J. B. 1980. The reaction albite = jadeite + quartz determined experimentally in the range 600–1200°C. *American Mineralogist*, **65**, 129–134.
- Holland, T. J. B. 1983. The experimental determination of activities in disordered and short-range ordered jadeitic pyroxenes. *Contributions to Mineralogy and Petrology*, **82**, 214–220.
- Hughes, D. and Nishitake, T. 1963. Measurements of elastic wave velocity in armco iron and jadeite under high pressure and high temperatures. In: *Geophys. Papers Dedicated to Prof. Kenzo Sassa*. Kyoto Univ., Kyoto, Japan.
- Hull, D. 1979. *Introduction to Dislocations*. Pergamon Press.
- Hyndman, R. D. and Wang, K. 1993. Thermal constraints on the zone of major thrust earthquake failure: the cascadia subduction zone. *Journal of Geophysical Research*, **98**(B2), 2039–2060.
- Ingrin, J., Latrous, K., Doukhan, J. C. and Doukhan, N. 1989. Water in diopside: an electron microscopy and infrared spectroscopy study. *Eu. J. Mineral.*, **1**, 327–341.
- Jena, A. K. and Chaturvedi, M. C. 1992. *Phase Transformations in Materials*. Prentice Hall.
- Jin, Z. M., Zhang, J., Green II, H.W. and Jin, S. 2001. Eclogite rheology: implications for subducted lithosphere. *Geology*, **29**(8), 667–670.
- Johannes, W. 1978. Pressure comparing experiments with NaCl, AgCl, talc, and pyrophyllite assemblies in a piston cylinder apparatus. *N. Jb. Miner. Mh.*, **H2**, 84–92.
- Kandelin, J. and Weidner, D. J. 1988. The single-crystal elastic properties of jadeite. *Physics of the Earth and Planetary Interiors*, **50**, 251–260.
- Karato, S., Wang, Z., Liu, B. and Fujino, K. 1995. Plastic deformation of garnets: systematics and implications for the rheology of the mantle transition zone. *Earth Planetary Science Letters*, **130**, 13–30.

- Karato, S.-I. 1989. Plasticity-crystal structure systematics in dense oxides and its implications for the creep strength of the Earth's deep interior: a preliminary result. *Physics of the Earth and Planetary Interiors*, **55**, 234–240.
- Kearey, P. 1993. *The Encyclopedia of the Solid Earth Sciences*. Oxford: Blackwell Scientific Publications.
- Keith, H. D. and Padden, F. J. 1964. Spherulitic crystallization from the melt, 1, Fractionation and impurity segregation and their influence on the kinetics of crystallisation. *J. Appl. Phys.*, **35**, 1270.
- Kim, K.-T., Vaidya, S. N. and Kennedy, G. C. 1972. Effect of pressure on the temperature of the eutectic minimums in two binary systems: NaF-NaCl and CsCl-NaCl. *Journal of Geophysical Research*, **77**(35), 6984–6989.
- Kim, Ki-Tae. 1974. Analysis of pressure generated in a piston-cylinder type apparatus. *Journal of Geophysical Research*, **79**(23), 3325–3333.
- Kirby, S. H. 1980. Tectonic stresses in the lithosphere: constraints provided by the experimental deformation of rocks. *Journal of Geophysical Research*, **85**(B11), 6353–6363.
- Kirby, S. H. and Kronenberg, A. K. 1984. Deformation of clinopyroxenite: evidence for a transition in flow mechanisms and semibrittle behaviour. *Journal of Geophysical Research*, **89**(B5), 3177–3192.
- Kollé, J. J. and Blacic, J. D. 1982. Deformation of single-crystal clinopyroxene: 1. mechanical twinning in diopside and hedenbergit. *Journal of Geophysical Research*, **87**(B5), 4019–4034.
- Konrad, K. 1997. *Experimentelle Deformation von Aragonit*. Diploma thesis, Institut für Geophysik der Ruhr-Universität Bochum.
- Kronenberg, A. K. and Tullis, J. 1984. Flow strength of quartz aggregates: grain size and pressure effects due to hydrolytic weakening. *Journal of Geophysical Research*, **89**(B6), 4281–4297.
- Kumazawa, M. 1969. The elastic constant of polycrystalline rocks and nonelastic behaviour inherent to them. *Journal of Geophysical Research*, **74**(22), 5311–5320.
- Kushiro, I. 1976. Changes in viscosity and structure of melt of NaAlSi₂O₆ composition at high pressures. *Journal of Geophysical Research*, **81**(35), 6347–6350.
- Lawlis, J. and Orzol, J. 2000. *Stiffness and friction characteristics of the axial column in the griggs apparatus*. Unpublished report. Institut für Geophysik, Ruhr Universität Bochum.
- Leistner, H. 1979. Temperaturgradienten-Messungen in Piston-Zylinder-Pressen. *Fortschr. Mineral.*, **57**(Beiheft 1), 81–82.
- Lofgren, G. 1971. Spherulitic textures in glassy and crystalline rocks. *Journal of Geophysical Research*, **76**(23), 5635–5648.
- Lofgren, G. 1974. An experimental study of plagioclase crystal morphology: isothermal crystallisation. *American Journal of Science*, **274**(March), 243–273.

- Lorimer, G. W. 1976. The plastic deformation of minerals. *In: Strens, R. G. (ed), The Physics and Chemistry of Minerals and Rocks*. John Wiley and Sons.
- Luan, F.C. and Paterson, M.S. 1992. Preparation and deformation of synthetic aggregates of quartz. *Journal of Geophysical Research*, **97**, 301–320.
- Lüttge, A., Neumann, U. and Lasaga, A. C. 1998. The influence of heating rate on the kinetics of mineral reactions: an experimental study and computer models. *American Mineralogist*, **83**, 501–515.
- Mauler, A., Bystricky, M., Kunze, K. and Mackwell, S. 2000. Microstructures and lattice preferred orientations in experimentally deformed clinopyroxene aggregates. *Journal of Structural Geology*, **22**, 1633–1648.
- Mauler, A., Godard, G. and Kunze, K. 2001. Crystallographic fabrics of omphacite, rutile and quartz in Vendée eclogites (Armorican Massif, France). Consequences for deformation mechanisms and regimes. *Tectonophysics*, **342**, 81–112.
- Mei, S., Majumder, S. and Kohlstedt, D. L. 2001. Influence of water on creep behaviour of diopside aggregates. *Eos. Trans. AGU*, **82**(47). Fall Meet. Suppl. Abstract T21C-09.
- Mercier, J.-C. C., Anderson, D. A. and Carter, N. L. 1977. Stress in the lithosphere: inferences from steady state flow of rocks. *Pure and Applied Geophysics*, **115**, 199–227.
- Mirwald, P. W., Getting, I. C. and Kennedy, G. C. 1975. Low-friction cell for piston-cylinder high-pressure apparatus. *Journal of Geophysical Research*, **80**, 1519–1525.
- Molnar, P. and England, P. 1990. Temperatures, heat flux, and frictional stress near major thrust faults. *Journal of Geophysical Research*, **95**(B4), 4833–4856.
- Müller, G. 1991. *Inversionstheorie geophysikalischer Beobachtungen*. Universität Frankfurt.
- Newton, M. S. and Kennedy, G. C. 1968. Jadeite, analcite, nepheline, and albite at high temperatures and pressures. *American Journal of Science*, **266**, 728–735.
- Nicolas, A. 1989. *Structure of Ophiolites and Dynamic of Oceanic Lithosphere*. Kluwer Academic Publishers.
- Nicolas, A. and Poirier, J. P. 1976. *Crystalline Plasticity and Solid State Flow in Metamorphic Rocks*. Selected Topics in Geological Sciences. John Wiley and Sons.
- Nowlan, E. U., Schertl, H. P. and Schreyer, W. 2000. Garnet-omphacite-phengite thermobarometry of eclogites from the coesite-bearing unit of the southern Dora-Maira Massif, Western Alps. *Lithos*, **52**, 197–214.
- Pacaud, L., Ingrin, J. and Jaoul, O. 1999. High-temperature diffusion of oxygen in synthetic diopside measured by nuclear reaction analysis. *Mineralogical Magazine*, **63**(5), 673–686.
- Paterson, M. S. 1982. The determination of hydroxyl by infrared absorption in quartz, silicate glass and similar materials. *Bull. Minéral.*, **105**, 20–29.
- Paterson, M. S. 1987. Problems in the extrapolation of laboratory rheological data. *Tectonophysics*, **133**, 33–43.

- Paterson, M. S. 2001. Relating experimental and geological rheology. *International Journal of Earth Sciences*, **90**(1), 157–168.
- Peacock, S. M. 1996. Thermal and petrological structure of subduction zones. *In*: Bebout, G. E., Scholl, D. W., Kirby, S. H. and Platt, J. P. (eds), *Subduction: Top to Bottom*, vol. Geophysical Monograph 96. American Geophysical Union.
- Pelton, A. D. 1991. Thermodynamics and phase diagrams of materials. *In*: Haasen, P. (ed), *Phase Transformations in Materials*. Materials Science and Technology, Vol. 5. VCH.
- Philippot, P. and van Roermond, H. L. M. 1992. Deformation processes in eclogitic rocks: evidence for the rheological delamination of the oceanic crust in deeper level of subduction zones. *Journal of Structural Geology*, **14**, 1059–1077.
- Piepenbreier, D. and Stöckhert, B. 2001. Plastic flow of omphacite in eclogites at temperature below 500°C - implications for interplate coupling in subduction zones. *International Journal of Earth Sciences*, **90**, 197–210.
- Pieri, M., Kunze, K., Burlini, L., Stretton, I., Olgaard, D. L., Burg, J.-P. and Wenk, H.-R. 2001. Texture development of calcite by deformation and dynamic recrystallisation at 1000 K during torsion experiments of marble to large strains. *Tectonophysics*, **330**, 119–140.
- Poirier, J. P. 1985. *Creep of Crystals*. Cambridge University Press.
- Poirier, J. P. 1995. Plastic rheology of crystals. *In*: Ahrens, T. J. (ed), *Mineral Physics and Crystallography*. A Handbook of Physical Constants, Vol. AGU Reference Shelf 2. American Geophysical Union, Washington, D. C.
- Poirier, J. P., Sotin, C. and Beauchesne, S. 1990. Experimental deformation and data processing. *In*: Barber, D. J. and Meredith, P. G. (eds), *Deformation Processes in Minerals and Rocks*. Unwin Hyman Ltd.
- Popp, R. K. and Frantz, J. D. 1977. Diffusion of hydrogen in gold. *Carnegie Inst. Wash. Yearb.*, **76**(1730), 662–664.
- Porter, D. A. and Easterling, K. E. 1997. *Phase Transformations in Metals and Alloys*. 2. edn. Chapman and Hall.
- Prior, D. J., Boyle, A. P., Brenker, F., Cheadle, M. C., Day, A., Lopez, G., Peruzzo, L., Potts, G. J., Reddy, S., Spiess, R., Timms, N. E., Trimby, P. and Wheeler, J. and Zetterström, L. 1999. The application of electron backscatter diffraction and orientation contrast imaging in the SEM to textural problems in rocks. *American Mineralogist*, **84**, 1741–1759.
- Putnis, A. and McConnell, J. D. C. 1980. *Principles of Mineral Behaviour*. Blackwell Scientific Publications.
- Raleigh, C. B. and Talbot, J. L. 1967. Mechanical twinning in naturally and experimentally deformed diopside. *American Journal of Science*, **265**, 151–165.
- Ranalli, G. 1984. Grain size distribution and flow stress in tectonites. *Journal of Structural Geology*, **6**(4), 443–447.

- Ranalli, G. 1995. *Rheology of the Earth*. Chapman and Hall.
- Rao, C. N. R. and Rao, K. J. 1978. *Phase Transitions in Solids*. McGraw-Hill International Book Company.
- Read, W. T. 1953. *Dislocations in Crystals*. McGraw Hill.
- Renner, J. 1996. *Experimentelle Untersuchung zur Rheologie von Coesit*. Berichte des Instituts für Geophysik der Ruhr-Universität Bochum, Reihe A, Nr. 48.
- Renner, J., Zerbian and Stöckhert, B. 1997. Microstructures of synthetic polycrystalline coesite aggregates. The effect of pressure, temperature, and time. *Lithos*, **41**, 169–184.
- Renner, J., Stöckhert, B., Zerbian, A., Röller, K. and Rummel. 2001. An experimental study into the rheology of synthetic polycrystalline coesite aggregates. *Journal of Geophysical Research*, **106**, 19411–19429.
- Ricoult, D. L. and Kohlstedt, D. L. 1985. Experimental evidence for the effect of chemical environment upon the creep rate of olivine. *Pages 171–184 of: Schock, R. N. (ed), Mineral Physics 1: Point Defects of Minerals*. Geophysical Monograph, Vol. 31. AGU, Washington, D.C.
- Robertson, E. C., Birch, F. and MacDonald, G. J. F. 1957. Experimental determination of jadeite stability relation to 25000 bars. *American Journal of Science*, **255**, 115–137.
- Ruff, L. J. and Tichelaar, B. W. 1996. What controls the seismogenic interface in subduction zones? *In: Bebout, G. E., Scholl, D. W., Kirby, S. H. and Platt, J. P. (eds), Subduction: Top to Bottom*. American Geophysical Union. Geophysical Monograph 96.
- Rummel, F. 1982. Fracture and flow of rocks and minerals. *In: Angenheister, G. (ed), Landolt-Börnstein: Zahlenwerte und Funktionen aus Naturwissenschaft und Technik, Neue Serie, Gruppe 5, Bd. 1b*. Springer Verlag, Berlin. 141-238.
- Rummel, F. and Fairhurst, C. 1970. Determination of the post-failure behaviour of brittle rock using a servo-controlled testing machine. *Int. J. Rock Mech.*, **2**, 189–204.
- Rummel, F., Stöckhert, B., Lawlis, J. and Orzol, J. 2002. Rheologie gesteinsbildender Minerale unter hohem Umschließungsdruck. *In: Rheologie der Erde - von der Oberkruste bis in die Subduktionszone*. Ruhr-Universität Bochum. Berichtsband für den Finanzierungszeitraum 1999/2. Halbjahr-2000-20001-2002/1. Halbjahr.
- Rutter, E. H. 1993. Experimental rock deformation: techniques, results and application to tectonics. *Geology Today*, **9**(2), 61–65.
- Rybacki, E. 1991. *Experimentelle Festigkeitsuntersuchungen an inhomogen - anisotropen Gneisen und Granuliten bei hohen Drücken und Temperaturen*. Berichte des Instituts für Geophysik der Ruhr-Universität Bochum, Reihe A, Nr. 31.
- Rybacki, E., Rummel, F. and Stöckhert, B. 1995. Synthesis and experimental deformation of polycrystalline aragonite. *Bochumer geologische und geotechnische Arbeiten*, **44**, 189–194.

- Rybacki, E., Renner, J., Konrad, K., Harbott, W., Rummel, F. and Stöckhert, B. 1998. A servohydraulically-controlled deformation apparatus for rock deformation under conditions of ultra-high pressure metamorphism. *Pure and Applied Geophysics*, **152**, 579–606.
- Ryerson, F. J. and McKeegan, K. D. 1994. Determination of oxygen self-diffusion in akermanite, anorthite, diopside and spinel: Implications for oxygen isotopic anomalies and the thermal histories of Ca-Al-rich inclusions. *Geochimica et Cosmochimica Acta*, **58**, 3713–3734.
- Schairer, J. F. 1951. *Phase Transformations in Solids*. Wiley, New York.
- Schmid, S. M. 1982. Microfabric studies as indicators of deformation mechanisms and flow laws operative in mountain building. In: Hsue, K. (ed), *Mountain building processes*.
- Schmidt, N. H. and Olesen, N. 1989. Computer-aided determination of crystal-lattice orientation from electron-channeling patterns in the SEM. *Can Mineral*, **27**, 15–22.
- Scholz, C. H. 1980. Shear heating and the state of stress on faults. *Journal of Geophysical Research*, **85**(B11), 6174–6184.
- Scholz, C. H. and Koczyński, T. A. 1979. Dilatancy anisotropy and the response of rock to large cyclic loads. *Journal of Geophysical Research*, **84**(B10), 5525–5534.
- Seifert, F. and Langer, K. 1971. *Arbeitsvorschriften und Tabellen zum Praktikum „Experimentelle Petrologie“*. Unpublished report. Institut für Mineralogie, Ruhr-Universität Bochum.
- Simmons, G. and Brace, W. F. 1965. Comparison of static and dynamic measurements of compressibilities of rocks. *Journal of Geophysical Research*, **70**, 5649–5656.
- Skogby, H., Bell, D. R. and Rossman, G. R. 1990. Hydroxide in pyroxenes: Variations in the natural environment. *American Mineralogist*, **75**, 764–774.
- Smyth, J. R., Bell, D. R. and Rossman, G. R. 1991. Incorporation of hydroxyl in upper-mantle clinopyroxenes. *Nature*, **351**, 732–735.
- Stöckhert, B. 2002. Stress and deformation in subduction zones - insight from the record of exhumed metamorphic rocks. In: de Meer, S., Drury, M. R., de Bresser, J. H. P. and Pennock, G. M. (eds), *Deformation Mechanisms, Rheology and Tectonics: Current Status and Future Perspectives*. Geological Society Special Publication, Vol. 200. The Geological Society of London.
- Stöckhert, B. and Renner, J. 1998. Rheology of crustal rocks at ultrahigh pressure. In: Hacker, B.R. and Liou, J.G. (eds), *When Continents Collide: Geodynamics and Geochemistry of Ultrahigh-Pressure Rocks*. Kluwer Academic Publishers. 57-95.
- Stöckhert, B., Masonne, H.-J. and Nowlan, E. U. 1997. Low differential stress during high-pressure metamorphism: the microstructural record of a metapelite from the Eclogite Zone, Tauern Window, Eastern Alps. *Lithos*, **41**, 103–118.
- Tarantola, A. and Valette, B. 1982. Generalized nonlinear inverse problems solved using the least squares criterion. *Reviews of Geophysics and Space Physics*, **20**(2), 219–232.

- Tingle, T., Green, H. W., Young, T. E. and Koczyński, T. A. 1993. Improvements to Griggs-type apparatus for mechanical testing at high pressure and temperature. *Pure and Applied Geophysics*, **141**, 523–543.
- Trepmann, C. and Stöckhert, B. 2001. Mechanical twinning of jadeite - an indication of synseismic loading beneath the brittle-plastic transition. *International Journal of Earth Sciences*, **90**(1), 4–14.
- Tsenn, M. C. and Carter, N. L. 1987. Upper limits of power law creep in rocks. *Tectonophysics*, **136**, 1–26.
- Tullis, J. 1990. Experimental studies of deformation mechanisms and microstructures in quartzo-feldspathic rocks. *Chap. 8, pages 190–227 of: Barber, D. J. and Meredith, P.G. (eds), Deformation Processes in Minerals, Ceramics and Rocks*. The Mineralogical Society Series. Unwin Hyman.
- Tullis, J. and R., Yund. 1985. Dynamic recrystallisation of feldspar: a mechanism for ductile shear zone formation. *Geology*, **13**, 238–241.
- Tullis, T. E. 1980. The use of mechanical twinning in minerals as a measure of shear stress magnitudes. *Journal of Geophysical Research*, **85**(B11), 6263–6268.
- Turcotte, D. L. and Schubert, G. 2002. *Geodynamics*. John Wiley and Sons.
- Twiss, R. J. 1977. Theory and applicability of a recrystallized grain size paleopiezometer. *Pure and Applied Geophysics*, **115**, 227–244.
- Underwood, E. E. 1969. *Quantitative Stereology*. Addison-Wesley Publishing Company.
- van der Klauw, B., Reinecke, T. and Stöckhert, B. 1997. Exhumation of ultrahigh-pressure metamorphic oceanic crust from Lago di Cignana, Piemontese zone, western Alps: the structural record in metabasites. *Lithos*, **41**, 79–102.
- Wang, K. and He, J. 1999. Mechanics of low-stress forearcs: Nankai and Cascadia. *Journal of Geophysical Research*, **104**(B7), 15.191–15.205.
- Wang, Z. and Ji, S. 2000. Diffusion creep of fine-grained garnetite: implications for the flow strength of subducting slabs. *Geophysical Research Letters*, **27**(15), 2333–2226.
- Waterwiese, T., Chatterjee, N. D., Dierdorf, I., Göttlicher, J. and Kroll, H. 1995. Experimental and thermodynamic study of heterogeneous and homogeneous equilibria in the system $\text{NaAlSiO}_4\text{-SiO}_2$. *Contributions to Mineralogy and Petrology*, **121**, 65–73.
- Weertman, J. 1968. Dislocation climb theory of steady-state creep. *In: Hirth, J. (ed), Dislocation Climb and High-Temperature Creep Processes*. Transactions of the ASM, Vol. 61.
- Weibel, E. R. 1967. Structure in space and its appearance on sections. *In: Elias, H. (ed), Stereology*, vol. Proceedings of the second international congress for stereology. Springer Verlag.
- Yoder, H. S. 1950. The jadeite problem. *American Journal of Science*, **248**, 225–248.

- Zhang, J., Green, H. W., Jin, Z. and Bozhilov, K. 2001. Rheological implications of dissolution of hydroxyl in eclogite. *Eos. Trans. AGU*, **82**(47). Fall Meet. Suppl. Abstract T21C-09.
- Zhao, T., Yan, X., Cui, S. and Zhu, Y. 1995. Synthesis of the clinopyroxenes join $\text{CaMgSi}_2\text{O}_6$ - $\text{NaAlSi}_2\text{O}_6$ for jewellery. *Journal of Materials Science*, **30**(4), 1117–1123.

A Overview of deformation experiments

This Appendix summarizes details of the deformation experiments. T denotes the average temperature obtained from the thermocouple readings and deviations from that, a question mark denotes that one thermocouple failed. OP is the relative oven power, v_p the velocity of the axial piston. Δl is the final change of sample length determined from measurements before and after the experiment. For step tests it is split up to the single cycles. cm gives the material used for jacketing, m_{pre} and m_{post} give slopes of the linear portions of the force vs. displacement curves before and after the hit-point. Information on the alignment of the sample is also given. 'Sample tilting' is denoted by "o", "•" marks samples which are well aligned with the pistons. For some samples tilting is very low, these are denoted by a star.

Sample	T [°C]	OP %	v_p [mm/s]	Δl [mm]	cm	m_{pre} [kN/mm]	m_{post} [kN/mm]	alignment
JD43.1	891 ± 37	63	1.32 · 10 ⁻⁴	1.17	Au	1.6	15.4	●
JD44.C	973 ± 37	64	1.32 · 10 ⁻⁴	1.91	Au	0.8	7.8	●
JD44.B	998 ± 2	64	1.32 · 10 ⁻⁴	1.32	Pt	1.5	15.7	○
JD43.2	921 ± 79	69	1.33 · 10 ⁻⁴	0.78	Pt	1.0	5.54	○
JD15.B	945 ± 55	67	1.32 · 10 ⁻⁴	1.17	Pt	2.4	-	●
JD38.A	992 ± 8	68	1.34 · 10 ⁻⁴	1.35	Pt	0.7	4.7	★
JD41.C	913 ± 13	69	7.00 · 10 ⁻⁵	0.15	Au	1.7	-	
JD45.B-1	882 ± 18	61	1.32 · 10 ⁻⁴	0.75	Au	1.7	18.4	●
JD45.B-2	880 ± 20	62	3.00 · 10 ⁻⁵	0.52	Au	2.9	22.2	●
JD46.C-1	973 ± 27	65	1.33 · 10 ⁻⁴	0.85	Au	1.4	9.3	○
JD46.C-2	973 ± 27	65	3.01 · 10 ⁻⁵	0.45	Au	3.2	10.3	○
JD46.C-3	973 ± 27	65	4.41 · 10 ⁻⁴	0.45	Au	5.5	25.7	○
JD46.A-1	792 ± 8	60	1.32 · 10 ⁻⁴	?	Au	2.6	7.5	
JD46.A-2	892 ± 8	64	1.18 · 10 ⁻⁴	?	Au	2.5	-	
JD46.B-1	991 ± 9	68	6.61 · 10 ⁻⁵	0.46	Au	1.0	13.5	○
JD46.B-2	891 ± 9	68	6.11 · 10 ⁻⁵	0.48	Au	3.6	20.1	○
JD46.B-3	794 ± 6	63	5.61 · 10 ⁻⁵	0.41	Au	7.5	22.1	○
JD49.B	897 ± 3	65	3.31 · 10 ⁻⁵	1.40	Au	1.0	12.2	●
JD48.A-1	985 ± 15	-	1.32 · 10 ⁻⁴	0.69	Au	1.1	14.0	●
JD48.A-2	885 ± 15	-	1.16 · 10 ⁻⁴	0.61	Au	3.3	24.6	●
JD53.B-1	992 ± 8	68	1.30 · 10 ⁻³	0.87	Pt	1.7	20.4	★
JD53.B-2	992 ± 8	68	3.01 · 10 ⁻⁵	0.64	Pt	1.0	15.6	★
JD53.A-1	1096 ± 4	72	6.61 · 10 ⁻⁴	0.84	Au	0.8	7.2	
JD53.A-2	1010 ± 10	72	3.31 · 10 ⁻⁵	0.40	Au	1.0	12.2	
JD56.B	1024 ± 24	72	3.31 · 10 ⁻⁵	0.71	Pt	1.9	4.5	●
JD57.B-1	990 ± 10	71	2.64 · 10 ⁻⁴	0.78	Pt	1.1	13.6	★
JD57.B-2	893 ± 7	67	2.34 · 10 ⁻⁴	0.46	Pt	5.7	23.6	★
JD57.B-3	794 ± 6	-	2.16 · 10 ⁻⁴	0.46	Pt	8.1	31.6	★

Table 16: Details of deformation experiments.

Sample	T [°C]	OP %	v_p [mm/s]	Δl [mm]	cm	m_{pre} [kN/mm]	m_{post} [kN/mm]	alignment
JC-1	aborted during set-up of conditions							
JDC2-1	996 ± 4	70	$1.32 \cdot 10^{-4}$	0.55	Pt	1.1	14.1	•
JDC2-2	899 ± 1	65	$1.10 \cdot 10^{-4}$	0.39	Pt	3.4	36.1	•
JDC3	$1000 \pm ?$	73	$1.32 \cdot 10^{-4}$	-	Pt	0.4	8.7	•
JD57.A-1	$900 \pm ?$	68	$2.00 \cdot 10^{-5}$	0.91	Au	0.7	18.7	◦
JD57.A-2	$900 \pm ?$	68	$1.70 \cdot 10^{-4}$	0.97	Au	3.1	26.9	◦
JD56.C	808 ± 8	64	$2.00 \cdot 10^{-5}$	1.54	Au	2.2	15.7	
JD48.C-1	788 ± 15	64	$6.61 \cdot 10^{-5}$	1.3	Au	4.1	19.0	◦
JD48.C-2	886 ± 14	67	$6.01 \cdot 10^{-5}$	-	Au	4.5	27.0	◦
JD48.C-3	985 ± 15	-	$5.51 \cdot 10^{-5}$	-	Au	5.3	19.8	◦
JD58.B	997 ± 3	65	$2.00 \cdot 10^{-5}$	0.76	Au	3.3	13.6	◦
JD60.B	aborted during set-up of conditions							
JD60.C	aborted due to core failure							
JD61.A	990 ± 10	66	$1.40 \cdot 10^{-5}$	0.98	Pt	2.2	15.6	◦
JD63.1-1	995 ± 5	59	$3.31 \cdot 10^{-5}$	0.42	Pt	0.6	18.0	★
JD63.1-2	993 ± 7	59	$1.20 \cdot 10^{-4}$	0.26	Pt	3.6	27.9	★
JD63.1-3	993 ± 7	59	$4.33 \cdot 10^{-4}$	-	Pt	3.3	21.8	★
FC3-1	$1000 \pm ?$	60	$3.31 \cdot 10^{-5}$	0.65	Pt	0.9	22.0	•
JD63.2	975 ± 25	58	$2.92 \cdot 10^{-3}$	0.33	Pt	2.4	16.6	•
FC3-2	898 ± 2	57	$3.31 \cdot 10^{-5}$	0.58	Pt	0.9	21.5	•
FC3-4	1111 ± 11	63	$3.31 \cdot 10^{-5}$	0.70	Pt	1.1	15.1	•
FC3-5	1000 ± 0	60	$3.31 \cdot 10^{-5}$	0.46	Pt	0.9	21.6	•
FC3-6-1	988 ± 12	58	$6.51 \cdot 10^{-5}$	0.92	Pt	1.8	15.5	•
FC3-6-2	986 ± 14	58	$2.76 \cdot 10^{-4}$	0.23	Pt	4.0	17.3	•
FC3-7	990 ± 10	62	$1.30 \cdot 10^{-5}$	0.56	Pt	0.6	16.5	•
JD61.C	883 ± 17	58	$1.40 \cdot 10^{-5}$	1.01	Pt	0.5	22.4	•
FC3-8-1	895 ± 5	58	$1.30 \cdot 10^{-5}$	0.23	Pt	0.9	17.3	•
FC3-8-2	845 ± 5	57	$1.20 \cdot 10^{-5}$	0.21	Pt	2.3	41.3	•

Table 16 continued.

B Force versus displacement curves

The force vs. displacement curves are displayed in this Appendix. The axial load is given in kN, the piston displacement is given in μm . T denotes the average temperature obtained from the thermocouple readings, v_p gives the velocity of the axial piston. For step test, all cycles are displayed together and the corresponding conditions are given in the order the cycles were performed. In some experiments cycles were done at a high piston velocity to locate the sample prior to deformation. These cycles are not displayed here.

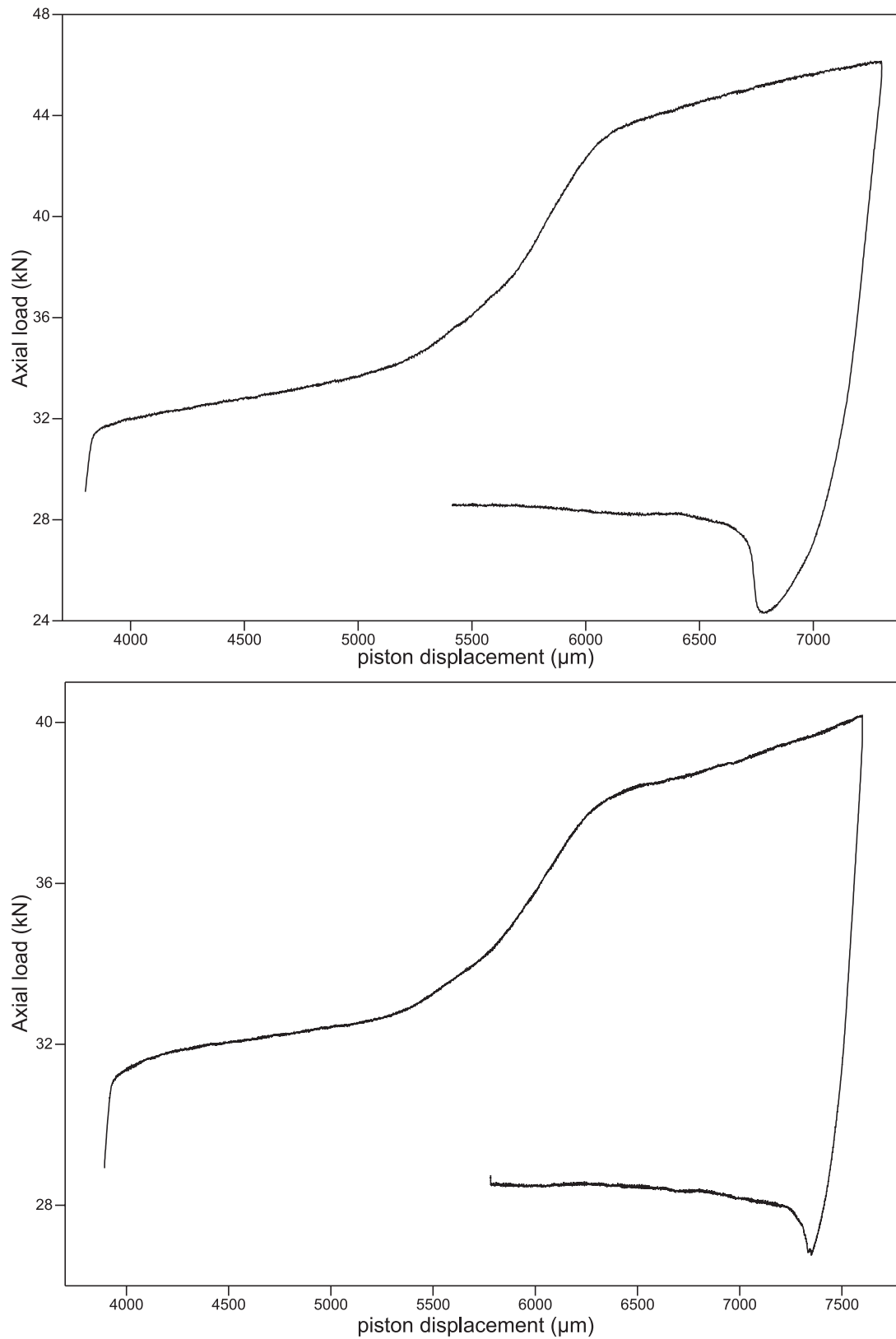


Figure 1: JD43.1 (top): $T = 891^{\circ}\text{C}$, $v_p = 1.32 \cdot 10^{-4}\text{mm/s}$ and JD44.C (bottom): $T = 973^{\circ}\text{C}$, $v_p = 1.32 \cdot 10^{-4}\text{mm/s}$.

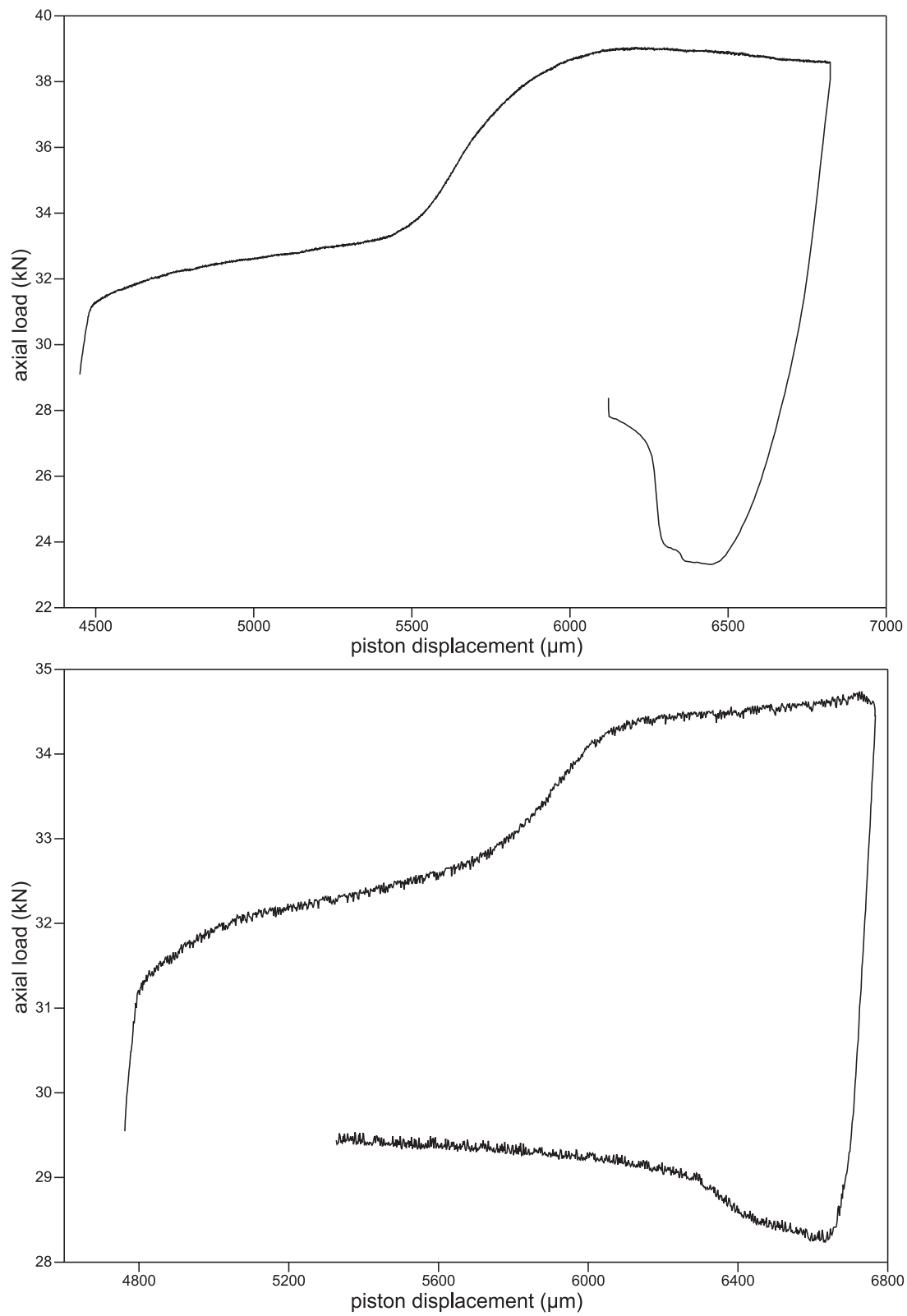


Figure 2: JD44.B (top): $T = 998^{\circ}\text{C}$, $v_p = 1.32 \cdot 10^{-4}\text{mm/s}$ and JD43.2 (bottom): $T = 921^{\circ}\text{C}$, $v_p = 1.33 \cdot 10^{-4}\text{mm/s}$.

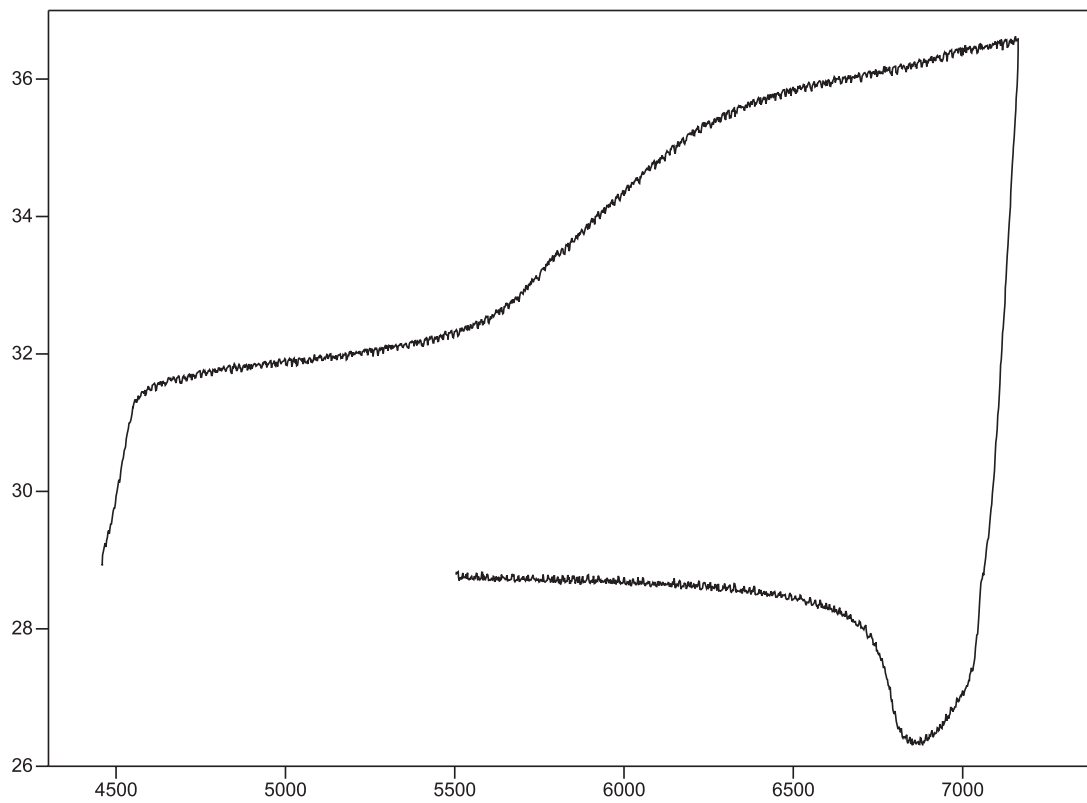
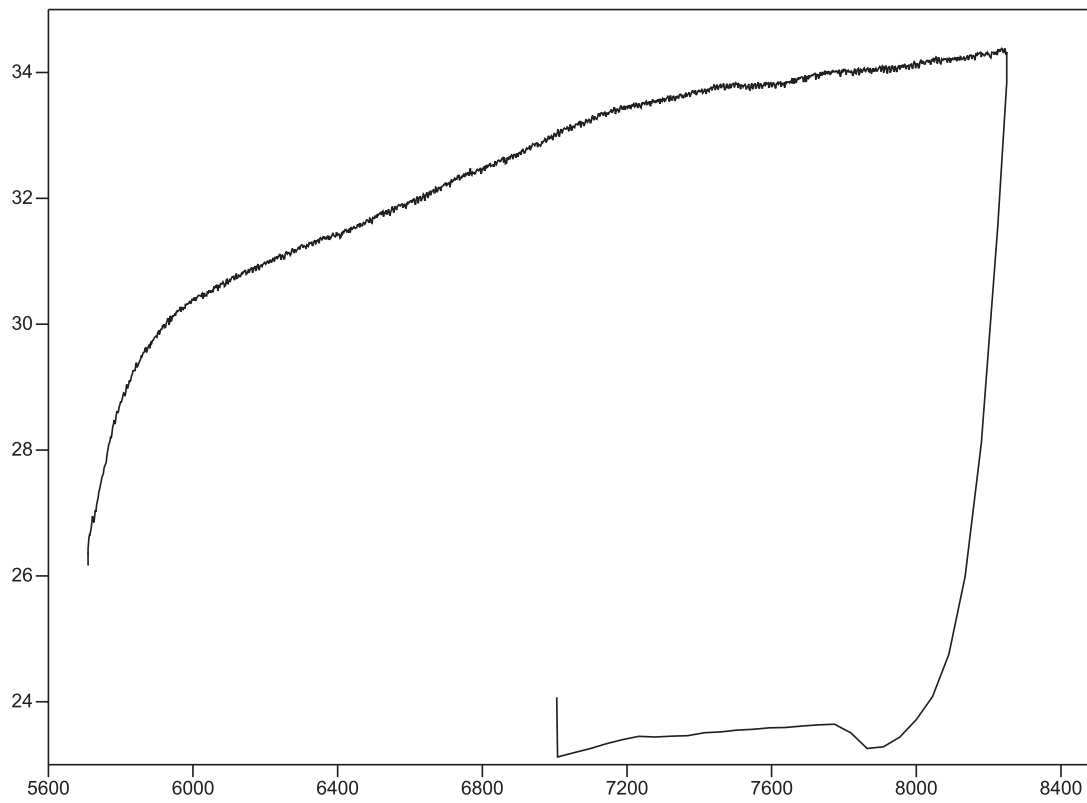


Figure 3: JD15.B (top): $T = 945^{\circ}\text{C}$, $v_p = 1.32 \cdot 10^{-4}\text{mm/s}$ and JD38.A (bottom): $T = 992^{\circ}\text{C}$, $v_p = 1.34 \cdot 10^{-4}\text{mm/s}$.

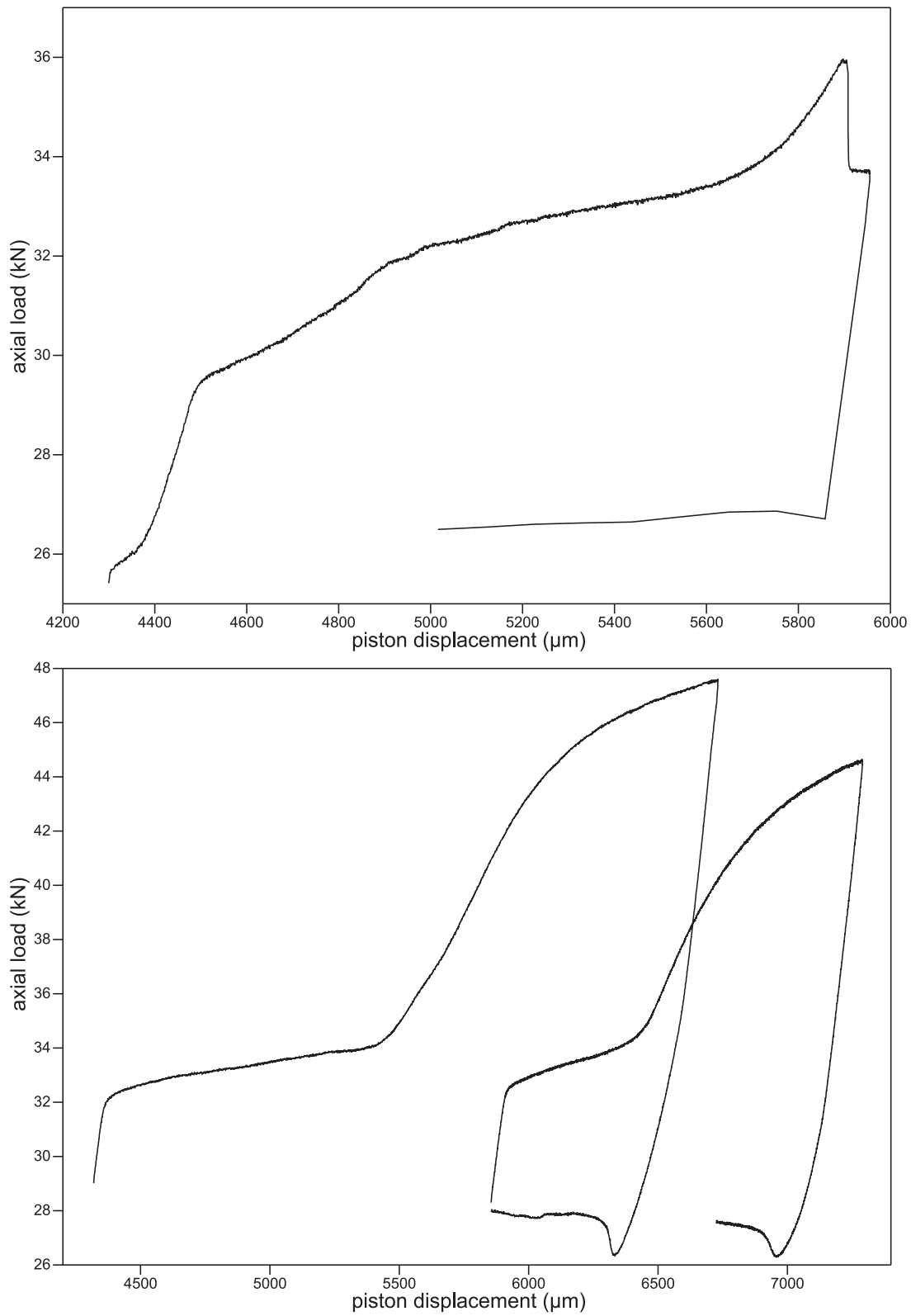


Figure 4: JD41.C (top): LiCl was used as a pressure medium, $T = 913^{\circ}\text{C}$, $v_p = 7.00 \cdot 10^{-5}\text{mm/s}$ and JD45.B (bottom): $T = 882^{\circ}\text{C}$, $v_p = 1.32 \cdot 10^{-4}\text{mm/s}$ and $T = 880^{\circ}\text{C}$, $v_p = 3.00 \cdot 10^{-5}\text{mm/s}$.

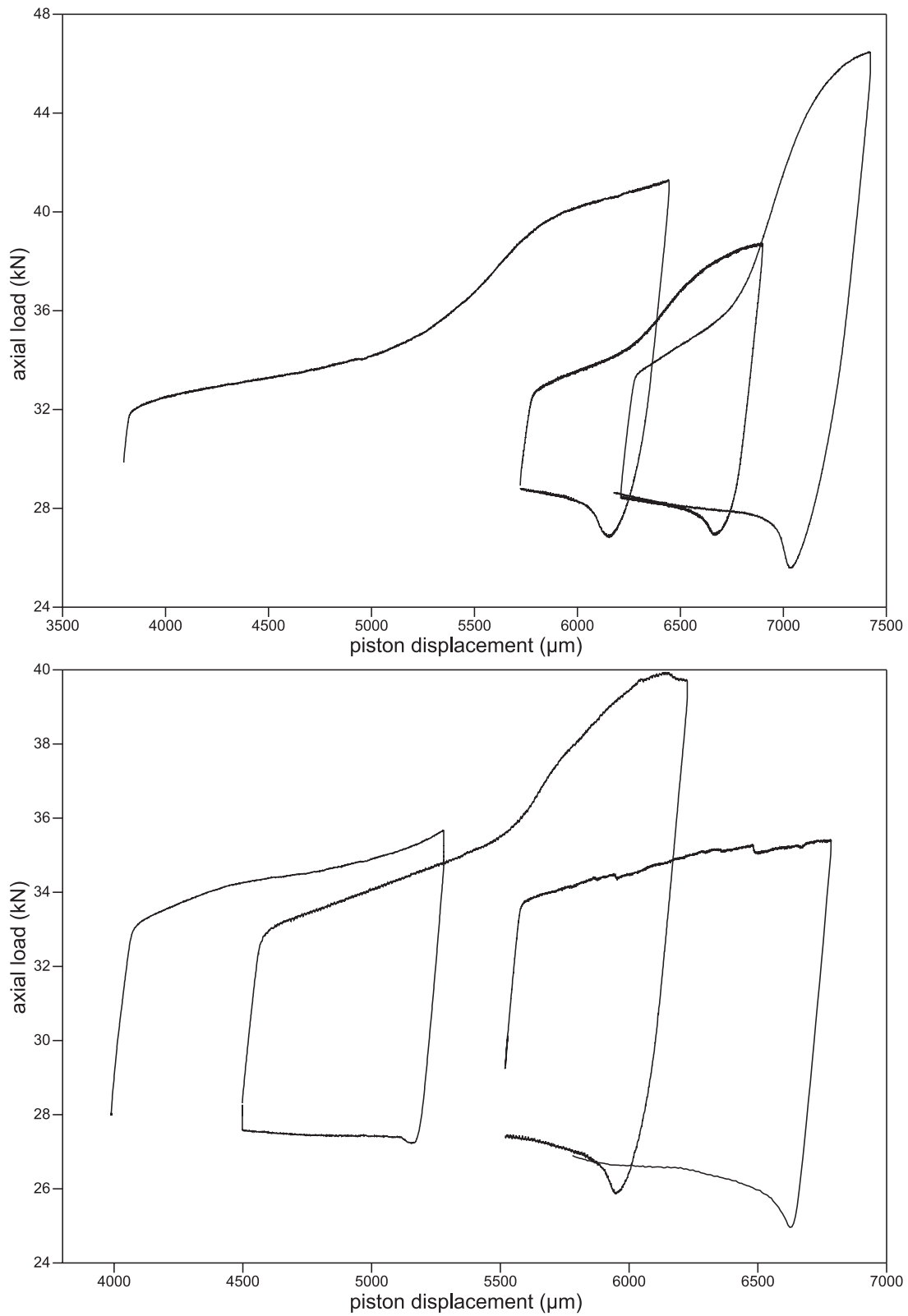


Figure 5: JD46.C (top): $T = 973^{\circ}\text{C}$, $v_p = 1.33 \cdot 10^{-4}\text{mm/s}$ and $v_p = 3.01 \cdot 10^{-5}\text{mm/s}$ and $v_p = 4.41 \cdot 10^{-4}\text{mm/s}$ and JD46.A (bottom): $T = 792^{\circ}\text{C}$, $v_p = 1.32 \cdot 10^{-4}\text{mm/s}$ and $T = 892^{\circ}\text{C}$, $v_p = 1.18 \cdot 10^{-4}\text{mm/s}$.

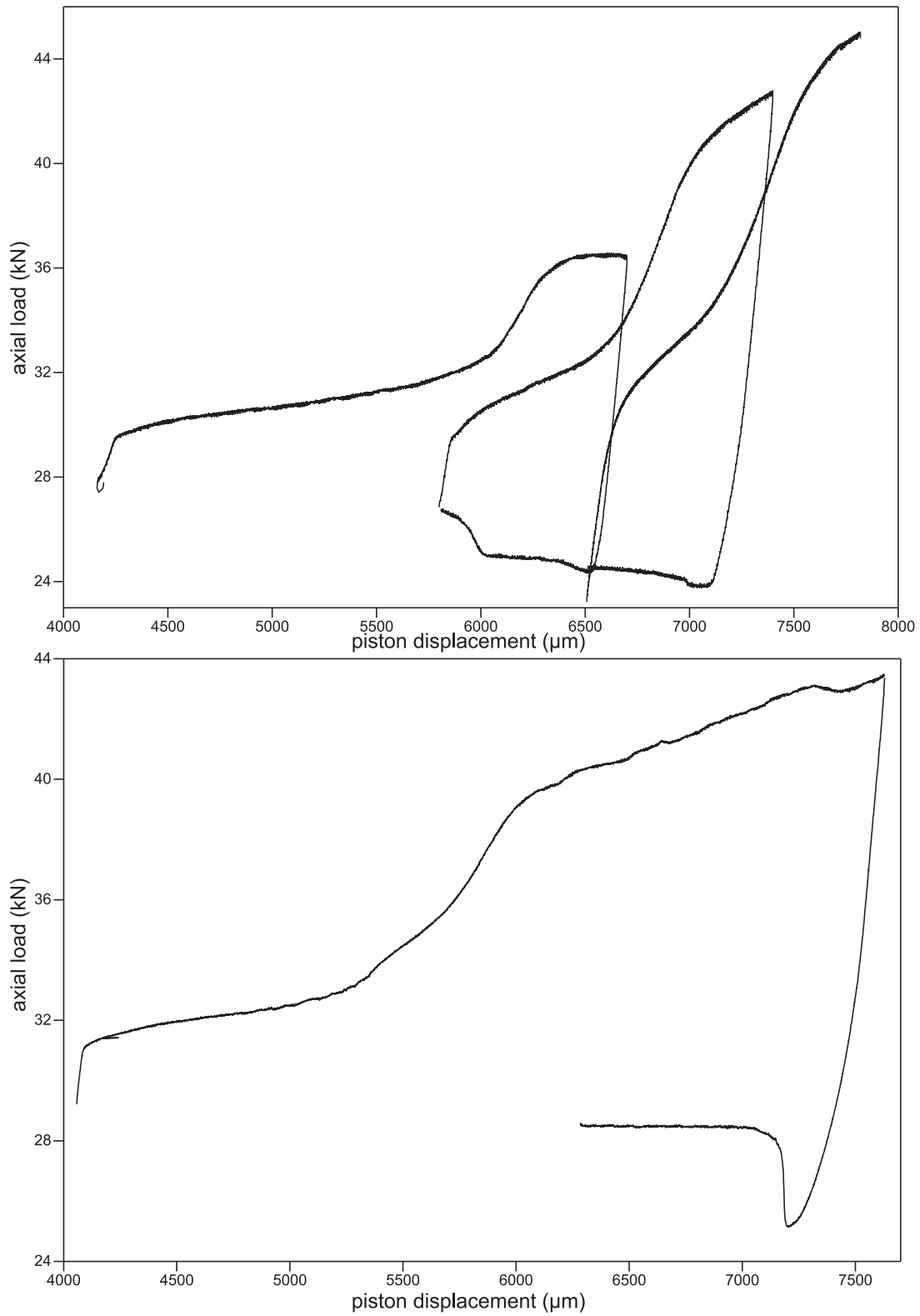


Figure 6: JD46.B (top): $T = 991^{\circ}\text{C}$, $v_p = 6.61 \cdot 10^{-5} \text{mm/s}$ and $T = 891^{\circ}\text{C}$, $v_p = 6.11 \cdot 10^{-5} \text{mm/s}$ and $T = 794^{\circ}\text{C}$, $v_p = 5.61 \cdot 10^{-5} \text{mm/s}$ and JD49.B (bottom): $T = 897^{\circ}\text{C}$, $v_p = 3.31 \cdot 10^{-5} \text{mm/s}$.

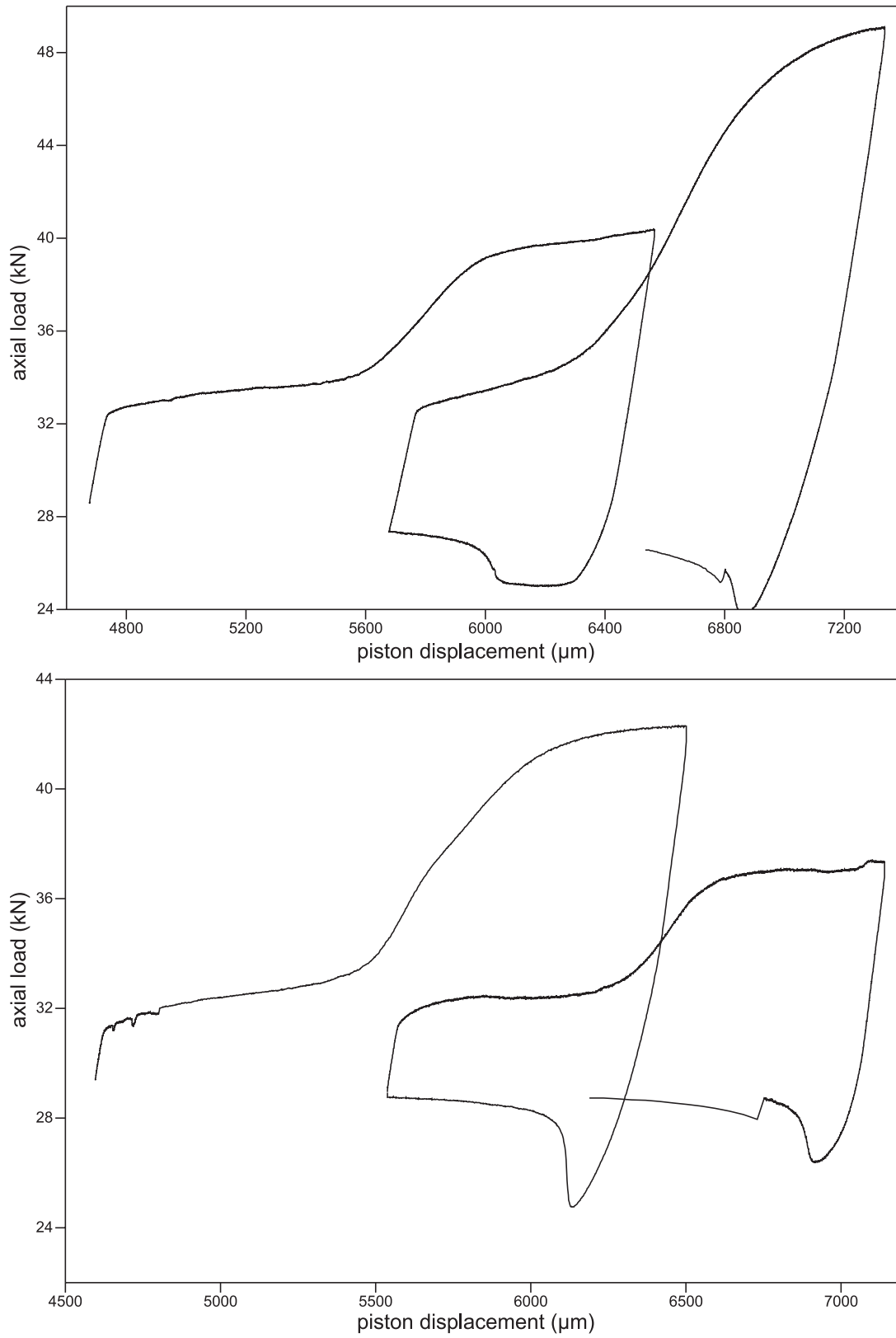


Figure 7: JD48.A (top): $T = 985^{\circ}\text{C}$, $v_p = 1.32 \cdot 10^{-4} \text{mm/s}$ and $T = 885^{\circ}\text{C}$, $v_p = 1.16 \cdot 10^{-4} \text{mm/s}$ and JD53.B (bottom): $T = 992^{\circ}\text{C}$, $v_p = 1.30 \cdot 10^{-3} \text{mm/s}$ and $v_p = 3.01 \cdot 10^{-5} \text{mm/s}$.

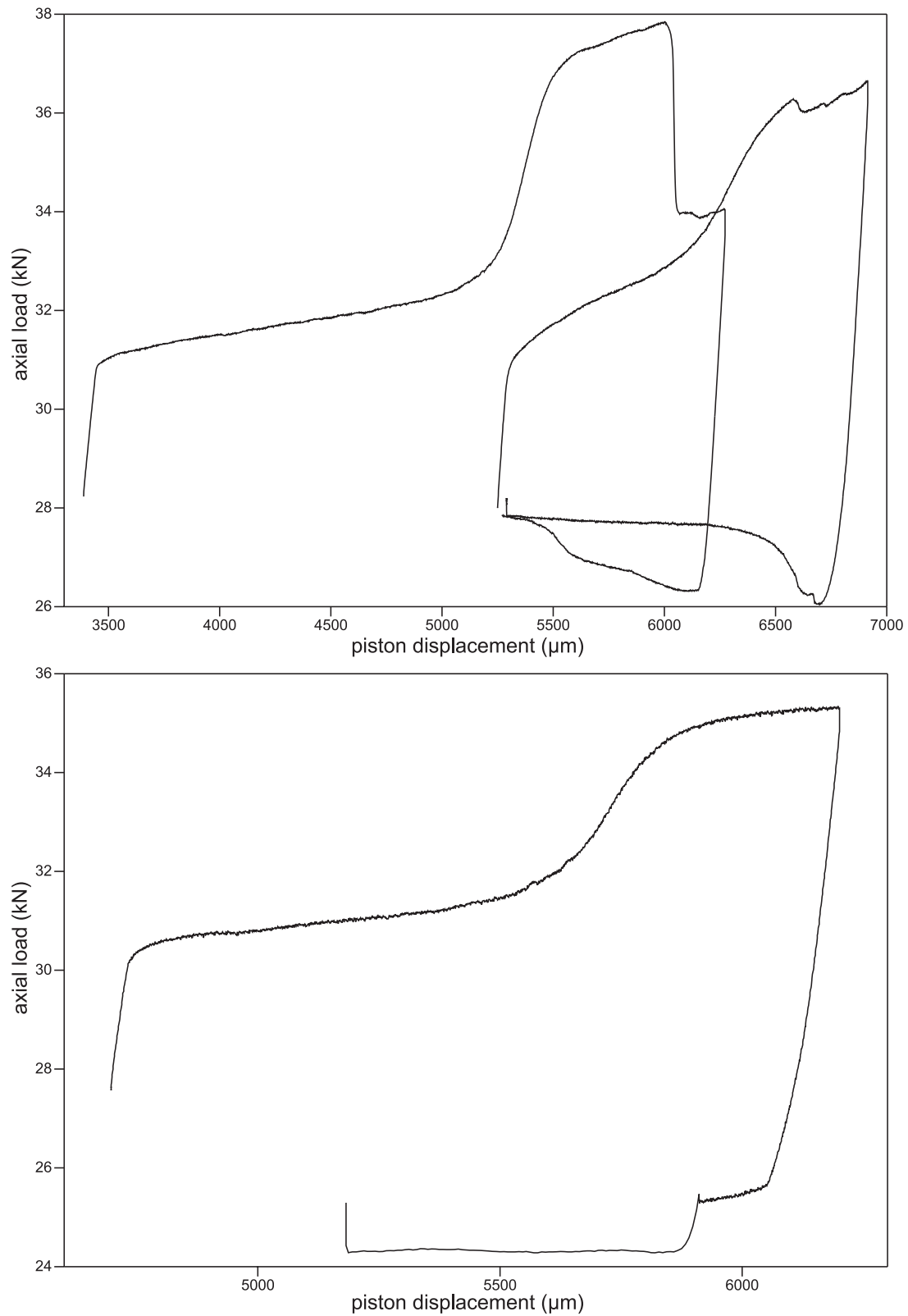


Figure 8: JD53.A (top): $T = 1096^{\circ}\text{C}$, $v_p = 6.61 \cdot 10^{-4} \text{mm/s}$ and $T = 1010^{\circ}\text{C}$, $v_p = 3.31 \cdot 10^{-5} \text{mm/s}$ and JD56.B (bottom): $T = 1024^{\circ}\text{C}$, $v_p = 3.31 \cdot 10^{-5} \text{mm/s}$.

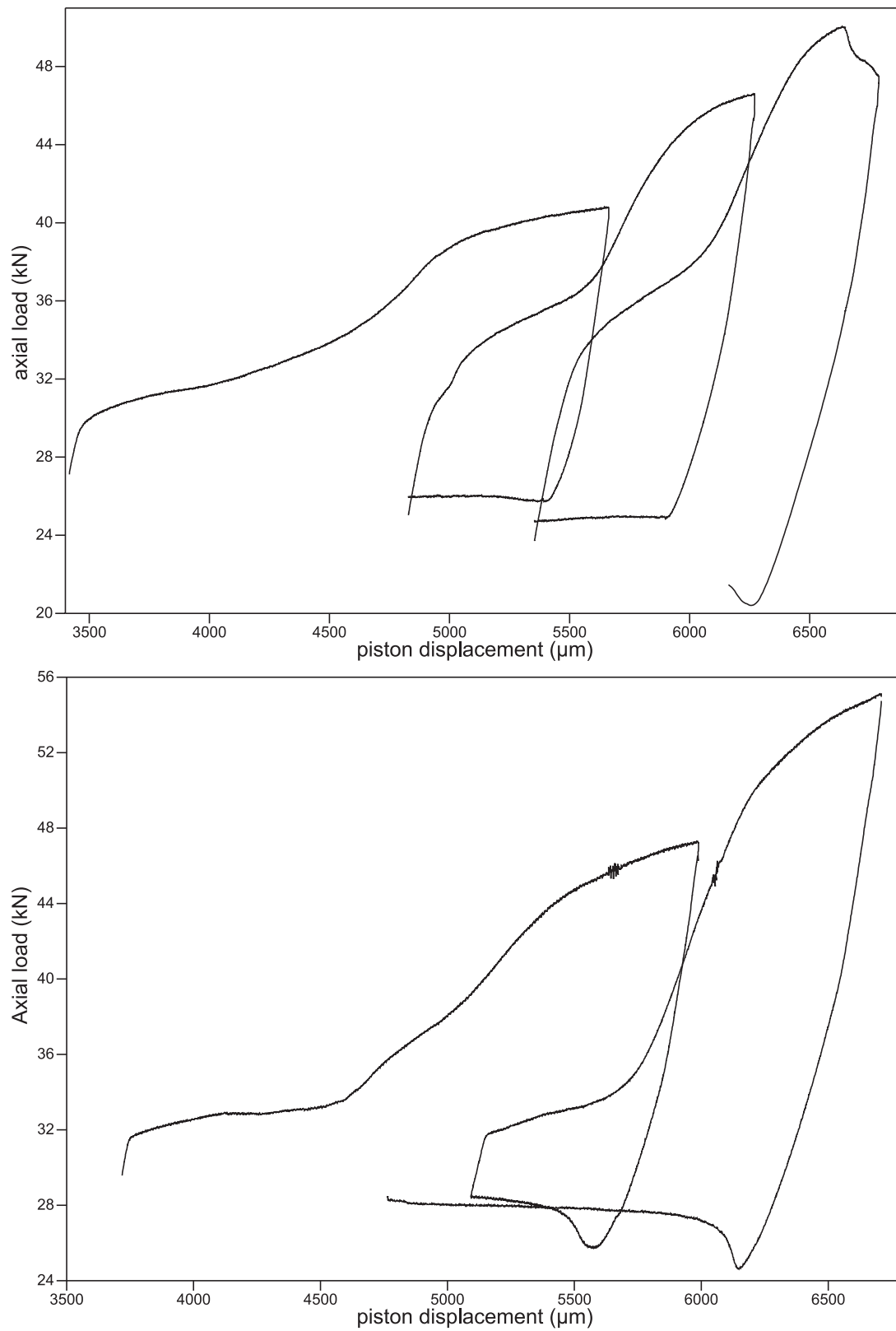


Figure 9: JD57.B (top): $T = 990^{\circ}\text{C}$, $v_p = 2.64 \cdot 10^{-4}\text{mm/s}$ and $T = 893^{\circ}\text{C}$, $v_p = 2.34 \cdot 10^{-4}\text{mm/s}$ and $T = 794^{\circ}\text{C}$, $v_p = 2.16 \cdot 10^{-4}\text{mm/s}$ and JC-2 (bottom): $T = 996^{\circ}\text{C}$, $v_p = 1.32 \cdot 10^{-4}\text{mm/s}$ and $T = 899^{\circ}\text{C}$, $v_p = 1.10 \cdot 10^{-4}\text{mm/s}$.

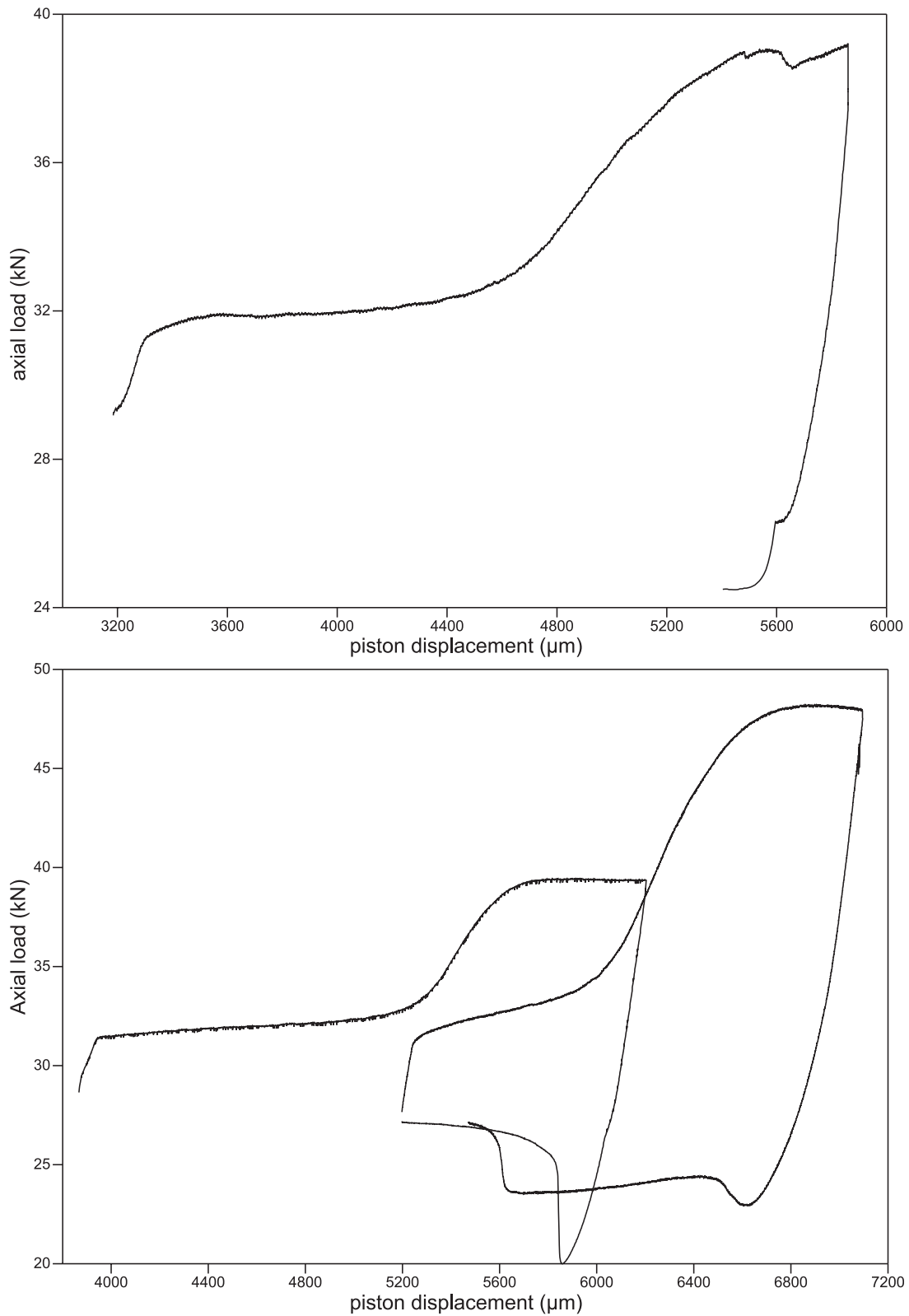


Figure 10: JC-3 (top): $T = 1000^{\circ}\text{C}$, $v_p = 1.32 \cdot 10^{-4}\text{mm/s}$ and JD57 .A (bottom): $T = 900^{\circ}\text{C}$, $v_p = 2.00 \cdot 10^{-5}\text{mm/s}$ and $T = 900^{\circ}\text{C}$, $v_p = 1.70 \cdot 10^{-4}\text{mm/s}$.

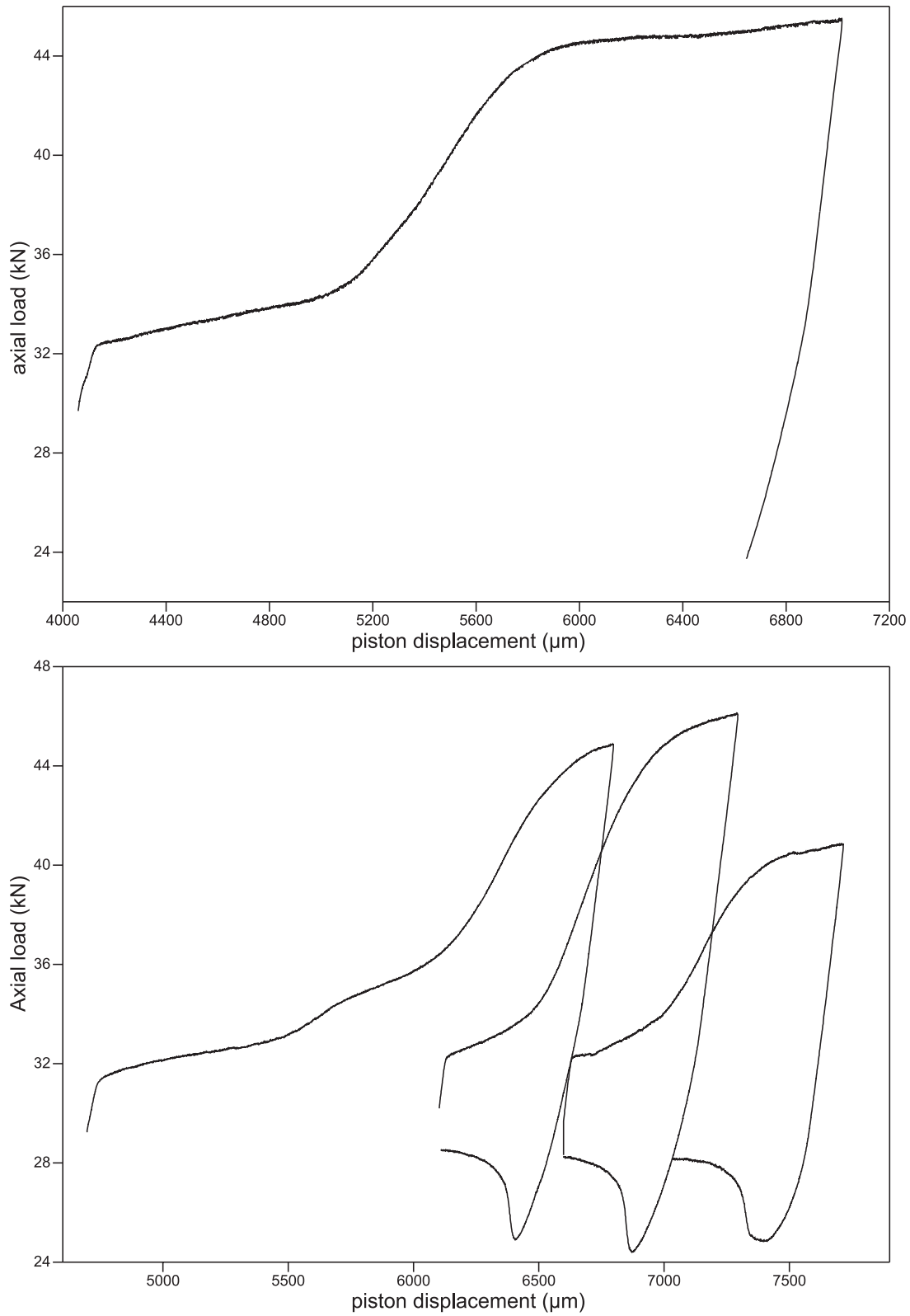


Figure 11: JD56.C (top): $T = 808^{\circ}\text{C}$, $v_p = 2.00 \cdot 10^{-5}\text{mm/s}$ and JD48.C (bottom): $T = 788^{\circ}\text{C}$, $v_p = 6.61 \cdot 10^{-5}\text{mm/s}$ and $T = 886^{\circ}\text{C}$, $v_p = 6.01 \cdot 10^{-5}\text{mm/s}$ and $T = 985^{\circ}\text{C}$, $v_p = 5.51 \cdot 10^{-5}\text{mm/s}$.

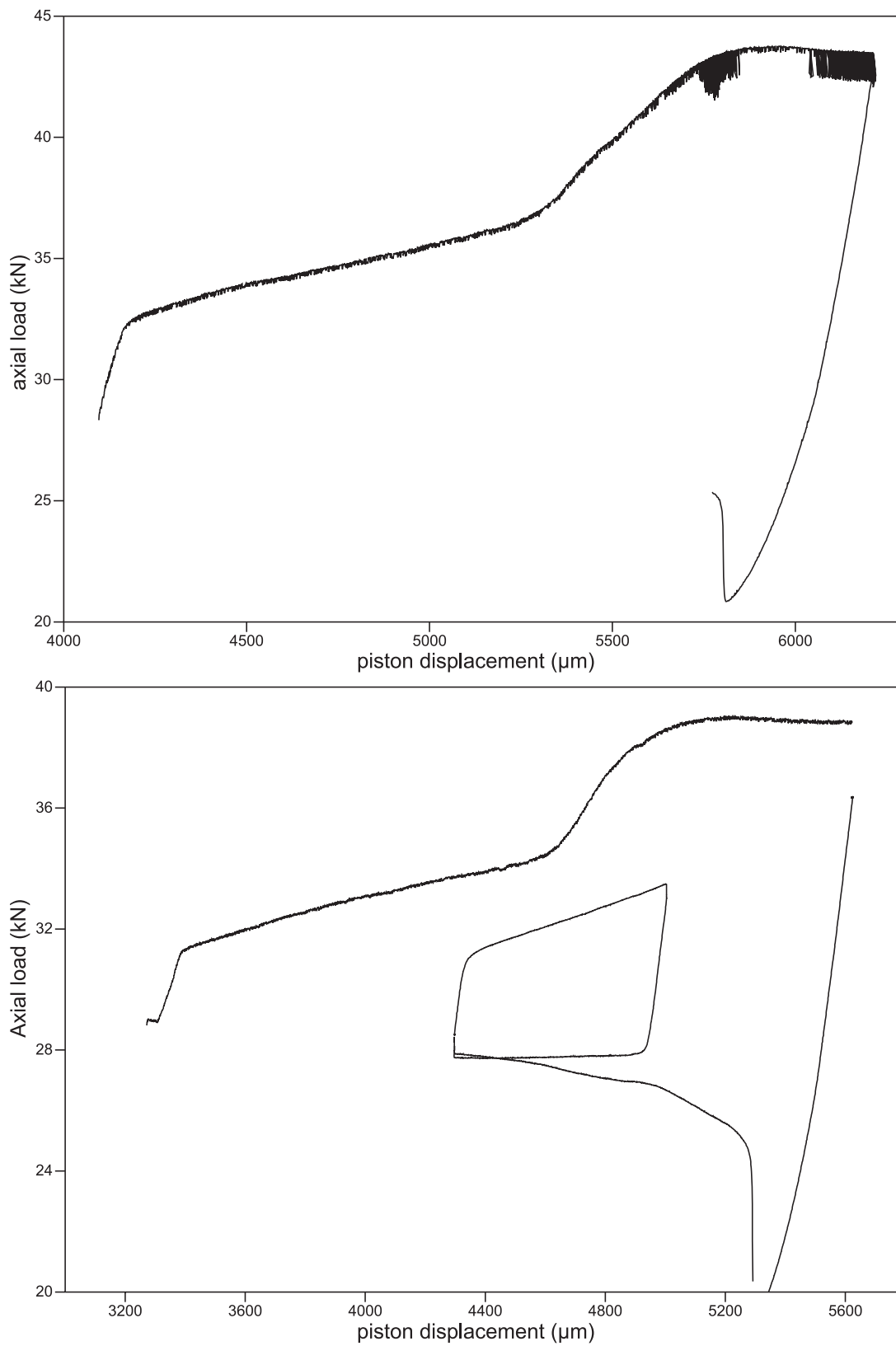


Figure 12: JD58.B (top): $T = 997^{\circ}\text{C}$, $v_p = 2.00 \cdot 10^{-5}\text{mm/s}$ and JD61.A (bottom): $T = 990^{\circ}\text{C}$, $v_p = 1.40 \cdot 10^{-5}\text{mm/s}$.

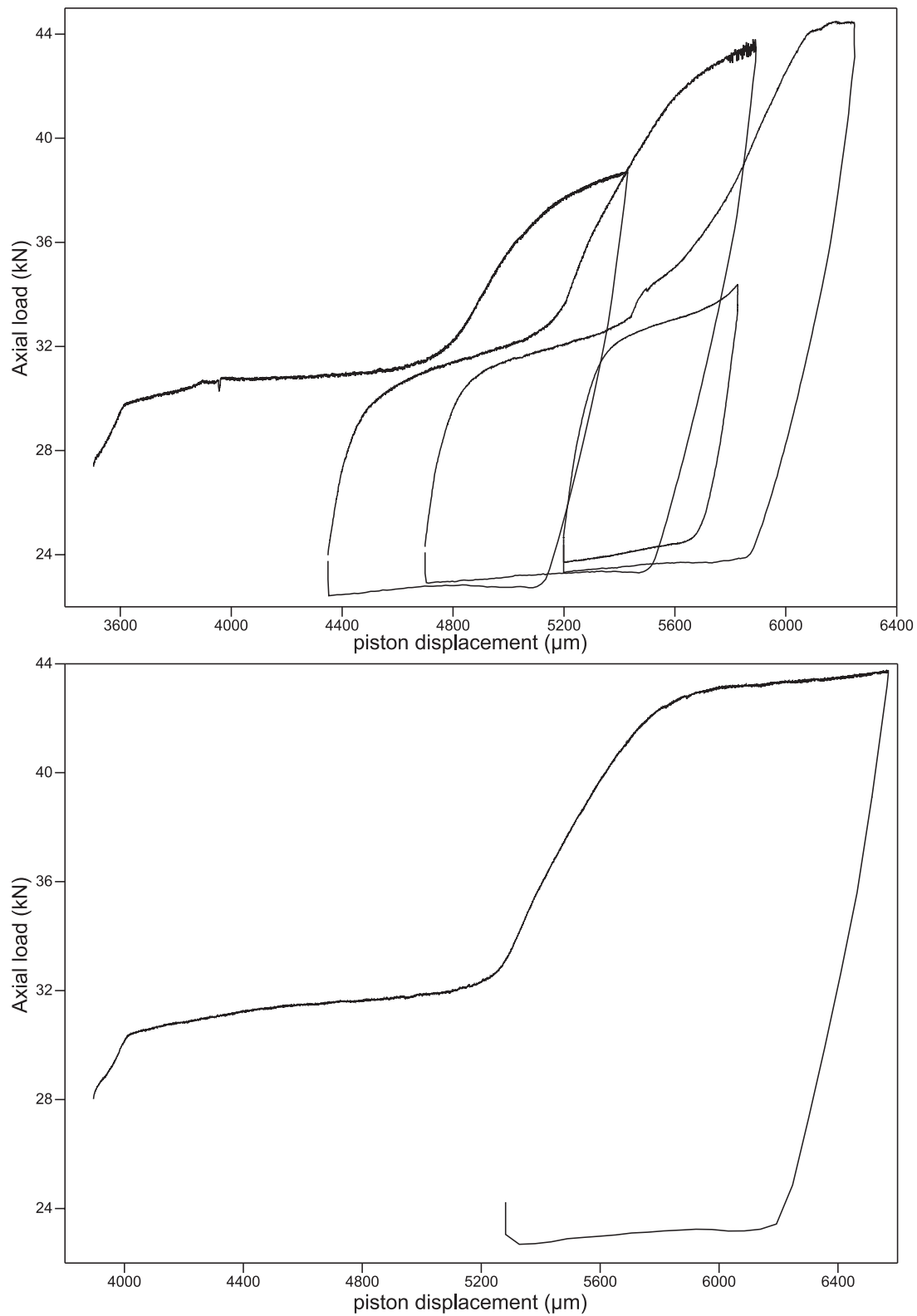


Figure 13: JD63.1 (top): $T = 995^\circ\text{C}$, $v_p = 3.31 \cdot 10^{-5}\text{mm/s}$ and $T = 993^\circ\text{C}$, $v_p = 1.20 \cdot 10^{-4}\text{mm/s}$ and $T = 993^\circ\text{C}$, $v_p = 4.33 \cdot 10^{-4}\text{mm/s}$ and FC3-1 (bottom): $T = 1000^\circ\text{C}$, $v_p = 3.31 \cdot 10^{-5}\text{mm/s}$.

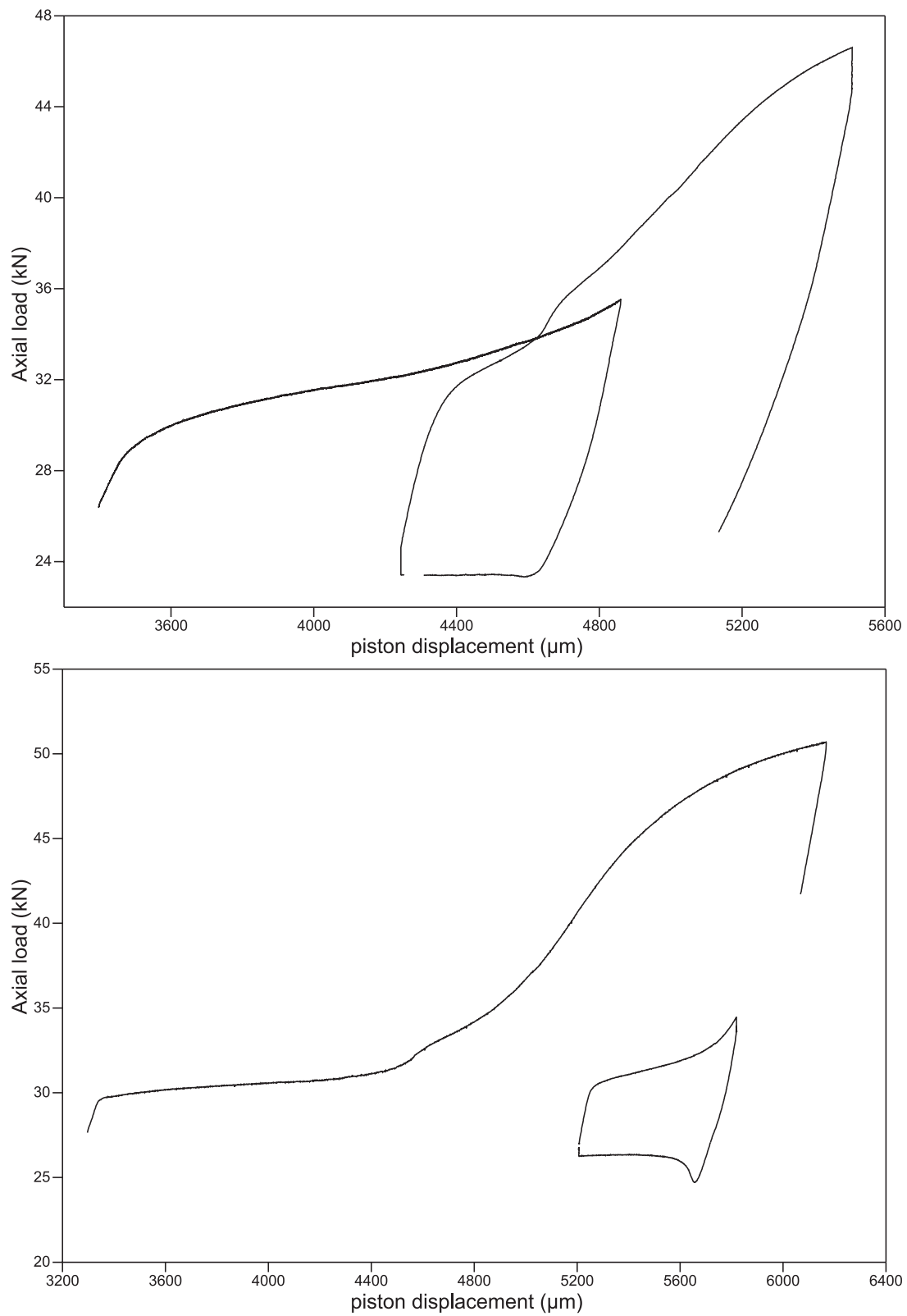


Figure 14: JD63.2 (top): $T = 975^{\circ}\text{C}$, $v_p = 2.92 \cdot 10^{-3} \text{mm/s}$ and FC3-2 (bottom): $T = 898^{\circ}\text{C}$, $v_p = 3.31 \cdot 10^{-5} \text{mm/s}$.

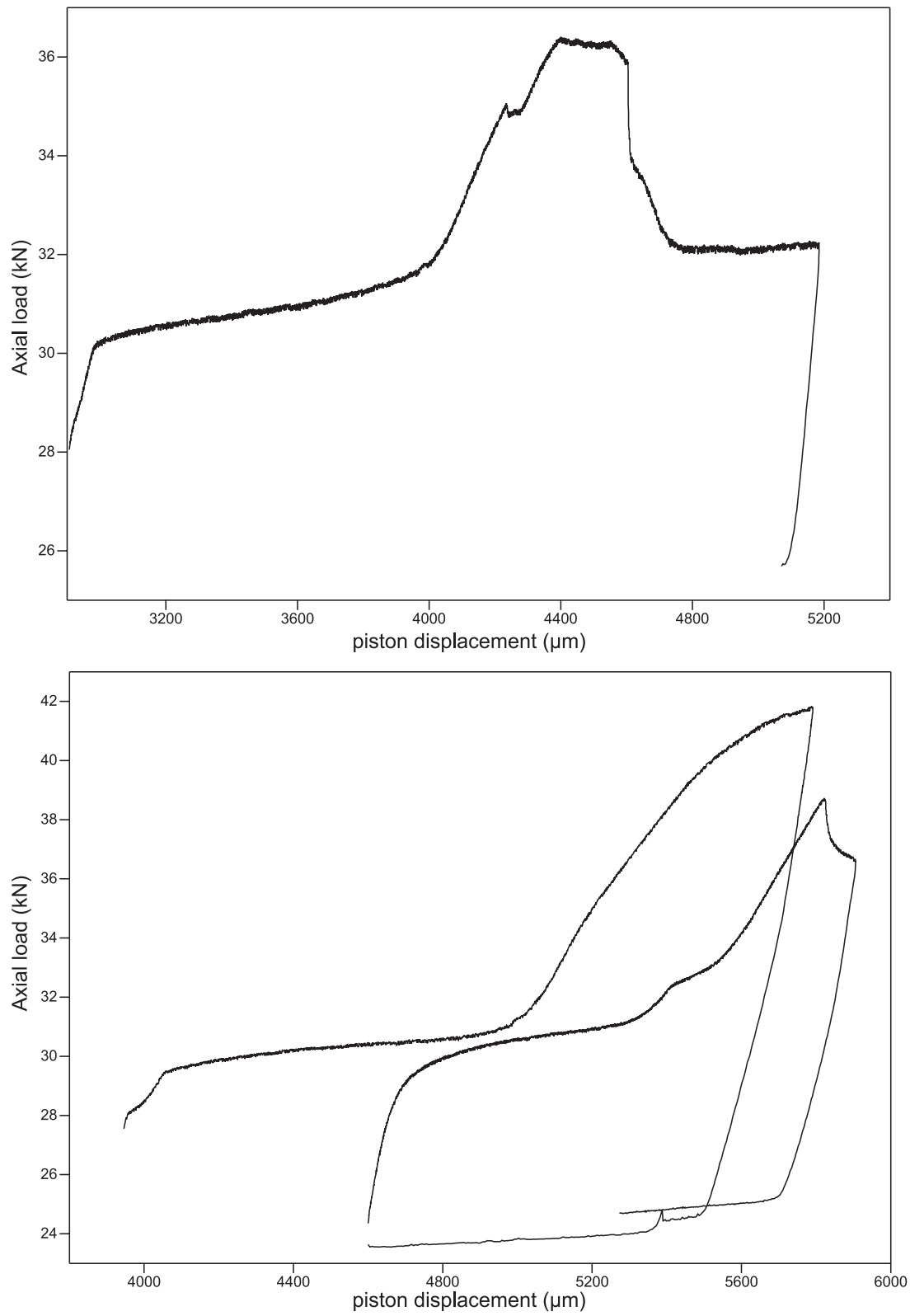


Figure 15: F3-4 (top): $T = 1111^{\circ}\text{C}$, $v_p = 3.31 \cdot 10^{-5} \text{mm/s}$ and FC3-5 (bottom): $T = 1000^{\circ}\text{C}$, $v_p = 3.31 \cdot 10^{-5} \text{mm/s}$.

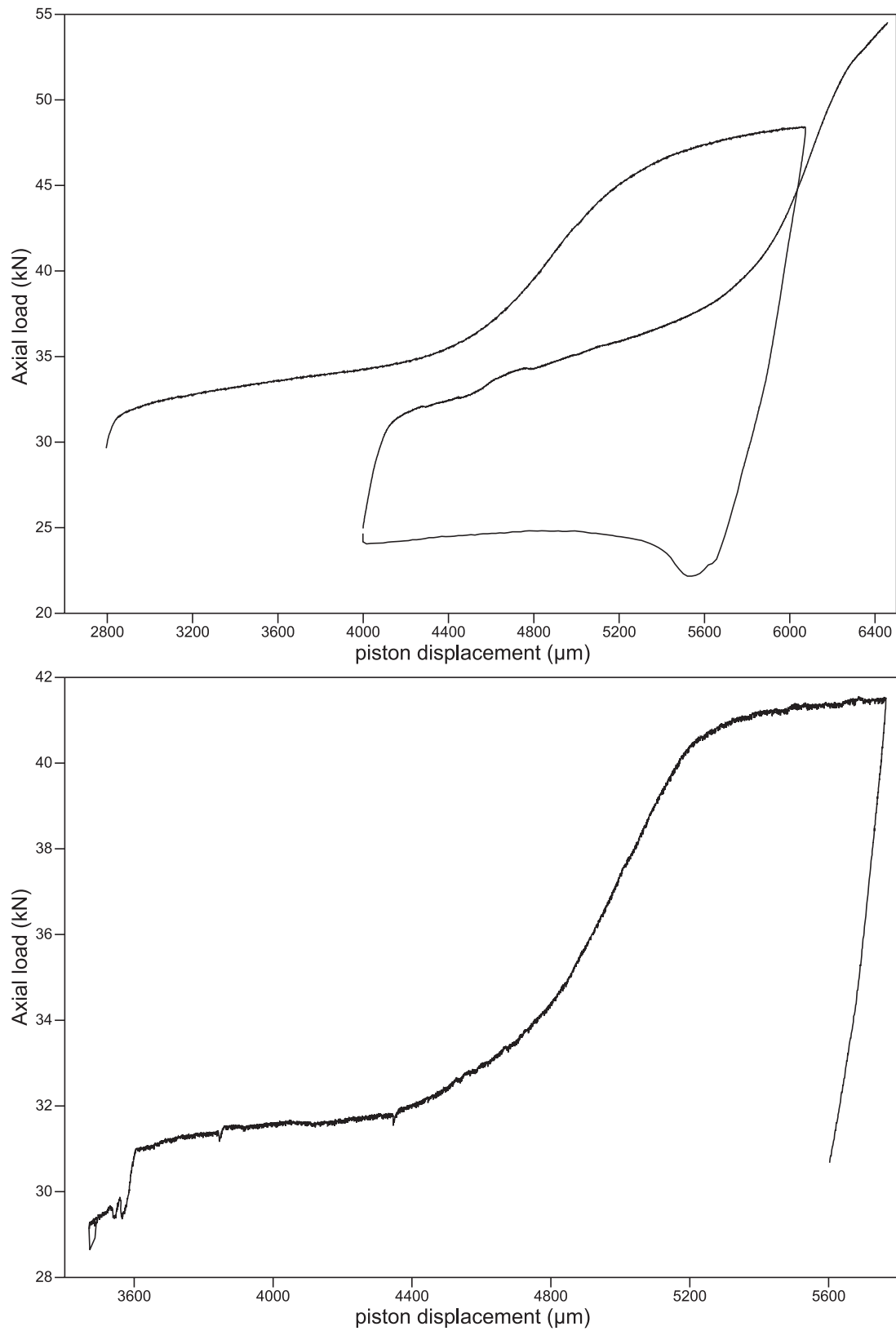


Figure 16: FC3-6 (top): $T = 988^{\circ}\text{C}$, $v_p = 6.51 \cdot 10^{-5} \text{mm/s}$ and $T = 986^{\circ}\text{C}$, $v_p = 2.76 \cdot 10^{-4} \text{mm/s}$ and FC3-7 (bottom): $T = 990^{\circ}\text{C}$, $v_p = 1.30 \cdot 10^{-5} \text{mm/s}$.

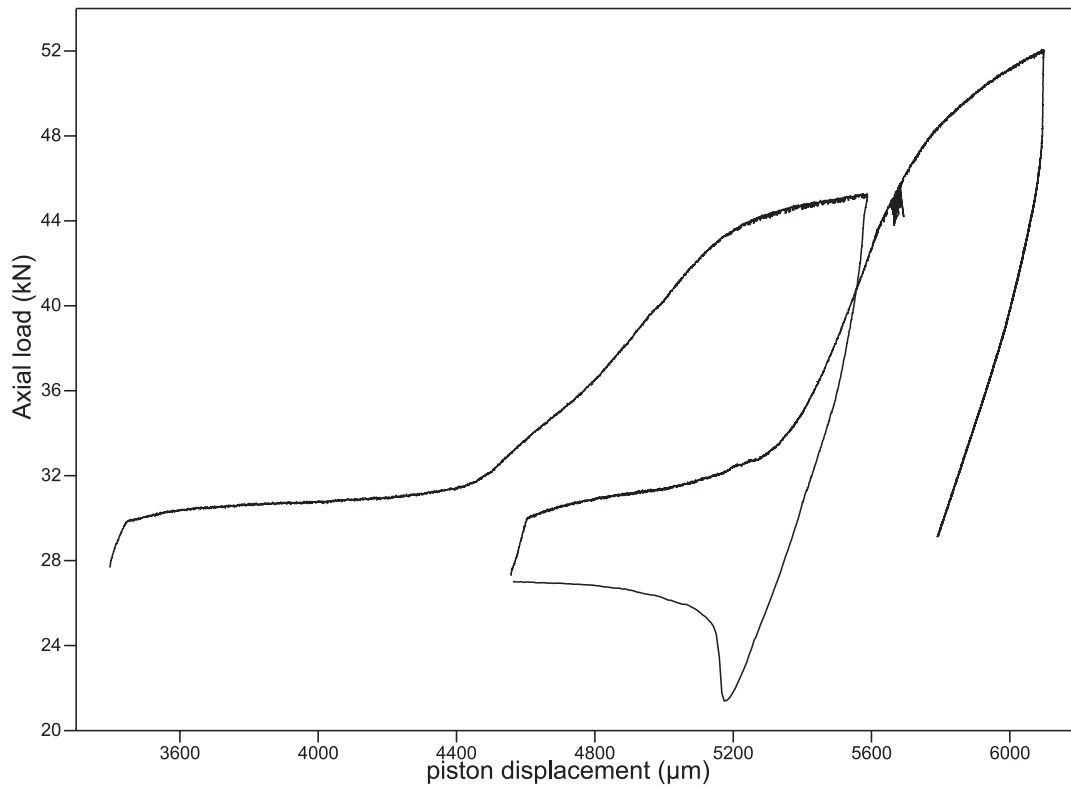
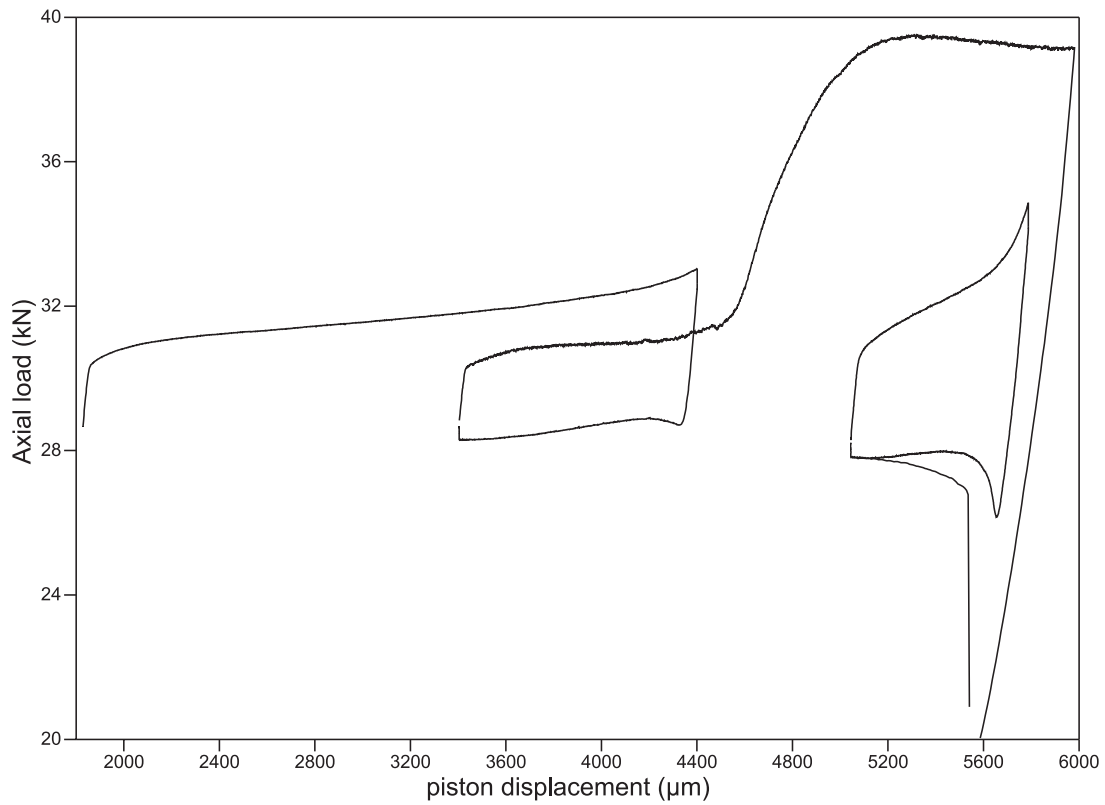


Figure 17: JD61.C (top): $T = 883^{\circ}\text{C}$, $v_p = 1.40 \cdot 10^{-5} \text{mm/s}$ and FC3-8 (bottom): $T = 895^{\circ}\text{C}$, $v_p = 1.30 \cdot 10^{-5} \text{mm/s}$ and $T = 845^{\circ}\text{C}$, $v_p = 1.20 \cdot 10^{-5} \text{mm/s}$.

C Stress versus strain curves

The stress vs. strain curves are displayed in this Appendix. The differential stress is given in MPa, the strain in %. T denotes the average temperature obtained from the thermocouple readings, $\dot{\varepsilon}$ gives the strain-rate. For step test, all cycles are displayed together and the corresponding conditions are given in the order the cycles were performed.

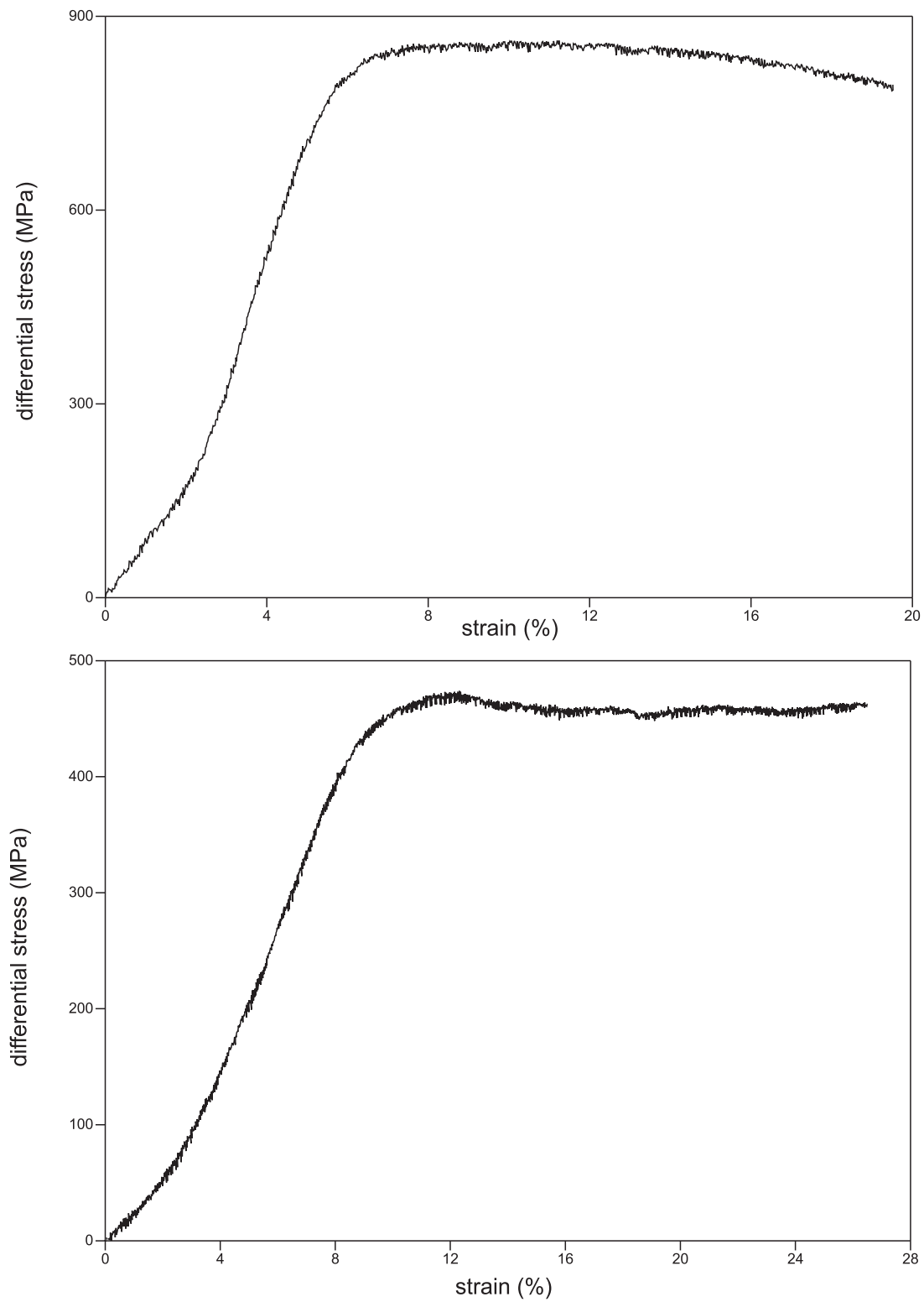


Figure 18: JD43.1 (top): $T = 891^{\circ}\text{C}$, $\dot{\epsilon} = 2 \cdot 10^{-5}\text{s}^{-1}$ and JD44.C (bottom): $T = 973^{\circ}\text{C}$, $\dot{\epsilon} = 2 \cdot 10^{-5}\text{s}^{-1}$.

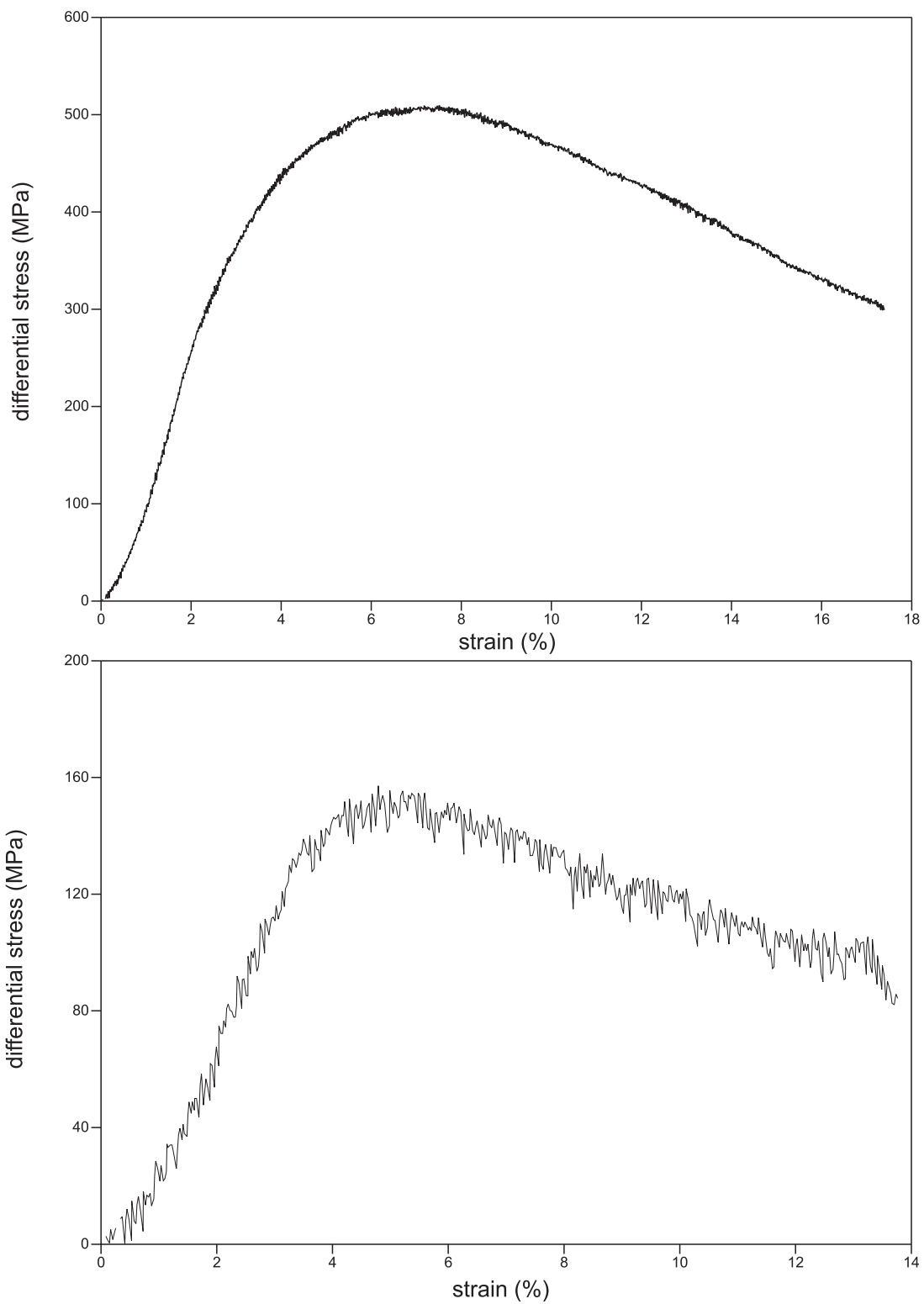


Figure 19: JD44.B (top): $T = 998^{\circ}\text{C}$, $\dot{\epsilon} = 2 \cdot 10^{-5}\text{s}^{-1}$ and JD43.2 (bottom): $T = 921^{\circ}\text{C}$, $\dot{\epsilon} = 2 \cdot 10^{-5}\text{s}^{-1}$.

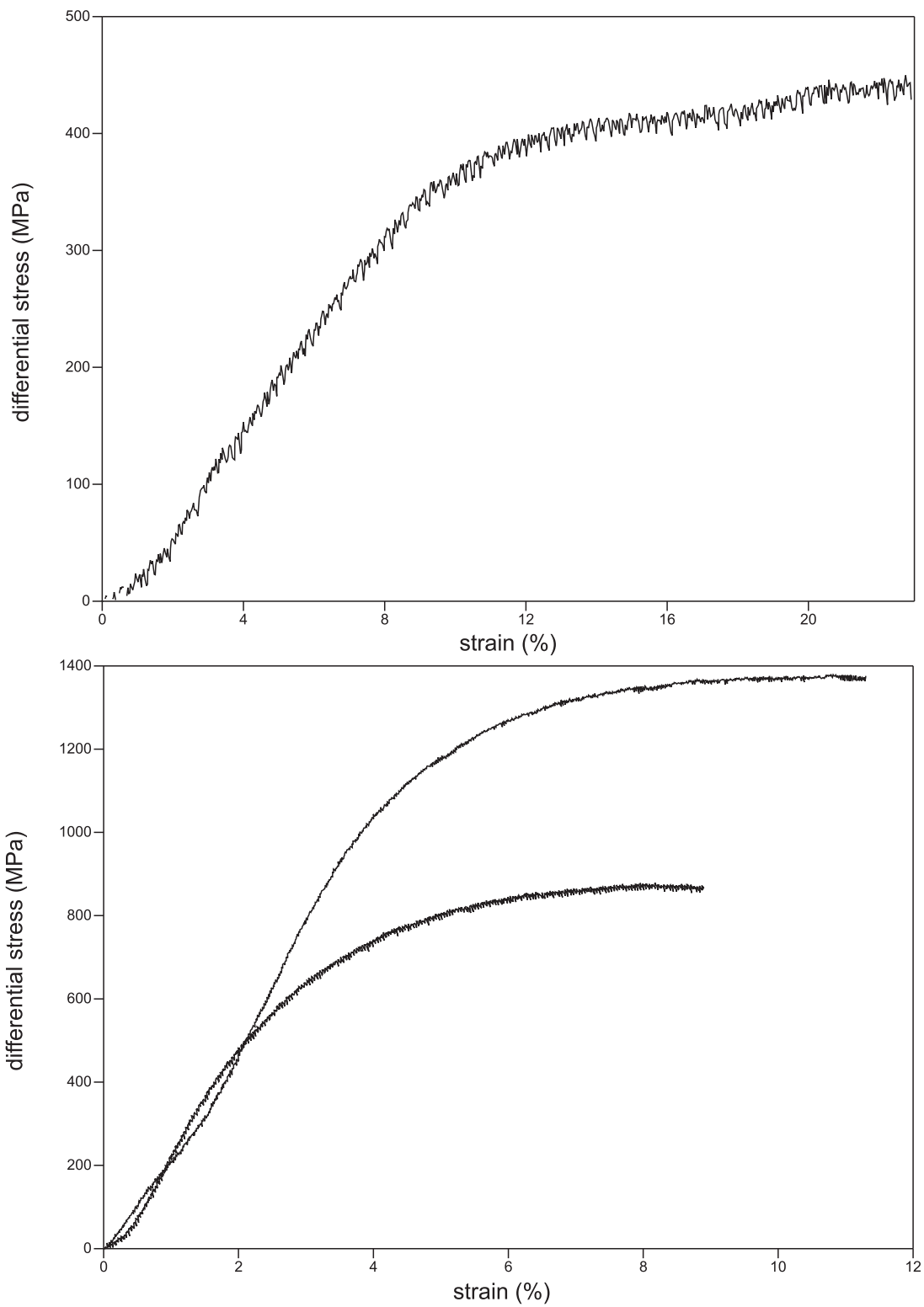


Figure 20: JD38.A (top): $T = 992^{\circ}\text{C}$, $\dot{\epsilon} = 2 \cdot 10^{-5}\text{s}^{-1}$ and
JD45.B (bottom): $T = 882^{\circ}\text{C}$, $\dot{\epsilon} = 2 \cdot 10^{-5}\text{s}^{-1}$ and $T = 880^{\circ}\text{C}$, $\dot{\epsilon} = 5 \cdot 10^{-6}\text{s}^{-1}$.

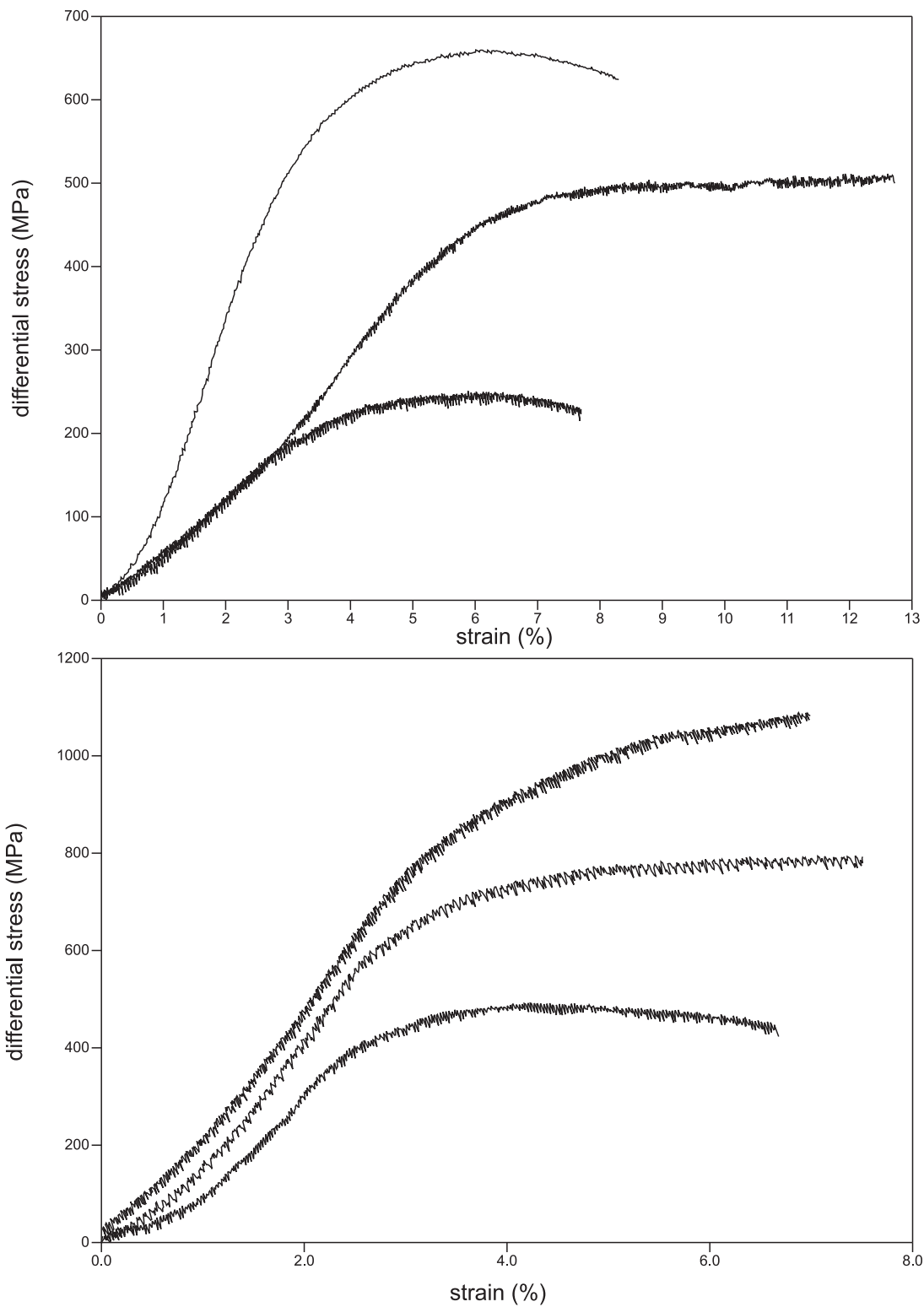


Figure 21: JD46.C (top): $T = 973^{\circ}\text{C}$, $\dot{\epsilon} = 2 \cdot 10^{-5} \text{s}^{-1}$ and $\dot{\epsilon} = 5 \cdot 10^{-6} \text{s}^{-1}$ and $\dot{\epsilon} = 8 \cdot 10^{-5} \text{s}^{-1}$ and JD46.B (bottom): $\dot{\epsilon} = 1 \cdot 10^{-5} \text{s}^{-1}$, $T = 991^{\circ}\text{C}$ and $T = 891^{\circ}\text{C}$ and $T = 794^{\circ}\text{C}$.

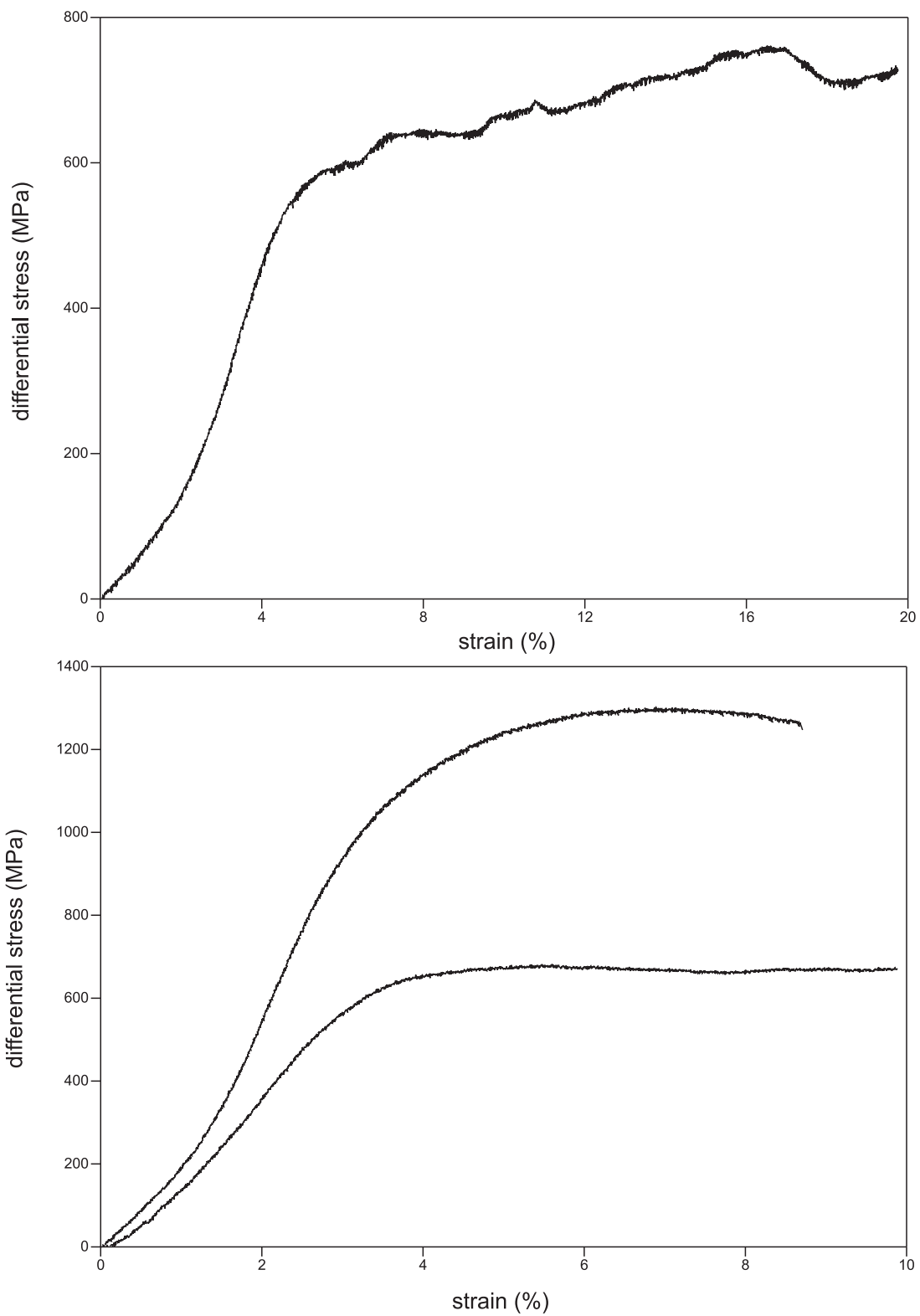


Figure 22: JD49.B (top): $T = 897^{\circ}\text{C}$, $\dot{\epsilon} = 5 \cdot 10^{-6}\text{s}^{-1}$ and
JD48.A (bottom): $T = 985^{\circ}\text{C}$, $\dot{\epsilon} = 2 \cdot 10^{-5}\text{s}^{-1}$ and $T = 885^{\circ}\text{C}$, $\dot{\epsilon} = 2 \cdot 10^{-5}\text{s}^{-1}$.

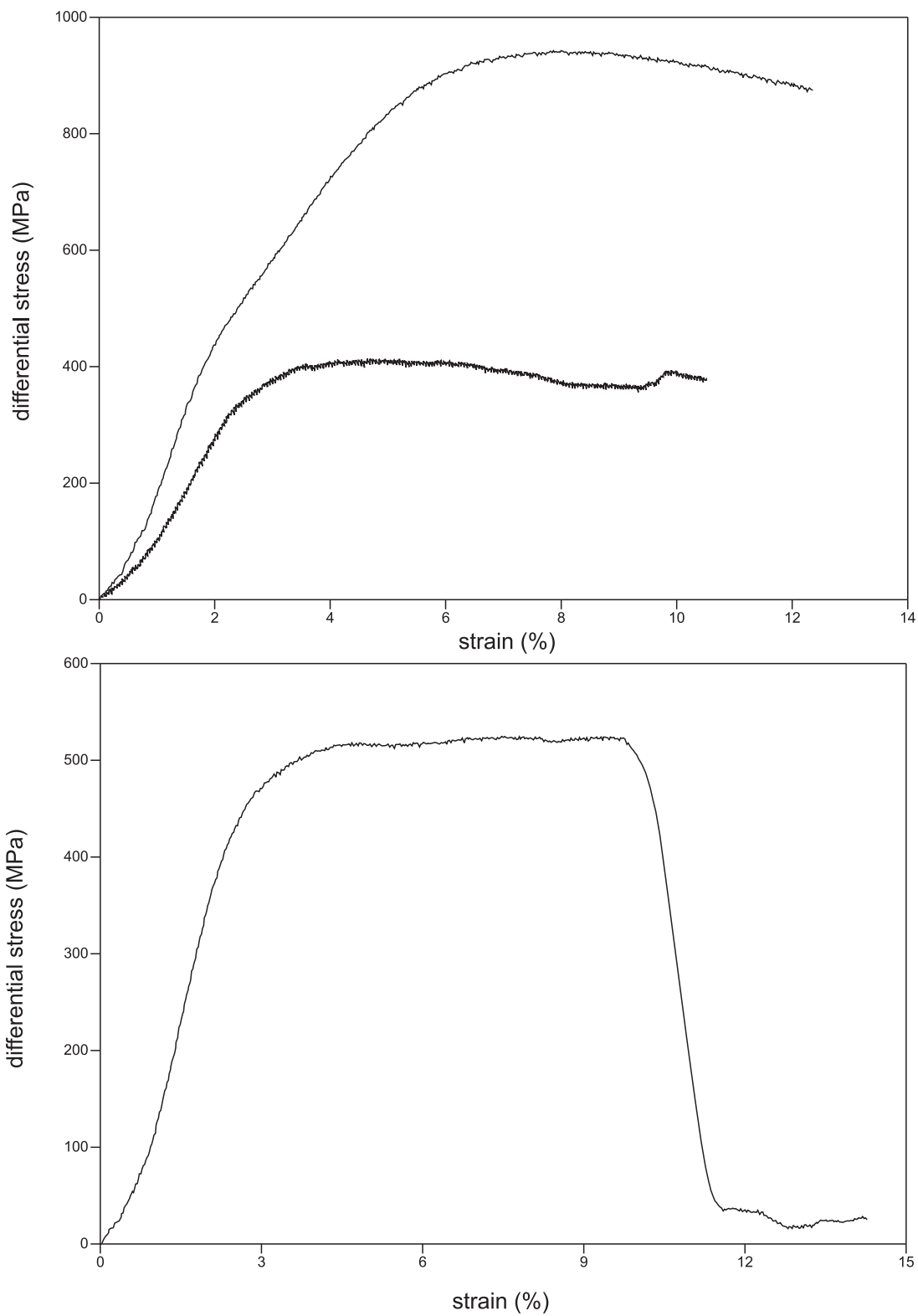


Figure 23: JD53.B (top): $T = 992^\circ C$, $\dot{\epsilon} = 2 \cdot 10^{-4} s^{-1}$ and $\dot{\epsilon} = 5 \cdot 10^{-6} s^{-1}$ and JD53.A (bottom): $T = 1096^\circ C$, $\dot{\epsilon} = 9 \cdot 10^{-5} s^{-1}$.

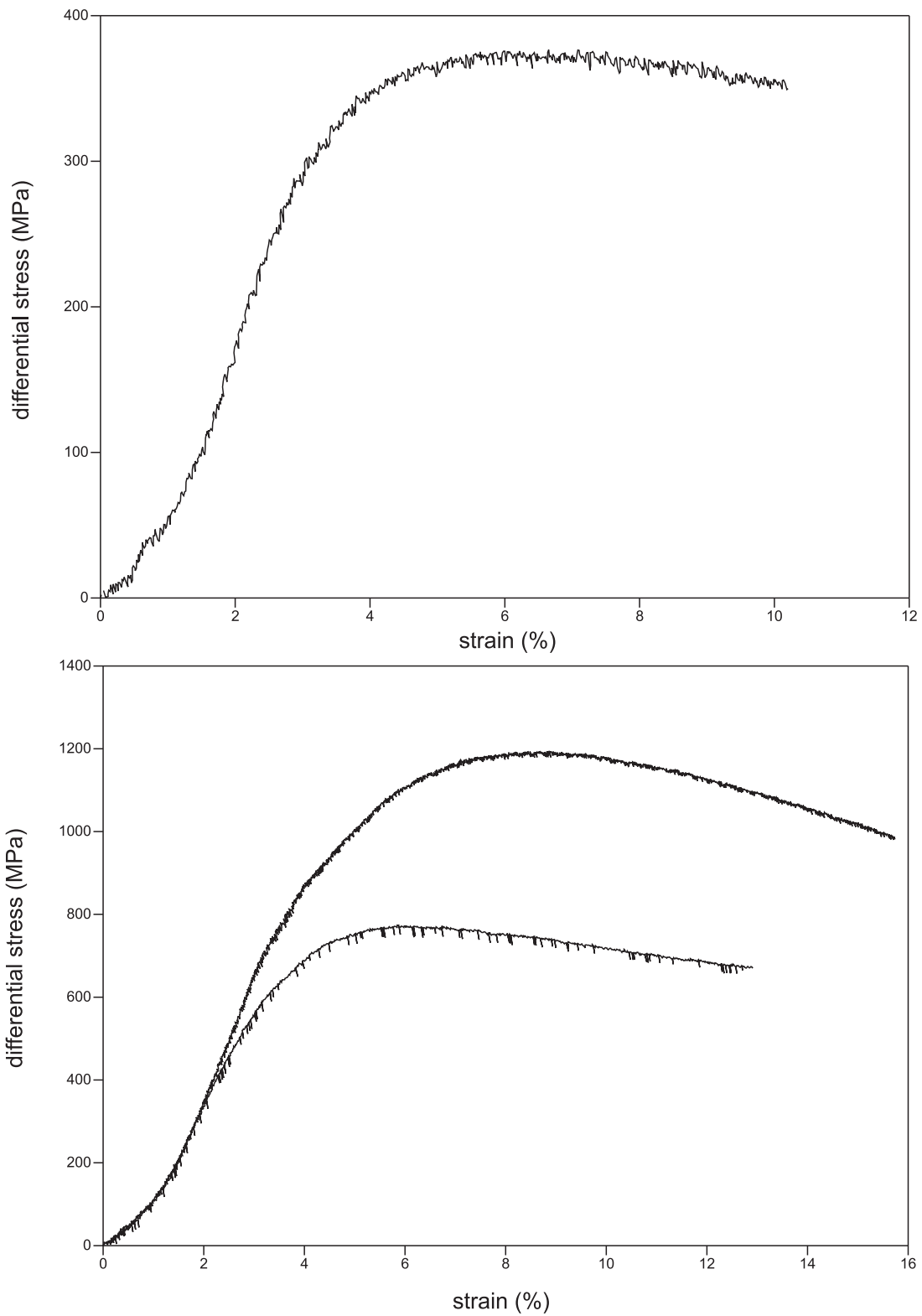


Figure 24: JD56.B (top): $T = 1024^{\circ}\text{C}$, $\dot{\epsilon} = 4 \cdot 10^{-4}\text{s}^{-1}$ and
JD57.A (bottom): $T = 900^{\circ}\text{C}$, $\dot{\epsilon} = 3 \cdot 10^{-6}\text{s}^{-1}$ and $\dot{\epsilon} = 3 \cdot 10^{-5}\text{s}^{-1}$.

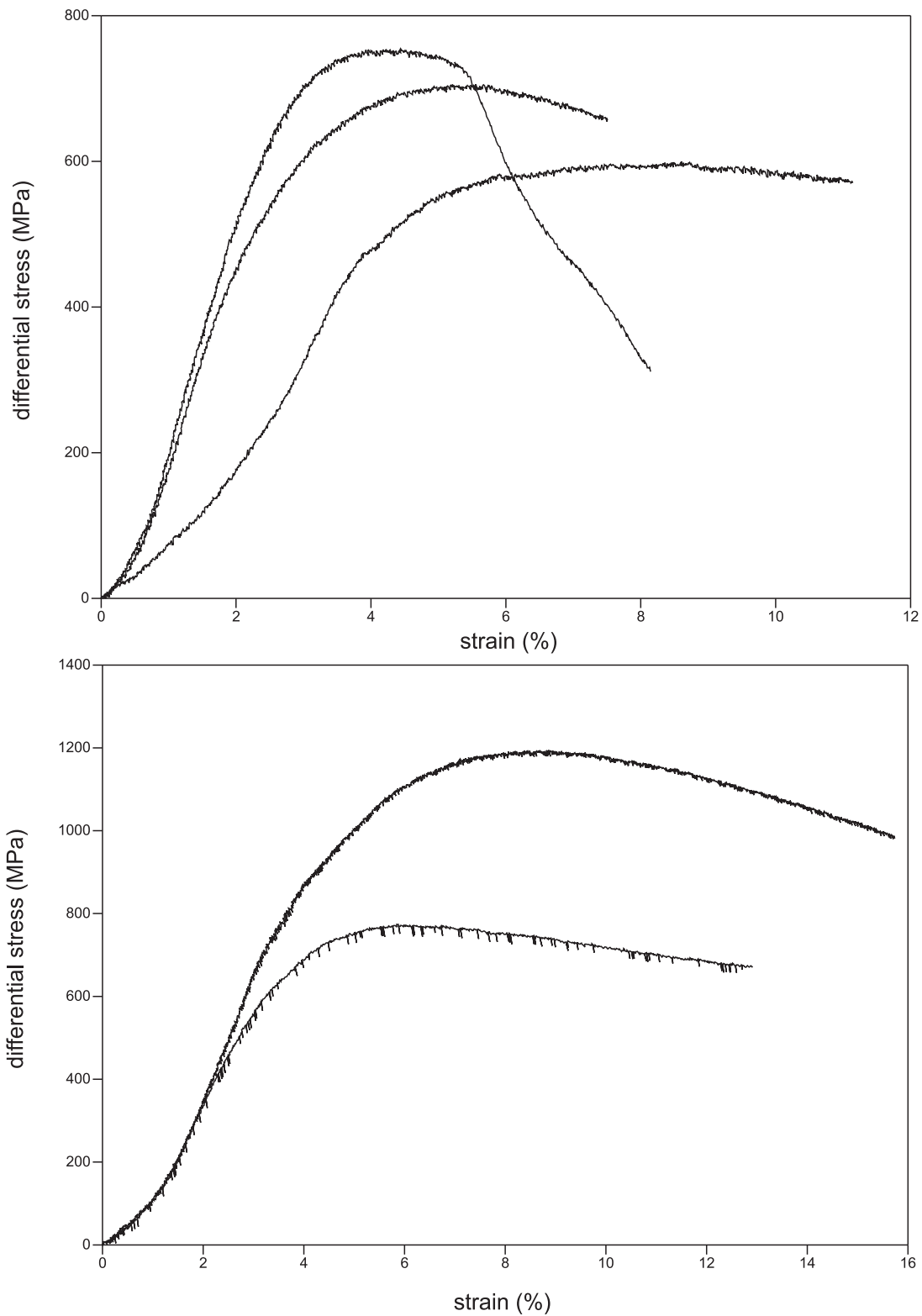


Figure 25: JD57.B (top): $T = 990^{\circ}\text{C}$, $\dot{\epsilon} = 4 \cdot 10^{-5}\text{s}^{-1}$ and $T = 893^{\circ}\text{C}$, $\dot{\epsilon} = 4 \cdot 10^{-5}\text{s}^{-1}$ and $T = 794^{\circ}\text{C}$, $\dot{\epsilon} = 4 \cdot 10^{-5}\text{s}^{-1}$ and JD57.A (bottom): $T = 990^{\circ}\text{C}$, $\dot{\epsilon} = 3 \cdot 10^{-6}\text{s}^{-1}$ and $\dot{\epsilon} = 3 \cdot 10^{-5}\text{s}^{-1}$.

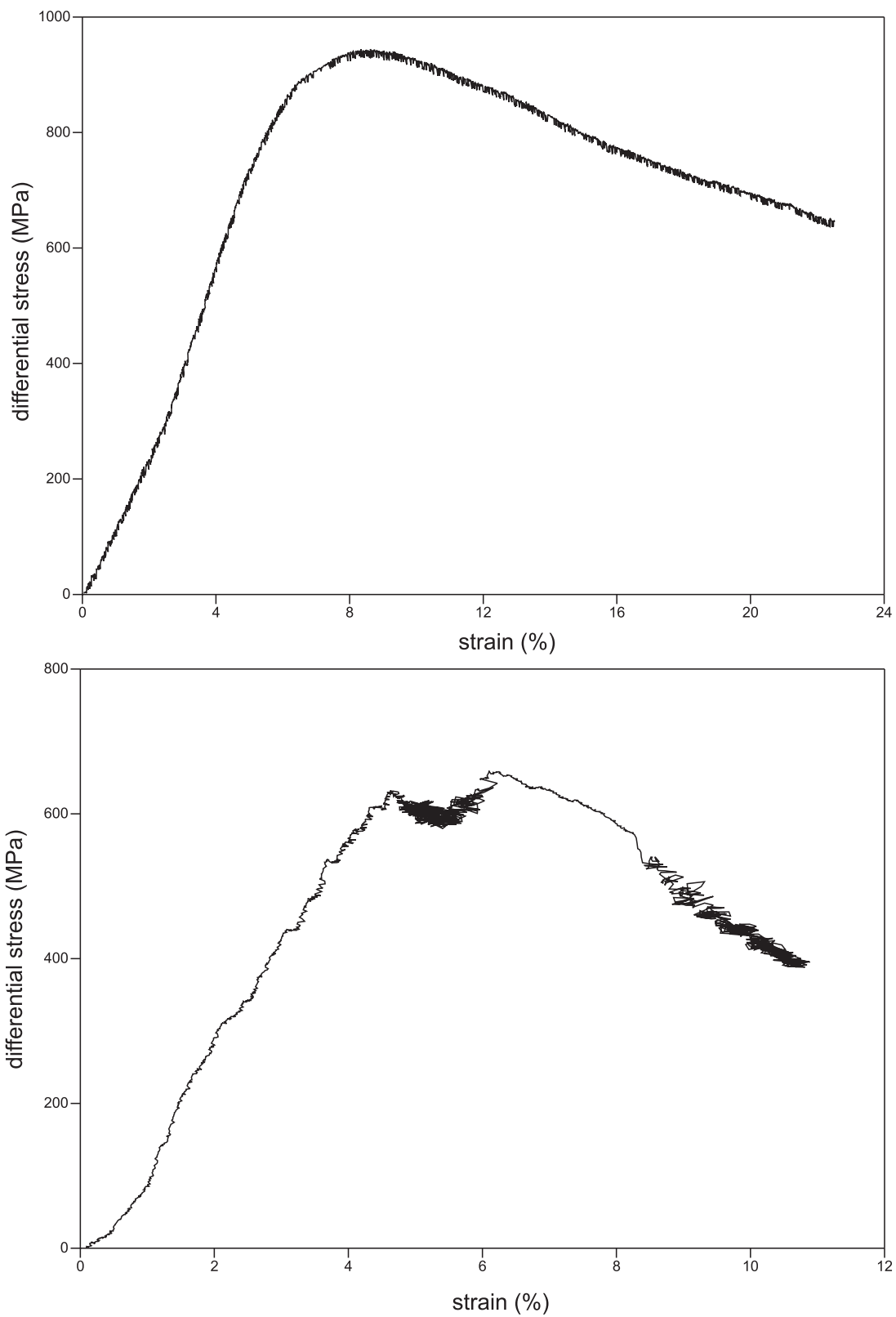


Figure 26: JD56.C (top): $T = 808^{\circ}\text{C}$, $\dot{\epsilon} = 3 \cdot 10^{-6}\text{s}^{-1}$ and JD58.B (bottom): $T = 997^{\circ}\text{C}$, $\dot{\epsilon} = 3 \cdot 10^{-6}\text{s}^{-1}$.

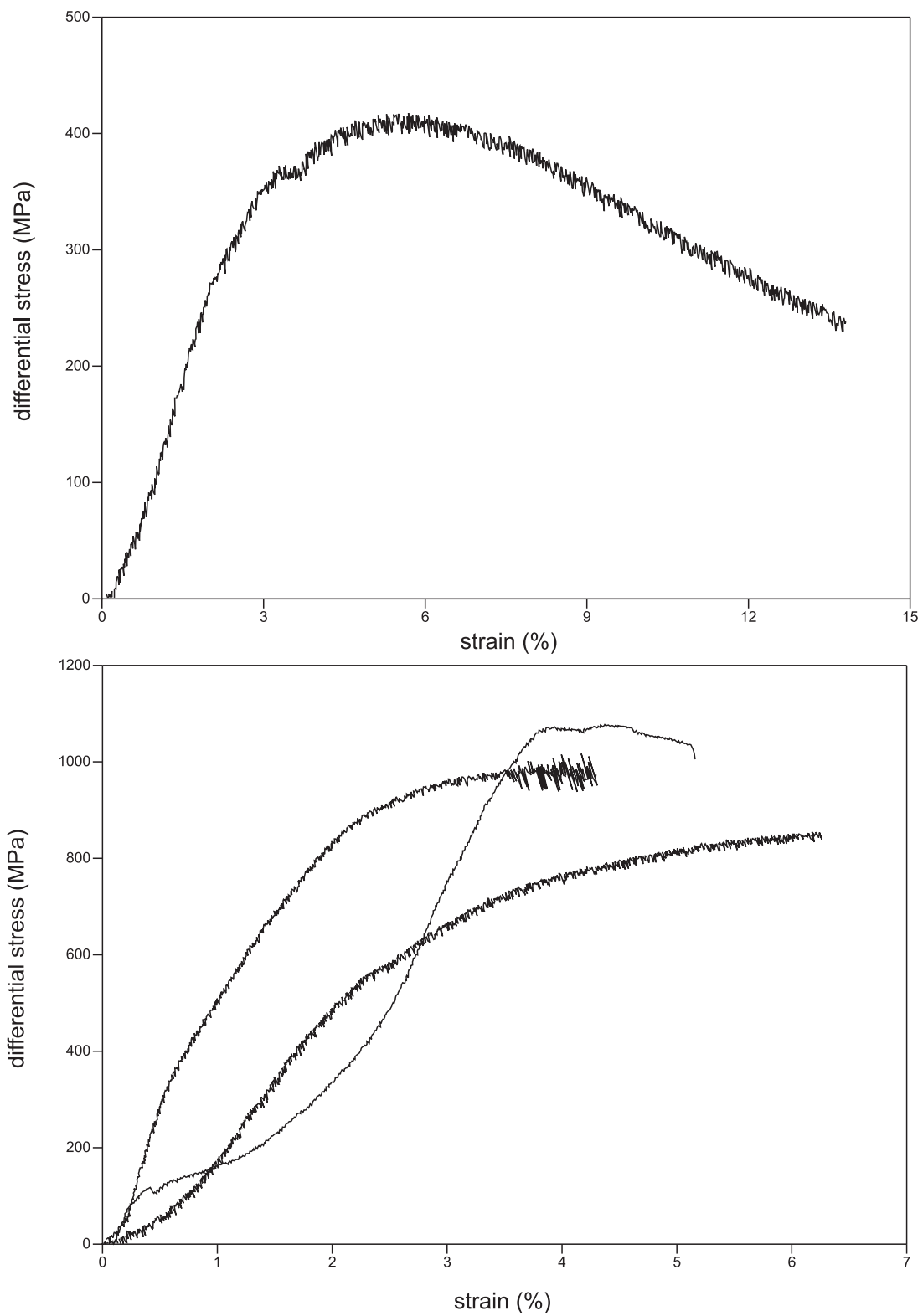


Figure 27: JD61.A (top): $T = 990^{\circ}\text{C}$, $\dot{\epsilon} = 2 \cdot 10^{-6}\text{s}^{-1}$ and JD63.1 (bottom): $T = 995^{\circ}\text{C}$, $\dot{\epsilon} = 5 \cdot 10^{-6}\text{s}^{-1}$ and $T = 993^{\circ}\text{C}$, $\dot{\epsilon} = 2 \cdot 10^{-5}\text{s}^{-1}$ and $T = 993^{\circ}\text{C}$, $\dot{\epsilon} = 8 \cdot 10^{-5}\text{s}^{-1}$.

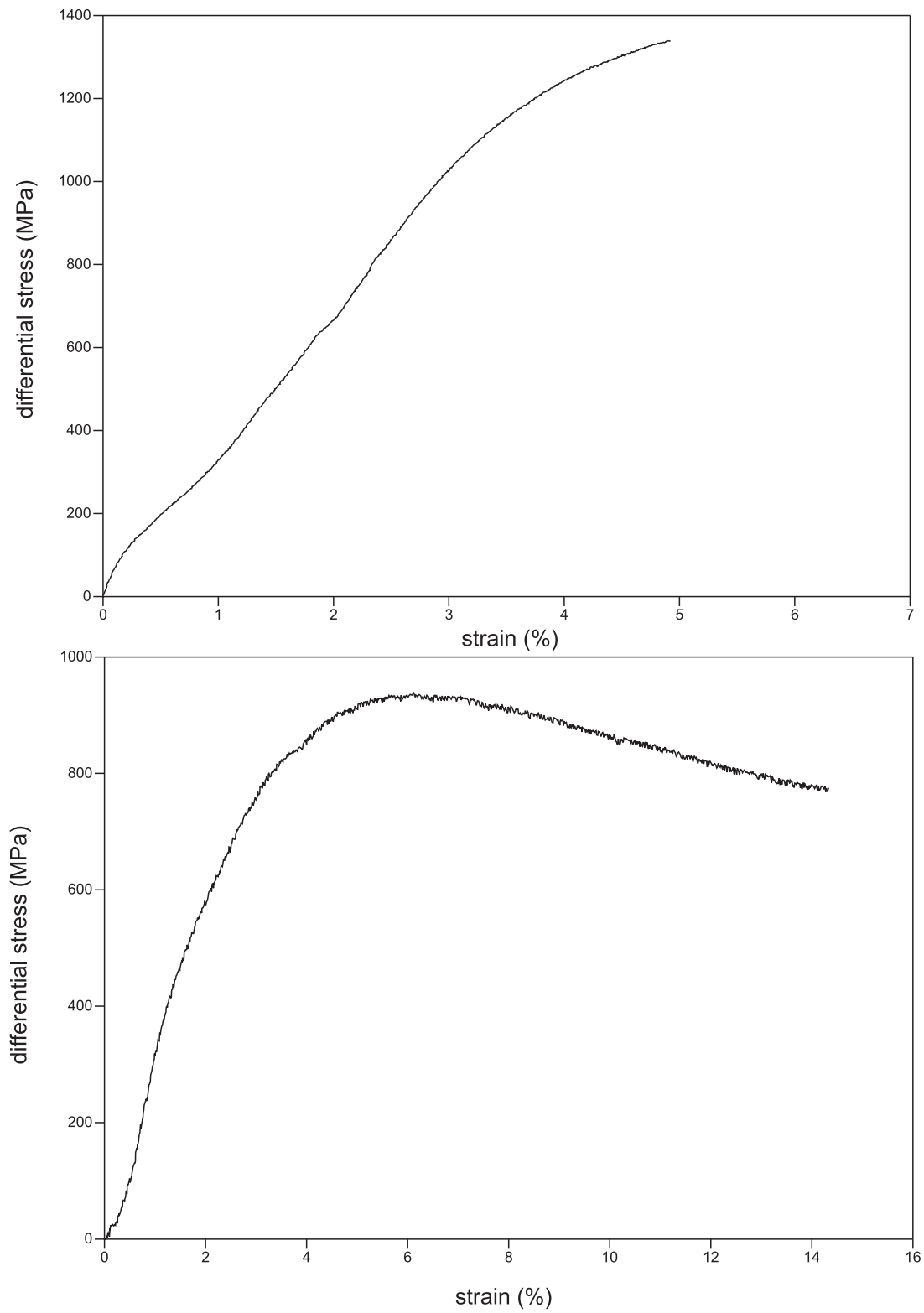


Figure 28: JD63.2 (top): $T = 975^{\circ}\text{C}$, $\dot{\epsilon} = 4 \cdot 10^{-4}\text{s}^{-1}$ and JD61.C $T = 883^{\circ}\text{C}$, $\dot{\epsilon} = 2 \cdot 10^{-6}\text{s}^{-1}$.

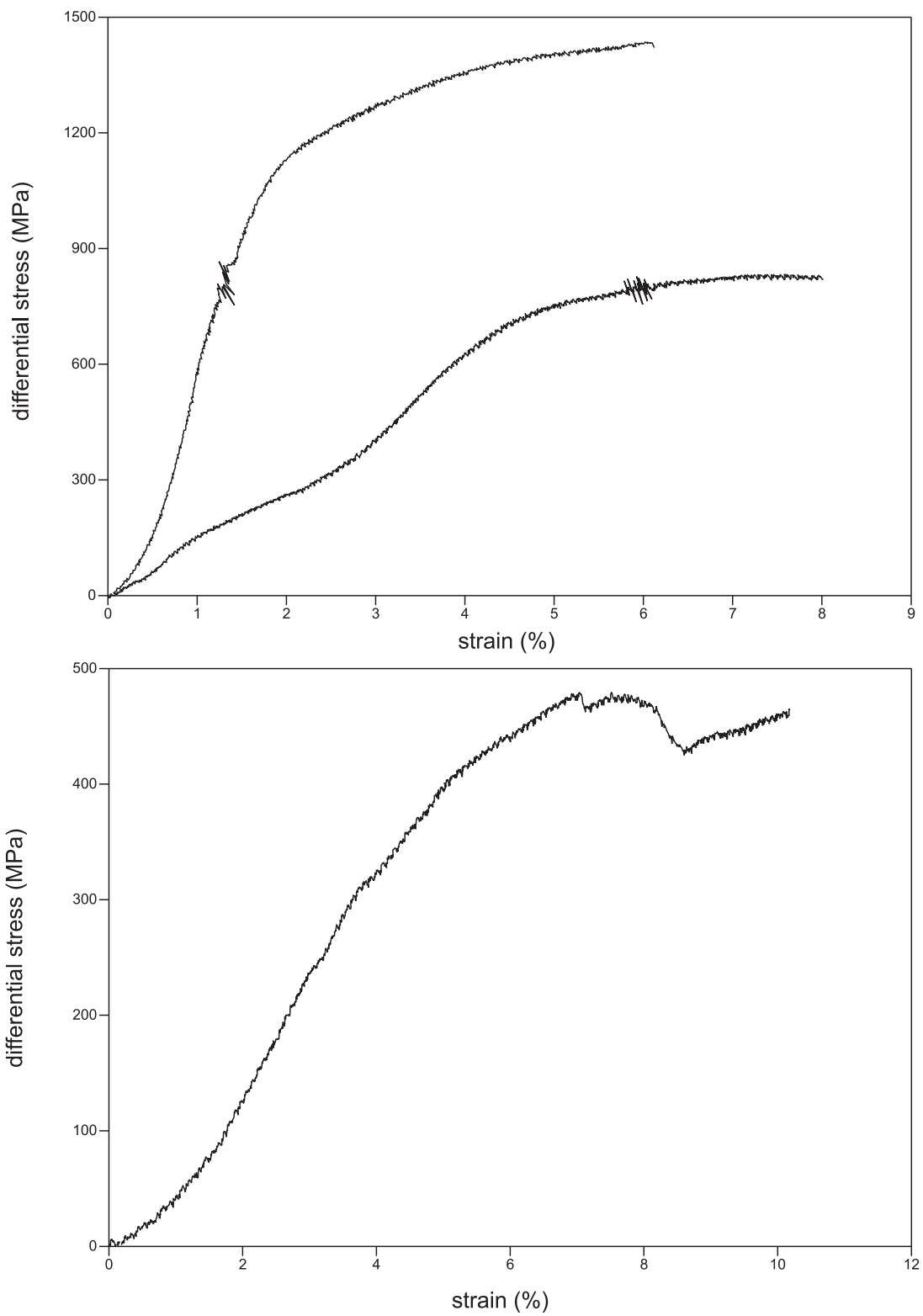


Figure 29: JC-2 (top): $T = 996^{\circ}\text{C}$, $\dot{\epsilon} = 2 \cdot 10^{-5}\text{s}^{-1}$ and $T = 899^{\circ}\text{C}$, $\dot{\epsilon} = 2 \cdot 10^{-5}\text{s}^{-1}$ and JC3-3 (bottom): $T = 1000^{\circ}\text{C}$, $\dot{\epsilon} = 2 \cdot 10^{-5}\text{s}^{-1}$.

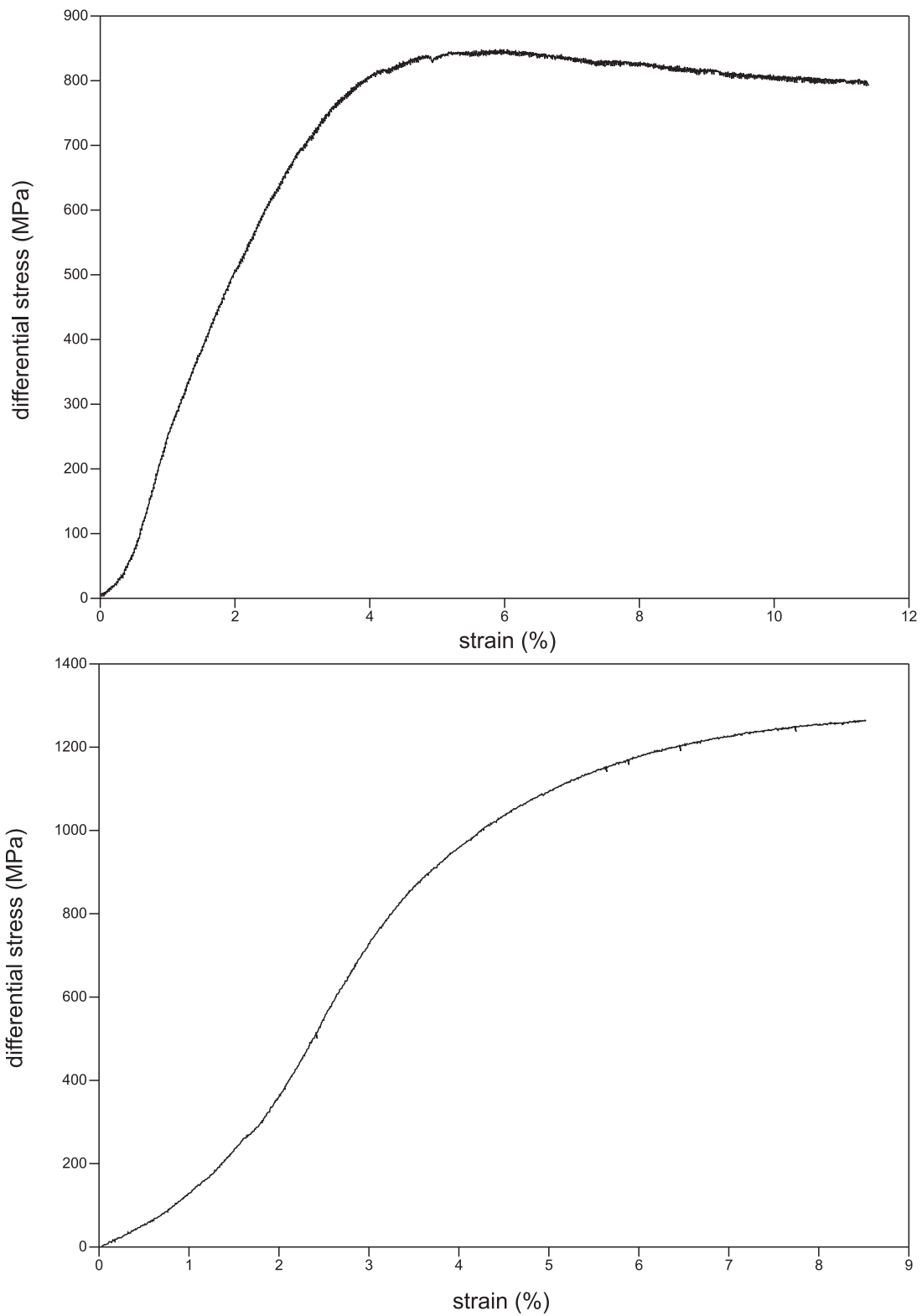


Figure 30: FC3-1 (top): $T = 1000^{\circ}\text{C}$, $\dot{\epsilon} = 5 \cdot 10^{-6}\text{s}^{-1}$ and FC3-2 (bottom): $T = 898^{\circ}\text{C}$, $\dot{\epsilon} = 5 \cdot 10^{-6}\text{s}^{-1}$.

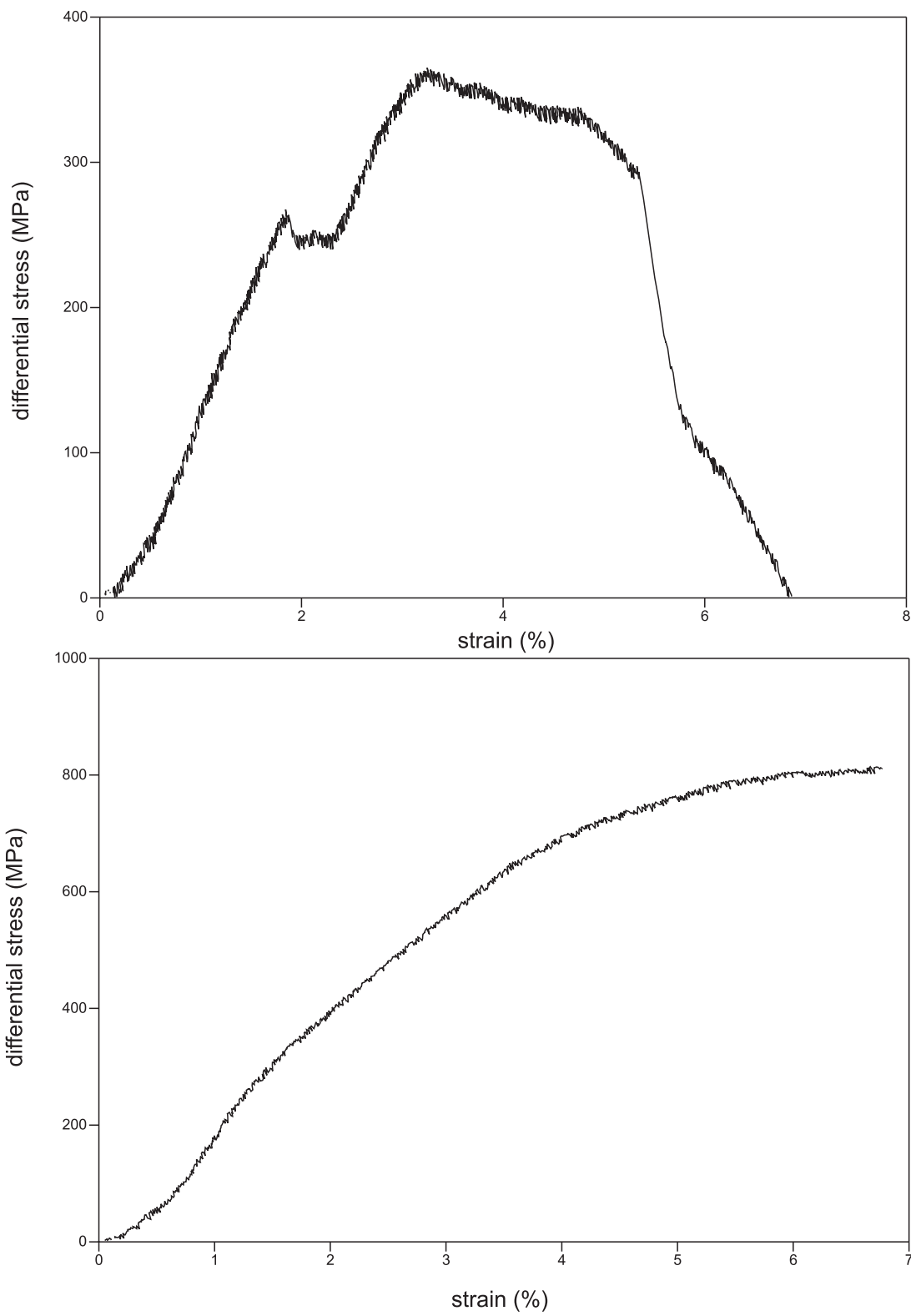


Figure 31: FC3-4 (top): $T = 1111^{\circ}\text{C}$, $\dot{\epsilon} = 5 \cdot 10^{-6}\text{s}^{-1}$ and FC3-5 (bottom): $T = 1000^{\circ}\text{C}$, $\dot{\epsilon} = 5 \cdot 10^{-6}\text{s}^{-1}$.

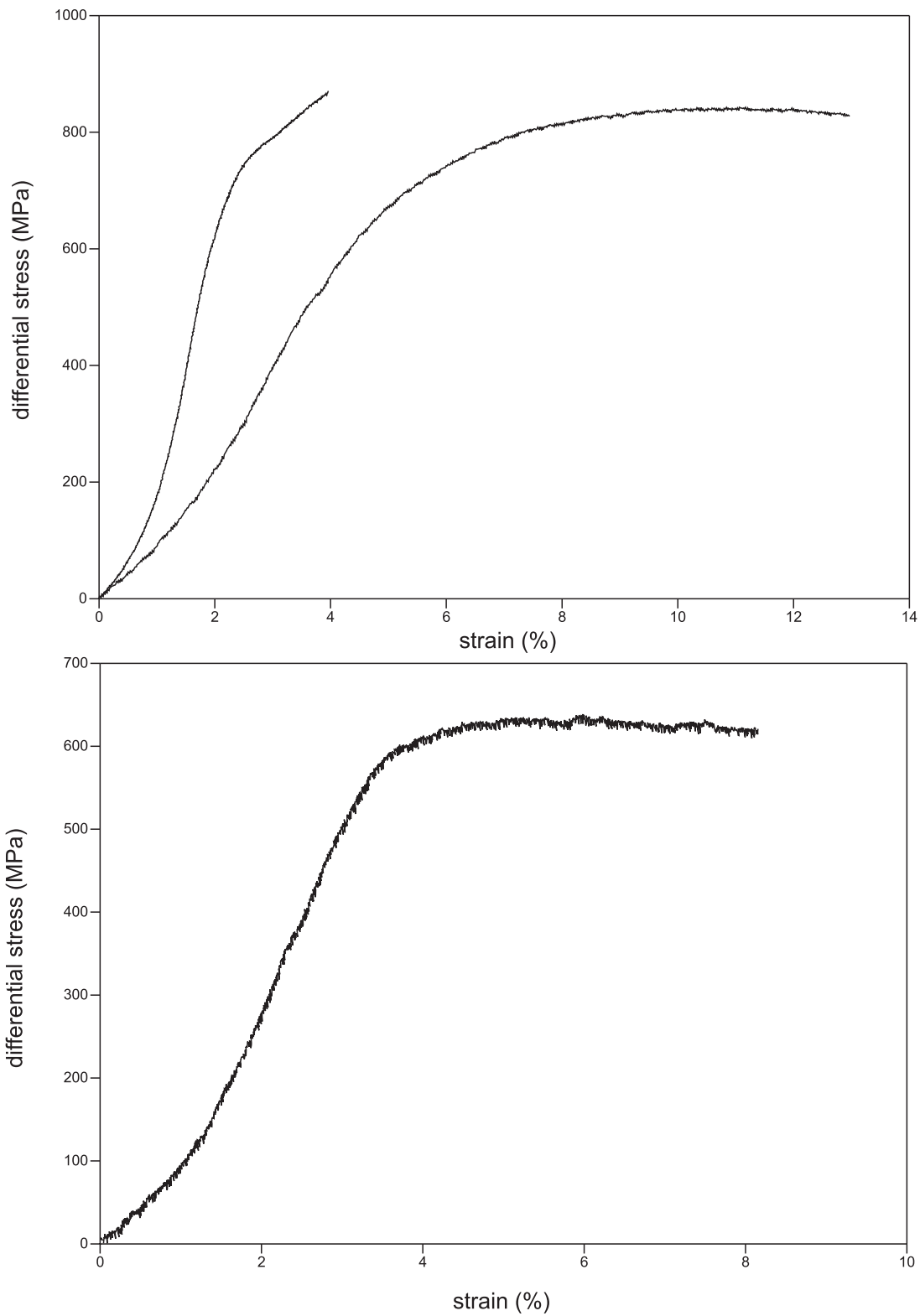


Figure 32: FC3-6 (top): $T = 988^\circ\text{C}$, $\dot{\epsilon} = 9 \cdot 10^{-5}\text{s}^{-1}$ and $T = 986^\circ\text{C}$, $\dot{\epsilon} = 5 \cdot 10^{-5}\text{s}^{-1}$ and FC3-7 (bottom): $T = 990^\circ\text{C}$, $\dot{\epsilon} = 2 \cdot 10^{-6}\text{s}^{-1}$.

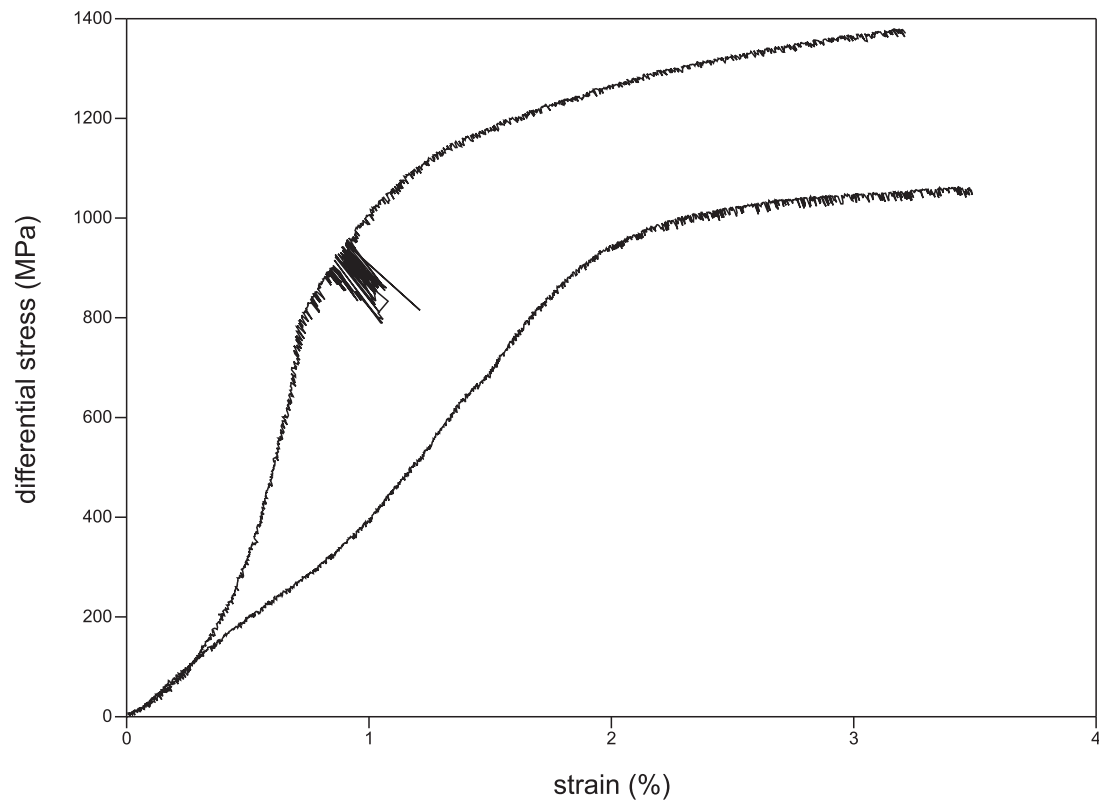


Figure 33: FC3-8: $T = 895^{\circ}\text{C}$, $\dot{\epsilon} = 5 \cdot 10^{-6}\text{s}^{-1}$ and $T = 845^{\circ}\text{C}$, $\dot{\epsilon} = 2 \cdot 10^{-6}\text{s}^{-1}$.

Lebenslauf

Zur Person:

Jens Orzol
Drusenbergstraße 22
44789 Bochum
geboren am 5. Februar 1974 in Essen
deutsche Staatsangehörigkeit
ledig

Schulbildung

1980 - 1984 Grundschule in Essen
1984 - 1993 Carl Humann-Gymnasium in Essen
05.1993 Abitur

Hochschulbildung

09.1993 Beginn des Geophysik-Studiums an der Ruhr-
Universität Bochum
06.1999 Abschluss des Studiums als Diplom-Geophysiker
Titel der Diplomarbeit: Experimentelle
Deformation von Jadeit
09.1999 Beginn der Promotion am Institut für
Geologie, Mineralogie und Geophysik

Berufstätigkeit

07.1997 bis 09.1997 Angestellter der BGR, Hannover
seit 09.1999 wissenschaftlicher Mitarbeiter an der
Ruhr-Universität Bochum im SFB 526

Acknowledgements

First, I would like to express my thanks to my advisors Prof. Dr. F. Rummel and Prof. Dr. B. Stöckhert: Prof. Dr. Rummel for his ongoing motivation and support especially at times when experimental problems dominated the work and Prof. Dr. B. Stöckhert for analysis and discussions of microstructures.

Machining of all parts necessary for the experiments and maintaining of the equipment was done by R. Bleiwei's, W. Harbott, M. Krisch and A. Tomlik. Their very good work was an absolute basic requirement to successful experimental work. They remained patient despite many unsuccessful experiments at early stages ruining their work within a few hours.

Excellent thin sections and other sample preparation was provided by D. Dettmar, E. Kessler and T. Westphal.

For analytical work on the samples I had to rely on experts. I would like to thank Dr. R. Neuser for SEM analysis, Dr. K. Röller for FTIR measurements and Dr. T. Reinecke and U. Trombach for X-ray diffraction analysis. Dr. C. Trepmann did EBSD measurements and helped in determining the critical resolved shear stress for twinning.

Though most of them have since left, the working group, namely A. Bertram, T. Hettkamp, G. Fuhrmann, D. Teza and M. Witthaus, created a good climate in the lab and helped to overcome frustrations.

I also have to thank Dr. J. Lawlis for many discussions and for thorough reading of the thesis.

D. Dorner supplied lots of criticism which was hard, but contributed substantially to improvement of the thesis. Many thanks for that.

This work was carried out within the SFB 526, Rheology of the Earth-From the Upper Crust to the Subduction Zone